



**XIX International Workshop  
on New Approaches to High-Tech:  
Nano-Design, Technology, Computer Simulations**

Нанопроектирование, технология,  
компьютерное моделирование – NDTCS-2021

October 28–29, 2021 | Minsk, Belarus

# BOOK OF ABSTRACTS

**Organizers**



Belarusian State University  
of Informatics and Radioelectronics



MIREA – Russian Technological University

**Partners**



Министерство образования Республики Беларусь  
Учреждение образования «Белорусский государственный университет  
информатики и радиоэлектроники»

**НАНОПРОЕКТИРОВАНИЕ, ТЕХНОЛОГИЯ,  
КОМПЬЮТЕРНОЕ МОДЕЛИРОВАНИЕ – NDTCS-2021**

Тезисы докладов XIX Международного симпозиума  
(Республика Беларусь, Минск, 28-29 октября 2021 года)

Book of abstracts of XIX International Workshop  
(Republic of Belarus, Minsk, October 28-29, 2021)

УДК 620.3+004.94  
ББК 30.6+32.844.2  
Н25

Редакционная коллегия:  
*В.А. Богуш* (БГУИР), *С.А. Кудж* (РТУ МИРЭА),  
*А.С. Сигов* (РТУ МИРЭА), *А.И. Мелькер* (СПбПУ),  
*В.Р. Стемпицкий* (БГУИР), *Р.В. Шамин* (РТУ МИРЭА),  
*А.Н. Юрасов* (РТУ МИРЭА)

Editorial board:  
*V.A. Bogush* (BSUIR), *S.A. Kudzh* (RTU MIREA),  
*A.S. Sigov* (RTU MIREA), *A.I. Melker* (SPbPU),  
*V.R. Stempitsky* (BSUIR), *R.V. Shamin* (RTU MIREA),  
*A.N. Yurasov* (RTU MIREA)

Н25 **Нанопроектирование, технология, компьютерное моделирование –**  
NDTCS-2021 : тез. докл. XIX Междунар. симпозиума (Республика Беларусь,  
Минск, 28-29 октября 2021 года) / редкол. : В. А. Богуш [и др.]. – Минск : БГУИР,  
2021. – 131 с.  
ISBN 978-985-543-633-2.

В сборнике представлены тезисы докладов, отобранные программным комитетом. Представлены результаты научных исследований и разработок в области электроники, наноматериалов и нанотехнологий, разноуровневого компьютерного моделирования. Сборник трудов посвящается профессору А. Л. Санину.

**УДК 620.3+004.94**  
**ББК 30.6+32.844.2**

ISBN 978-985-543-633-2

© УО «Белорусский государственный  
университет информатики  
и радиоэлектроники», 2021

## Program Committee

### Co-Chairs

**Vladimir Labunov**, Academician of NAS of Belarus, Prof., D.Sc., Professor of Micro- and Nanoelectronics Department, Head of R&D Lab “Integrated Micro- and Nanosystems”, BSUIR, Belarus.

**Anatoly Belous**, Cor.Mem. of NAS of Belarus, Prof., D.Sc., Deputy General Director of JSC “Integral” – Management Company of “Integral” Holding, Belarus.

**Alexander Melker**, Prof., D.Sc., Peter the Great Saint Petersburg Polytechnic University, Russia.

### Members

**Aleksandr Nikitin**, PhD, Assoc. Prof., Associate Professor of Department of Theoretical Physics and Heat Engineering, Yanka Kupala State University of Grodno, Belarus.

**Alexander Danilyuk**, PhD, Assoc.Prof., Associate Professor of Department of Micro- and Nanoelectronics, BSUIR, Belarus.

**Alexander Gurskij**, Prof., D.Sc., Professor of Information Security Department, BSUIR, Belarus.

**Alexander Sigov**, Academician of RAS, Prof., D.Sc., President of FSBEIHE “MIREA - Russian Technological University», Russia.

**Anatoly Gulai**, PhD, Assoc.Prof., Head of Intellectual and Mechatronic Systems Department, Belarusian National Technical University, Belarus.

**Anna Krivosheeva**, D.Sc., Leading Researcher of R&D Center “Nanoelectronics and Advanced Materials”, BSUIR, Belarus.

**Dmitri Migas**, Prof., D.Sc., Head of Department of Micro- and Nanoelectronics, BSUIR, Belarus.

**Hamit Topuz**, Prof., D.Sc., Manager of Environmental & Energy Research Center, Head of Department of Natural Sciences, Engineering Faculty, Maltepe University, Turkey.

**Hanna Bandarenka**, PhD, Assoc.Prof., Head of R&D Lab “Applied Plasmonics”, BSUIR, Belarus.

**Igor Abramov**, Prof., D.Sc., Professor of Micro- and Nanoelectronics Department, Head of R&D Lab “Physics of Micro- and Nanoelectronic Devices”, BSUIR, Belarus.

**Igor Vrublevsky**, PhD, Assoc.Prof., Head of R&D Lab “Materials and Components of Electronics and Superconducting Equipment”, Associate Professor of Information Security Department, BSUIR, Belarus.

**Jelena Tamuliene**, PhD, Senior Researcher at Institute of Theoretical Physics and Astronomy, Physics Faculty, Vilnius University, Lithuania.

**Matanat Mehrabova**, D.Sc., Assoc. Prof., Leading Researcher, Institute of Radiation Problems of Azerbaijan National Academy of Sciences, Azerbaijan.

**Mirosław Najbuk**, M.Sc., Leading Researcher, Computer Science Institute, University of Białystok, Poland.

**Nguyen Thanh Tung**, Assoc. Prof., PhD, Vice Director of Institute of Materials Science, Vietnam Academy of Science and Technology, Vietnam.

**Nikolai Gaponenko**, Prof., D.Sc., Head of R&D Lab “Nanophotonics”, BSUIR, Belarus.

**Roman Shamin**, Prof., D.Sc., Director of Institute of Physics and Technology, RTU MIREA, Russia.

**Sergei Lazarouk**, D.Sc., Head of R&D Lab “Electrochemical nano-structure materials”, BSUIR, Belarus.

**Serghej Prischepa**, Prof., D.Sc., Professor of Information Security Department, BSUIR, Belarus.

**Vazgen Melikyan**, Cor.Mem. of NAS of Armenia, Prof., D.Sc., Director of Synopsys Armenia Educational Department, NASA Presidium Member, Armenia.

**Victor Borisenko**, Prof., D.Sc., Professor of Micro- and Nanoelectronics Department, Head of R&D Center “Nanoelectronics and Advanced Materials”, BSUIR, Belarus.

**Vladimir Borzdov**, Prof., D.Sc., Head of Physical Electronics and Nano Technologies Department, Belarusian State University, Belarus.

**Yuri Pisetsky**, Prof., D.Sc., Dean of Joint Faculty of Information Technologies TUIT-BSUIR, Head of Department of Technologies of Mobile Communication, Tashkent University of Information Technologies named after Muhammad al-Khwarizmi, Uzbekistan.

**Xuan-Tu Tran**, PhD, Assoc. Prof. of Faculty of Electronics and Communications, Vietnam National University – University of Engineering and Technology, Vietnam.

## Organizing Committee

### Chair

**Vadim Bogush**, Prof., D.Sc., Rector of Belarusian State University of Informatics and Radioelectronics (BSUIR), Belarus.

**Stanislav Kudzh**, D.Sc., Rector of FSBEIHE “MIREA - Russian Technological University”, Russia.

### Members

**Viktor Stempitsky**, PhD, Assoc.Prof., Vice-Rector for R&D of Belarusian State University of Informatics and Radioelectronics (BSUIR), Scientific Supervisor of R&D Lab “Computer-aided design of micro- and nanoelectronic systems”, BSUIR, Belarus.

**Ludmila Shichko**, M.Sc., Deputy Head of R&D Department, BSUIR, Belarus.

**Ivan Lovshenko**, M.Sc., Head of R&D Lab “Computer-aided design of micro- and nanoelectronic systems”, BSUIR, Belarus.

**Elena Bakunova**, Head of Marketing and Science Communication Department, BSUIR, Belarus.

### Organizers



Belarusian State University of Informatics and Radioelectronics (BSUIR) was founded in 1964 as Minsk Radioengineering Institute. Today, it has become a large educational, scientific and innovation center in Belarus. BSUIR is the national coordinator of research on protection against inadvertent interference and on electromagnetic compatibility of radioelectronics including scientific, technical and organizational support of the State Radio Frequency Commission under the Security Council of the Republic of Belarus. The university comprises 8 faculties and 32 departments that are offering ca. 100 B.Sc., M.Sc., PhD and postdoc programmes. In addition, there are the Institute of Information Technologies (staff retraining and professional skills upgrading courses), the Minsk Radioengineering College (vocational education training), and the Research and Development Department (RDI activities).



MIREA – Russian Technological University is one of the leaders in the field of training of highly qualified specialists for quickly developing knowledge-intensive branches of science and technology: telecommunications, information and computer technologies, automatic equipment, cybernetics, radio engineering and electronics, chemistry and biotechnologies. The University implements a unique system of training «higher education institution – base chair – base enterprise» which provides high efficiency of educational process and guarantees fast adaptation of graduates to real conditions of modern production environment. Today, MIREA – Russian Technological University has more than 50 base chairs at Research Institutes of the Russian Academy of Sciences, design offices and hi-tech enterprises of the Moscow region.

### Partners



Make life good. LG Electronics and appliances feature innovative technology and sleek designs to suit your life and your style. LG Electronics focused on developing new innovations across the globe. We are committed to providing electronic products that help customers live better. To support this, we wish to continue bringing added value to the lives of consumers. We offer a wide range of products across areas including, TV & Home Entertainment, Kitchen, Laundry, Computers, Air Conditioning & Solar.



JSC “Integral” – Management Company of “Integral” Holding is the major manufacturer of electronic components in the Eastern Europe and provides (full cycle of development and production of more than 3500 types of microcircuits and semiconductor devices; design standards up to 0.35 microns; a wide range of technological processes: basic CMOS, CMOS with built-in high-voltage units, radiation-resistant CMOS, options for bipolar processes, including radiation-resistant, BiCMOS, BiCDMOS, MOSFET processes for high-power high-speed and high-voltage transistors, etc.)

## CONTENTS

<b>N. Krylova, E. Ovsyuk, A. Ivashkevich, V. Red'kov</b> Maxwell electrodynamics in media, geometry effects on constitutive relations .....	8
<b>A. Baran, V. Kudryashov</b> Energy levels of electron in circular quantum dot in the presence of spin-orbit interactions .....	9
<b>T. Sidorova, A. Danilyuk</b> Tunneling and magnetoresistance in ferromagnet/wide-gap semiconductor/ferromagnet nanostructure .....	11
<b>D. Ponkratov, E. Chudakov, A. Sotsky, V. Minkovich</b> Computer simulation of modal characteristics of photonic crystalline fibers with a layered coating .....	13
<b>O. Kulakovich</b> Plasmonic enhancement of luminescence efficiency in light emitting structures .....	15
<b>A. Kuraptsova, A. Danilyuk</b> Charging properties of the silicon / zinc oxide nanoparticle heterostructure ...	16
<b>L. Trotsiuk, A. Muravitskaya, O. Kulakovich, M. Artemyev, S. Gaponenko</b> Emission enhancement of semiconductor nanocrystals by gold nanorods: a recipe .....	18
<b>A. Felsharuk, D. Podryabinkin, A. Danilyuk</b> Plasmon effects in a graphene nanostructure .....	20
<b>H. Grushevskaya, G. Krylov</b> Electrically confined graphene quantum dots: theoretical treatment .....	22
<b>A. Ivashkevich, V. Red'kov, V. Kisel</b> Electrodynamics, complex rotation group, media .....	23
<b>A. Danilyuk, A. Trafimenko, S. Prischepa</b> Low temperature magnetoresistance in silicon doped by antimony .....	25
<b>M. Baranava, V. Stempitsky</b> <i>Ab initio</i> study of exchange interactions in the magnetic systems based on $Cr_2Ge_2X_6$ (X=S, Se, Te) .....	27
<b>T. Mikhailova, T. Myasoedova</b> Investigation of the structure of manganese-doped silicon-carbon films obtained by electrochemical method .....	28
<b>A. Baglov, L. Khoroshko</b> Atom species energy dependence on magnetic configurations in the perovskite yttrium orthoferrite .....	30
<b>H. Grushevskaya, A. Timoshchenko, I. Lipnevich</b> Emergence of topological defects in a bilayer of multiwalled carbon nanotubes irradiated by gamma-rays .....	32
<b>V. Volcheck, D. Hvazdouski, M. Baranava, V. Stempitsky</b> Temperature dependence of the thermal conductivity of Wurtzite Aluminum Nitride, Gallium Nitride and Aluminum-Gallium Nitride .....	33
<b>Moumita Pal, Reshmi Maity, Niladri Pratap Maity</b> Silicon carbide membranes for microelectromechanical systems based CMUT with influence factors .....	35
<b>N. Krylova, V. Red'kov</b> KCC-invariants-based geometrization of a theory of electromagnetic and spinor fields on the background of the Schwarzschild spacetime .....	37
<b>A. Bezrukova, O. Vlasova</b> Information - statistical approach to inverse optical problem solution for 3D disperse systems with nano and micro particles .....	38
<b>A. Basalaev, V. Kuz'michev, M. Panov, A. Petrov, O. Smirnov</b> Modeling the fragmentation of 2,5-diketopiperazine ions .....	40
<b>V. Murav'ev, V. Mishchenka</b> <i>Ab-initio</i> simulation of hydrogenated graphene properties .....	42
<b>D. Hvazdouski, V. Stempitsky</b> First-principles calculation of electronic properties of monoelement 2D materials .....	43
<b>A. Leonovich, Yu. Vyblyi</b> Spherical wave-type solution in Relativistic Theory of Gravitation .....	45
<b>A. Ponyavina, K. Barbarchyk, A. Zamkovets, S. Tikhomirov</b> Modeling of optical properties of hybrid metal-organic nanostructures .....	46
<b>V. Zalessky, A. Konoiko, V. Kravchenko, A. Kuzmitskaya</b> Minimizing the influence of temperature changes in the environment on the performance criteria of thermo-optical processor based on Fabri-Perot and Smith microresonator .....	48
<b>P. Badikova, D. Zav'yalov, D. Zharikov</b> Circular photovoltaic effect in an anisotropic graphene superlattice in the presence of a constant electric field .....	50
<b>N. Demidovich, D. Zav'yalov, A. Polikarpova</b> Development of a package for automating the pipeline processing of quantum-chemical calculations using GAMESS on a cluster with a slurm queuing system ....	52

<b>N. Vorsin, A. Gladyshchuk, T. Kushner, N. Tarasiuk, S. Chugunov, M. Borushko</b> Modeling AlGaIn p-i-n photodiodes .....	53
<b>O. Romanov, Ya. Shtykov, I. Timoshchenko</b> Photoacoustic effect in micro- and nanostructures: numerical simulations of lagrange equations .....	55
<b>G. Kostrov, D. Zav'yalov</b> Influence of supply voltage on the velocity of flight of domains in a Gunn diode .	56
<b>I. Staroverov, R. Dzerzhinsky</b> Analysis and prediction of the development of microprocessor characteristics .....	58
<b>M. Mehrabova, N. Panahov, N. Hasanov</b> <i>Ab Initio</i> calculations of electronic band structure of CdMnS semimagnetic semiconductors .....	59
<b>D. Shimanovich, D. Tishkevich, A. Vorobjova, A. Trukhanov</b> Effects of technological regimes and surface morphology on wettability properties of porous Al <sub>2</sub> O <sub>3</sub> coatings .....	60
<b>P. Vyaznikov, I. Kotilevets</b> Developing a Seq2Seq neural network using visual attention to transform mathematical expressions from images to LaTeX .....	61
<b>V. Volcheck, I. Lovshenko, V. Stempitsky</b> Design optimization of the Gallium Nitride heterostructure field-effect transistor with a graphene heat-removal system.....	63
<b>A. Khinevich, A. Stsiapanau, A. Smirnov</b> Machine learning methods for predict electrophysical properties of semiconductor materials for optoelectronic and energy storage devices .....	65
<b>I. Lovshenko, A. Voronov, P. Roshchenko, R. Ternov, V. Stempitsky</b> The proton flux influence on electrical characteristics of a dual-channel HEMT based on GaAs .....	66
<b>D. Zavyalov, E. Sivashova, E. Denisov</b> The effect of a high-frequency electromagnetic field on the breather-electric effect in a non-additive superlattice .....	68
<b>D. Shimanovich, D. Tishkevich</b> The comparative analysis of technological regimes for improving the electrical insulation strength of double-sided alumina bases with vias .....	70
<b>A. Kupchishin, M. Niyazov, B. Taipova, D. Utepova, B. Tronin</b> Study of the influence of temperature and load on the mechanical properties of unirradiated and irradiated plexiglass of different types in the flat straight bending test .....	71
<b>N. Voronova, A. Kupchishin, A. Kupchishin, T. Shmygaleva</b> Computer modeling of cascade probabilistic functions, energy spectra of PKA and concentration of vacancy clusters in materials irradiated with light ions .....	73
<b>S. Miskiewicz, A. Komarov, F. Komarov, V. Yuvchenko, G. Zayats</b> Simulation of radiation damage of the semiconductor devices .....	74
<b>V. Kovtun-Kuszhel, M. Bachko, Ya. Drobatau</b> The effect of the electromagnetic radiation wavelength on the near-field characteristics of finite-length dielectric cylinders .....	75
<b>I. Vrublevsky, A. Tuchkovsky, N. Lushpa, Pham Gia Vu, Tran Dai Lam</b> Effect of thermal treatment on the electrical and photovoltaic characteristics of methylammonium lead triiodide perovskite films .....	76
<b>A. Rudnitsky, N. Poleschuk</b> Study of photonic nanojets in the diffraction wave fields of complex-shape dielectric particles .....	78
<b>S. Lazarouk, U. Dudzich, A. Klyutsky, A. Dolbik, V. Labunov</b> Photosensitive properties of avalanche LEDs based on nanostructured silicon .....	79
<b>L. Kushner, I. Kuzmar</b> Non-stationary electrolysis for nickel nanocomposite plating.....	80
<b>A. Poznyak, A. Kukhta</b> Modification of anodic alumina by laser irradiation during anodizing .....	82
<b>A. Kistanov, R. Botella, E. Korznikova, A. Smirnov, S. Zhuk</b> Density functional theory-based study of Cu <sub>2</sub> TiSnS <sub>4</sub> and Cu <sub>2</sub> VSnS <sub>4</sub> for photovoltaic applications.....	84
<b>S. Biran, D. Korotkevich, A. Korotkevich, K. Garifov, A. Dashkevich</b> Influence of radiation expoure on the properties of dielectric layers based on anodic aluminum oxide .....	85
<b>A. Hubarevich, Ya. Mukha, A. Smirnov</b> Optical properties of thin metallic nano-patterned films for display applications .....	86
<b>D. Bykouski, A. Charkovskij</b> Development of the library for 3D modeling and computer-aided design of plated knitted fabrics.....	88
<b>Dao Dinh Ha, V. R. Stempitsky</b> Design and simulation of 3D magnetic field sensors with integrated magnetic concentrator .....	89

<b>A. Golovach, N. Kovalchuk, M. Mikhailik, Y. Kukuts, L. Dronina, I. Komissarov, S. Prischepa</b> Schottky barrier height and ideality factor of CVD graphene/n-Si heterojunction .....	91
<b>Tran Van Trieu, I. Lovshenko, V. Sadchenko, V. Stempitsky</b> Studying the influence of microbolometer structure and geometry on the parameters of infrared detectors .....	93
<b>A. Belko, N. Babarika, I. Zeylikovich, A. Nikitin</b> Modification of the RLA model for presenting a cluster system of a composite material with a fractal filler structure .....	95
<b>E. Zhuravleva, L. Studenikina</b> Forecasting the level of assimilation of mathematical knowledge as a stage in modeling the educational process of a university in a blended learning environment .....	97
<b>I. Zeylikovich, A. Nikitin, A. Belko</b> Integration of general physics experiments with mathematical simulation.....	98
<b>I. Drozdov</b> Time series analysis of water pollution data .....	100
<b>A. Shatina, A. Cheshkova</b> Delaunay variables in model problems of celestial mechanics and cosmodynamics .....	102
<b>A. Fomchenko</b> Comparison of hybrid approaches in classification using decision trees and neural networks.....	104
<b>A. Verkner, A. Asanov</b> Mathematical modeling of the dynamics of a four-point platform of a heavy-duty vehicle.....	105
<b>V. Aristov, A. Stroganov, A. Yastrebov</b> Mathematical simulation of the spatial spread of COVID-19 waves in Russia .....	106
<b>Y. Hudak, D. Parfenov, A. Beskin, I. Dragileva</b> Model of lossy layered systems .....	107
<b>N. Lomov, A. Shelepin</b> 3D cave model with sparse data .....	108
<b>V. Sleptsov, A. Ablaeva</b> Determination of quality indicators of controlled electric drives at the design stage by the method of circuit simulation .....	109
<b>A. Shmeleva, I. Goldobin, E. Klimova, A. Moskvina, Y. Lygarev</b> Machine learning methods for evaluating innovative projects.....	111
<b>M. Beskhamel'nov, N. Shmeleva, S. Shilkov, M. Lygarev</b> Distance learning as an imperative for digitalization of education .....	113
<b>V. Kulagin, A. Alexandrov</b> Destruction processes in power plants as a practical example for the course of mathematical modeling.....	114
<b>A. Kryuchkov, A. Korolkov</b> Simulation of some security tasks for secure telecommunications using a quantum-computing simulator in one of the quantum programming languages .....	116
<b>V. Skobtsov, N. Lapitskaja</b> Software tool for evaluation of reliability and survivability of complex technical system bases on logical-probabilistic methodology .....	118
<b>A. Asanov, E. Guryanova</b> Representation of a transmission model with continuous power flow in state space .....	119
<b>A. Markov, A. Paramonov</b> Parameters of load testing models: approaches to estimation.....	122
<b>R. Shatovkin, Y. Parshenkova, V. Filatov</b> Effectiveness indicators of modeling the air situation.....	124
<b>R. Shatovkin, A. Rusakov, B. Anufriev</b> Methodology for assessing the effectiveness of modeling the air situation .....	126
<b>R. Shatovkin, O. Trubienko, A. Khudyakov</b> Analytical-simulation modeling of the air situation .....	128
<b>V. Feodorov, S. Harlamov</b> On the restoration of the blurred image of a moving object .....	130



# MAXWELL ELECTRODYNAMICS IN MEDIA, GEOMETRY EFFECTS ON CONSTITUTIVE RELATIONS

N.G. Krylova<sup>1</sup>, E.M. Ovsyuk<sup>2</sup>, A.V. Ivashkevich<sup>3</sup>, V.M. Red'kov<sup>3</sup>

<sup>1</sup> Belarusian state agrarian technical university, Minsk, Belarus

<sup>2</sup> Mozyr State Pedagogical University, Mozyr, Belarus

<sup>3</sup> B.I. Stepanov Institute of Physics of the National Academy of Science of Belarus, Minsk, Belarus

## I. INTRODUCTION

The problems of constitutive relations in Maxwell electrodynamics, their possible form, its behavior under the motion of the reference frame, its connection with Special Relativity theory, interplay between constitutive relations and gravity are reviewed. The main accent in our treatment is the known possibility to simulate material media by geometrical methods.

These problems have a long history. We can track interest to the problem in the huge literature that has been produced on this issue. Note that Gordon [2] was first seemed largely interested in trying to describe dielectric media by an effective metrics; Gordon tried to use a gravitational field to mimic a dielectric medium. The idea was taken up and developed by Tamm and Mandel'stam [3, 4]; also see [5-20].

## II. GEOMETRICAL MODELING OF THE CONSTITUTIVE RELATIONS IN ELECTRODYNAMICS

The basic relations are as follows. Effective constitutive equation generated by the Riemannian geometry with metric  $g_{\alpha\beta}(x)$  have the form

$$D^i = \epsilon_0 \epsilon^{ik}(x) E_k + \epsilon_0 c \alpha^{ik}(x) B_k, \quad H^i = \epsilon_0 c \beta^{ik}(x) E_k + \mu_0^{-1} (\mu^{-1})^{ik}(x) B_k.$$

Four dimensionless  $(3 \times 3)$ -matrices  $\epsilon, \alpha, \beta, \mu^{-1}$  are not independent because they are bilinear functions of only 10 components of the symmetrical tensor  $g_{\alpha\beta}(x)$ :

$$\epsilon^{ik} = \sqrt{-g}(g^{00}g^{ik} - g^{0i}g^{0k}), \quad \alpha^{ik} = +\sqrt{-g}g^{ij}g^{0l}\epsilon_{ljk},$$

$$\beta^{ik} = -\sqrt{-g}g^{0j}\epsilon_{jil}g^{lk}(x), \quad (\mu^{-1})^{ik} = 12\sqrt{-g}\epsilon_{imn}g^{ml}g^{nj}\epsilon_{ljk}(\mu^{-1})^{ik}.$$

These tensors obey the following symmetry constraints:  $\epsilon^{ik} = +\epsilon^{ki}$ ,  $(\mu^{-1})^{ik} = +(\mu^{-1})^{ki}$ ,  $\beta^{ki}(x) = \alpha^{ik}$ ; so the  $(6 \times 6)$ -matrix defining constitutive equations is symmetrical. Metrical tensors which are the most interesting in the General relativity have a quasi-diagonal structure  $g_{0i}(x) = 0$ , and the corresponding constitutive relations simplify

$$\epsilon^{ik} = \sqrt{-g}g^{00} \begin{vmatrix} g^{11} & g^{12} & g^{13} \\ g^{21} & g^{22} & g^{23} \\ g^{31} & g^{32} & g^{33} \end{vmatrix}, \quad (\mu^{-1})^{ik} = \sqrt{-g} \begin{vmatrix} G^{11} & G^{12} & G^{13} \\ G^{21} & G^{22} & G^{23} \\ G^{31} & G^{32} & G^{33} \end{vmatrix},$$

where  $G^{ik}(x)$  stand for (algebraic) co-factors to the elements  $g^{ik}(x)$ . According to this, two tensor  $\epsilon(x)$  and  $\mu^{-1}(x)$  obey the following constraint

$$\epsilon(x)\mu^{-1}(x) = I.$$

Thus, the metric tensors with quasi-diagonal structure effectively describe media with following constitutive relations

$$D = -\epsilon_0 \epsilon(x) E, \quad B = \mu_0 \mu(x) H, \quad \mu(x) = -\epsilon(x),$$

$$(\epsilon^{ik})(x) = \sqrt{-g(x)} g^{00}(x) \begin{vmatrix} g^{11}(x) & g^{12}(x) & g^{13}(x) \\ g^{21}(x) & g^{22}(x) & g^{23}(x) \\ g^{31}(x) & g^{32}(x) & g^{33}(x) \end{vmatrix}.$$

## III. CONCLUSIONS

Application of the Riemannian geometry permits to simulate effective media which constitutive equations are determined by the metrical structure of the Riemann spaces. Because there are known numerous Riemannian geometries, the number of such effective media is enormous as well.

## REFERENCES

- [1] Minkowski, H., Die Grundlagen für die electromagnetischen Vorgänge in bewegten Körpern. Nachrichten von der Königlichen Gesellschaft der Wissenschaften zu Göttingen, mathematisch-physikalische Klasse. 1908. 53–111; reprint in Math. Ann. 1910. 68. 472–525.
- [2] Gordon W. Zur Lichtfortpanzung nach der Relativitätstheorie. Ann. Phys. (Leipzig): 1923;72: 421–456.

- [3] Tamm IE. Elektrodinamika anizotropnoi sredy v spetsialnonoi teorii otноситelnosti. Zh. R, F, Kh. O, Fiz. dep.: 1924;56(2–3): 248–262. Tamm IE. Kristallogoptika teorii otноситelnosti v svyazi s geometriei bikvadratichnoi formuy. Zh. R, F, Kh. O, Fiz. dep.: 1925;54(3–4): 1.
- [4] Mandelstam LI, Tamm IE. Elektrodynamik der anisotropen Medien und der speziellen Relativitatstheorie. Math. Annalen: 1925;95: 154–160.
- [5] Landau LD, Lifsjitz EM. Theoretical physics. Vol. 2. Field theory. Moscow: Science; 1973.
- [6] Balazs NL. Effect of a gravitational field, due to a rotating body, on the plane of polarization of an electromagnetic wave. Phys. Rev.: 1958;110: 236–239.
- [7] Tomil'chik LM, Fedorov FI. Magnetic anisotropy as metrical property of space. Crystallography.: 1959;4(4): 498–504.
- [8] Post E. Formal Structure of Electrodynamics. General Covariance and Electromagnetics. Amsterdam: North–Holland; 1962.
- [9] De Felice F. On the gravitational field acting as an optical medium. Gen. Relat. Grav.: 1971;2: 347–357.
- [10] Bolotovskiy BM, Stolyarov SN. Modern state of electrodynamics of moving media. Uspekhi Fizicheskikh Nauk: 1974;114(4): 489–529.
- [11] Schleich W, Scully MO. General relativity and modern optics. In: New Trends in Atomic Physics, Les Houches, Session XXXVIII, 1982. Eds.: G. Grynberg, R. Stora. Amsterdam: North–Holland, 1984.
- [12] Hillion P. Constitutive relations and Clifford algebra in electromagnetism. Adv. Appl. Clifford Alg.: 1995;5: 141–158.
- [13] Leonhardt U. Space–time geometry of quantum dielectrics. Phys. Rev. A.: 2000;62: 012111.
- [14] De Lorenci WA, Klippert R, Obukhov YN. On optical black holes in moving dielectrics. Phys. Rev. D.: 2003;68: 061502.
- [15] Hehl FW, Obukhov YN. Linear media in classical electrodynamics and the Post constraint. Phys. Lett. A.: 2005;334: 249–259.
- [16] Novello M, Salim JM. Effective electromagnetic geometry. Phys. Rev. D.: 2001;63: 083511.
- [17] Novello M, Perez Bergliaffa S, Salim J. Analog black holes in flowing dielectrics. Class. Quant. Grav.: 2003;20: 859–872.
- [18] Nandi KK et al. Analog of the Fizeau effect in an effective optical medium. Phys. Rev. D.: 2003;67: 025002.
- [19] Red'kov VM. Particle fields in Riemannian space and the Lorentz Group. Minsk: Belarusian Science; 2009.
- [20] A.V. Ivashkevich, E.M. Ovsyuk, V.V. Kisel, V.M. Red'kov. Spinor Maxwell equations in Riemannian space-time and the geometrical modeling of constitutive relations in electrodynamics. Materials Physics and Mechanics. 2020. Vol. 45, no 1, P. 104–131.

## ENERGY LEVELS OF ELECTRON IN CIRCULAR QUANTUM DOT IN THE PRESENCE OF SPIN-ORBIT INTERACTIONS

A.V. Baran, V.V. Kudryashov

Institute of Physics, National Academy of Sciences of Belarus, Minsk, Belarus

[a.baran@dragon.bas-net.by](mailto:a.baran@dragon.bas-net.by)

### I. INTRODUCTION

The motion of an electron in an inner layer of a double semiconductor heterostructure is usually treated as two-dimensional. In addition, the planar motion is also restricted if an electron is placed in quantum dot localized in a middle layer of heterostructure. The Rashba [1] and Dresselhaus [2] spin-orbit interactions are presented by the formulas  $V_R = \alpha_R (\sigma_x p_y - \sigma_y p_x) / \hbar$  and  $V_D = \alpha_D (\sigma_x p_x - \sigma_y p_y) / \hbar$ , where  $\sigma_x$  and  $\sigma_y$  are the standard Pauli spin-matrices. The Rashba interaction strength can be controlled by an external electric field, and the Dresselhaus interaction strength can be varied by changing the width of quantum well along the  $z$  axis. In the general case the whole spin-orbit interaction has the form  $V_R + V_D$ . At the same time, the

considerable attention is paid to the special case, when the spin-orbit interactions of Rashba and Dresselhaus have equal strengths  $\alpha_R = \alpha_D$ .

As a rule, the circular quantum dot is simulated with the help of axially symmetric confinement potentials  $V(\rho)$ , where  $\rho = \sqrt{x^2 + y^2}$ . In [3, 4], the simple but sufficiently adequate rectangular potential of finite depth was proposed. This model with discontinuous potential describes the main properties of circular quantum dots but without taking into account the individual characteristics. In [5], the smooth confinement potential of new type was applied in the case of  $\alpha_R = \alpha_D$ . Now we use this potential in order to calculate the energy levels of electron for unequal but close strengths  $\alpha_R \neq \alpha_D$ .

## II. METHODS AND RESULTS

The circular quantum dot of radius  $\rho_0$  is described by means of the confinement potential  $V(\rho) = V_0 v(r)$ , where  $V_0$  is the depth of potential well. The function  $v(r)$  depends on ratio  $r = \rho / \rho_0$  in the following way:  $v(r) = 0$  for  $0 < r < g$ ,  $v(r) = v_1(r)$  for  $g < r < s$ ,  $v(r) = v_2(r)$  for  $s < r < 1$ , and  $v(r) = 1$  for  $r > 1$ . The functions  $v_1(r)$  and  $v_2(r)$  are of the form

$$v_1(r) = \frac{1}{2} \frac{(1+s^2)}{(1-g^2)(s^2-g^2)} \left( r - \frac{g^2}{r} \right)^2, \quad v_2(r) = 1 - \frac{1}{2} \frac{(g^2+s^2)}{(1-g^2)(1-s^2)} \left( r - \frac{1}{r} \right)^2. \quad (1)$$

The parameters  $g$  and  $s$  change within ranges  $0 < g < 1$  and  $g < s < 1$ .

The total Hamiltonian can be written as a sum  $H = H_0 + H_1$ , where  $H_0 = (p_x^2 + p_y^2) / 2\mu + V(\rho) + (\alpha_R + \alpha_D)(\sigma_x - \sigma_y)(p_x + p_y) / 2\hbar$ ,  $\mu$  is the effective electron mass and  $H_1 = \gamma(\alpha_R + \alpha_D)(\sigma_x + \sigma_y)(p_y - p_x) / 2\hbar$ ,  $\gamma = (\alpha_R - \alpha_D) / (\alpha_R + \alpha_D)$ . It is easy to show that the solutions of the unperturbed Schrödinger equation  $H_0 \Psi_0 = E_0 \Psi_0$  admit a factorization

$$\Psi_0^\pm(x, y) = \frac{1}{\sqrt{2}} \left\{ \begin{array}{c} 1 \\ \pm e^{-i\pi/4} \end{array} \right\} \exp \left[ \mp \frac{(\alpha_R + \alpha_D)\mu}{\sqrt{2}\hbar} (x \mp y) \right] e^{im\phi} u(\rho), \quad m = 0, \pm 1, \pm 2, \dots \quad (2)$$

Here  $m$  is the angular momentum quantum number. Introducing dimensionless quantities  $e_0 = 2\mu\rho_0^2 E_0 / \hbar^2$ ,  $v_0 = 2\mu\rho_0^2 V_0 / \hbar^2$  and  $a = \mu\rho_0(\alpha_R + \alpha_D) / \hbar$  we get the radial equation

$$\frac{d^2 u}{dr^2} + \frac{1}{r} \frac{du}{dr} - \frac{m^2 u}{r^2} + (e_0 + a^2 - v_0 v(r)) u = 0. \quad (3)$$

In the regions  $0 < r < g$  and  $r > 1$ , the exact solutions of this equation are expressed via the Bessel functions and in the region  $g < r < s$ , we get the solutions in terms of the confluent hypergeometric functions.

We introduce the dimensionless perturbation  $h_1 = 2\mu\rho_0^2 H_1 / \hbar^2$ . Since each energy level of the unperturbed system is doubly degenerate with two eigenfunctions  $\Psi_0^\pm$  we consider the contribution of  $h_1$  with the help of the perturbation theory in the degenerate case for the small value of  $\gamma$ . We have the following equalities  $\langle \Psi_0^+ | h_1 | \Psi_0^+ \rangle = \langle \Psi_0^- | h_1 | \Psi_0^- \rangle = 0$ ,  $\langle \Psi_0^+ | h_1 | \Psi_0^- \rangle = \langle \Psi_0^- | h_1 | \Psi_0^+ \rangle = \gamma\delta$ , where

$$\delta = -2ma \int_0^\infty J_1(2ar) u^2(r) dr / \int_0^\infty u^2(r) r dr. \quad (4)$$

Then we obtain splitting  $e^\pm = e_0 \pm \gamma\delta$  for energy levels. Further, we calculate the dependence of energy on potential parameters.

Now we present some numerical results in the case  $m = 1$ ,  $a = 1$  for the lower energy levels. If  $v_0 = 100$  then  $e_0 = 78.2272$ ,  $\delta = 1.87550$  for  $g = 0.1$ ,  $s = 0.325$  and  $e_0 = 12.1710$ ,  $\delta = 1.65410$  for  $g = 0.9$ ,  $s = 0.975$ . If  $v_0 = 400$  then  $e_0 = 154.175$ ,  $\delta = 1.95605$  for  $g = 0.1$ ,  $s = 0.325$  and  $e_0 = 13.6850$ ,  $\delta = 1.68944$  for  $g = 0.9$ ,  $s = 0.975$ .

### III. CONCLUSIONS

The confinement model potential for quantum dot considered in the present paper is smooth, has finite depth and width and permits the exact solutions of the separated unperturbed Schrödinger equation for electron states in the presence of spin-orbit interaction of Rashba and Dresselhaus. The contribution of perturbation is really small in comparison with the unperturbed energy  $e_0$  if the strength  $\alpha_R$  is sufficiently close to the strength  $\alpha_D$  ( $\gamma \ll 1$ ).

### REFERENCES

- [1] Yu.A. Bychkov, E.I. Rashba, "Oscillatory effects and the magnetic susceptibility of carriers in inversion layers", J. Phys. C., Vol. 17, pp. 6039–6045, 1984.
- [2] G. Dresselhaus, "Spin-orbit coupling effects in zinc blende structures", Phys. Rev., Vol. 100, pp. 580–586, 1955.
- [3] V. V. Kudryashov, "Electron in a quantum dot with account of the Rashba spin-orbit interaction", Proc. of the XIII Intern. School-Conference «Foundations and Advances in Nonlinear Science», Vol. 13, pp. 125–130, 2006.
- [4] A.V. Chaplik, L.I. Magarill, "Bound states in a two-dimensional short range potential induced by the spin-orbit interaction", Phys. Rev. Lett., Vol. 96, p. 126402, 2006.
- [5] V.V. Kudryashov, A.V. Baran, "Influence of Rashba and Dresselhaus Spin-Orbit Interactions of Equal Strengths on Electron States in Circular Quantum Dot", Nonlinear Dynamics and Applications. Vol. 27, pp. 24–30, 2021.

## TUNNELING AND MAGNETORESISTANCE IN FERROMAGNET/WIDE-GAP SEMICONDUCTOR/FERROMAGNET NANOSTRUCTURE

T. N. Sidorova, A. L. Danilyuk

Belarussian States University of Informatics and Radioelectronics, Minsk, Belarus

[sharsu\\_antea@bk.ru](mailto:sharsu_antea@bk.ru)

### I. INTRODUCTION

Ferromagnet/wide-gap semiconductor/ferromagnet (FM/WGS/FM) nanostructures attract a great interest during the last decade regarding their prospects for creating information-processing devices, including spintronic devices. Previously, the tunneling magnetoresistance (TMR) in such nanostructures was calculated using one-band insulator model. In this article the charge carrier transport model in the ferromagnet/wide-gap semiconductor/ferromagnet based on two-band Franc-Keine model (FKM) and phase function model is proposed [1]. It is taken into account that tunneling barrier with the width  $d$ , which was founded by the band gap, does not represent the potential step, but the energy band-gap. Its upper border is the bottom of the conduction band  $E_C$ , and the bottom part is the top of the valence band  $E_V$ . Inside this area the wave vector of the electron is an imaginary value.

### II. MODEL

In FKM in order to calculate tunnel current density following equation is used [1,2]:

$$J(V) = \frac{4\pi q m_i}{h^3} \int_0^\infty dE [f_L(E) - f_R(E, V)] \int_0^{(m/m_i)E} dE_p T_\sigma(E, E_p, V), \quad (1)$$

where  $E$  is the full electron energy,  $E_p$  is the electron energy component which is parallel to the tunneling barrier surface,  $m$  and  $m_i$  are the electron effective masses in electrode and WGS,  $q$  is the electron charge,  $f_L(E)$ ,  $f_S(E)$  are the Fermi-Dirac distribution functions for left and right electrodes,  $T_\sigma(E, E_p, V)$  is the tunnel transparency of the barrier,  $\sigma$  is the spin index (spin –up and spin-down).

To find the transmission coefficients we develop a model on the basis of phase functions [3]. The model takes into account the barrier parameters, the image force potential and allows including the potential relief at the interfaces and in the volume of the wide-gap semiconductor. The main feature of the phase function method is that to obtain the transmission coefficients, so it is not necessary to approximate the potential barrier by rectangular potentials and to link the Schrödinger equation solutions from different regions. This process is too laborious for the potential of complex shape, besides it is very difficult to estimate faults of the results. In the phase function method not a wave function, but only its changes, as a result of potential actions, are calculated. Using phase function method it is possible to calculate tunneling transmission for potentials of any complexity, including complex and potentials depending from energy.

The tunneling transmission coefficient is [3]:

$$T_{\sigma} = \exp \left[ \frac{1}{k_{\sigma}} \int_0^d U_{eff}(z) [b_{\sigma}(z) \cos(2k_{\sigma}z) - a_{\sigma}(z) \sin(2k_{\sigma}z)] dz \right]. \quad (2)$$

Here  $U_{eff}$  – effective potential which defines the potential relief of the structure,  $a_{\sigma}$  and  $b_{\sigma}$  functions are defined by the equations based on the Phase function method,  $a, b$  are WGS layer coordinates,  $k_{\sigma}$  is the wave number,  $k_{\sigma}^2 = (2m/h^2 E_G)[(E-E_c)(E-E_v)] - k_p^2$ . Where  $k_z, k_p$  are wave number components which are perpendicular and parallel to the barrier, correspondingly,  $E_G$  is the band-gap width,  $h$  is the Planck constant. According to the dispersion law, states located in the midgap sustain the largest attenuation in the barrier. Therefore if Fermi level of the observed nanostructure is located near the bottom of the band-gap, the bias voltage  $V$  shifts the levels of the tunneling electrons to the area of the lower barrier transparency. This shifting is the reason of the tunneling current decrease.

### III. RESULTS AND DISCUSSION

Tunneling transmission coefficient depending from applied bias  $V$  at the variation of the layer thickness (WGS  $d$ ) was calculated, Fig. 1. Received dependences are oscillating and characterized by the maximums (picks) shiftings and changings of their amplitude at the variation of the thickness  $d$ . When thickness value increases from  $d=1\text{nm}$  to  $2\text{ nm}$  first pick is moving from  $V=1\text{ V}$  to  $2\text{ V}$ , and the second pick from  $V=2$  to  $4\text{ V}$ . And opposite at decreasing thickness value up to  $d=0.5\text{ nm}$  3 picks are observed: at  $0.45, 1.9$  and  $4\text{ V}$ . Picks amplitude also depends on  $d$ . At thickness value rising from  $c\ 1\text{nm}$  to  $2\text{nm}$  first pick amplitude increases, but the second pick amplitude falls. At  $d=0.5\text{ nm}$ , vice-versa, first pick amplitude is the lowest, but the third pick amplitude has the maximal value.

We have also calculated dependencies of tunneling current at fixed WGS thickness and changeable value of band, Fig.2. In this case no picks moving is observed, only picks amplitude is changed. Picks' maximums are at  $1\text{ V}$  и  $3.9\text{ V}$  accordingly. So, at increasing  $E_G$  from  $7.5\text{ eV}$  to  $8.5\text{ eV}$  current density at the first pick is changed from  $125\text{ A/m}^2$  to  $180\text{ A/m}^2$ , but at the second pick from  $120\text{ A/m}^2$  to  $175\text{ A/m}^2$ , Fig.2. Tunneling magnetoresistance (TMR) from WGS thickness was also calculated. Its value is  $3\text{-}8\%$ , Fig.3.

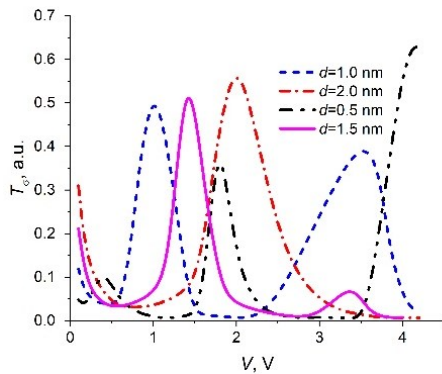


Figure 1. Transmission coefficient vs applied bias  $V$ :  $d=0.5\text{-}2\text{ nm}$ ,  $E_G=8\text{ эВ}$

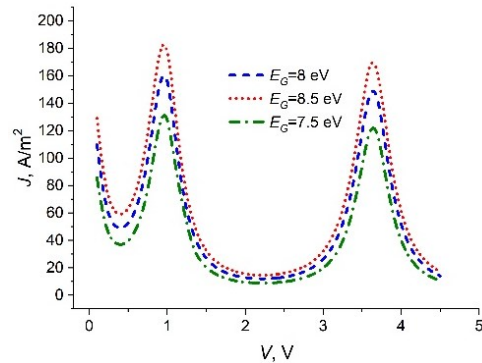


Figure 2. Current density vs applied bias  $V$ :  $E_G=7.5\text{-}8\text{ эВ}$ ,  $d=2\text{ nm}$

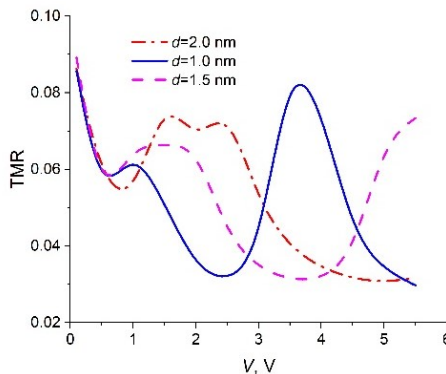


Figure 3. TMR vs WGS thickness,  $d=1\text{-}2\text{ nm}$

TMR dependences at different thicknesses  $d$  are non-monotonous, first maximums are shifted to the areas of the higher biases at increasing WGS thickness. Amplitude of the first maximums rises from  $6$  to  $7.5\%$ . Second maximums shift to the areas of the higher bias  $V$  with  $d$  increasing, but the values of their amplitudes are falling. Maximum TMR value is  $8\%$  at  $d=1\text{nm}$  and  $V=3.9\text{ V}$  (line 2).

### III. CONCLUSIONS

Tunneling coefficient, current density and TMR in FM/WGS/FM structure based on two-band Franc-Keine model and phase function method were calculated. It was shown that parameter oscillates at applied bias increasing. It explains by the presence of the alternate areas with the high and low tunneling transparency, where tunneling electrons layers exist. This area burst because of the changing of the Fermi quasi-layer position and generation of the additional tunneling channels in two-band wide gape semiconductor. Oscillation of the transmission coefficient sustain phase and amplitude changings, При этом осцилляции коэффициента прохождения претерпевают фазовые и амплитудные изменения, conditioned by the height and thickness of the WGS potential barrier. Represented dependencies of the TMR from the applied bias are explained by the combination spin polarization of the tunneling electrons and non-monotonous dependence transmission coefficient from energy.

### REFERENCES

- [1] T.A. Khachaturova, A.I. Khachaturov "Negative differential conductivity of metal-insulator-metal tunneling structures" JETP, Vol.107, pp. 864-869, 2008.
- [2] K.N. Gundlach "Theory of metal-insulator-metal tunneling for a simple two-band model" J. Appl. Phys, Vol. 44, pp. 5005-5010, 1973.
- [3] V.V. Babikov, Phase Function Method in the Quantum Mechanics (Nauka, Moscow, 1976) [in Russian].

## COMPUTER SIMULATION OF MODAL CHARACTERISTICS OF PHOTONIC CRYSTALLINE FIBERS WITH A LAYERED COATING

D. Ponkratov<sup>1</sup>, E. Chudakov<sup>1</sup>, A. Sotsky<sup>1</sup>, V. Minkovich<sup>2</sup>

<sup>1</sup> Mogilev State A. Kuleshov University, Mogilev, Belarus

<sup>2</sup> Centro de Investigaciones en Optica, Leon, Mexico

[d1monka@inbox.ru](mailto:d1monka@inbox.ru)

### I. INTRODUCTION

Currently, the most spread methods for computer modeling of transmission properties of photonic-crystal fibers (PCFs) are the finite difference method and the finite element method. Their implementation requires a limited 2D computational window surrounding the fiber cross-section. But PCFs are open 3D dielectric structures. In this case, perfectly matching layers (PMLs) are used to model open space, placed at the boundaries of the computational window. However, only unlimited planar PMLs, which cannot be used to bound the 2D computational window, can completely absorb the radiation incident on them. This leads to uncontrollable errors in the calculation of the mode attenuation coefficients caused by confinement losses. This limitation makes it difficult to estimate the transmission spectra of PCFs, that are necessary for the design of fiber-optic sensors.

To correctly take into account the open nature of the electrodynamics problem, the method of Green's functions can be used [1]. In its initial form this method has been formulated for PCFs formed in a dielectric matrix by air channels of circular cross section. In this case mode field components are represented by rows in cylindrical functions and the standard Graph addition theorem for the two dimensional Green's function is used. But if the channels have more complicated cross sections this approach loses its applicability. In addition, the method [1] is not applicable in the case when a layered absorbing coating is applied to the outer surface of the PCF, which is a key element of the currently intensively studied fiber-optic sensors, using the lossy mode resonance effect [2].

This report presents the development of the method of Green's functions, performed with the aim of overcoming the above limitations. On the basis of the relations obtained, the modulation characteristics of a photonic crystal sensor of hydrogen concentration in the atmosphere are assessed.

### II. DESIGN RATIOS

As the electrodynamics potential functions, we choose the longitudinal components of the electromagnetic field of a PCF mode  $E_z$  and  $H_z$  ( $0z$  is the PCF uniformity axis). Let the PCF consists of parallel air channels located in a dielectric matrix with permittivity  $\epsilon_s$ . The cross-sectional perimeter of the  $i$ -th channel is described by a function  $\rho_i(\varphi_i)$  (for a circular channel  $\rho_i(\varphi_i) = const$ ), where  $\rho_i$  and  $\varphi_i$  are the local polar coordinates of the channel. The following Fourier series can be written on the perimeter

$$\begin{aligned}
E_z &= \sum_{v=-m}^m e_v^{(j)} \exp(iv\varphi_j), \nabla_n E_z = \sum_{v=-m}^m e_v'^{(j)} \exp(iv\varphi_j), \\
H_z &= \sum_{v=-m}^m h_v^{(j)} \exp(iv\varphi_j), \nabla_n H_z = \sum_{v=-m}^m h_v'^{(j)} \exp(iv\varphi_j),
\end{aligned} \tag{1}$$

where  $\nabla_n$  denotes the normal derivatives of the functions,  $e_v^{(i)}$ ,  $e_v'^{(i)}$ ,  $h_v^{(i)}$ ,  $h_v'^{(i)}$  are unknown coefficients,  $m$  is the order of the Fourier polynomials. The outer surface of the PCF is coated with  $n$  layers. The thickness and permittivity of  $j$ -th layer are  $d_j$  and  $\varepsilon_j$ , respectively. Series similar to (1) with unknowns  $e_v^{(0)}$ ,  $e_v'^{(0)}$ ,  $h_v^{(0)}$ ,  $h_v'^{(0)}$ , take place on the perimeter of the PCF outer surface:

$$\begin{aligned}
E_z &= \sum_{v=-m}^m e_v^{(0)} \exp(iv\varphi), \nabla_n E_z = \sum_{v=-m}^m e_v'^{(0)} \exp(iv\varphi), \\
H_z &= \sum_{v=-m}^m h_v^{(0)} \exp(iv\varphi), \nabla_n H_z = \sum_{v=-m}^m h_v'^{(0)} \exp(iv\varphi),
\end{aligned} \tag{2}$$

where  $\varphi$  is the global polar angle.

Application of the Green's theorem to the known second-order differential equations, to which potential functions  $E_z$  and  $H_z$  obey in the whole space, leads to functional equations

$$\int_0^{2\pi} \left[ \Phi \nabla_n G - G \nabla_n \Phi \sqrt{\left(\frac{d\rho_0}{d\varphi}\right)^2 - \rho_0^2} \right] d\varphi - \sum_{j=1}^N \int_0^{2\pi} \left[ \Phi \nabla_n G - G \nabla_n \Phi \sqrt{\left(\frac{d\rho_j}{d\varphi}\right)^2 - \rho_j^2} \right] d\varphi_j = 0, \tag{3}$$

where  $\Phi = E_z(\mathbf{r})$  or  $\Phi = H_z(\mathbf{r})$ ,  $N$  is a number of air channels in the PCF,

$$G = 0.25i\pi H_0^{(2)} \left( \frac{2\pi}{\lambda} k_s |\mathbf{r}' - \mathbf{r}| \right), \tag{4}$$

is the two-dimensional electrodynamics Green's function,  $k_s = \sqrt{\varepsilon_s - \beta^2}$ ,  $\beta$  is the dimensionless mode propagation constant, the radius vector  $\mathbf{r}$  runs through the perimeters of the outer boundary of the PCF and the cross sections of the air channels with the variables of integration,  $\mathbf{r}'$  is the radius vector of the observation point that can be located in any of the air channels or outside the PCF.

Substitution of series (1), (2) into Eqs (3) and application of the Green's addition theorem to the function (4) leads to a homogeneous algebraic system

$$MX = 0, \tag{5}$$

where  $M$  is a matrix of dimensions  $(N+1)(4m+2) \times (N+1)(4m+2)$ ,  $X$  is a column vector composed of the unknown coefficients  $e_v^{(i)}$ ,  $h_v^{(i)}$  ( $i = \overline{0, N}$ ). The possible values of the mode propagation constant are found from the equation

$$\det M(\beta) = 0. \tag{6}$$

Fig. 1 illustrates the application of the developed method to the design of a photonic crystal sensor for detecting hydrogen in the atmosphere. Sensor action is based on the lossy mode resonance, in which the fundamental mode of the fiber interacts with the mode of the absorbing coating. Calculations are performed for two-layered cover consists of 1  $\mu\text{m}$   $\text{TiO}_2$  layer and 8nm Pd layer. The PCF is supposed to be formed by two hexagonal rings of air channels of diameter 3  $\mu\text{m}$  and pitch 8.8  $\mu\text{m}$  in quartz glass. Outer radius of the PCF is 61.7  $\mu\text{m}$ .

The arrow in Fig.1a indicates the main direction of the mode electric field. Fig1a refers to the wavelength  $\lambda=1.2178 \mu\text{m}$ , at which the maximal mode attenuation is observed. According to Fig.1a, the lossy mode resonance is due to the formation of standing waves in the PCF cladding.

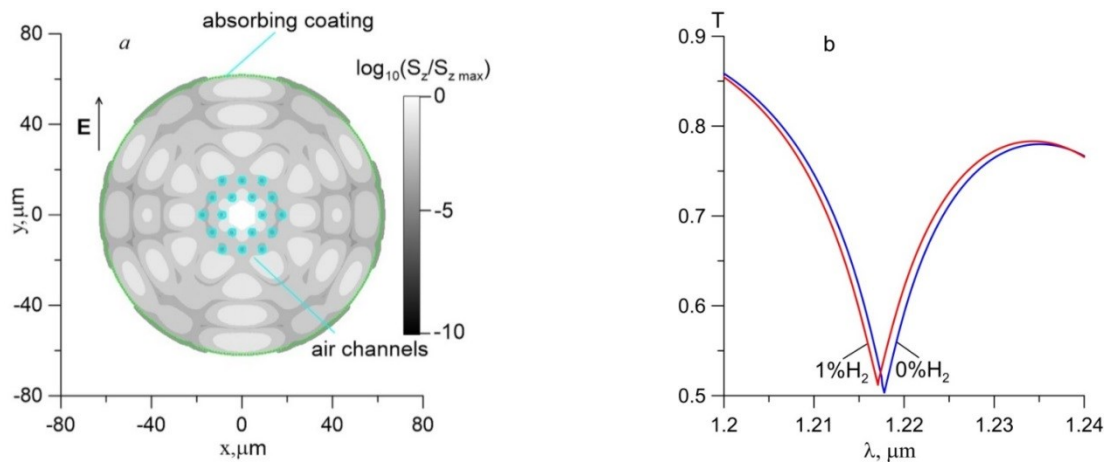


Figure 1. Lossy mode resonance in PCF hydrogen sensor: the fundamental mode intensity distribution over the PCF cross section (a) and the resonance transmission of the sensor due to the lossy mode resonance when the concentration of hydrogen in the atmosphere changes (b)

### III. CONCLUSIONS

The developed method of Green's functions is effective for calculating PCF sensors using the lossy mode resonance phenomenon.

### ACKNOWLEDGEMENT

This work was financially supported by the State Program of Scientific Research of the Republic of Belarus 1.15“Photonics and Electronics for Innovations.”

### REFERENCES

- [1] Sotsky, A.B. *Theory of Optical Waveguide Elements* / A.B. Sotsky // Mogil. Gos. Univ. im. A. A. Kuleshova, Mogilev, 2011) [in Russian].
- [2] Ozcariz, A.: A Comprehensive Review: Materials for the fabrication of optical fiber refractometers based on lossy mode resonance / Ozcariz, A., Ruiz-Zamarreño, C., Arregui, F.J. // *Sensors***20**(7), 1972 (1-23) (2020), <https://doi.org/10.3390/s20071972>.

## PLASMONIC ENHANCEMENT OF LUMINESCENCE EFFICIENCY IN LIGHT EMITTING STRUCTURES

O.S. Kulakovich

B.I. Stepanov Institute of Physics, National Academy of Sciences of Belarus, Minsk, Belarus

[o.kulakovich@ifanbel.bas-net.by](mailto:o.kulakovich@ifanbel.bas-net.by)

### I. INTRODUCTION

The last year's show the following promising trends in light-emitting diode (LED) production: the development of new colloidal LED technologies replacing in some cases epitaxial LED (based on GaN or InGaN quantum well heterostructures) and thereby using of quantum dots (CdSe, InP, perovskites) as building blocks in all types of LEDs. There are some advantages of semiconductor nanoparticles for LEDs such as: the emission color can be tuned by simply changing particle size, the narrow emission band, color purity and eye-friendly lighting, covering full visible spectrum by single excitation source, high photo- and thermal stability. Also colloidal technologies are less expensive than epitaxial and allow producing flexible devices. The actual aim remains the optimizing of LED design to get better devices performance. One of the ways to improve the performance of light emitting structures is nanoplasmonics.

The main idea is that metal nanostructures strongly enhance light – matter interaction owing to high local concentration of electromagnetic field [1]. In certain “hot spots” substances emit light with higher intensity than in air or in solution. Metal nanostructures act as nanoantenna and effect both on excitation of luminophore through local field enhancement as well as on emission through density of states modifying.

So, in certain conditions plasmonic can help to improve photo- and electroluminescence features of light emitting materials.



## II. RESULTS

In 2002 our group obtained the first experimental realization of the plasmon amplification of the photoluminescence of quantum dots with the help of metallic nanoparticles [2]. Several processes are realized near a metal nanoparticle surface: some promote photoluminescence enhancement (an increase in the intensity of the electromagnetic field at the plasmon resonance frequency, an increase in the radiative decay rates due to Purcell effect), while others contribute to quenching (an increase of the nonradiative decay rates due to of energy and electron transfer from luminophore to the metal). For possible electroluminescence enhancement metal nanoparticles can affect only on emission. The resulting luminescence enhancement or quenching will depend on the contribution of each process. Plasmon-enhanced fluorescence is a complex process depending on multiple parameters including sizes and morphologies of the metal nanostructures, distance between metal and luminophore, position of luminophore absorption and emission toward plasmon resonance (for photoluminescence). In all cases (enhancement or quenching of luminescence) decreasing of excited state lifetime ( $\tau$ ) can lead to diminish the role of the Auger process and to photostability enhancement [3] and modulation rate enhancement for LEDs.

The next plasmonic advantage is possible anisotropy of optical response. Possible polarization of luminescence using anisotropic plasmonic nanoparticles is important for improve the backlight sources in LCD devices [4] as well as the enhancement of the directionality of light emission allows to reduce light dissipations and to maximize light output [5]. These results can be explained by anisotropy of luminophore excitation and emission near nonspherical plasmonic nanoparticles [6].

## III. CONCLUSIONS

There are successful evidences of plasmonic nanoparticle utility for QLEDs efficiency for both photo- and electroluminescence. The potentially promising plasmonic enhancement of LED performance consists in: photo- and electroluminescence intensity enhancement; decay rate enhancement, modulation rate enhancement; luminophore photostability enhancement; improving light directionalities and light polarization of LEDs.

## ACKNOWLEDGMENTS

This work includes results obtained within the F20PTI-004 project of the Belarusian Basic Research Foundation.

## REFERENCES

- [1] S.V. Gaponenko, H.V. Demir, Applied Nanophotonics, Cambridge University Press, Cambridge, 2018.
- [2] O. Kulakovich, N. Strekal, A. Yaroshevich, S. Maskevich, S. Gaponenko, I. Nabiev, U. Woggon, M. Artemyev, Enhanced Luminescence of CdSe Quantum Dots on Gold Colloids”, Nano Lett. Vol. 2 pp. 1449-1452, 2002.
- [3] O.Kulakovich, L.Gurinovich, Hui Li, A.Ramanenka, L.Trotsiuk, A.Muravitskaya, Jing Wei, Hongbo Li, N. Matveevskaya, D. V. Guzatov, S.Gaponenko “Photostability enhancement of InP/ZnSe/ZnSeS/ZnS quantum dots by plasmonic nanostructures”, Nanotechnology, v. 32 035204, 2021.
- [4] L. I. Gurinovich, L. L. Trotsiuk, O. S. Kulakovich, N. I. Sushko, H. V. Demir, and S. V. Gaponenko, “Polarization Properties of Photoluminescence of Anisotropic Polymer Films Containing Aligned Au Nanorods and Semiconductor Nanoparticles of Various Shape”, Semiconductors, Vol. 52, pp. 2052–2054, 2018.
- [5] Giessen, H., & Lippitz, M., Directing Light Emission from Quantum Dots. Science, 329,pp. 910–911,2010.
- [6] Trotsiuk, L., Muravitskaya, A., Kulakovich, O., Guzatov, D., Ramanenka, A., Kelestemur, Y., Demir, H.V. and Gaponenko, S.,” Plasmon-Enhanced Fluorescence in Gold Nanorod-Quantum Dot Coupled Systems”. Nanotechnology, v. 31, pp. 105201 (1-10), 2020.

## CHARGING PROPERTIES OF THE SILICON / ZINC OXIDE NANOPARTICLE HETEROSTRUCTURE

A. A. Kuraptsova, A. L. Danilyuk

Belarussian State University of Informatics and Radioelectronics, Minsk, Belarus

[anku21qwerty@gmail.com](mailto:anku21qwerty@gmail.com)

## I. INTRODUCTION

Zinc oxide ZnO is a semiconductor with a direct band gap of 3.37 eV at room temperature, which makes ZnO a promising material for use in many areas, such as photocatalytic water and air purification, photocatalytic

water splitting, optoelectronics, gas sensors, gas sensors [1]. Zinc oxide also has a number of advantages over other materials used in photocatalysis: low cost, non-toxicity, low reflectance in the solar spectrum, the ability to create low-dimensional structures using chemical etching (amphoterism), resistance to high-energy radiation, flexible changing of electrophysical and optical properties by doping it with various impurities and controlling the conditions for its production [2]. The implementation of p-type ZnO is difficult because pure ZnO with a wurtzite structure naturally occurs in the form of an n-type semiconductor. It is caused by oxygen vacancies, excess zinc, and the presence of hydrogen atoms, [3].

On the other hand, much attention is paid to the creation and study of silicon / zinc oxide heterostructures containing ZnO nanoparticles. This is important for the production of composite materials with a developed surface for photovoltaics.

## II. MODEL

The Si/nanosized ZnO heterostructure was simulated using the Comsol Multiphysics software package. A two-dimensional diffusion-drift model of the heterostructure with the solution of the Maxwell system of equations was used. Properties of silicon [4] and zinc oxide [5], respectively, are: band gap 1.12 eV and 3.37 eV; electron affinity 4.05 eV and 4.3 eV; the lifetime of charge carriers is 10  $\mu$ s and 0.79 ns; electron mobility 1450  $\text{cm}^2/(\text{V}\cdot\text{s})$  and 200  $\text{cm}^2/(\text{V}\cdot\text{s})$ ; hole mobility 500  $\text{cm}^2/(\text{V}\cdot\text{s})$  and 50  $\text{cm}^2/(\text{V}\cdot\text{s})$ ; impurity concentration  $10^{17} \text{cm}^{-3}$  and  $10^{16} \text{cm}^{-3}$ . The real and imaginary parts of the refractive index for silicon and zinc oxide were set in a table [6, 7]. The heterostructure is a zinc oxide nanoparticle with a size of 500x500 nm in a silicon substrate.

## III. RESULTS AND DISCUSSION

The height of the barrier for electrons from the silicon side in the n-Si/n-ZnO heterostructure is 0.133 eV, after passing which they enter the region in zinc oxide enriched with electrons, thereby creating an excess negative charge at the the oxide nanoparticle zinc boundary (width  $\approx 70$  nm). The barrier for holes in the zinc oxide is 0.092 eV. In the n-Si/p-ZnO heterostructure, the barrier for electrons in silicon is 0.104 eV, and for holes in zinc oxide it is 0.567 eV. For the p-Si/p-ZnO heterostructure, these values are 0.028 eV and 0.57 eV, respectively. There are no such barriers in the p-Si/n-ZnO heterostructure which allows electrons generated in silicon and holes generated in zinc oxide to flow freely into another semiconductor.

Generation of charge carriers in ZnO occurs at wavelength  $< 375$  nm, in silicon at all wavelengths and it has a peak at  $\sim 950$  nm. The generation is also observed in silicon under a ZnO particle at a rate of about  $(1-3)\cdot 10^{15} \text{cm}^{-3} \text{s}^{-1}$  at wavelengths 375-1150 nm.

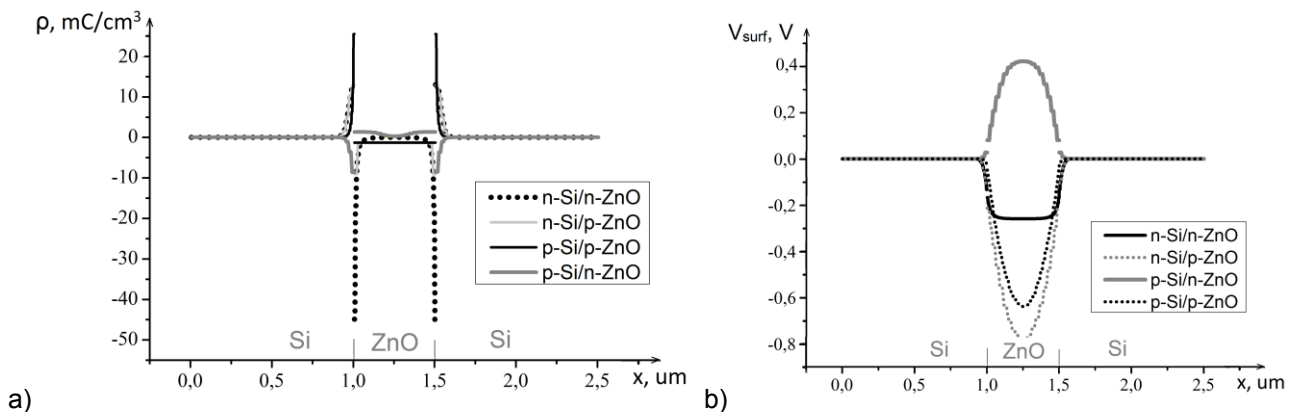


Figure 1. Electric charge density (a) and electric potential (b) on the surface of heterostructures

Due to the redistribution of charge carriers during irradiation an excess electric charge is formed on the surface of the heterostructures, it's bulk density  $\rho$  for a radiation wavelength of 500 nm is shown in Fig. 1a. The electric potential  $V_{\text{surf}}$  arising on the surface of the structures is shown in Figure 1b.

## IV. CONCLUSIONS

Simulation of the charge properties and currents in zinc oxide nanoparticle in silicon heterostructures for cases of n- and p-types of conductivity demonstrated differences in the electric charge and potential on the surface of heterostructures without significant differences depending on the wavelength of incident radiation.

It is shown that the silicon / p-type zinc oxide nanoparticle heterostructure provides a negative potential and a negative surface charge on the surface of a zinc oxide nanoparticle regardless of the wavelength of solar radiation.

It opens up additional possibilities for the photocatalytic use of zinc oxide in a wider emission spectrum than its own absorption spectrum.

Achieving stable p-type conductivity of zinc oxide opens up many possibilities for creating optoelectric devices based on materials with a large conduction band. This will require better control over the natural n-type conductivity of zinc oxide which can compensate acceptor impurities.

## REFERENCES

- [1] N. A. Vorobyeva, M. N. Romyantseva, P. A. Forsh, A. M. Gaskov, "Conductivity of nanocrystalline ZnO(Ga)", *Semiconductors*, Vol. 47, pp. 650–654, 2013.
- [2] C.G. Van de Walle, "Hydrogen as a Cause of Doping in Zinc Oxide", *Physical review letters*, Vol. 85, pp. 1012-1015, 2000.
- [3] C.Y. Tsay, W. Y. Chiu, "Enhanced Electrical Properties and Stability of P-Type Conduction in ZnO Transparent Semiconductor Thin Films by Co-Doping Ga and N", *Coatings*, Vol. 10, pp. 1069-1081, 2020.
- [4] S.M. Sze, K. Ng. Kwok, *Physics of Semiconductor Devices*. 3<sup>rd</sup> edition. Hoboken: John Wiley & Sons; 2006.
- [5] U. Özgür, Ya. I. Allivov, C. Lui, A. Teke, M. A. Reshchnikov, S. Doğan, V. Avrutin, S.-J. Cho, Morkoç H., "A comprehensive review of ZnO materials and devices", *Journal of applied physics*, Vol. 98, pp. 041301, 2005.
- [6] M. A. Green, "Self-consistent optical parameters of intrinsic silicon at 300K including temperature coefficients", *Solar Energy Materials and Solar Cell*, Vol. 92, pp. 1305-1310, 2019.
- [7] O. Aguilar, S. de Castro, M. de Godoy, M. Dias, "Optoelectronic characterization of Zn<sub>1-x</sub>Cd<sub>x</sub>O thin films as an alternative to photonic crystals in organic solar cells", *Optical Materials Express*, Vol. 9, pp.3638-3648, 2019.

## EMISSION ENHANCEMENT OF SEMICONDUCTOR NANOCRYSTALS BY GOLD NANORODS: A RECIPE

L. Trotsiuk<sup>1</sup>, A. Muravitskaya<sup>2</sup>, O. Kulakovich<sup>1</sup>, M. Artemyev<sup>3</sup>, S. Gaponenko<sup>1</sup>

1 B.I. Stepanov Institute of Physics, National Academy of Sciences of Belarus, 220072 Minsk, Belarus

2 Department of Physics & Mathematics, University of Hull, HU6 7RX Hull, United Kingdom

3 Research Institute for Physico-Chemical Problems of Belarusian State University, 220006 Minsk, Belarus

[l.trotsiuk@ifanbel.bas-net.by](mailto:l.trotsiuk@ifanbel.bas-net.by)

## I. INTRODUCTION

Semiconductor nanocrystals have attracted great interest of researchers and industries over the last few decades due to their fascinating electronic and optical properties caused by the strong carrier confinement. Narrow-band emission, high quantum efficiency and photostability make them promising objects for optoelectronic (lasers, colloidal LEDs, solar cells etc.) and biomedical (e.g. imaging) applications [1]. Despite the huge progress in the synthesis of semiconductor nanocrystals with nearly unit quantum efficiency in organic phase, aqueous nanocrystals still suffer from several problems. For instance, ligand exchange reactions, which used for the transfer of nanocrystals from organic to aqueous solutions, lead to a dramatic fall in quantum efficiency [2]. Plasmonic nanoparticles, which are the optical analogues of antennas and able to amplify optical signals from emitter in their vicinity, are often proposed to improve optical properties of semiconductor nanocrystals. Among many plasmonic structures, gold nanorods (GNRs) are especially promising due to their anisotropic shape and adjustable plasmonic properties [3].

In this work, we experimentally and theoretically investigated conditions of the emission enhancement of semiconductor nanocrystals (on the example of CdSe-based quantum dots, QDs) by GNRs [4].

## II. RESULTS

GNRs with the longitudinal localized surface plasmon resonance (LSPR) at 615 nm were synthesized via seed-mediated growth method [5]. To manipulate the plasmonic antenna efficiency and investigate the influence of distance between GNR and QDs, GNRs were coated with 0, 2, 4 and 6 polyelectrolytes (PE) layers (Fig. 1(a-b)) that corresponded to app. 3 (due to the surfactant bilayer on the GNR surface), 5, 7, and 9 nm separation.

We chose two types of QDs with emission maxima at 595 and 620 nm, which fell on the shortwave and longwave slopes of the longitudinal LSPR, correspondingly (Fig.1c). The fluorescence enhancement

occurred only in the complexes with QD emission at 620 nm, which can be attributed to the higher nanoantenna efficiency at this wavelength. Also, we established the inverse dependence of the enhancement factor on the QD concentration in the complexes, due to the augmentation of QDs adsorbed on GNR sides. We found theoretically that the GNR sides feature lower enhancement of the electric field and emitter quantum efficiency than GNR tips, which results in the fluorescence quenching for the high QD concentration. Moreover, we found that an increase in the GNR-QD separation led to the fall of fluorescence enhancement (Fig.1d).

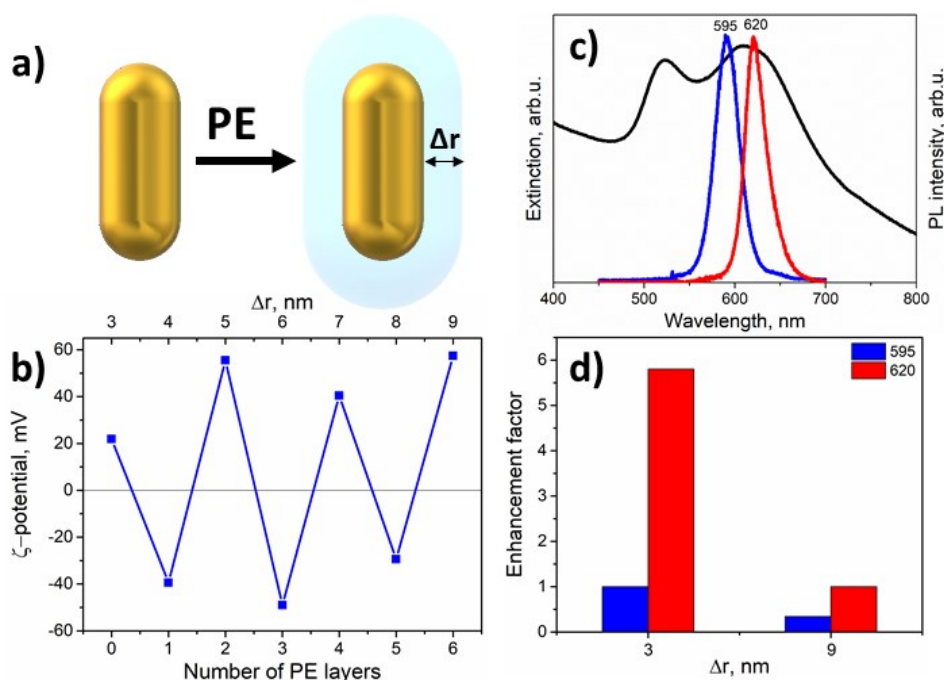


Figure 1. a) scheme of a GNR coated by PE shell; b) zeta-potential measurements of GNRs coated by PE; c) Extinction (black) spectrum of GNRs and fluorescence spectra of CdSe/ZnS (blue) and CdSe/CdZnS (red) QDs; d) Dependence of fluorescence enhancement factor on the thickness ( $\Delta r$ ) of PE shell on GNRs

### III. CONCLUSIONS

We demonstrated the influence of QDs localization, concentration, excitation and emission wavelengths as well as their separation with GNRs on the fluorescence enhancement [4]. We achieved almost 11-fold fluorescence enhancement in GNR-QDs complexes, in which the emission band overlapped with the longwave slope of the longitudinal plasmon resonance of GNRs, and the strong emission suppression for QDs with emission at the shortwave slope.

### ACKNOWLEDGMENTS

This work was supported by the joint BRFFR-BIT project No F20PTI-015. M.A acknowledges CHEMREAGENTS grant 2.1.04.01.

### REFERENCES

- [1] M.A. Cotta, " Quantum Dots and Their Applications: What Lies Ahead?" ACS Appl. Nano Mater., Vol. 3, pp.4920–4924, 2020.
- [2] M. Kovalenko [et al], " Prospects of Nanoscience with Nanocrystals", ACS Nano, Vol. 9, Is. 2, pp. 1012-1057, 2015.
- [3] J. Zheng, X. Cheng, H. Zhang, X. Bai, R. Ai, L. Shao, J. Wang, "Gold Nanorods: The Most Versatile Plasmonic Nanoparticles", Chem. Rev., Vol.121, Is. 19, pp. 10789-10901, 2021.
- [4] L. Trotsiuk, A. Muravitskaya, O. Kulakovich, D. Guzatov, A. Ramanenka, Y. Kelestemur, H.V. Demir, S. Gaponenko, "Plasmon-Enhanced Fluorescence in Gold Nanorod-Quantum Dot Coupled Systems", Nanotechnology, Vol. 31, p.105201 (10pp), 2020.
- [5] N.D. Burrows, S. Harvey, F.A. Idesis, C.J. Murphy, "Understanding the Seed-Mediated Growth of Gold Nanorods through a Fractional Factorial Design of Experiments", Langmuir, Vol. 33, Is. 8, pp.1891-1907, 2017.

# PLASMON EFFECTS IN A GRAPHENE NANOSTRUCTURE

A. V. Felsharuk, D. A. Podryabinkin, A. L. Danilyuk  
Belarussian State University of Informatics and Radioelectronics, Minsk, Belarus

[danilyuk@bsuir.by](mailto:danilyuk@bsuir.by)

## I. INTRODUCTION

Plasmons are collective excitations of electrons in solids. The ability to change their properties by an electric field in low-dimensional materials and structures, such as graphene, which makes them promising for the use in a variety of optoelectronic devices, such as sensors, detectors, radiation sources, etc [1]. The interaction between plasmonic oscillations in graphene leads to a strong shift in the absorption spectrum of light in the far- infrared range. Thus, it was experimentally found that the interaction of plasmons in graphene on a dielectric substrate leads to a strong redshift of the absorption spectrum in comparison to the plasmon spectrum in isolated graphene. The absorption spectra of graphene due to the interaction of plasmons cover the far IR range (photon energies from 10 meV to 200 meV), which, in turn, coincides with the vibrational spectra of most biological molecules. This provides the opportunities for the design and manufacture of graphene-based biosensors. In this regard, it's important to simulate plasmon spectra for their use in optoelectronics and biosensorics [2]. Even though plasmon spectra in isolated graphene have already been well studied, for the effective operation of real optoelectronic devices, it is relevant to study plasmon effects in graphene on various substrates, as well as in the composition of nanostructures.

Also, the relevance of plasmon studies is related to the issue of replacing copper interconnects in integrated circuits (ICs). For many years, the reduction in design standards for elements in silicon technology remained sufficient to increase the performance of ICs. Because of this, there was no need for manufacturers to develop devices based on new physical principles or search new materials to replace silicon. However, now everyone agrees that scaling has come to its limit. The need for a further increase in the IC performance forces us to look for new materials with improved electronic properties [3]. Over the past few decades, researchers arrived at the conclusion that it is possible to obtain the surface plasmons on the conductor/dielectric interface with the same frequency as external electromagnetic waves, but with a much shorter wavelength. This will allow to use plasmons in nanostructures to transfer information inside the chip. Plasmonic interconnects would be a real breakthrough in the field of increasing the operating frequencies of ICs. In this regard, a promising direction for solving such kind of problem is the study of plasmon oscillations in the terahertz frequency range and the usage of graphene on a dielectric substrate. However, a plenty of technological and physical problems for the excitation, propagation, and detection of plasmonic oscillations with controlled parameters need to be solved before that.

## II. MODEL

To simulate plasmonic effects, a heterostructure that includes graphene on a dielectric substrate with a gate electrode was chosen. First, we calculated the complex dynamic conductivity  $\sigma(\omega)$ . The dispersion equation for two-dimensional plasmon waves propagating over the surface of a given structure includes the dielectric constants of the environment and the substrate, as well as the dynamic conductivity of graphene. It follows from the dispersion equation that the value of the wavevector and, consequently, the attenuation length of the plasmon wave directly depends on the dynamic conductivity of graphene. In the case of a monatomic graphene layer, the dynamic conductivity is determined by the formulas, generalized in [4], and including the chemical potential of graphene,  $\mu$ , relaxation time of the electron pulse,  $\tau$ , ambient temperature, frequency of electromagnetic external radiation,  $\omega$  (EMR). To determine the propagation coefficients  $\text{Re}(\rho)$  and absorption  $q$  of surface plasmon waves, the components of the electric  $E$  and magnetic  $H$  fields along the graphene plane  $z$  were found using Maxwell's equations [3]. The complex propagation coefficient of surface plasmons ( $\rho$ ) is related to the wave number of the surface plasmon by the relation  $q = \text{Im}(\rho\omega/c)$ . Here  $c$  is the speed of light. As a result, the equation for the dispersion of surface plasmons was obtained [4]:

$$\sqrt{n^2 - \rho^2} + n^2 \sqrt{1 - \rho^2} + \left(\frac{4\pi}{c\epsilon_0}\right) \sigma(\omega) \sqrt{n^2 - \rho^2} \sqrt{1 - \rho^2} = 0, \quad (1)$$

where  $n$  is the refractive index at the boundary of the medium and graphene,  $\epsilon_0$  is the electrical constant of the vacuum.

Solving equation (1) with respect to  $\rho$ , it becomes possible to find the propagation coefficient  $\text{Re}(\rho)$  and the absorption coefficient  $\text{Im}(\rho\omega/c)$ , which is the plasmon spectrum. In the case when the refractive index of the medium  $n$  is equal to 1, Eq. (1) is simplified and analytically resolved for  $\rho$ .

To determine the chemical potential in graphene  $\mu$ , which value self-consistently depends on the gate voltage  $V_g$ , the dielectric capacitance, and the charge carrier concentration in graphene, an integral expression for the charge carrier concentration is used depending on the value of the chemical potential and

the electrostatic equation for the graphene/dielectric/gate electrode heterostructure [5]. The electrostatic equation includes the chemical potential of graphene, the charge carrier concentration, the dielectric capacitance, the quantum capacitance of graphene, and the capacitance of the graphene/dielectric interface.

The integral expression for the charge carrier concentration in graphene depends on the chemical potential and is determined by the density of states in graphene and the Fermi-Dirac statistics. The electrostatic equation for the considered heterostructure is determined as follows [5]:

$$eV_g = \mu + \frac{e^2 n_s}{C_{ox}} + \frac{C_{it}}{C_{ox}} \mu, \quad (2)$$

where  $n_s(\mu)$  is the charge carrier concentration in graphene;  $C_{ox}$  is the capacitance per unit area of the gate insulator,  $C_{it}$  is the capacitance per unit area of the interface states.

### III. RESULTS AND DISCURSSION

The calculations of the transmission and absorption coefficients, as well as the values of the wavevector of plasmons, have been conducted. Frequency dependences of the propagation coefficient are obtained for different values of the gate voltage for different materials of the gate insulator at temperatures of 77 and 300 K. It is shown that its value can both increase with frequency and change nonmonotonically in the frequency range 1-20 THz. Monotonic dependences of the propagation coefficient were obtained in the range of 1-12 THz at values of the chemical potential of graphene 0.01-0.02 eV and the refractive index at the medium/graphene interface  $n=1-3$ . In this case, the value of the propagation coefficient increases with frequency up to values of 5-40 with increasing  $n$ . For a non-monotonic dependence, the maximum value of the propagation coefficient corresponds to the value  $\text{Re}(\rho) = 10-14$ , and the frequency at which the peaks are observed lies in the range of 7-16 THz, depending on the capacitance of the dielectric and the potential of the gate electrode. These parameters varied in the range  $C_{ox} = 1-5 \mu\text{F}/\text{m}^2$ ,  $V_g = 0.02-0.12 \text{ V}$ . Moreover, with an increase in the potential of the gate electrode, the maximum shifts towards an increase in frequency.

The frequency dependences of the absorption coefficient are obtained for different values of the gate voltage for different materials of the gate dielectric at temperatures of 77 and 300 K. It is shown that its value varies non-monotonically in a given frequency range, taking both positive and negative values with varying  $C_{ox}$  and  $V_g$  in the same ranges as indicated above. A significant change in the absorption coefficient is observed at a frequency of more than 5 THz. Its negative value reaches a value of  $-3 \cdot 10^5 \text{ cm}^{-1}$  at a frequency of 13 THz and then, with an increase in the frequency of EMR, it sharply increases and takes positive values up to  $4 \cdot 10^5 \text{ cm}^{-1}$ . The obtained results indicate that, depending on the ratio of the parameters of the nanostructure and the frequency of the EMR, the modes of both absorption of EMR and its amplification due to plasmon oscillations can be realized.

The frequency dependences of the wavevector of plasmon oscillations were obtained at various gate voltages  $V_g$  for various materials of the gate insulator at a temperature of 77-300 K. Surface plasmons with a wavevector  $q \sim 10^5 \text{ cm}^{-1}$ , which corresponds to a wavelength of  $\lambda \sim 1 \mu\text{m}$  or less, are in the considered frequency range of EMR. The decrease in the wavelength of plasmon oscillations in graphene in the terahertz frequency range is due to the strong localization of plasmons in graphene.

### IV. CONCLUSIONS

Simulations of the frequency dependences of the propagation and absorption coefficients of EMR by a graphene heterostructure were modeled. The regularities of influence of the electrophysical parameters of the heterostructure on the amplification of plasmon oscillations and a decrease in their wavelength to  $1 \mu\text{m}$  and less have been established.

### REFERENCES

- [1] An Introduction to Graphene Plasmonics. Ed. by P.A.D Gonçalves and N.M.R. Peres. World Scientific Publishing Co. Pte. Ltd., (2016), 431p.
- [2] V. Semenenko, S. Schuler, A. Centeno, A. Zurutuza, T. Mueller, V. Perebeinos "Plasmon–Plasmon Interactions and Radiative Damping of Graphene Plasmons" ACS Photonics Vol. 5(9), pp.3459–3465, 2018.
- [3] H. Subbaraman, X. Xu, A. Hosseini, X. Zhang, Y. Zhang, D. Kwong, R.T. Chen, "Recent advances in silicon-based passive and active optical interconnects", Optical Express, Vol. 23, pp.2487-2511, 2015.
- [4] A.A. Dubinov, V. Mitin, T. Otsuji, "Terahertz surface plasmons in optically pumped graphene structures", J. Phys.: Condens. Matter. Vol. 23, pp. 145302, 2011.
- [5] G.I. Zebrev, "Graphene Field Effect Transistors: Diffusion-Drift Theory/ 23 Chapter in Physics and Applications of Graphene-Theory. Ed. by S. Mikhailov, InTech, 2011, pp. 476– 498.

# ELECTRICALLY CONFINED GRAPHENE QUANTUM DOTS: THEORETICAL TREATMENT

H. Grushevskaya, G. Krylov

Department of Computer Simulation, Faculty of Physics, Belarusian State University, Minsk, Belarus

[krylov@bsu.by](mailto:krylov@bsu.by)

## I. INTRODUCTION

Nanometer sized quasi-circular graphene monolayer patches look very promising as a main component of quantum devices. Such structures can be chemically synthesized [1] but more preferable from the point of operational easiness are those produced by application of an electrical field of the STM tip to a graphene plane which are called tip-induced or electrically confined graphene quantum dots (GQD) [2]. Theoretical treatment of this type of quantum dots attracts a lot of attention last two decades. Theoretical consideration of a quasi-circular GQD with a radius  $r_0$  has been performed in [3,4,5] on the basis of free pseudo-Dirac fermion model with a step-like confining potential  $V(r)=V_0\theta(r-r_0)$ . The authors of [4,5] assume the existence of quasi-bound states (with a complex energy where the imaginary part of the energy corresponds to the inverse life-time of the state) which represent themselves resonances in a scattering amplitude for the system under consideration. Such an approach attracts much attention both from theoretical point of view [6,7] and from the experimental one [8,9], though its mathematical ground seems not enough clear. Moreover, the pseudo-Dirac fermion models give no consistent description especially for the so called "quasi-zero energy" levels of the system. Natural questions arise what is a precise meaning of the resonance conditions and either exist real reasons to transfer consideration of the problem into the energy complex plane. These are the motives for our reconsideration of the problem. In this report we focus attention on applicability of free pseudo-Dirac fermion models to the problem of GQDs and the existence of quasi-bound states for the GQDs.

## II. THEORETICAL APPROACH

For two dimensional systems, solutions of the radial part of the pseudo-Dirac equation in a regions with a constant potential are given as a linear combination of the Bessel functions  $J_m(|\xi|r)$ ,  $Y_m(|\xi|r)$  of the first and second kind ( $m$  is a magnetic quantum number related to radial and polar angle variables separation,  $\xi$  is defined as a difference of the energy and the value of the confining potential being a constant 0 or  $V_0$  in two regions  $r < r_0$ ,  $r > r_0$ ). The Bessel functions behave as sine and cosine functions at large values of their argument. It means non-normalization of the solutions in a whole space and, accordingly, the absence of the bound states in such a model system. We construct eigenstates for this problem of circular GQD with a step-like potential by matching the wave functions on the boundary of the quantum dot. Inside GQD we choose a non-zero coefficient  $c_{1,in}$  at first kind Bessel function and  $c_{2,in}$  equal to zero at second kind Bessel function (because this function is singular in the origin) in the linear combination. Outside the dot the coefficients are chosen from the condition of the continuity of the both component of the spinor wave function. This condition determines unknown coefficients  $c_{1,in}$ ,  $c_{1,out}$ ,  $c_{2,out}$  up to a common factor as it should be for linear equations. The solution exists for real energies (real eigenvalues) and corresponds to a scattering state (see Figure 1).



Figure 1. Upper and lower components of the spinor eigenfunction for the case  $m=0$ ,  $\epsilon=0.09$ ,  $V_0=3$ .

## III. RESULTS AND DISCUSSION

We have shown that there is no resonant condition (associated with appearance of quasi-bound state) as it was erroneously stated in [4]. The origin of the mistake in [4] was an assumption on the value for the phase of the wave function at infinity that led to additional condition between  $c_{1,out}$ ,  $c_{2,out}$  besides the matching ones. The last made the linear system to be overcomplete and, as a result, inconsistent for all real energies except  $\epsilon=V_0$  (state at the edge of the well). We also reproduce the appropriate theoretical derivation for the scattering problem (when one assumes the plane wave incidence on the GQD) and demonstrate explicitly that the resonance condition found in [5] corresponds to the inconsistent system of linear equations obtained from the spinor wave function matching conditions on the boundary of a quantum dot. , or (in the above mentioned special case  $\epsilon=V_0$ ) directly to a regime of a total wave reflection from a quantum dot rather

than to a some kind of temporal trap regime that could be associated with quasi-bound states. The results of our consideration can be stated as the necessity of alternative approaches to the QGD theoretical description.

In our recent publication [10] it has been demonstrated that electronic properties of such electrically confined QGDs can be described by application of the concept of pseudo-potential together with the usage of the quasi-relativistic graphene model developed earlier in [11] (see also references in [10]). QGD in this consideration is represented as a supercell with a definite type of boundary conditions. These boundaries are connected with two topologies of the QGDs: 2D-sphere and 2D-torus. On the basis of this model it has been demonstrated a nice correspondence between our theoretical and experimental results [8,9] on quasi-zero energy part of QGD spectra of a system under consideration contrary to existing toy models (see [4-6] and the references therein).

#### ACKNOWLEDGMENTS

This work has been support in part by the projects within the State Programs of Fundamental Researches of the Republic of Belarus "Convergence2025" and "Energetics".

#### REFERENCES

- [1] Jia Zhang, Shu-Hong Yu, Carbon dots: large-scale synthesis, sensing and bioimaging. *Materials Today*. Vol. 19, p.382, 2016.
- [2] N.M. Freitag et al. Electrostatically Confined Monolayer Graphene Quantum Dots with Orbital and Valley Splittings. *Nano Lett.* Vol 16, p.5798, 2016.
- [3] A.H. Castro Neto, F. Guinea, N.M.R. Peres, K.S. Novoselov, A.K.Geim. The electronic properties of graphene. *Rev. Mod. Phys.* Vol. 81, p.109, 2009.
- [4] P. Hewageegana and V. Apalkov Trapping of an electron in coupled quantum dots in graphene *Phys. Rev. B* Vol. 79 p115418, 2009.
- [5] A. Matulis and F. M. Peeters, Quasibound states of quantum dots in single and bilayer graphene *Phys. Rev.B* Vol. 77, p.115423, 2008.
- [6] T D Linh Dinh et al. Quasibound states in single-layer graphene quantum rings, *J. Phys.: Condens. Matter* Vol. 30, p.315501, 2018.
- [7] M. Grujic, M.Zarenia, A. Chaves, M.Tadic, G.A. Farias, F.M. Peeters. Electronic and optical properties of a circular graphene quantum dot in a magnetic field: Influence of the boundary conditions. *Phys. Rev. B* Vol. 84, p.205441, 2011.
- [8] Y. Jiang et.al Tuning a circular p-n junction in graphene from quantum confinement to optical guiding. *Nat. Nanotechnology* Vol. 12, p.1045, 2017.
- [9] J. Lee et al. Imaging electrostatically confined Dirac fermions in graphene quantum dots. *Nature Physics*. Vol. 12, p.1032, 2016.
- [10] H. V. Grushevskaya et al. Electronic properties and quasi-zero-energy states of graphene quantum dots *Phys. Rev. B* Vol. 103, p.235102, 2021.
- [11] H. V. Grushevskaya et al. Electronic Structure and Transport in Graphene: Quasi Relativistic Dirac-Hartree-Fock Self-Consistent Field Approximation. // In: *Graphene Science Handbook: Electrical and Optical Properties*. Vol. 3. Eds. M. Aliofkhazraei, N. Ali, W.I. Milne, C.S. Ozkan, S. Mitura, J.L. Gervasoni. (Taylor and Francis Group, CRC Press, USA, UK, 2016). pp. 117-132.

#### ELECTRODYNAMICS, COMPLEX ROTATION GROUP, MEDIA

A.V. Ivashkevich<sup>1</sup>, V.M. Red'kov<sup>1</sup>, V.V. Kisel<sup>2</sup>

1 B.I. Stepanov Institute of Physics of the National Academy of Science of Belarus, Minsk, Belarus

2 Belarus State University of Informatics and Radio-electronics, Minsk, Belarus

[v.redkov@ifanbel.bas-net.by](mailto:v.redkov@ifanbel.bas-net.by)

#### I. INTRODUCTION

In 1931, Majorana and Oppenheimer proposed to consider the Maxwell theory of electromagnetism as the wave mechanics of the photon. They introduced a complex 3-vector wave function satisfying the massless Dirac-like equations. Before Majorana and Oppenheimer, the most crucial steps were made by Silberstein, he showed the possibility to have formulated Maxwell equation in term of complex 3-vector entities.



Silberstein writes that the complex form of Maxwell equations has been known before; he refers this to the second volume of the lecture notes on the differential equations of mathematical physics by Riemann that were edited and published by H. Weber in 1901.

## II. MATRIX FORM IN THE VACUUM

Let us introduce 3-dimensional complex vector  $\psi^k = E^k + icB^k$ , then equations can be joint into the one matrix equation (see notations in [1])

$$(-i\partial_0 + \alpha^j \partial_j) \Psi = J, \quad \Psi = \begin{pmatrix} 0 \\ E^1 + icB^1 \\ E^2 + icB^2 \\ E^3 + icB^3 \end{pmatrix}, \quad J = 1\epsilon_0 \begin{pmatrix} j^0 \\ i j^1 \\ i j^2 \\ i j^3 \end{pmatrix}$$

$$(\alpha^i)^2 = -I, \quad \alpha^1 \alpha^2 = -\alpha^2 \alpha^1 = \alpha^3, \quad \alpha^2 \alpha^3 = -\alpha^3 \alpha^2 = \alpha^1, \quad \alpha^3 \alpha^1 = -\alpha^1 \alpha^3 = \alpha^2.$$

## III. MINKOWSKI ELECTRODYNAMICS FOR THE UNIFORM MEDIUM

Let us introduce the quantities with simple transformation properties under the Lorentz group:

$$f = E + icB, \quad h = 1\epsilon_0 (D + iH/c);$$

where  $f$  and  $h$  are complex 3-vectors under the group  $SO(3, C)$ , the latter is isomorphic to the Lorentz group. Let us introduce the new quantities

$$M = (h + f)/2, \quad N = (h^* - f^*)/2, \quad M' = O M, \quad N' = O^* N.$$

they are different 3-vectors under the group  $SO(3, C)$ . In terms of the variables  $M$  and  $N$ , the Maxwell equations in the uniform medium read in the matrix form

$$(-i\partial_0 + \alpha^i \partial_i) M + (-i\partial_0 + \beta^i \partial_i) N = J, \quad M = \begin{pmatrix} 0 \\ M \end{pmatrix}, \quad N = \begin{pmatrix} 0 \\ N \end{pmatrix}, \quad J = 1\epsilon_0 \begin{pmatrix} \rho \\ i j \end{pmatrix},$$

where three additional matrices  $\beta^i$  are used.

## IV. MINKOWSKI CONSTITUTIVE RELATIONS IN THE COMPLEX FORM

Let us examine how the constitutive relations for the uniform medium behave under the Lorentz transformations. We start with these relations in the rest reference frame

$$D = \epsilon_0 \epsilon E, \quad Hc = 1\mu_0 \mu 1c^2 cB = \epsilon_0 \mu cB,$$

whence it follows their different representation in terms of complex vectors

$$2h = (\epsilon + 1\mu) f + (\epsilon - 1\mu) f^*, \quad 2h^* = (\epsilon + 1\mu) f^* + (\epsilon - 1\mu) f;$$

$$2f = (1\epsilon + \mu) h + (1\epsilon - \mu) h^*, \quad 2f^* = (1\epsilon + \mu) h^* + (1\epsilon - \mu) h.$$

Let us apply the Lorentz transformations

$$f' = O f, \quad f'^* = O^* f^*, \quad h' = O h, \quad h'^* = O^* h^*,$$

then we get

$$2h' = (\epsilon + 1\mu) f' + (\epsilon - 1\mu) O(O^{-1})^* f'^*, \quad 2h'^* = (\epsilon + 1\mu) f'^* + (\epsilon - 1\mu) O^* O^{-1} f'.$$

$$2f' = (1\epsilon + \mu) h' + (1\epsilon - \mu) O(O^{-1})^* h'^*, \quad 2f'^* = (1\epsilon + \mu) h'^* + (1\epsilon - \mu) O^* O^{-1} h'.$$

In general, we notice evident modifications of the constitutive relations in the moving reference frame. In this point one should distinguish between two cases: Euclidean rotations and Lorentzian boosts. Indeed, for any Euclidean rotation we have identities  $O^* = O \Rightarrow O(O^{-1})^* = I, O^* O^{-1} = I$ ; therefore in this case the constitutive relations preserve their form. However, for any pseudo-Euclidean rotation we have other identities

$$O^* = O^{-1} \Rightarrow O(O^{-1})^* = O^2, \quad O^* O^{-1} = O^{*2};$$

therefore the constitutive relations are modified.

**Extensions.** The previous results can be extended to more generale media, let us restrict ourselves to linear media. Arbitrary linear media is characterized by the following constitutive equations:

$$D = \epsilon_0 \epsilon(x) E + \epsilon_0 c \alpha(x) B, \quad H = \epsilon_0 c \beta(x) E + 1\mu_0 \mu(x) B,$$

where  $\epsilon(x), \mu(x), \alpha(x), \beta(x)$  are  $(3 \times 3)$ -dimensionless matrices. These equations may be re-written in terms of complex vectors  $f, h$ :

$$h = [(\epsilon + \mu) + i(\beta - \alpha)]f + [(\epsilon - \mu) + i(\beta + \alpha)]f^* ,$$

$$h^* = [(\epsilon + \mu) - i(\beta - \alpha)]f^* + [(\epsilon - \mu) - i(\beta + \alpha)]f .$$

For Euclidean rotations, the constitutive relations preserve their form. For Lorentzian boosts, however these relations change their form in the moving reference frame in accordance with the rules

$$h' = [(\epsilon + \mu) + i(\beta - \alpha)]f' + [(\epsilon - \mu) + i(\beta + \alpha)]O^2 f'^* ,$$

$$h'^* = [(\epsilon + \mu) - i(\beta - \alpha)]f'^* + [(\epsilon - \mu) - i(\beta + \alpha)]O^{*2} f' .$$

## V. CONCLUSIONS

The matrix form of the Maxwell theory in the form of Riemann – Silberstein – Majorana – Oppenheimerand, based on the theory of complex rotation group  $SO(3, C)$ , may be effectively used in practical calculation when studying electromagnetic problems. This representation is closely related to spinor formalism in Maxwell theory (see in [2]).

## REFERENCES

- [1] Fedorov, F.I., The Lorentz group. Moscow, 1978 [in Russian].
- [2] A.V. Ivashkevich, E.M. Ovsiyuk, V.V. Kisel, V.M. Red'kov. Spinor Maxwell equations in Riemannian space-time and the geometrical modeling of constitutive relations in electrodynamics. Materials Physics and Mechanics. 2020. Vol. 45, no 1, P. 104–131.

## LOW TEMPERATURE MAGNETORESISTANCE IN SILICON DOPED BY ANTIMONY

A. L. Danilyuk, A. G. Trafimenko, S. L. Prischepa  
Belarussian States University of Informatics and Radioelectronics, Minsk, Belarus

[danilyuk@bsuir.by](mailto:danilyuk@bsuir.by)

## I. INTRODUCTION

Magnetoresistance and magnetotransport in silicon and silicon-based nanostructures has great impact on the development of silicon spintronics and quantum information processing [1,2]. This is due to the importance of silicon technology and by the non-triviality of spin-dependent processes in silicon doped with various impurities. Within this framework, the investigations of the non-linear electrical effects are also relevant. Their implementation along with the spin dependent processes can pave the way to a novel energy efficient information processing devices based on silicon technology. In Refs. [3,4] authors investigated low temperatures non-linear I-V curves in silicon doped by antimony. It was shown that, with the temperatures decrease, the crossover from spin-dependent electron hopping ( $T = 5-20$  K) to the activation mechanism ( $T = 1.9-4$  K) occurs. During this, with an increase in the current density, a region of negative differential resistance arises [3,4].

In this contribution, the magnetoresistance (MR) of Si doped by Sb with the concentration of  $N_d = 10^{18} \text{ cm}^{-3}$  and temperature  $T = 2$  K within the current range  $0.015 - 0.048 \text{ A/cm}^2$  in magnetic field up to 8 T is considered. Samples were grown by Czochralski method.

## II. RESULTS AND DISCUSSION

The MR was determined from measured I-V curves at  $T = 2$  K and  $B$  in the range of  $0 - 8$  T. Such a procedure allows determining the MR and various bias currents. It was obtained that, at  $0.0015 < j < 0.034 \text{ A/cm}^2$  the MR is positive (PMR), whereas at  $j > 0.041 \text{ A/cm}^2$  the MR is negative (NMR). In the intermediate current region,  $0.034 < j < 0.041 \text{ A/cm}^2$  we obtained a series of crossovers from PMR to NMR with the  $B$  increase. In the latter case, with an increase in the current density, the magnitude of the magnetic field induction at which the transition to the NMR occurs decreases.

System under consideration is characterized by the processes of localization of the injected electrons on the neutral states  $D^0$  of Sb and by the nucleation of negatively charged  $D^-$  states in the region of relatively small currents [3,4]. The concentration of  $D^-$  states is up to  $(1-3)10^{17} \text{ cm}^{-3}$  [4]. In addition, this region is characterized by the drop of the differential resistance (DR) from 300 to 10-20  $\Omega \text{ cm}$  and small time of momentum relaxation, 3-5 fs. With the increase of the current density the delocalization of the  $D^-$  states occurs. This process is accompanied by further decrease of the DR down to a few of  $\Omega \text{ cm}$  and increase of the momentum relaxation time up to 10-15 fs and greater.

Taking into account the general trend of transition from PMR to NMR with an increase in current density, we associate the results obtained with the manifestation of weak localization (WL), the action of a magnetic field

on it, which is accompanied by competing spin-dependent processes. The dephasing in WL is determined by inelastic processes of scattering of conduction electrons on phonons,  $D^-$  states, as well as on paramagnetic antimony impurities with a mutual spin reversal. Inelastic scattering on  $D^-$  states is associated with the process of their ionization. The energy of the conduction electrons is about 1.3-5 meV, depending on their concentration, and the binding energy of the  $D^-$  state is 1.48 meV. This leads to the process of ionization of  $D^-$  states due to an electron impact. Estimates of the dephasing time of the conduction electrons are carried out. As the results showed, the main contribution in this case is made by the processes of ionization of  $D^-$  states and scattering on neutral impurities with a mutual spin reversal. The dephasing time varies in a wide range ( $\tau_\phi = 4 \cdot 10^{-14} - 10^{-11}$  s) depending on the energy of the conduction electrons.

The MR related to WL in the presence of the spin orbit interaction (SOI) demonstrates peculiar properties. The interference additive to WL remaining after the spin flip increases the conductivity. The final sign of the correction depends on which spin state gives the greater contribution, singlet or triplet. The intensity of spin-orbit scattering strongly depends on the atomic weight of the impurity. The effect of the spin-orbit interaction is stronger in materials containing heavy elements. In the case of the Si:Sb system, Sb atoms induce SOI in silicon with a constant equal to 0.3 meV.

In the case of spin-orbit scattering on impurity atoms, the dependence of conductivity on the magnetic field is significantly different for singlet and triplet spin states. In a weak magnetic field, the main role is played by the singlet contribution, which has the opposite sign compared to WL in a magnetic field, which gives PMR. As the magnetic field increases and the saturation of the field dependence of the singlet component, the role of the triplet contribution increases, which leads to the appearance of a maximum in the PMR first, and then the NMR.

Estimations of the time of spin orbit scattering  $\tau_{so} = \tau (g/\delta g)^2$  depending on the momentum relaxation time  $\tau$  have been performed. Here  $g$  is the  $g$ -factor of a conduction electron,  $\delta g$  is the variation of  $g$ -factor due to SOI. According to the known results for Si:Sb in the nearest range of the metal to insulator crossover  $\delta g \approx 3 \cdot 10^{-2}$  [5]. The value of  $\tau$  varies in a wide range, 2-10 fs [4]. Accordingly, the time of spin orbit scattering is  $\tau_{so} = 2 \cdot 10^{-12} - 10^{-11}$  s.

Calculations of the MR were performed within the model of WL for 3D samples considering different scattering mechanisms. Theory of WL was developed by many authors. The main results for 3D case were obtained by Kawabata [6]. He deduced the main equation for the 3D case. In the present work we apply the model [7] in which WL includes mechanisms of scattering on magnetic impurities, spin-flip scattering due to SOI, inelastic scattering.

As a result, the following patterns of MR manifestation in Si:Sb were established. In the region of small currents, the singlet contribution, which has the opposite sign compared to WL in a magnetic field, plays the main role. In this case, the interference contribution to the conductivity is positive. Sometimes this is called anti-localization. This leads to a positive magnetoresistance. In this region of currents, PMR occurs when the spin-orbit scattering time is less than the dephasing time, i.e.,  $\tau_{so} < \tau_\phi$ . In the region of intermediate current densities, the spin-orbit scattering time increases, and as the magnetic field induction increases and the field dependence of the singlet contribution saturates, the role of the triplet contribution increases, which leads to the appearance of a maximum in the PMR first, and then the NMR. In its pure form, NMR occurs at large spin-orbit scattering times, when this process is suppressed by other scattering mechanisms. Since WL is dominated by MR, which occurs due to a dephasing of coherent backscattering, the magnetic field gives an additional phase difference in the interference of electrons. Its appearance destroys coherence and leads to an increase in conductivity. Experimentally, this phenomenon was observed in the form of an NMR. In other words, the magnetic field destroys the interference additive to the conductivity and thus suppresses WL. This is due to the destruction of the coherence of the conjugated electron waves, since the magnetic field introduces a phase difference into the scattering amplitude and thereby reduces the probability of localization. As a result, the NMR manifests.

### III. CONCLUSIONS

The MR of antimony-doped silicon was studied at an impurity concentration of  $10^{18} \text{ cm}^{-3}$  and a temperature of 2 K. It was shown that at low current densities, the manifestation of positive MR is due to the prevailing contribution of spin-orbit scattering. At increased current densities, the manifestation of negative MR is associated with the suppression of a weak localization by a magnetic field. At intermediate current densities, the manifestation of crossovers from positive to negative MR is associated with the competition of spin-orbit scattering and inelastic scattering, which causes a dephasing of interfering electrons.

### REFERENCES

[1] R. Jansen, "Silicon spintronics" Nature Mater., Vol. 11, pp. 400–408, 2012.

- [2] T. Ladd, F. Jelezko, R. Laflamme, Y. Nakamura, C. Monroe, J.L. O'Brien "Quantum computers" Nature, Vol. 464, pp.45–53, 2010.
- [3] A.L. Danilyuk, A.G. Trafimenko, A.K. Fedotov, I.A. Svito, and S.L. Prischeпа, "Negative Differential Resistance in n-Type Noncompensated Silicon at Low Temperature" Appl. Phys. Letters, Vol. 109, p.222104, 2016.
- [4] A.L. Danilyuk, S.L. Prischeпа, A.G. Trafimenko, A.K. Fedotov, I.A. Svito, N. Kargin, "Low temperature injected-caused charge carrier instability in n-type silicon below insulator-to-metal transition" *J. Phys.: Condens. Matter*, Vol.32, p. 225702, 2020.
- [5] V. Zarifis, T.G. Castner, "ESR linewidth behavior for barely metallic n-type silicon" Phys. Rev. B, Vol. 35, pp. 6198-6201, 1987.
- [6] A. Kawabata, "Theory of Negative magnetoresistance in three-dimensional systems" Solid State Communications, Vol. 34, pp.431-432, 1980.
- [7] D.V. Baxter, R. Richter, M. L. Trudeau, R.W. Cochrane, J.O. Strom-Olsen, "Fitting to magnetoresistance under weak localization in three dimensions" Journal de Physique, Vol. 50, pp. 1673-1688, 1989.

## **AB INITIO STUDY OF EXCHANGE INTERACTIONS IN THE MAGNETIC SYSTEMS BASED ON $\text{Cr}_2\text{Ge}_2\text{X}_6$ (X=S, Se, Te)**

M. Baranova, V. Stempitsky

R&D Department, Belarusian State University of Informatics and Radioelectronics, Minsk, Belarus

[baranova@bsuir.by](mailto:baranova@bsuir.by)

### I. INTRODUCTION

Limiting the dimension of the spin sublattice (atoms with a magnetic moment) leads in most cases to the destruction of the long-range magnetic order. However, layered van der Waals structures (vdW materials) appear low-dimensional magnetism. Recently, the first 2D magnet based on an intrinsic vdW Ising compound ( $\text{FePS}_3$ ) was exfoliated [1] from crystals with 3D magnetic order. 2D vdW monolayers are a promising class of materials as a functional layer in spintronic devices.

Magnetic exchange energy plays a key role in the formation of magnetic order. This type of energy is determined by the integral of the exchange interaction, which characterizes the degree of the electrons wave functions overlap (or atomic orbitals).

The exchange interaction integral is calculated using *ab initio* simulation and the Heisenberg model. The values of the exchange interaction integral can help to establish the ground magnetic order. The article presents the results of the exchange interaction integrals calculations for  $\text{Cr}_2\text{Si}_2\text{X}_6$  (where X = S, Se, Te) compounds.

### II. RESULTS

We calculated the exchange interaction integral by using first principles calculations and the classical Heisenberg model together. This technique contains two main stages: quantum mechanical (QM) calculations and calculation of the exchange interaction integral using the Heisenberg magnetic model.

At the QM stage, we calculated the energies of atomic systems for various magnetic configurations at absolute zero temperature. The ground and excited magnetic states of the system were determined. These calculations were performed in a software package VASP, which implements the density-functional theory (DFT) method [2]. The main source of DFT simulation errors is inaccurate accounting of correlation energies. This is one of the terms that make up the total energy of the system. This should be especially taken into account in materials with localized (narrow) zones (d-electrons) due to an increase in the proportion of the correlation component in the energy characteristic of the system. The most common way to help neutralize this simulation flaw is the local spin-density approximation (LSDA+U), which was used in this work (U = 3 eV, J = 0.9 eV for Cr d-orbitals).

Exchange interaction integrals are calculated by comparing the value of the total energy obtained in the quantum mechanical simulation with the corresponding expression in the Heisenberg model.

Atomic systems were simulated with preliminary structural relaxation taking into account spin polarization. Next, static self-consistent calculations were performed to determine the electronic properties.

The magnetic exchange interaction weakens sharply with an increase in the distance between interacting electrons. Often, this type of interaction is significant only between the two nearest neighboring atoms. While

for all other combinations, it does not need to be taken into account due to a too small value. However, in this work, to analyze the spin-dependent properties in 2D vdW structures ( $\text{CrSiX}_3$ , where  $X = \text{S, Se, Te}$ ), the exchange interaction integrals were calculated for atoms located at a distance of up to 10 Å. This was done in order to confirm the absence of competition between magnetic orders.

To calculate the exchange interaction integrals ( $J_n$ , where  $n=1, 2, 3$  the order of the atom in accordance with the distance),  $2 \times 2 \times 1$  supercells were created. The orientations of the magnetic moment (spin) were set for each Cr atom in such a way as to form 4 magnetic configurations. One of which had a ferromagnetic order (FM), the other three were antiferromagnetic (AFM). Structural optimizations were performed for all configurations.

Table 1. Simulation results of  $\text{Cr}_2\text{Si}_2\text{X}_6$  structure, magnetic and electronic properties

Compound	$J_1$ , meV	$J_2$ , meV	$J_3$ , meV	$\frac{J_{1, \text{meV}}}{\text{Hubbard correction}}$	$\frac{J_{2, \text{meV}}}{\text{Hubbard correction}}$	$\frac{J_{3, \text{meV}}}{\text{Hubbard correction}}$	Magnetic order
$\text{Cr}_2\text{Si}_2\text{S}_6$	2.47	-0.07	0.04	0.84	-0.22	0.01	AFM
$\text{Cr}_2\text{Si}_2\text{Se}_6$	-1.59	0.18	-0.04	-1.88	0.13	-0.06	FM
$\text{Cr}_2\text{Si}_2\text{Te}_6$	-1.26	0.09	-0.17	-1.61	0.05	0.60	FM

Here, if the exchange integral is less than zero, then the atomic system is a ferromagnet. According to results,  $\text{Cr}_2\text{Si}_2\text{Se}_6$  and  $\text{Cr}_2\text{Si}_2\text{Te}_6$  structures ferromagnets. However,  $\text{Cr}_2\text{Si}_2\text{S}_6$  exhibits strong antiferromagnetic order. Almost all the contribution to the exchange interaction is made by  $J_1$ . Therefore, there is no competition in the magnetic moment.

### III. CONCLUSIONS

Structural and geometric optimizations were carried out using quantum mechanical simulation in a specialized software package VASP, and the main magnetic states were established. Two structures under study demonstrate ferromagnetic order ( $\text{Cr}_2\text{Si}_2\text{Se}_6$  and  $\text{Cr}_2\text{Si}_2\text{Te}_6$ ) and one structure is antiferromagnet.

### ACKNOWLEDGMENTS

This work was supported by the grant of The Belarusian Republican Foundation for Fundamental Research (contract № F20V-008).

### REFERENCES

- [1] J. U. Lee, S. Lee, J. H. Ryoo, S. Kang, T. Y. Kim, P. Kim, C. H. Park, J. G. Park, H. Cheong, Nano Lett. 16 (2016) 7433.  
 [2] G. Kresse and D. Joubert, Phys. Rev. B 59 (1999) 1758.

## INVESTIGATION OF THE STRUCTURE OF MANGANESE-DOPED SILICON-CARBON FILMS OBTAINED BY ELECTROCHEMICAL METHOD

T. Mikhailova, T. Myasoedova  
 Southern Federal University, Taganrog, Russia

[tmihaylova@sfnu.ru](mailto:tmihaylova@sfnu.ru)

### I. INTRODUCTION

Silicon-carbon films are derived from diamond-like carbon materials that have numerous useful properties:

- high coating hardness value,
- low coefficient of friction,
- high corrosion and wear resistance [1-4],
- high electrical resistance (up to  $10^{16}$  Ohm·cm) [5],
- optical bandgap width up to 3.6 eV [6],
- high thermal conductivity (up to 10 W/(m·K)),
- low-temperature coefficient of expansion,
- chemical stability [7-8].

Due to their properties, diamond-like carbon films have multifunctional applications in optical, electrical, and biomedical systems.

But this material also has disadvantages. The main problems are limited adhesion and low thermal stability. These factors greatly limit their practical application. Silicon-carbon films are devoid of these disadvantages while maintaining the advantages of diamond-like carbon films. However, they are very difficult to obtain. This fact makes relevant research in the search for new methods for producing silicon-carbon films.

## II. EXPERIMENTAL

In this work, silicon-carbon films were obtained by electrochemical deposition from an electrolyte solution. The ease of implementation and the ability to control the thickness of the films during their growth are the advantages of this method [9]. The choice of a dielectric with a thin copper sublayer as a substrate was justified in [10]. The deposition was carried out in two stages. At the first stage, a "pure" silicon-carbon film was obtained from a solution of methanol ( $\text{CH}_3\text{OH}$ ) with hexamethyldisilazane (HMDS) taken in a ratio of 9:1. The deposition time was 8 hours. Then manganese sulfate ( $\text{MnSO}_4 \cdot 5\text{H}_2\text{O}$ ) was added to the solution and precipitation was carried out for another 10 minutes. The embedding of manganese atoms into the structure of a silicon-carbon film was proved by X-ray phase diffractometry [11]. The thickness of the obtained films was about 100  $\mu\text{m}$ .

The structure of silicon-carbon films was studied using the *inVia Raman Microscope* Raman scattering spectrometer (Renishaw, UK). The results of the study are shown in Figure 1.

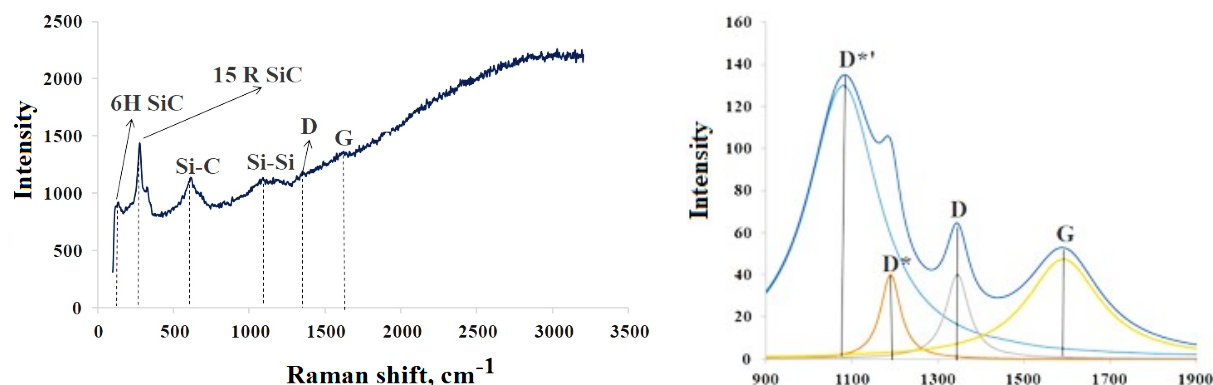


Figure 1. Raman spectrum and decomposition spectrum of peaks D and G of manganese-doped silicon-carbon films (peaks D\* and D' characterize disordered carbon)

The structure of the silicon-carbon film is multiphase and is characterized by the presence of a predominantly hexagonal phase of the 6H SiC polytype with inclusions of the rhombohedral phase of 15R SiC [12]. The presence of the Si-C bond responsible for the presence of the amorphous phase of silicon carbide was also found. The sample is characterized by the presence of D and G peaks. The G peak characterizes carbon in the plane of the vibrational mode  $\text{sp}^2$ . This parameter displays the degree of crystallization of the material. The D-band displays the degree of structural disorder (disorderliness) near the edge of the microcrystalline structure, which reduces the symmetry of the structure [13, 14]. The D and G peaks are positioned at  $1346 \text{ cm}^{-1}$  and  $1593 \text{ cm}^{-1}$ , respectively.

The procedure for decomposing Raman peaks allows you to see the "hidden" peaks. A detailed analysis of the spectral parameters was obtained by fitting the curve profile using the Lorentz function. A band of D\*-D\* peaks was detected on the spectra of the sample in the region of  $\sim 1200 \text{ cm}^{-1}$ . The appearance of D\*-D\* peaks may be associated with the presence of a phase of an unordered graphite layer with inclusions of ionic impurities [15].

## III. CONCLUSIONS

Thus, the electrochemical deposition method makes it possible to obtain silicon-carbon complex structures. The influence of the structure of the obtained films on their properties requires further study.

## REFERENCES

- [1] F.M. Kimock, "Commercial applications of ion beam deposited diamond-like carbon (DLC) coatings", *Surf. and Coatings Techn.*, Vol. 56, № 3, pp. 273-279, 1993.
- [2] G. Fanchini [et al.], "Effect of isotopic substitution on IR and ESR properties of mass selected ion beam deposited ta-C films", *Diamond and Related Mater.*, Vol. 12, № 3, pp. 900-904, 2003.
- [3] A.H. Lettington, C. Smith, "Optical properties and applications of diamond-like carbon coatings", *Diamond and Related Mater.*, Vol. 1, № 7, pp. 805-809, 1992.

- [4] C.H. Su [et al.], "Mechanical and optical properties of diamond-like carbon thin films deposited by low temperature process", *Thin Solid Films*, Vol. 498, № 1, pp. 220-223, 2006.
- [5] A. Grill, "Electrical and optical properties of diamond-like carbon", *Thin Solid Films*, Vol. 355, pp. 189-193, 1999.
- [6] K.B.K. Teo [et al.], "Highest optical gap tetrahedral amorphous carbon", *Diamond and Related Mater.*, Vol. 11, № 3, pp. 1086-1090, 2002.
- [7] M. Shamsa [et al.], "Thermal conductivity of diamond-like carbon films", *Appl. Phys. Lett.*, Vol. 89, № 16, pp. 1619-2113, 2006.
- [8] A.A. Balandin, "Thermal properties of graphene and nanostructured carbon materials", *Nature Mater.*, Vol. 10, № 8, pp. 569-581, 2011.
- [9] N. Basman, R. Uzun, E. Gocer, "Electrodeposition of Si-DLC nanocomposite film and its electronic application", *Mtcrosist. Technol.*, Vol. 24, pp. 2287-2294, 2018.
- [10] M.N. Grigoryev, T.S. Mikhailova, T.N. Myasoedova, "Resistive structures based on silicon-carbon films for gas sensors", *News of the SFU. Tech. Sci.*, Vol. 6, pp. 85-93, 2019.
- [11] T.S. Mikhailova, M.N. Grigoryev, T.N. Myasoedova, "The two-stage electrochemical deposition of a manganese-doped silicon-carbon film onto the silicon (100) substrate", <https://iopscience.iop.org/article/10.1088/1742-6596/14/10/1/012027>, doi:10.1088/1742-6596/14/10/1/012027, access mode, free.
- [12] N.K. Plugotarenko [et al.], "Electrochemical deposition of silicon-carbon films: a study on the nucleation and growth mechanism", *Nanomaterials*, Vol. 9., P. 1754, 2019.
- [13] Andrea C. Ferrari, "Raman spectroscopy of grapheme and graphite: Disorder, electron-phonon coupling, doping and nonadiabatic effects", *Solid State Commun*, Vol. 143, № 1-2, pp. 47-57, 2007.
- [14] E.I. Bîru, H. Iovu, "Graphene nanocomposites studied by raman spectroscopy", *Raman Spectroscopy*, pp. 178-201, 2018.
- [15] V. Sharma [et al.], "Structure and chemistry of crankcase and exhaust soot extracted from diesel engines", *Carbon*, Vol. 103, pp. 327-338, 2016.

## ATOM SPECIES ENERGY DEPENDENCE ON MAGNETIC CONFIGURATIONS IN THE PEROVSKITE YTTRIUM ORTHOFERRITE

A. Baglov<sup>1,2</sup>, L. Khoroshko<sup>1,2</sup>

1 Belarusian State University of Informatics and Radioelectronics, Minsk, Belarus

2 Belarusian State University, Minsk, Belarus

[baglov@bsuir.by](mailto:baglov@bsuir.by)

### I. INTRODUCTION

Multiferroics are materials which combine (ferro)magnetic and ferroelectric ordering. These materials are very interesting both for radioelectronic applications and new scientific directions, such as straintronics. Early we described the ground states for the different magnetic orderings in the perovskite  $\text{YFeO}_3$ , and the dependence of the structural properties on them were established [1]. The difference total energy and structural parameters of the various magnetic configurations of the  $\text{YFeO}_3$  appears due to interaction of iron d-shell electrons in magnetic sublattice, formed by iron ions, and interaction between iron ions and neighboring yttrium and oxygen ions which change electron density distribution and energy in the material. Unfortunately, contribution dependence for each atom species in various magnetic configurations of the  $\text{YFeO}_3$  are unknown. Changes d-shell electron energy of Fe ions for these states of the  $\text{YFeO}_3$  are unknown also. This information can be powerful for engineering magnetic properties of a multiferroics with perovskite structure for physical and technical applications. Thereby in this work we study energy dependence for each atom species and changes spin-resolved energy iron d-shell electrons of magnetic configurations of the  $\text{YFeO}_3$  by ab-initio method.

### II. METHOD

We performed our ab-initio calculations within the generalized gradient approximation (GGA) and the Perdew – Burke – Ernzerhof exchange-correlation functional with spin polarization as implemented in the OpenMX code [2-4]. We used pseudopotentials with the following valence states configuration: Y – 4s, 4p, 4d, and 5s states; Fe – 3p, 3d, and 4s states; O – 2s and 2p states. We selected the basis sets with 2

pseudoatomic orbital (PAO) functions for each electronic state and 1 adding PAO function as polarized. The integration over the  $4 \times 3 \times 5$  regular  $\Gamma$ -centered k-points mesh were performed. Calculation of the total and orbitally decomposed energy were performed after finding a total energy minimum point for each magnetic configuration through structure relaxation.

### III. RESULTS AND DISCUSSION

Each atom species and Fe  $t_{2g}$ - and  $e_g$ -orbitals contribution dependence to the total energy on different magnetic configurations of the  $YFeO_3$  multiferroic are given on Fig. 1. For all cases, the zero energy is a relative value. The total energy of the  $YFeO_3$  is monotonously decreasing from ferromagnetic (FM) to antiferromagnetic (AFM) state with close energies between neighboring magnetic configurations. Decomposition of the total energy on atoms species show that energy states decreasing in a series FM  $\rightarrow$  A-AFM  $\rightarrow$  C-AFM due to the yttrium ions, and only G-AFM state related with the Fe and O ions contribution due to inversion their energy behavior.

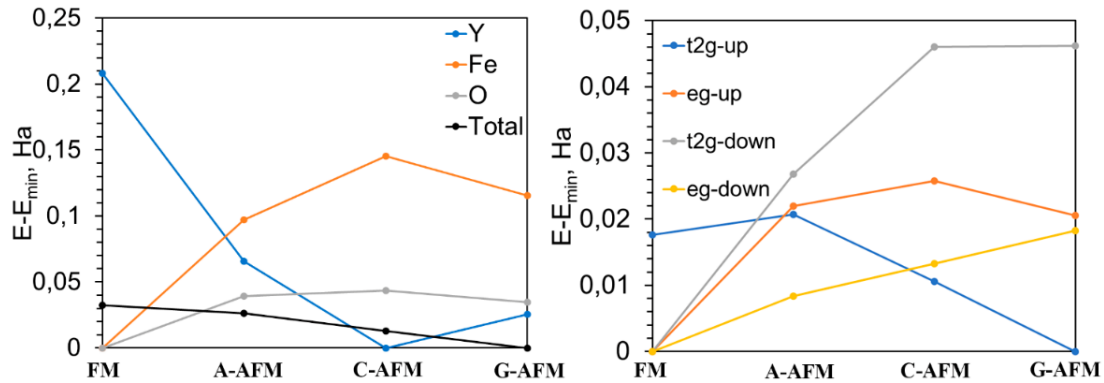


Figure 1. Energy dependence in different magnetic configurations of  $YFeO_3$ : left panel – each atoms species contributions; right panel – Fe  $t_{2g}$ - and  $e_g$ -orbitals contribution

The lowest energy state for iron d-electrons corresponds to ferromagnetic ordering, but not for  $t_{2g}$  spin up states, which has lowest energy in G-AFM ordering. In general, increasing of d-electrons energy at FM – AFM transition and decreasing of total energy due to yttrium ions stabilize G-AFM phase of  $YFeO_3$ .

### IV. CONCLUSIONS

Thus, in this work we studied energy contribution dependence for each atom species for various magnetic states in the  $YFeO_3$  perovskite multiferroic by ab-initio methods. It was shown, that stabilization of the experimentally observed G-AFM ordering in the  $YFeO_3$  take place due to interaction between d-electrons in magnetic sublattice, formed by iron ions, with combination of decreasing total energy of system due to yttrium ions. We suppose that substitution yttrium ions by magnetic ions, for example 4f-elements ions, can change main magnetic configuration from G-AFM to another AFM or FM ordering. It also can vary the energy gap between neighboring magnetic states, which is of interest for magnetic memory devices and other straintronics applications.

### ACKNOWLEDGMENTS

The authors acknowledge partial financial support from Belarusian Republican Foundation for Fundamental Research, Republic of Belarus (Grant F20MV-022).

### REFERENCES

- [1] L. Khoroshko, A. Baglov, "Magnetic configurations in  $YFeO_3$  multiferroic", Proceedings of VI International conference "Applied Problems of Optics, Informatics, Radiophysics and Condensed Matter Physics", pp. 251–253, 2021.
- [2] T. Ozaki "Variationally optimized atomic orbitals for large-scale electronic structures", Phys. Rev. B, Vol. 67, 155108-1–155108-5, 2003.
- [3] T. Ozaki, H. Kino "Numerical atomic basis orbitals from H to Kr", Phys. Rev. B, Vol. 69, pp. 195113-1–195113-19, 2004.
- [4] T. Ozaki, H. Kino "Efficient projector expansion for the ab initio LCAO method", Phys. Rev. B, Vol. 72, pp. 045121-1–045121-8, 2005.



# EMERGENCE OF TOPOLOGICAL DEFECTS IN A BILAYER OF MULTIWALLED CARBON NANOTUBES IRRADIATED BY GAMMA-RAYS

H. Grushevskaya, A. Timoshchenko, I. Lipnevich  
Physics Faculty, Belarussian State University, Minsk, Belarus

[grushevskaja@bsu.by](mailto:grushevskaja@bsu.by)

## I. INTRODUCTION

Among applications of graphene-like materials in nuclear technologies the development of radiation-resistant materials and of protective shielding nanostructured coatings is in a great demand. Graphene is stable to irradiation because the knocked-on neutral carbon atoms reside on the graphene plane. The radiation resistance of graphene can be caused by an interaction of gamma-quanta with the graphene charge vortical carriers of the pseudo-Majorana type [1,2]. A mechanism of the interaction between gamma-quanta and the pseudo-Majorana charge carriers in the graphene plane leading to a Compton scattering on super-dense fluxes of the pseudo-Dirac charge carriers has been not ascertained yet.

In the paper we will study gamma-ray scattering on rolled graphene atomic layers of high-ordered multiwalled-carbon-nanotubes (MWCNTs) which organized a bilayer. Our goal is to reveal radiation high-energy topological defects of a type of pseudo-Majorana pairs "vortex-antivortex" in graphene electron and hole densities.

## II. MATERIALS AND METHODS

MWCNT bundles decorated by the organometallic complexes were fabricated utilizing Langmuir-Blodgett (LB) nanotechnology. The two MWCNT LB-monolayers were deposited on the interdigital structure of aluminium electrodes, on the surface of which a layer of nanoporous anodic alumina (pores with a diameter of 10 nm) were previously formed as an insulator coating.

The standard low-intensive source of ionizing radiation (IRS)  $^{137}\text{Cs}$  (CsJ) was utilized. We registered about 9200 events. MWCNTs were exposed to radiation for 1 hour.

An analysis of secondary electrons spectra has been performed by a lab-quality radiation spectrometric facilities "Nuclear Physics" (BSU, Minsk, Belarus). The scintillation crystal thallium-activated sodium iodide, NaI(Tl) (a diameter of 25 mm, a height of 40 mm) was utilized as a detector crystal.

## III. RESULTS AND DISCUSSION

Response functions of the detector with and without the absorber are shown in Figure 1. The IRS response function  $R_{\text{Cs}}$  features peaks of photoelectric absorption (photopeak) and a characteristic X-ray at the lower and highest pulse heights respectively. The characteristic X-ray photons are emitted by free electrons filling non-occupied electron  $K$ -shells in atoms of the lead collimator. The radiation spectrum of CsJ is a typical one recorded from the NaI(Tl) scintillation detectors. The photopeak appears at the energy of original  $^{137}\text{Cs}$  gamma-ray photon. A Compton scattering gives rise a single Compton continuum of energies and multiple-Compton-scattering events in the IRS spectra. The multiple Compton scattering occurs due sufficiently large size of the detector crystal. One observes also a peak caused by the bremsstrahlung generated in stopping the beta particles by the IRS shield and the backscatter peak caused by photons Compton scattered at large angles in materials immediately surrounding the scintillator crystal (see Figure 1a).

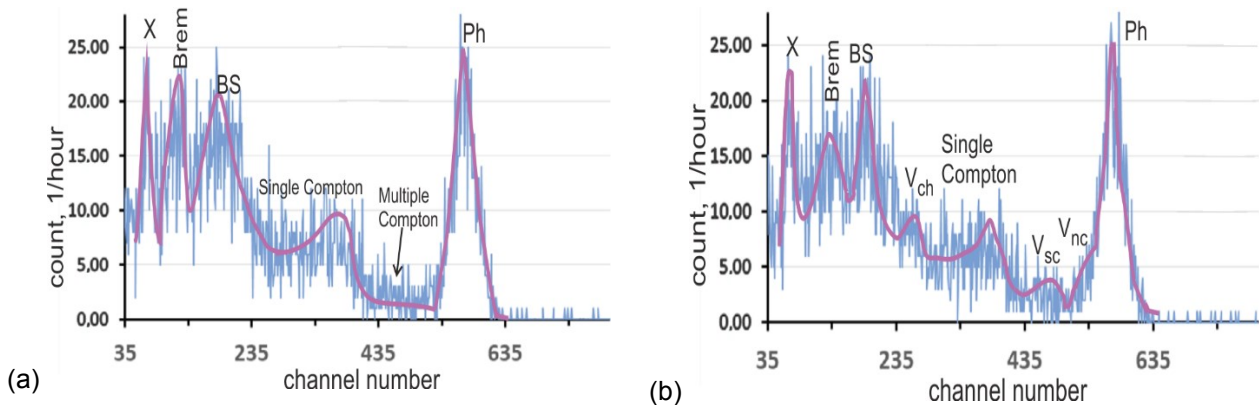


Figure 1. Pulse height spectra  $R_{\text{Cs}}$  (a) and  $R_{\text{CsG}}$  (b) for photons beam incoming from IRS  $^{137}\text{Cs}$  through the collimator without and with the absorber, respectively, and scattering on the detector crystal; a radiation background has been subtracted from original distributions.

In Figure 1 the backscatter peak, the photopeak, the characteristic X-ray peak, and the contribution from the bremsstrahlung are labeled by "BS", "Ph", "X", and "Brem", respectively; the absorber escape peaks of the pseudo-Majorana chiral, semichiral, nonchiral fermions, which are created at the interaction between graphene and gamma-ray, are called as " $V_{ch}$ ", " $V_{sc}$ ", and " $V_{nc}$ ", respectively. The single Compton continuum and area of multiple Compton scattering are labeled by "Single Compton" and "Multiple Compton", respectively.

Let us analyze MWCNT effects on the incoming  $^{137}\text{Cs}$  gamma-quanta beam. After placing the electromagnetic-radiation absorber with the bilayer of ordered MWCNT bundles decorated by the organometallic compound into the collimator, three additional peaks reveal themselves in the  $^{137}\text{Cs}$ -radiation spectrum of secondary electrons along with the photopeak, the single Compton continuum, the backscatter peak, the X-ray escape peak, and the bremsstrahlung. The spectra indicate narrowing of the  $^{137}\text{Cs}$ -radiation peaks. The shape of the single Compton continuum of  $^{137}\text{Cs}$ -radiation spectrum with maximum being approximately in 360th channel after placing of the MWCNT sample into the collimator. Maxima of the three new peaks are approximately in 260th, 460th and 535th channels. It testifies that in creating pairs of charge carriers in the graphene the gamma-quanta escape from the detector. Collisions between the radiation graphene defects and the photons from the bremsstrahlung process leads to decreasing of the peak "Brem".

Now we will utilize the experimental data to elucidate a pseudo-Majorana nature of the graphene charge carriers. To do it we offer a following mechanism of graphene radiation resistivity through creation of neutral vacancies  $V_0$  with knocked-on neutral carbon atoms  $C^0$  fixed on the graphene monolayer by radiation defects of a pseudo-Majorana type. The gamma-rays can escape from the detector crystal owing to a production of radiation-defect pairs in a form of topologically nontrivial defects of delocalized electron (hole) density in a one part of the graphene monolayer plane and topologically nontrivial defects of hole (delocalized electron) density in another graphene part. The pseudo-Majorana vortex-antivortex pairs are created at the Compton scattering of the gamma-rays on the MWCNT graphene planes. Accordingly, the radiation defects decrease the energy deposited in the detector and it results in the appearance of the additional peaks  $V_{ch}$ ,  $V_{sc}$  and  $V_{nc}$  in the response function  $R_{CsG}$  (see Figure 1b). At colliding with C atoms the free pseudo-Majorana fermions are de-excited and confined by hexagonal symmetry near the Dirac touching valent and conductivity graphene bands. Meanwhile the graphene pseudo-Majorana band structure is degenerated and, accordingly, the vortex pairs transit from the flat area to conical one of the graphene band. It signifies that the branches of the vortex begin to move inconsistently. The vortex decay leads to an emergence of an electron-hole avalanche.

### III. CONCLUSIONS

So, scattering in MWCNTs the 661.7-keV gamma-rays create pairs of topologically nontrivial radiation defects and antidefects. These high-energy graphene pairs of scattering centers are pseudo-Majorana vortical and antivortical fermions. Annihilating and scattering on carbon electron density the pseudo-Majorana quasiparticles avalanche-likely produce electron-hole configurations of graphene charge density.

### REFERENCES

- [1] H. Grushevskaya, A. Timoshchenko, E. Avdanina, I. Lipnevich, "Clustering artificial atoms induced by high-frequency electromagnetic radiation in graphene monolayers of multiwalled carbon nanotubes", *Int. J. Nonlin. Phenom. in Compl. Sys.*, Vol. 23, pp. 342-356, 2020.
- [2] H. Grushevskaya, G. Krylov, "Vortex dynamics of charge carriers in the quasi-relativistic graphene model: high-energy kp approximation", *Symmetry*. Vol. 12, p. 261, 2020.

## TEMPERATURE DEPENDENCE OF THE THERMAL CONDUCTIVITY OF WURTZITE ALUMINUM NITRIDE, GALLIUM NITRIDE AND ALUMINUM-GALLIUM NITRIDE

V. Volcheck, D. Hvazdouski, M. Baranova, V. Stempitsky  
Belarusian State University of Informatics and Radioelectronics, Minsk, Belarus

[vlad.volchek@bsuir.by](mailto:vlad.volchek@bsuir.by)

### I. INTRODUCTION

Over the last decades, much attention has been focused on III-nitride semiconductors aluminum nitride (AlN), gallium nitride (GaN) and aluminum-gallium nitride (AlGaN) as promising materials for the application in high-power radio-frequency electronic and optoelectronic devices. Although the structural, electronic and optical properties have been extensively studied, relatively little work, both analytical and experimental, has

to date been reported on their thermal conductivity ( $\kappa$ ). Meanwhile, this thermoelectric parameter a measure of the ability to conduct heat is important from both fundamental and applied aspects [1].

In this paper, we make a thorough analysis of the structural and phonon properties of wurtzite AlN, GaN and AlGaN in the framework of the *ab initio* (or “first-principles”) formalism [2] to determine the thermal conductivity at various temperatures ( $T$ ).

## II. CALCULATION PROCEDURE

The first-principles method combines an exact iterative solution of the phonon Boltzmann transport equation in the single-mode relaxation time approximation with accurate computations of the second-order (harmonic) and third-order (anharmonic) interatomic force constants. We perform the first-principles calculations using a plane-wave basis set within the framework of the density-functional theory as implemented in the Vienna Ab initio Simulation Package [3]. The Perdew-Burke-Ernzerhof parameterization is employed for the exchange-correlation functional [4]. Projector-augmented wave potentials are used for Al, Ga and N atoms and the plane-wave cutoff energy is set to 520 eV. For the determination of the third- and second-order force constants, reciprocal spaces of the  $\alpha$ -quartz supercells are sampled by the  $3 \times 3 \times 3$  mesh and at  $\Gamma$  point only, respectively. Non-self-consistent calculations are made along the lines between the high-symmetry points L- $\Gamma$ -X and M-K- $\Gamma$ -A of the first Brillouin zone.

## III. RESULTS

Figure 1 shows the temperature dependence of the thermal conductivity of defect-free wurtzite AlN and GaN. The thermal conductivity at 300 K of AlN (GaN) along the [100] and [001] crystal directions is calculated to be 3.96 (2.59) and 4.62 (3.36) W/(cm·K), yielding an anisotropy factor of 1.17 (1.30). As the temperature grows to 700 K, the  $\kappa$  values of 1.37 (1.08) and 1.58 (1.36) W/(cm·K) are obtained, leading to an anisotropy factor of 1.15 (1.26) a slight decrease relative to the figures observed at very low temperatures. In a range from 300 to 700 K, the  $\kappa$  curves for AlN [100] and AlN [001] have slopes of -1.28 and -1.29. The thermal conductivity of GaN [100] and GaN [001] falls off as  $T^{-1.03}$  and  $T^{-1.07}$ , respectively.

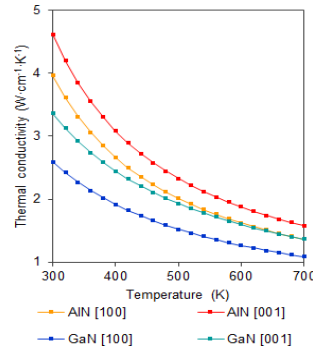


Figure 1. Thermal conductivity of wurtzite AlN and GaN as a function of temperature

In Figure 2, the dependence of the thermal conductivity of defect-free wurtzite  $\text{Al}_x\text{Ga}_{1-x}\text{N}$  on composition ( $x$ ) at different temperatures is given. In semiconductor alloys fabricated from AlN and GaN, the resistive phonon-phonon scattering increases greatly resulting in  $\kappa$  values far lower than those of their end-point materials. At 300 K,  $\text{Al}_{0.42}\text{Ga}_{0.58}\text{N}$  [100] and  $\text{Al}_{0.48}\text{Ga}_{0.52}\text{N}$  [001] are characterized by the lowest thermal conductivity of 1.83 and 1.63 W/(cm·K), respectively. In a range from 300 to 700 K, the bowing parameter can be approximated by  $3.649118 \cdot 10^{-3}T - 0.2210367$  for  $\text{Al}_x\text{Ga}_{1-x}\text{N}$  [100] and by  $6.390055 \cdot 10^{-3}T - 0.5105837$  for  $\text{Al}_x\text{Ga}_{1-x}\text{N}$  [001].

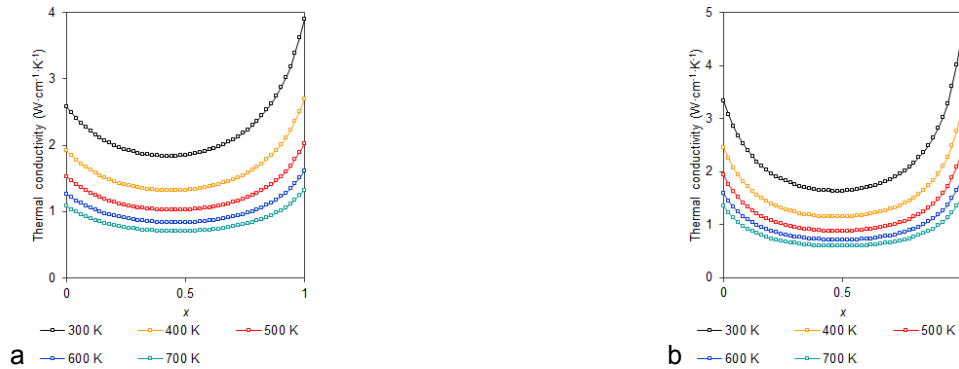


Figure 2. Thermal conductivity of wurtzite  $\text{Al}_x\text{Ga}_{1-x}\text{N}$  as a function of composition at various temperatures: a – [100]; b – [001]

#### IV. CONCLUSIONS

We have made a careful analysis of the structural and phonon properties of wurtzite AlN, GaN and AlGaIn in the framework of the *ab initio* formalism to determine their thermal conductivity at various temperatures. The mathematical models for  $\kappa$  that account for crystal direction, composition and temperature were presented.

#### ACKNOWLEDGMENTS

This work is supported by the grant 3.1 of Belarusian National Scientific Research Program “Photonics and Electronics for Innovations”.

#### REFERENCES

- [1] Z. Yan, G. Liu, J. M. Khan, A. A. Balandin, “Graphene Quilts for Thermal Management of High-Power GaN Transistors”, Nat. Commun., Vol. 3, Art. no. 827, 2012.
- [2] L. Lindsay, D. A. Broido, T. L. Reinecke, “Thermal Conductivity and Large Isotope Effect in GaN from First Principles”, Phys. Rev. Lett., Vol. 109, Art. no. 095901, 2012.
- [3] G. Kresse, J. Furthmuller, “Efficient Iterative Schemes for Ab Initio Total-Energy Calculations Using a Plane-Wave Basis Set”, Phys. Rev. B, Vol. 54, pp. 11169-11186, 1996.
- [4] J. P. Perdew, K. Burke, M. Ernzerhof, “Generalized Gradient Approximation Made Simple”, Phys. Rev. Lett., Vol. 77, pp. 3865-3868, 1996.

### SILICON CARBIDE MEMBRANES FOR MICROELECTROMECHANICAL SYSTEMS BASED CMUT WITH INFLUENCE FACTORS

Moumita Pal, Reshmi Maity, Niladri Pratap Maity

Department of Electronics & Communication Engineering, Mizoram University (A Central University, Govt. of India), Aizawl, India

[maity\\_niladri@rediffmail.com](mailto:maity_niladri@rediffmail.com)

#### I. INTRODUCTION

Microelectromechanical Systems (MEMS) based capacitive micromachined ultrasonic transducer (CMUT) has many applications in medical imaging [1]. Ultrasonic transducer technology has been long dominated by piezoelectric transducers, particularly in the medical ultrasound imaging. The best popular materials used for fabricating CMUT membranes are silicon nitride ( $\text{Si}_3\text{N}_4$ ), polysilicon, chromium and aluminum are characteristically used to shape electrodes on top of these membranes. But current technology of CMUT demands the silicon carbide (SiC) for membrane material where the electrode instead of being on top of the membrane is placed beneath the membrane. It offers greatest contiguity of the upper and subordinate electrodes. For this it decreases the transduction gap enlightening the electro-mechanical coupling and sensitivity of the device. Aside from this, it is reported that the CMUT has a resonance frequency of 1.7 MHz and a 3 dB-bandwidth of 0.15 MHz. Also, the higher Young's modulus (260 GPa) of SiC with its little residual stress ( $\pm 30$  MPa). Consequences in great strength and resilient CMUT membranes, which led to the studies presented in this paper. All the results are validated by FEM simulation.

#### II. PROPOSED MODEL

The SiC membranes based CMUT with a membrane radius of 55  $\mu\text{m}$  consists of six layers. A single cell CMUT consists of a silicon carbide layer as the vibrating membrane and an electrode made of aluminum which acts as the top electrode, followed by a cavity which acts as an electrostatic transduction gap. A second electrode is formed using aluminum with more thickness to form the lowermost electrode. A layer of dielectric  $\text{Si}_3\text{N}_4$  film as an insulator is introduced among the cavity and the lowermost electrode to prevent the two electrodes from shorting in case of contact. The bottom layer is silicon dioxide acting as a substrate on which all the above layers are formed. The materials used and their thicknesses taken for the structural modeling of the device is given in Table 1.

Table 1. Materials used with thickness

Material Used	Thickness	Layer
Silicon Carbide (SiC)	2 $\mu\text{m}$	Top membrane
Aluminum (Al)	60 nm	Top electrode
Cavity (Air)	450 nm	Electrostatic transduction gap
Aluminum (Al)	300 nm	Bottom electrode
Silicon Nitride ( $\text{Si}_3\text{N}_4$ )	500 nm	Dielectric film as an insulator
Silicon Dioxide ( $\text{SiO}_2$ )	2 $\mu\text{m}$	Substrate

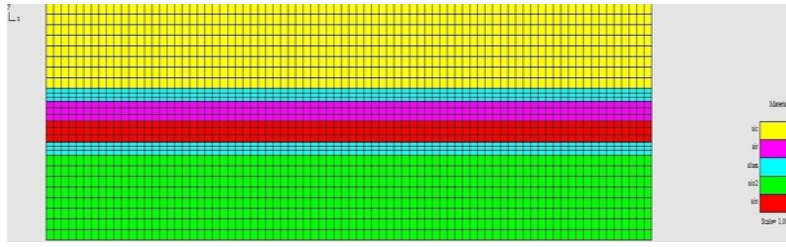


Figure 1. FEM simulated 2D model of SiC CMUT element

The modeling of the device is first carried out by calculating the equivalent capacitance of the device. Although in previous studies like in literature there are two capacitances one of which is contributed by the vibrating membrane and the other by the insulating material, while in this studies the two capacitances are contributed by the transduction gap and the insulating material since the top electrode is beneath the membrane as discussed in the first section. Also, a 2D view of the device simulated using PZFlex based on the finite element method is also provided in Fig. 1. The coupling factor, also known as the  $k$  factor of an electromechanical transducer is its capability to transform electrical into mechanical energy, and vice versa. As soon as the CMUT functions as a transmitter with an electrical input, the coupling factor  $k$  is the ratio of amount of mechanical energy transported to the load to whole energy put in storage in the device.

### III. RESULTS & DISCUSSION

Characterization of the device to maximize its performance in terms of sensitivity, energy conversion efficiency and operating point, the capacitance behavior, coupling factor, and collapse voltage of the CMUT are analyzed based on mathematical model. Smaller gap thickness and insulator thickness represent smaller spacing between the two electrodes producing greater field force (voltage across the plates) and a superior flux (charge composed on the plates) for any voltage applied across the two electrodes which result in larger capacitance. Materials with high dielectric constant have greater permittivity which allows them to proposal less disagreement to field flux for a specified amount of field force than materials with less permittivity. All these results can be understood from simple observation of conventional capacitor plates, an estimation of capacitance for any pair of disconnected conductors can be computed with the analytical model. All the results are validated by FEM simulation. The device capacitance calculated for the CMUT at a 55  $\mu\text{m}$  membrane radius is 0.1627 pF producing a force of 1.264  $\mu\text{N}$ .

As the coupling distance (effective gap distance) increases, the coupling capacitance will decrease reducing the intensity of the output energy. In CMUT the membrane transports in the direction of the applied electric field and the membrane vibration in the transverse direction is negligible [2]. Also in a CMUT, the coupling distance is a function of both the gap distance and insulator thickness. It is found that the coupling factor of the proposed device at a 40 V DC bias voltage is 0.383 i.e., the coupling efficiency of the CMUT is 38.3%. When the surface tension increases, it shrinks the membrane surface area causing the coupling capacitance to decrease which leads to a reduction in the coupling factor.

Many studies shown that CMUTs can operate both in the conventional mode and collapse mode [3]. The collapse voltage calculated is 78.06 V with a coupling factor of 0.7, this means the operating DC bias strongly dictates the performance of the transducer by improving the coupling factor. From the characteristics of collapse voltage, we can understand that the collapse voltage is lower for a larger membrane radius and increases when the membrane thickness is increased respectively. This is because the spring constant of the membrane decreases making the membrane less stiff and increases make the membrane stiffer that means higher elasticity. Here also, all the results are validated by FEM simulation.

### IV. CONCLUSIONS

The general behaviour of silicon carbide membranes capacitive micromachined ultrasonic transducers with its influence factors is demonstrated in this paper. The device capacitance depends on the transduction gap thickness, insulator thickness, membrane radius, and the material used as an insulator. A larger device capacitance means greater force generated by the membrane, which means higher sensitivity. So, to get a high sensitive CMUT the transduction gap and the insulator layer thickness must be very small with a large the membrane radius and the material used as an insulating layer must have high relative permittivity. This paper also presents the coupling factor ( $k_w^2$ ) and how it is affected by the collapse voltage. This observation tells us that, increasing the membrane thickness as we increase the membrane radius and balancing the two can give high capacitance and high coupling factor resulting in better sensitivity and efficient energy conversion of the device, provided the effective gap distance is as small as possible. A finite element analysis can be performed using FEM simulators. These simulated results can be associated with the outcomes presented in this paper for future generation and design of CMUTs.

## ACKNOWLEDGMENTS

The Authors are highly indebted to University Grant Commission, Govt. of India and Mizoram University (A Central University, Govt. of India), for supporting this technical work.

## REFERENCES

- [1] R. Maity, N. Maity, S. Baishya, "An Efficient Model of Nanoelectromechanical Systems Based Ultrasonic Sensor with Fringing Field Effects" IEEE Sensor Journals, Vol. 20, No. 4, pp. 1746-1753, 2020.
- [2] G. Yaralioglu, A. Ergun, B. Bayram, E. Haeggstrom, B. Khuri-Yakub, "Calculation and measurement of electromechanical coupling coefficient of capacitive micromachined ultrasonic transducers" IEEE Transactions on Ultrasonics, Ferroelectrics and Frequency Control, Vol. 50, No.4, pp. 449–456, 2003.
- [3] K. Park, O. Oralkan, B. Khuri-Yakub, "Comparison of conventional and collapse-mode CMUT in 1-D array configuration" IEEE International Ultrasonics Symposium, U.S.A., pp. 1000-1003, 18-21 October, 2011.

## KCC-INVARIANTS-BASED GEOMETRIZATION OF A THEORY OF ELECTROMAGNETIC AND SPINOR FIELDS ON THE BACKGROUND OF THE SCHWARZSCHILD SPACETIME

N. Krylova<sup>1</sup>, V. Red'kov<sup>2</sup>

1 Belarusian state agrarian technical university, Minsk, Belarus

2 B.I.Stepanov Institute of Physics of the National Academy of Science of Belarus, Minsk, Belarus

## I. INTRODUCTION

The Kosambi–Cartan–Chern geometrical approach (KCC-theory) is developed in detail in numerous mathematical books and papers [1–3]. KCC-theory allows to describe the evolution of a dynamical system in a configuration space of Lagrange type. At that, the dynamical system is given by the system of second-order differential equations, and its properties are described in terms of five KCC geometrical invariants. From the physical point of view, the most interesting invariant is the second one which is associated with the Jacobi stability of the system, i.e. convergence or divergence of the bundles of geodesics. In this work we apply the KCC-theory to study systems of differential equations which arise in theory of electro-magnetic and spinor fields on the background of the Schwarzschild spacetime.

## II. RESULTS AND DISCUSSION

The electromagnetic field on the background of the curved space-time of a Schwarzschild black hole has been considered. The first and second KCC-invariants for the second-order differential equations obtained after variable splitting in initial Maxwell equations both in the complex Majorana–Oppenheimer formalism and 10-dimensional Duffin-Kemmer–Petiau formalism. The second KCC-invariant determines Jacobi field for geodesics deviation, so it indicates how rapidly the different branches of the solution diverge from or converge to the intersection points. From physical point of view, the most interesting points are the singular points. The numerical calculated dependencies of the second invariant on the radial variable are shown in Figure 1a. Near the singular points the second invariant  $\Lambda$  behaves as follows:

$$\begin{array}{ll} x = \frac{r}{M} \rightarrow 0 & \Lambda \rightarrow -\frac{3}{4x^2} < 0; \\ x \rightarrow 1 (r \rightarrow r_g \equiv M) & \Lambda \rightarrow \frac{1 + 4M^2\omega^2}{4(x-1)^2} > 0; \\ x \rightarrow \infty (r \rightarrow \infty) & \Lambda \rightarrow \omega^2 > 0. \end{array}$$

It indicates that in the vicinity of  $x = 0$  the geodesics converge. Vice versa, near the Schwarzschild horizon  $x = 1$  and at  $x \rightarrow \infty$  the Jacobi instability exists and the geodesics diverge.

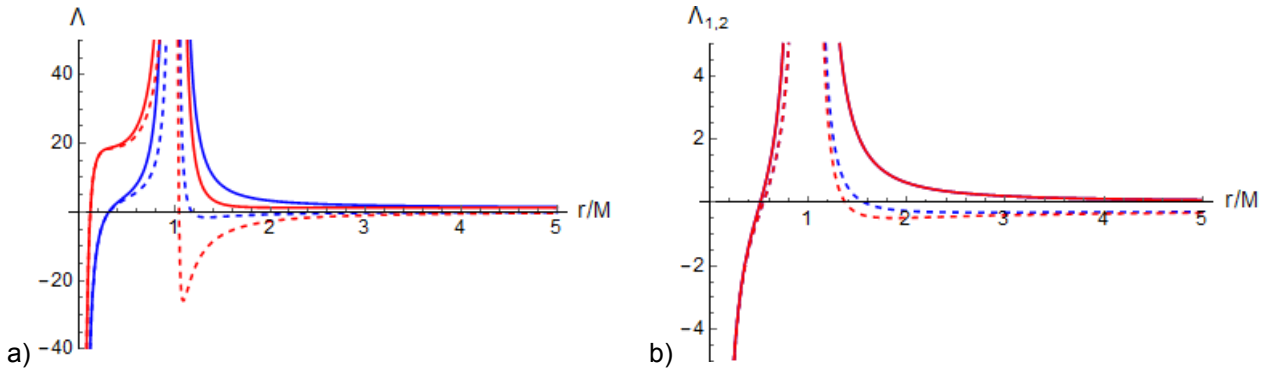


Figure 1. Typical dependencies of the second invariant eigenvalues on the radial coordinate  $x = \frac{r}{M}$  for the geometrized problem of the electromagnetic (a) and spinor (b) fields on the background of the Schwarzschild spacetime

For a spin  $\frac{1}{2}$  particle on the background of Schwarzschild spacetime the radial differential equation system obtained from Dirac equation after variable splitting has been studied. The first and second KCC-invariants are determined explicitly. The behavior of two different eigenvalues  $\Lambda_{1,2}$  of the second invariant has been analyzed numerically (see Figure 1b). In the vicinity of the singular points the real parts of the eigenvalues behave as follows:

$$\begin{aligned} r \rightarrow 0 & \quad \Lambda_{1,2} \rightarrow -\frac{5}{16r^2} < 0; \\ r \rightarrow M & \quad \text{Re}[\Lambda_{1,2}] \rightarrow \frac{r^2\varepsilon^2 + 3}{4(M-r)^2} > 0; \\ r \rightarrow \infty & \quad \Lambda_{1,2} \rightarrow \frac{1}{4}(\varepsilon^2 - m^2). \end{aligned}$$

In the vicinity of the Schwarzschild horizon the geodesics diverge at any energy  $\varepsilon$ , while at  $r \rightarrow \infty$  the geodesics diverge at  $\varepsilon > m$  and converge at  $\varepsilon < m$ .

The 3-d, 4-th and 5-th invariants for the both considered problems are equal to zero.

### III. CONCLUSIONS

So, we apply the KCC-geometrical approach to study the radial equation systems arising in two quantum-mechanical problems, i.e. electromagnetic and spinor fields on the background of the Schwarzschild spacetime. The stability analysis in terms of the second invariant demonstrate the difference in the behavior of geodesics at  $r \rightarrow \infty$  for these two problems that may be associated with different structure of solution (discrete and continuous spectra). The vanishing of the 3-d, 4-th and 5-th invariants means that, in geometrical terms, there exists a nonlinear connection on the tangent bundle, with zero torsion and curvature.

### REFERENCES

- [1] Gh. Atanasiu, V. Balan, N. Brinzei, M. Rahula, "Differential Geometry of The Second Order and Applications: Miron-Atanasiu theory" URSS, Moscow, 2010. P. 256. [In Russian].
- [2] P.L. Antonelli, L. Bevilacqua, S.F. Rutz "Theories and models in symbiogenesis", Nonlinear Analysis, Vol. 4, pp. 743-753, 2003.
- [3] P.L. Antonelli, I. Bucataru, "New results about the geometric invariants in KCC-theory", An. Şt. Univ. "Al.I.Cuza" Iaşi. Mat. N.S. Vol. 47, pp. 405-420, 2001.

### INFORMATION - STATISTICAL APPROACH TO INVERSE OPTICAL PROBLEM SOLUTION FOR 3D DISPERSE SYSTEMS WITH NANO AND MICRO PARTICLES

A. G. Bezrukova<sup>1</sup>, O. L. Vlasova<sup>2</sup>

1 St. Petersburg Academy of Sciences on Strength Problems, Peter the Great St. Petersburg Polytechnic University, Polytekhnicheskaya 29, 195251, St. Petersburg, Russian Federation

2 Institute of Biomedical Systems and Biotechnology, Peter the Great St. Petersburg Polytechnic University, Polytekhnicheskaya 29, 195251, St. Petersburg, Russian Federation

[bezr@pb1097.spb.edu](mailto:bezr@pb1097.spb.edu)

## I. INTRODUCTION

In nature, a class of objects called three-dimensional (*3D*) disperse systems (DS) is widely spread. For *3D* DS the dispersive mediums are most often air or water, and the disperse phase consists from particles of different origin [1]. In our study the particle sizes of *3D* DS can vary from nanometers to about ten micrometers. Earlier [2-7] it was reported that a set of optical parameters of the so-called second class (obtained as a result of processing experimental data without involving any a priori information about *3D* DS) is unique for each *3D* DS and implicitly reflects characteristics of *3D* DS: shape, refractive index of particles, distribution functions of number and mass of particles in size, etc. In other words, the characteristic of any *3D* DS can be represented as *ND* vector in the *N*-dimensional space of optical parameters of the second class. In this set there are parameters specific to the *3D* DS components. On the basis of theory and experiment it is possible to predict these specific parameters for a certain component. In the previous papers it was discussed the *3D* DS polymodality problem [4], optical characterization of *3D* DS mixtures [5], the use of unique optical vectors for monitoring the aggregation process [7]. This part of study is connected with creation of algorithm based on the information-statistical methodology [8-11], which can help in search of the most informative data for particles of interest.

## II. RESULTS AND DISCUSSION

One of the promising directions for studying the information content of various optical parameters for determining the component composition of natural *3D* DS is the information-statistical theory of observation interpretation [ 8-11]. The algorithms and programs developed on the base of this theory can allow identifying the components which presence in *3D* DS is the most probable. The probability of the component of interest presence is determined from the experimental quantitative values of the optical parameters of an unknown *3D* DS. For determination of these probabilities, it is necessary to have the representative so-called "training data" in the knowledge bank for each of the possible components of *3D* DS. On investigating model mixed *3D* DS, it is possible to analyze the algorithm efficiency even against the background of strong interactions of components and with various physical and chemical effects on the system. With increasing the component number in a complex *3D* DS, the number of parameters should also increase. It should be noted that a uniform representation of the input and output data provides the ability to add new parameters to those obtained earlier. Judgment about the reliability of the results allows the most informative unique parameters to be selected. The set of parameters from optical methods as: refractometry, absorbance, fluorescence, light scattering (integral and differential, static and dynamic, unpolarized and polarized) can be unique for each monocomponent *3D* DS. At the same time there are also general features. At the analysis of unknown polycomponent *3D* DS the comparison of measured parameters with known ones can help to identify the system under study. For this purpose a software package MULTALT [10] was used providing the process of interpretation and visualization of intermediate and final results with estimation of decision probability. The methodology was tested on mixed in different proportions experimental dispersions consisted of two monocomponent *3D* DS: kaolin clay and bacteria *Echerichia coli*. This approach can be of vital importance for the development of natural *3D* DS control on the presence of dangerous impurities.

## III. CONCLUSIONS

For differentiation of *3D* DS constituents in mixtures the dimension of *ND* vectors can be enlarged due to the involvement into consideration different measurement conditions such as wavelengths, angles and apertures of measurements, polarization, etc. Calculations are based only on experimental data and can be performed online.

## ACKNOWLEDGMENTS

Authors thank Prof. Vitaly J. Klenin, Prof. Rainer Reuter, Prof. Feodor M. Goltsman, Prof. Alexander I. Melker, Dr. Tatyana B. Kalinina, Dr. Margarethe Hofmann, Dr. Dmitriy F. Kalinin for the useful discussions. No external funding was received for this study.

## REFERENCES

- [1] V.J. Klenin, Thermodynamics of systems containing flexible chain polymers. Elsevier, 1999, 850 p.
- [2] A.G. Bezrukova, "Development of multiparametric optical assay for on-line environmental control", Remote Sensing of Vegetation and Water, and Standardization of Remote Sensing Methods, Giovanna Cecchi, Torsten Lamp, Rainer Reuter, Konradin Weber, Editors, Proceedings of SPIE, Vol. 3107, pp. 298-304, 1997.
- [3] A.G. Bezrukova, "Nondestructive testing of *3D* disperse systems with micro and nano particles: *N*-dimensional space of optical parameters ", Proceedings of SPIE, Vol. 6253, pp. 62530C1-C4, 2006.



- [4] A.G. Bezrukova, O.L. Vlasova, "Optical characterization of 3D disperse systems with nano and micro particles: polymodality of size distributions ", *Materials Physics and Mechanics*, Vol. 13, N2, pp.162 – 174, 2012.
- [5] A.G. Bezrukova, O.L. Vlasova, "Mixtures of 3D disperse systems with nano and micro particles: Optical characterization", *St. Petersburg Polytechnic University Journal, Physics and Mathematics*, Vol. 2, IN 4, pp. 316–321, 2016. <http://dx.doi.org/10.1016/j.spjpm.2016.11.004>.
- [6] A.G. Bezrukova, O.L. Vlasova, "Optical characterization of 3D disperse systems with nano and micro particles: Unique vectors", *Materials Physics and Mechanics*, Vol. 39, N1, pp. 81-86, 2018. doi: 10.18720/MPM.3912018\_13.
- [7] A.G. Bezrukova, O.L. Vlasova, "Nano and micro particle aggregation: unique optical vectors for control ", *Materials Physics and Mechanics*, Vol. 45, N 1, pp. 87-95, 2020. DOI: 10.18720/MPM.4512020\_9.
- [8] F.M. Goltsman, "Physical experiment and statistical conclusions", Leningrad University Publishing House, 1982, 192 p.
- [9] T. B. Kalinina, F.M. Goltsman, " Methodological problems of interpretation of gravitational and magnetic fields ", *Russian Geophysical Journal*, N. 2, pp. 63-68,1994.
- [10] F.M. Goltsman, D.F. Kalinin, T. B. Kalinina, "MULTALT computer technology for multi-alternative classification and forecasting for a complex of geodata ", *Russian Geophysical Journal*, N 17-18, pp. 64–70. 2000.
- [11] D.F. Kalinin, " Information and statistical prediction of mineral resources ", Geological Exploration Group Publishing House, St. Petersburg, 2011, 226 p.

## MODELING THE FRAGMENTATION OF 2,5-DIKETOPIPERAZINE IONS

A. Basalae<sup>1</sup>, V. Kuz'michev<sup>1</sup>, M. Panov<sup>1</sup>, A. Petrov<sup>2</sup>, O. Smirnov<sup>1</sup>

1 Ioffe Institute, St Petersburg, Russia

2 Institute of Chemistry, St. Petersburg State University, St. Petersburg, Russia

[kuzmichevv@mail.ru](mailto:kuzmichevv@mail.ru)

### I. INTRODUCTION

Cyclic dipeptides, often found in nature, are formed by linking amino-terminus of a linear dipeptide to its carboxyl - terminus by amide bond. All of them are derivatives of 2,5-diketopiperazine (DKP) or cyclo-Diglycine with the molecular formula  $C_4H_6N_2O_2$ .

### II. METHODS

To calculate the optimized geometry of molecules (Figure 1) and singly charged ions, as well as their total energies, the DFT method was used, using Dmol<sup>3</sup> module from the Materials Studio software package. We used B3LYP functional and the all-electron atomic basis DNP (ver.3.5) with unrestricted spin polarization [1, 2]. The energy convergence was less than  $1 \cdot 10^{-5}$  Ha and geometry convergence was less than  $5 \cdot 10^{-3}$  Å.

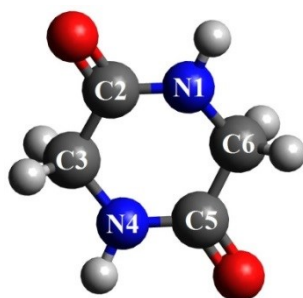


Figure 1. Structure of the DKP molecule

At the first stage we optimized geometry of molecules and ions with molecular mechanics using COMPASS II force field to minimize the interatomic interactions. The second stage includes DFT calculation of electronic structure with total geometry optimization. The calculated total energies of molecules and ions were used for further analysis. These data of the total energies make it possible to calculate the reaction energies for the channels of fragmentation of the formed ions. For the simulation, we chose the DKP ion fragmentation processes for which were observed experimentally the largest cross sections.

In the experiment DKP ionization occurred as a result of the capture of one electron by  $\text{He}^{2+}$  ions with an energy of 4 keV/u. The formed molecular ions were analyzed by mass and charge using a time-of-flight analyzer. Analysis of the measured mass spectra makes it possible to obtain the values of the relative cross sections the fragment ions formation. The fragments identification in our work was based on the assumption that the formation of compounds of mass  $m$  requires a minimum number of broken bonds and a minimum rearrangement of atoms between the formed ion and neutral fragments. It should be borne in mind that in the process of fragmentation, the processes of migration of hydrogen atoms are likely.

### III. RESULTS AND DISCUSSION

It was shown that the largest cross section has the process of  $\text{DKP}^+$  ion formation ( $\sigma=180$  rel.u.). The most probable mechanisms of the major cross-sectional channels for the  $\text{DKP}^+$  ion fragmentation were considered. (Table 1). The reaction energy ( $E_r$ ) was determined as the difference between the total energies of the fragments and the parent ion (Figure 2). The most intense fragment  $m=30$  (u) in the mass spectrum is formed when the C2—N1 and C5—C6 bonds (or symmetric to them) are broken and the hydrogen atom migrates to the charged fragment from the residue which was considered as four isomers. Ions with masses 42 and 72 (u) are formed upon cleavage of C2(5)—N1(4) and C3(6)—N4(1) bonds, and with masses 41 and 73 (u) upon cleavage of bonds N1(4)—C2(5) and C6(3)—C5(2). The charge with the same probability remains with either the light or the heavy fragment. It is also possible to form fragments with masses 28 and 86 (u), which are formed upon cleavage of the C2(5)—C3(6) and C2(5)—N1(4) bonds.

Table 1. Energy and relative cross section of the main channels of  $\text{DKP}^+$  ion fragmentation

Ion [ $m$ (u)]	Neutral fragment [ $m$ (u)]	$E_r$ (eV)	$\sigma$ (rel. u.)
$\text{CH}_4\text{N}$ [30]	$\text{C}_3\text{H}_2\text{NO}_2$ [84]	2.07 – 2.36	100
$\text{C}_2\text{H}_2\text{O}$ [42]	$\text{C}_2\text{H}_4\text{N}_2\text{O}$ [72]	4.68	28.6
$\text{C}_2\text{H}_4\text{N}_2\text{O}$ [72]	$\text{C}_2\text{H}_2\text{O}$ [42]	3.19	20.0
$\text{CHNO}$ [43]	$\text{C}_3\text{H}_5\text{NO}$ [71]	4.11	42.9
$\text{C}_3\text{H}_5\text{NO}$ [71]	$\text{CHNO}$ [43]	1.78	37.9
$\text{CO}$ [28]	$\text{C}_3\text{H}_6\text{N}_2\text{O}$ [86]	7.22	49.2
$\text{C}_3\text{H}_6\text{N}_2\text{O}$ [86]	$\text{CO}$ [28]	0.89	8.1

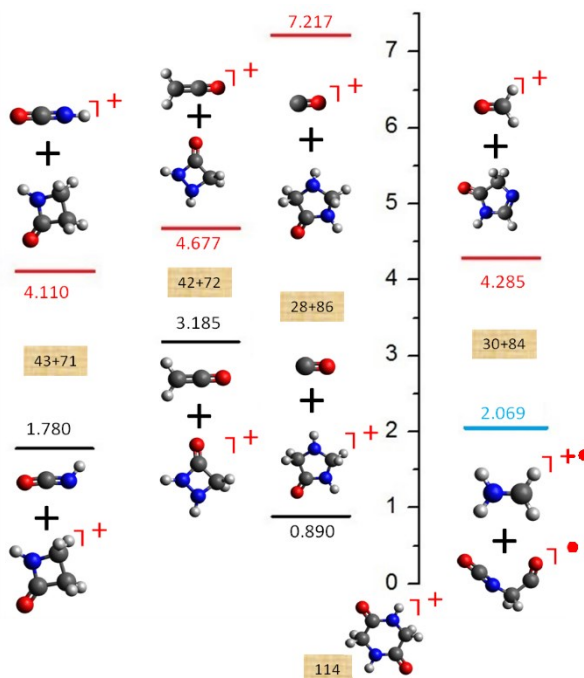


Figure 2. Energy diagram of  $E_r$  (eV)  $\text{DKP}^+$  fragmentation reactions. The filled rectangles show the masses of the fragments formed during the fragmentation of the initial molecular ion, from the energy of which  $E_r$  is counted. The segments correspond to  $E_r$  (eV) for the considered reactions

### IV. CONCLUSIONS

Quantum chemical calculations performed for the cyclo-Diglycine molecules showed that there is a correlation between the probability of the bond rupture and its length variation.

## ACKNOWLEDGMENTS

The calculations were carried out using the computing resources of the RC "Computing Center of St. Petersburg State University" (<http://cc.spbu.ru>).

## REFERENCES

- [1] B. Delley. "An all-electron numerical method for solving the local density functional for polyatomic molecules" J. Chem. Phys, Vol. 92, pp. 508-517, 1990.
- [2] B. Delley. "From molecules to solids with the DMol<sup>3</sup> approach" J. Chem. Phys, Vol. 113, pp. 7756-7764, 2000.

## AB-INITIO SIMULATION OF HYDROGENATED GRAPHENE PROPERTIES

V. Murav'ev, V. Mishchenka

Belarussian States University of Informatics and Radioelectronics, Minsk, Belarus

[mishchenko@bsuir.by](mailto:mishchenko@bsuir.by)

### I. INTRODUCTION

Graphene has been the subject of many recent investigations due to its peculiar transport properties [1]. But investigations are shown the problem connected with the lack of a graphene bandgap, which prevents its use in digital electronics. Chemical modification of graphene named as graphane has recently entered for investigation as possible candidate to solve this problem [2-3]. Graphane is the compound, which consist from two-dimensional graphene covalently bonded by some atoms of the hydrogen. Graphane is a semiconductor, which have of novel structure and low dimensionality. It provides a fertile playground for fundamental science and technological applications. To this purpose, in this work, main task is to investigate parameters and characteristics of the hydrogenated graphene by the ab-initio method.

### II. METHOD AND PECULIARITIES OF SIMULATION OF HYDROGENATED GRAPHENE PROPERTIES

Ab-initio calculations have been performed by means of the Quantum Espresso [4] code, using the Perdew-Burke-Ernzerhof (PBE) parametrization of the generalized gradient approximation (GGA). A 40 Ry wave function cutoff and 240 Ry charge density cutoff have been considered, while the Brillouin zone has been sampled using a 24 x 24 x 1 Monkhorst–Pack grid. A 20 bohr layer of vacuum is considered to separate the sheet from its periodical images. We have extracted the effective mass and other parameters from results of the density functional theory DFT-GGA simulations.

### III. RESULTS OF MODELING OF PARAMETERS AND CHARACTERISTICS OF THE HYDROGENATED GRAPHENE BY THE AB-INITIO METHOD

Relaxed structures for 100% and 50% hydrogenated and fluorinated graphene (from here on H100%, H50%, F100%, and F50%, respectively) are in agreement with results already shown in the literature [2-3]. We show some results for the considered H50% and H100% structures in Figures 1 and 2. Figure 1, a shows the peculiarities of the arrangement of carbon (C) and hydrogen (H) atoms and figure 1, b - the zone diagram in the structure of 50% hydrogenated graphene (or graphane of C<sub>2</sub>H<sub>1</sub> type).

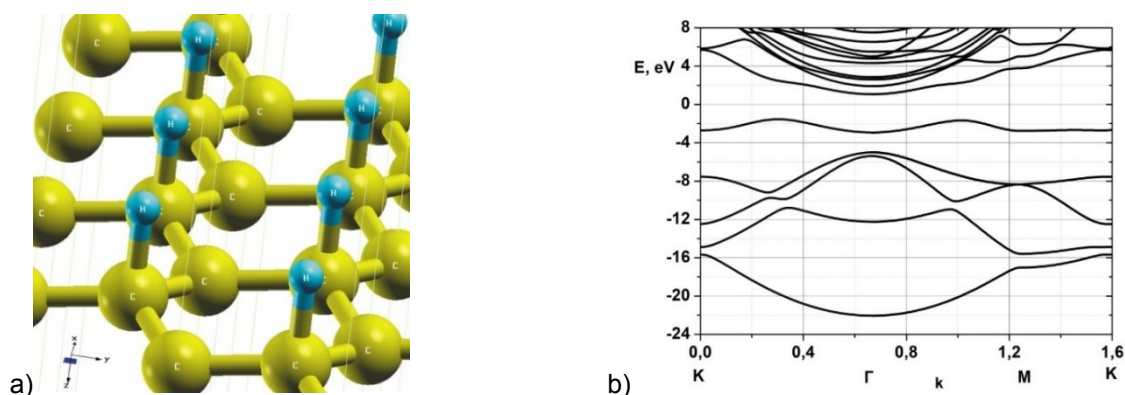


Figure 1. a) Features of arrangement of carbon (C) and hydrogen (H) atoms and b) zone diagram in the structure of 50% hydrogenated graphene (graphane of C<sub>2</sub>H<sub>1</sub> type)

Figure 2, a shows the peculiarities of the arrangement of carbon (C) and hydrogen (H) atoms and figure 2, b - the zone diagram in the structure of 100% hydrogenated graphene (or graphane of C<sub>2</sub>H<sub>2</sub> type). From the

analysis of this figures, which shows the dependences of the energy values  $E$  (eV) on the normalized value of the wave vector  $k$ , it is clear that the hydrogenated graphene is characterized by a three-valley  $\Gamma$ -M-K band diagram. Valley  $\Gamma$  is characterized by the smallest energy gap between the conduction and valence bands. When modeling the electronic characteristics and parameters of hydrogenated graphene it is necessary to analyze the parameters of all three valleys K, M and  $\Gamma$ .

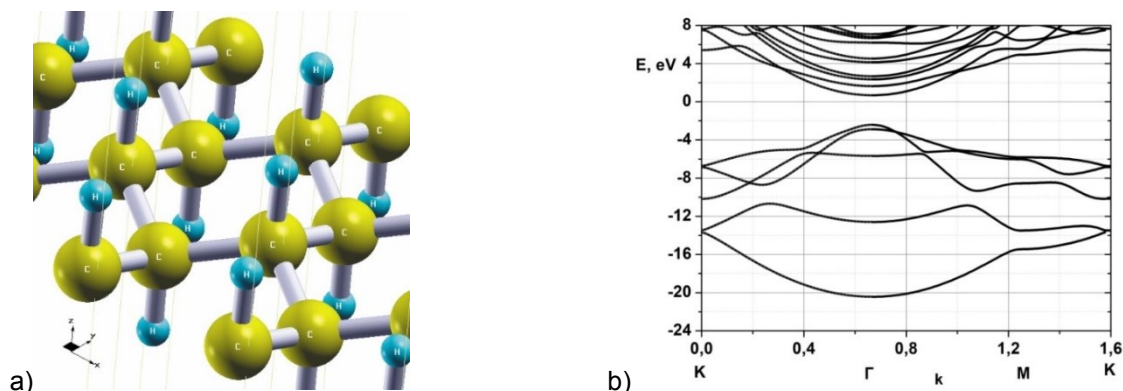


Figure 2. a) Features of arrangement of carbon (C) and hydrogen (H) atoms and b) zone diagram in the structure of 100% hydrogenated graphene (graphane of C<sub>2</sub>H<sub>2</sub> type)

Effective electron masses for graphane of C<sub>2</sub>H<sub>1</sub> and C<sub>2</sub>H<sub>2</sub> have been calculated taking into account the value of the parameter  $E_g$ , which is the energy gap between the conduction and valence bands for the  $\Gamma$ -M-K valleys.

#### IV. CONCLUSIONS

Modeling of electron transfer processes in three-dimensional semiconductor structure containing graphane is carried out. We have extracted the effective mass and other parameters from results of the density functional theory DFT-GGA simulations. Due to the use of graphane with such characteristics of transfer of charge carriers it is possible to achieve a graphene transistor structure with open bandgap. The high mobility and high speed of charge carriers make graphane a promising material for creating new semiconductor devices with good output characteristics.

#### REFERENCES

- [1] D. C. Elias, R. R. Nair, T. M. G. Mohiuddin, S. V. Morozov, P. Blake, M. P. Halsall, A. C. Ferrari, D. W. Boukhvalov, M. I. Katsnelson, A. K. Geim and K. S. Novoselov, *Science*, Vol. 323, pp. 610, 2009.
- [2] H. Sahin, O. Leenaerts, S. K. Singh, and F. M. Peeter "GraphAne: From Synthesis to Applications", 2015.
- [3] S. Bruzzone, G. Fiori "Ab-initio simulations of deformation potentials and electron mobility in chemically modified graphene and two dimensional hexagonal boron-nitride", *Appl Phys. Lett.*, Vol. 99, pp. 22108, 2011.
- [4] Giannozzi P., Baroni S., Bonini N., Calandra M., Car R., Cavazzoni C., Ceresoli D., Chiarotti G. L., Cococcioni M., Dabo I. et al., *J.Phys.:Condens.Matter* 29, 465901 (2017), <http://iopscience.iop.org/article/10.1088/1361-648X/aa8f79>.

### FIRST-PRINCIPLES CALCULATION OF ELECTRONIC PROPERTIES OF MONOELEMENT 2D MATERIALS

D. Hvazdouski, V. Stempitsky

Belarusian State University of Informatics and Radioelectronic, Minsk, Belarus

[gvozдовsky@bsuir.by](mailto:gvozдовsky@bsuir.by)

#### I. INTRODUCTION

Atomically thin two-dimensional (2D) materials have made their way to the forefront of several research areas including batteries, electrocatalysis, electronics, and photonics [1]. This development has been prompted by the intriguing and easily tunable properties of atomically thin crystals and is fueled by the constant discovery of new 2D materials and the emergent concepts of lateral [2] and vertical [3] 2D heterostructures, which opens completely new possibilities for designing materials with tailored and superior properties. So far more than fifty compounds have been synthesised or exfoliated as single layers. These include the well-known monoelemental crystals and their ligand functionalised derivatives, transition metal

dichalcogenides, transition metal carbides and -nitrides, group III-V semiconductors and insulators, transition metal halides, post-transition metal chalcogenides and organic-inorganic hybrid perovskites.

In the search for new materials with tailored properties or novel functionalities, first-principles calculations are playing an increasingly important role. The continuous increase in computing power and significant advancements of theoretical methods and numerical algorithms have pushed the field to a point where first-principles calculations are comparable to experiments in terms of accuracy and greatly surpass them in terms of speed and cost. Structural, thermal, and electronic properties, have been a cornerstone of materials science, and in the past decade, the experimental data have been augmented by an explosion of computational data obtained from first-principles calculations. Density functional theory (DFT) methods, when properly conducted, are quite reliable for ground state properties such as structural and thermodynamic properties, they are generally not quantitatively accurate for excited state properties such as electronic band structures and optical absorption spectra.

In this work we did DFT calculations to investigation electronic properties of monoelemental 2D materials previously unknown and potentially synthesisable monolayers.

## II. METHODS AND RESULTS

Calculations of the total energy and electronic structure of the materials under study were performed using the VASP software package. For the basis of plane waves, a cutoff energy of 520 eV was taken. To avoid mirror interactions of wave functions with each other arising from the translation of cells in a plane model of 2D systems, periodic plates were separated by a 15 Å-thick vacuum layer along the crystallographic direction *c*. The nonbonding van der Waals interaction (vdW) between atoms is taken into account when using the semiempirical Green's dispersion correction scheme with Becke and Johnson's corrections (BJ-damping). Integration in the momentum space of the Brillouin zone was carried out using a k-point grid generated by the Monkhorst-Pack scheme with an inverse spatial resolution of  $2\pi \times 0.03 \text{ \AA}^{-1}$ .

Electronic band structures are calculated along the high symmetry paths of 2D Bravais lattices. The band energies are computed within DFT using two different xc-functionals, namely PBE and HSE06. The electron density is determined self-consistently on a uniform k-point grid of density  $10.0/\text{ \AA}^{-1}$ . From this density, the PBE band structure is computed non-selfconsistently at 200 k-points distributed along the band path. The band structure is calculated non-selfconsistently using the range-separated hybrid functional HSE06 on top of a PBE calculation with k-point density  $12.0/\text{ \AA}^{-1}$  and 600 eV plane wave cutoff.

Table 1 shows the results of calculating the electronic properties of monoelement 2D materials using PBE and HSE06 xc-functionals. Band gap, and the type of semiconductor for the compounds under study is indicated. The results obtained may differ from the experimental ones in the direction of underestimating the band gap due to the well-known difficulties arising in the framework of the density functional theory.

Table 1. Electronic properties of monoelement 2D materials

XC-functional	Parameter	Monoelement 2D material								
		C <sub>2</sub>	Si <sub>2</sub>	Ge <sub>2</sub>	Sn <sub>2</sub>	Pb <sub>2</sub>	P <sub>2</sub>	As <sub>2</sub>	Sb <sub>2</sub>	Bi <sub>2</sub>
PBE	Band gat, eV	0.000				–	1.987	1.564	1.485	0.568
	Band character	Semimetallic				Metallic	Indirect			Direct
	Junction type	K - K				–	K - M	G - M	G - M	G - G
HSE06	Band gat, eV	0.000				–	2.753	2.189	1.183	0.977
	Band character	Semimetallic				Metallic	Indirect			Direct
	Junction type	K - K				–	G - M			G - G

The band structures of the studied monoelement 2D materials were obtained and according to which the type of conductivity was established. It was found that C<sub>2</sub>, Si<sub>2</sub>, Ge<sub>2</sub> and Sn<sub>2</sub> are semimetals with direct transitions. P<sub>2</sub>, As<sub>2</sub> and Sb<sub>2</sub> are indirect-gap semiconductors with bandgaps of 2.753, 2.189 and 1.183 eV, respectively. Bi<sub>2</sub> is a direct-gap semiconductor with a band gap of 0.977 eV. Pb<sub>2</sub> is a 2D metal-type material. The Fermi level in this case crosses the conduction bands.

## III. CONCLUSIONS

Analysis of band structures indicates the presence of semiconductors and conductors among the studied group of monoelement 2D materials. The results obtained quantitatively and qualitatively characterize the structural, electronic properties of crystal structures based on 2D materials and can be used in the development of methods for calculating the basic electrophysical parameters of promising devices for nanoelectronics and spintronics.

## ACKNOWLEDGMENT

This work was supported by the grant 3.02.3 of Belarusian National Scientific Research Program "Convergence-2025" and the grant of The Belarusian Republican Foundation for Fundamental Research for young scientists "Science M - 2021" (contract № F21M-122). Computing cluster of BSUIR was used for computer modeling.

## REFERENCES

- [1] A. C. Ferrari, F. Bonaccorso, V. Fal'ko et al. Science and technology roadmap for graphene, related two-dimensional crystals, and hybrid systems. *Nanoscale* 2015, 7, 4598–4810.
- [2] C. Huang, S. Wu, A. M. Sanchez, et al. Lateral heterojunctions within monolayer MoSe<sub>2</sub>-WSe<sub>2</sub> semiconductors. *Nature materials* 2014, 13, 1096–1101.
- [3] A. K. Geim, I. V. Grigorieva. Van der Waals heterostructures. *Nature* 2013, 499, 419–425.

## SPHERICAL WAVE-TYPE SOLUTION IN RELATIVISTIC THEORY OF GRAVITATION

A. Leonovich<sup>1</sup>, Yu. Vyblyi<sup>2</sup>

1 Belarusian State University of Informatics and Radioelectronics, Minsk, Belarus

2 Institute of Physics, National Academy of Sciences, Minsk, Belarus

[vyblyi@gmail.com](mailto:vyblyi@gmail.com)

### I. INTRODUCTION

As known, in General Relativity (GR) the energy of gravitational field is described with help the energy-momentum pseudotensor, but expression for corresponding tensor is absent. It is one of reasons for which the gravitational interaction may regarded as a tensor interaction in Minkowski space-time. The most consistently such approach was realized in relativistic theory of gravitation (RTG) [1,2]. This theory can regarded as a gauge theory of the group of Lie variations for dynamic variables. The related transformations are variations of the form of the function for generally covariant transformations. That the actions be invariant for this group under the transformations of the dynamical variables alone requires replacing the "nondynamical" Minkowski metric  $\gamma^{ik}$  with expression  $g^{ik} = \sqrt{-\gamma}(\gamma^{ik} + k\psi^{ik})$ , where  $\gamma = \det\gamma_{ik}$ ,  $g = \det g_{ik}$ ,  $k^2$  - is the Einstein constant, and thus introducing the gauge gravitational potential  $\psi^{ik}$ . The expression  $g^{ik}$  is interpreted here as the metric of the effective space-time, from which the connection - the Cristoffel brackets can be uniquely constructed. The RTG field equations at its massless variant are the Einstein ones for the effective metric, added the conditions, restricting the spin states  $D_i \psi^{ik} = 0$ , where  $D_i$  is the covariant derivative in Minkowski space. This conditions plays the significant role in RTG. It removes the gauge arbitrariness of Einstein equations and coincides with the Fock harmonic conditions in Galilean coordinates [3]. Note that the approach to gravitation in Minkowski space-time has a long history. This approach was considered in detail by R. Feynman in [4].

Although RTG field equations locally coincides with General Relativity ones, their global solutions, generally speaking, will be different, since this solutions are defined on the various manifolds. RTG, being founded on the simple space-time topology, allows to introduce the global Galilean coordinate system, that distinguishes RTG from bimetric theories, in which the flat space plays the auxiliary role and its topology does not define the character of the physical processes. This distinction may take place at interpretation of the field solutions, since the coordinate system is defined by Minkowski metric in RTG, but it is fixed by noncovariant coordinate conditions in GR. Just this situation takes place for spherically-symmetrical gravitational fields. In GR according the Birkhoff theorem any spherical gravitational field in vacuum is a static one. The proof of this theorem is grounded on the transformation of certain spherically-symmetrical metric to the coordinates in which it has a static form. But in RTG such transformation is the transfer from the spherical coordinates in Minkowski space to some "nonstatic" coordinates. The Birkhoff theorem means that in the case of spherically symmetry the coordinate system in which the vacuum metric depends from one coordinate always exists, but it is not means that the field was static in the starting coordinates. Hence the task of the investigation of nonstatic spherically symmetric solutions arises. In this paper one of the possible nonstatic spherically symmetric wave solutions in implicit form is founded and its energy characteristics is considered.

## II. METHODS AND RESULTS

To find the spherically symmetric wave solutions we use the Birkhoff theorem and present a nonstatic spherical wave solution in certain coordinate system  $(\tau, R, \theta, \phi)$  in the Schwarzschild metric form

$$ds^2 = \left(1 - \frac{2m}{R}\right) d\tau^2 - \left(1 - \frac{2m}{R}\right)^{-1} dR^2 - R^2 d\Omega^2. \quad (1)$$

To find this solution in spherical coordinates of Minkowski space  $(t, r, \theta, \phi)$  we use the coordinate transformation  $t = t(\tau, R), r = r(\tau, R)$  and the transformation coefficients will be found from the condition (1). The corresponding equations, connecting the variables  $(t, r)$  and  $(\tau, R)$ , will have the form

$$\frac{R}{R-2m} \frac{\partial^2 t}{\partial \tau^2} - R^{-2} \partial_R [(R^2 - 2mR) \frac{\partial t}{\partial R}] = 0, \quad (2)$$

$$\frac{R}{R-2m} \frac{\partial^2 r}{\partial \tau^2} - R^{-2} \partial_R [(R^2 - 2mR) \frac{\partial r}{\partial R}] + \frac{2r}{R^2} = 0. \quad (3)$$

We search the partial solution of this equations in the form  $\tau = t + T(u), R = r + m, u = t + f(r)$ , where  $u$  is retarded argument, which is finite at any values of  $R$ . In result the metric components of the spherical wave have the form

$$g_{00} = \frac{r-m}{r+m} (1 + T_u)^2, g_{01} = \frac{r-m}{r+m} T_u (1 + T_u) f_u, g_{11} = \frac{r-m}{r+m} (T_u)^2 (f_u)^2 - \frac{r+m}{r-m}, \quad (4)$$

$$g_{22} = -(r+m)^2, g_{33} = -(r+m)^2 \sin^2 \theta, \quad (5)$$

the function  $f$  is defined from the equations (2-3). We show also that this solution have the positive-definite density of energy and momentum [5].

## III. CONCLUSIONS

In relativistic theory of gravitation the nonstatic spherically-symmetrical solutions and in particular such wave solutions have a physical sense as far as the temporal coordinate of the Minkowski space-time has it. Although the receiving wave solution has enough formal character, it illustrates the possibility of existence of spherical gravitational waves. The realistic model must include also interior solution and matching it with the finding exterior one.

## REFERENCES

- [1] A.A. Logunov, M.A. Mestvirishvili, "Relativistic Theory of Gravitation", M. Mir, 329 p., 1989 (in Russian).
- [2] A. Logunov, "The Theory of Gravity", Nova Scifnce Publ., N.Y., 342 p., 1998.
- [3] V. Fock, "The Theory of Space, Time and Gravitation", 2nd edition. Pergamon Press, Macmillan Comp., 448 p., 1964.
- [4] R.P. Feunman, F.B. Morinigo and W.G. Wagner, "Feunman Lectures on Gravitation", Addison-Wesley Publishing Company, 280 p., 1995.
- [5] A. Leonovich and Yu. Vybyli "Spherical gravitational waves in the weak gravitational field", In Proc. of the IX International Conference Bolyai-Gauss-Lobachevsky, Minsk, p.130-135, 2016.

## MODELING OF OPTICAL PROPERTIES OF HYBRID METAL-ORGANIC NANOSTRUCTURES

A. Ponyavina, K. Barbarchyk, A. Zamkovets, S. Tikhomirov

B. I. Stepanov Institute of Physics of the National Academy of Sciences of Belarus, Minsk, Belarus

[kananovich.ek@gmail.com](mailto:kananovich.ek@gmail.com)

## I. INTRODUCTION

The development of modern nanotechnologies for the production of effective elements of nanophotonics, nanoplasmonics and nanoelectronics is largely aimed at the creation of hybrid nanostructures which include both plasmonic and organic components [1,2]. One of the types of such hybrid nanostructures are

ultradisperse media consisting of plasmonic metal-containing nanoparticles embedded in a matrix of organic semiconductors. With dense packing of nanoparticles in such nanocomposites, interparticle electrodynamic interactions associated with near-field scattering and coherent re-irradiation by particles of each other have the most important influence on their optical properties. By changing the material, size, shape or internal structure of plasmonic nanoparticles included in a hybrid metal-semiconductor nanocomposite, it is possible to adjust the degree of overlap of the spectral absorption bands of the nanocomposite components, which, in turn, affects the severity of near-field interparticle interactions. One of the ways to control the near-field scattering efficiency and absorption spectra characteristics of plasmon nanoparticles is to apply shells on their surfaces. This circumstance determines the importance of developing methods for modeling the optical properties of hybrid metal-organic nanostructures containing two-layer nanoparticles.

## II. METHOD AND RESULTS

To model the spectral characteristics of such nanostructures, the extended Mie theory was used, which makes it possible to calculate the extinction efficiency factor ( $Q_{ext}$ ) and the scattering efficiency factor in the near zone ( $Q_{NF}$ ) of two-layer spherical particles placed in an absorbing matrix [3,4]:

$$Q_{ext} = \frac{4m_i^2}{m_r[1 + e^\eta(\eta - 1)]} \operatorname{Re} \left\{ \frac{1}{m_i - im_r} \sum_{n=1}^{\infty} [(2n+1)(\psi_n^* \psi_n' - \psi_n \psi_n'^* + b_n \psi_n'^* \xi_n + b_n^* \psi_n \xi_n'^* - a_n \psi_n^* \xi_n' - a_n^* \psi_n' \xi_n^*)] \right\},$$

$$Q_{NF} = \frac{(4\pi m_i R)^2}{\lambda_0^2 [1 + e^\eta(\eta - 1)]} \sum_{n=1}^{\infty} \left\{ |a_n|^2 [(n+1)|h_{n-1}|^2 + n|h_{n+1}|^2] + (2n+1)|b_n|^2 |h_n|^2 \right\}.$$

Here  $\lambda_0$  – is the wavelength of the incident radiation,  $m = m_r - im_i$  – complex refractive index of the matrix,  $a_n$ ,  $b_n$  – Mie coefficients,  $a$  – particle radius,  $\eta = 4\pi am_i / \lambda_0$ . Riccati-Bessel functions and their derivatives ( $\psi_n$ ,  $\xi_n$ ,  $\psi_n'$ ,  $\xi_n'$ ), as the spherical Hankel function of the first kind of order  $h_n$  depend on the diffraction parameter  $\rho = 2\pi a / \lambda_0$ . In the case of two-layer spherical particles, the Mie coefficients are functions of the complex refractive indices of the nucleus and shell, the diffraction parameters of the particle as a whole and its nucleus.

The  $Q_{ext}$  value determines the attenuation of the intensity of the incident light beam caused by absorption in the particle and scattering on it. The  $Q_{NF}$  factor characterizes an increase in the intensity of the field along the surface of a sphere of radius  $R$  when nanoparticles are introduced into the center of this sphere.

Figures 1, 2 show the spectral dependences of  $Q_{ext}$  and  $Q_{NF}$  factors for two-layer plasmon nanospheres consisting of a metallic core (Ag, Cu) coated with a dielectric shell, placed in the organic semiconductor matrix of copper phthalocyanine (CuPc). The near-field scattering efficiency factor was calculated for  $R = R_2$ , where  $R_2$  is an external radius of a two-layer nanosphere. As one can see, dielectric shell allows shifting the surface plasmon resonance band of plasmonic nanoparticles absorption both to short- and long-wavelength spectral range depending on the relation between shell and matrix refractive indexes. However, for cases under consideration, the appearance of dielectric shells on the plasmonic core leads to strong decrease of the  $Q_{ext}$  and  $Q_{NF}$  values.

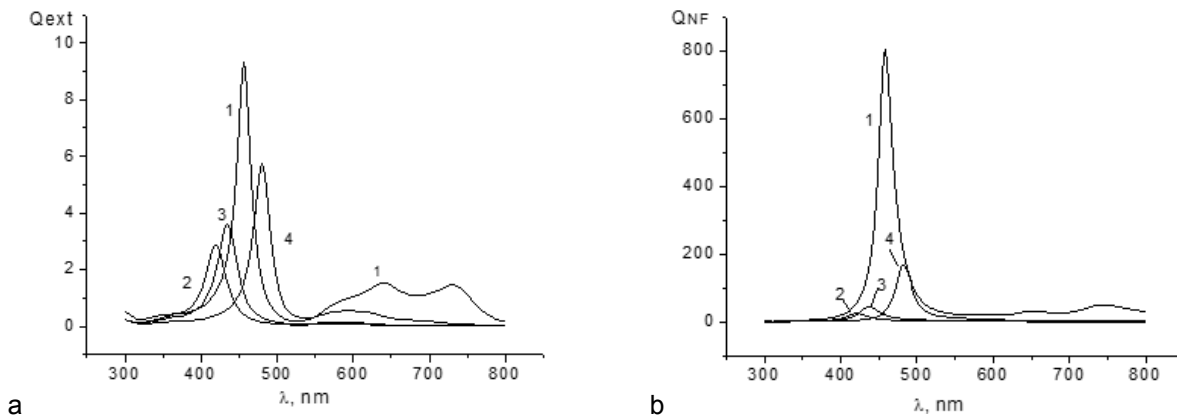


Figure 1. Spectral dependence of the extinction efficiency factor (a) and the near-field scattering efficiency factor (b) for silver nanoparticle (curve 1) and two-layer nanospheres with silver core and dielectric shell (curves 2-4) placed in the CuPc matrix. The radius of the silver core  $R_1 = 10$  nm, the outer radius of the two-layer sphere  $R_2 = 15$  nm. Refractive index of dielectric shell  $n = 1.35, 1.5, 2.0$  (curves 2, 3, 4 correspondingly)



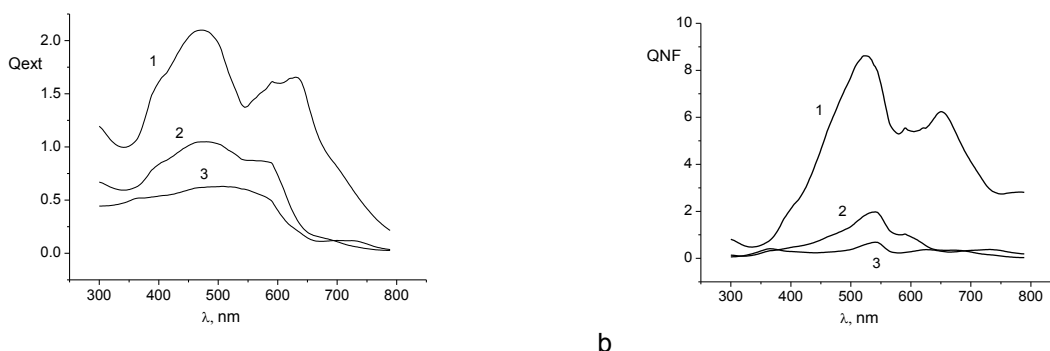


Figure 2. Spectral dependence of the extinction efficiency factor (a) and the near-field scattering efficiency factor (b) for two-layer Cu@SiO<sub>2</sub> nanospheres placed in the CuPc matrix. The radius of the copper core  $R_1 = 25$  nm, the outer radius of the two-layer sphere  $R_2 = 30$  nm (curve 1), 40 nm (curve 2), 50 nm (curve 3)

### III. CONCLUSIONS

Results of numerical simulations show that attenuation spectra of hybrid metal-organic nanostructures, as well as the near field effects at the spectral range of absorption bands of organic component, can be regulated by changing plasmonic nanoparticle material, their size or shell refractive index and thickness. Besides, the degree of near-field interactions with dense packaging can be regulated by the choice of the matrix in which the nanoparticles are placed.

### ACKNOWLEDGMENTS

The work was partially supported by the Belarusian Republican Foundation for Basic Research (grant №  $\Phi 20EA-006$ ).

### REFERENCES

- [1] Sergey Lepeshov, Alexander Krasnok, Pavel Belov, Andrey Miroschnichenko “Hybrid Nanophotonics”, Physics Uspekhi, V. 188, № 11, p. 1137-1154, 2018 [in Russian].
- [2] A. D. Zamkovets, E. I. Aksiment’eva, A. N. Ponyavina «Spectral manifestation of surface plasmon resonance in polyparaphenylene–silver nanostructures», Journal of Optical Technology, Vol. 78, Issue 2, pp. 84-87, 2011.
- [3] I. W. Sudiarta, P. Chylek, “Mie scattering formalism for spherical particles embedded in an absorbing medium,” J. Opt. Soc. Am. A 18, 1275–1278, 2001.
- [4] R. A. Dunich, A. N. Ponyavina, V. V. Filippov, «Local field enhancement near spherical nanoparticles in absorbing media», J.Appl.Spectr., V.76, pp.705-710, 2009.

## MINIMIZING THE INFLUENCE OF TEMPERATURE CHANGES IN THE ENVIRONMENT ON THE PERFORMANCE CRITERIA OF THERMO-OPTICAL PROCESSOR BASED ON FABRY-PEROT AND SMITH MICRORESONATOR

V.B. Zalessky, A.I. Konoiko, V.M. Kravchenko, A.S. Kuzmitskaya  
State Scientific and Production Association «Optics, Optoelectronics and Laser Technology»,  
68-1 Nezavisimosti avenue, 220072, Minsk, Belarus

[mickevichhanna@gmail.com](mailto:mickevichhanna@gmail.com)

### I. INTRODUCTION

The main disadvantage of using Fabry-Perot and Smith microcavities in thermo-optical converters is their sensitivity to environmental conditions (changes in its temperature) [1-3]. As a result, due to the energy absorbed by the resonator, its temperature increases and, consequently, its optical base changes, which leads to a shift in the spectral characteristics and deterioration of performance criteria [4-6].

### II. MATERIALS AND METHODS

In this work, a mathematical model was created with the help of which the conditions were obtained under which the dependence of the light flux of the readout radiation reflected by Fabry-Perot and Smith microcavities minimally depends on the initial temperature of the resonator.

### III. RESULTS

The main thermosensitive element of a thermo-optical converter is a matrix of film resonators (Figure 1), in which both Fabry-Perot and Smith microresonator can be used. It was found that the light modulation characteristics of the microresonator of the matrix under consideration are determined by the change in their temperature, the value of the spectral shift of the transmittance or reflection of each of the resonators, and the wavelength of the readout radiation.

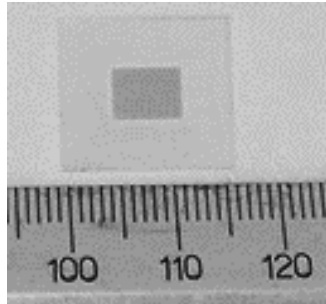


Figure 1. Matrix of microresonator

The dependences of the change in the luminous flux on the change in the initial temperature of the microcavities have extrema, near which the value of its change in absolute value is maximum and for the resonator under consideration practically does not change. Therefore, to obtain a more temperature-stable operation, it is necessary that their initial temperature corresponds to the extremum of the dependence of the change in the luminous flux on temperature. This can be realized by obtaining an appropriate value of their optical base or by technological formation of a dielectric layer between the mirrors, or by heating to an appropriate temperature. In this case, the dependences of the luminous flux and the change in the reflected light flux of the readout radiation without and under the influence of IR radiation on the change in the initial temperature of the resonator will have the form shown in Figure 2.

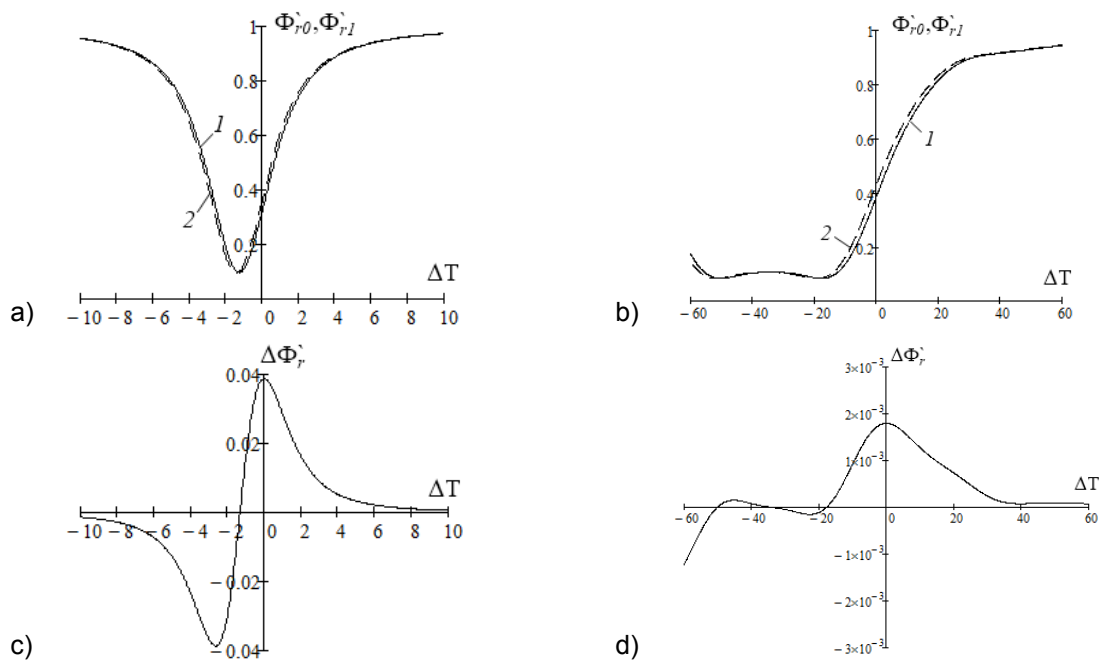


Figure 2. Dependences of the light flux of the readout radiation, reflected a) - Fabry-Perot microresonator; b) - Smith microresonator with a corrected initial temperature, without ( $\Phi_{r0}$ ) and under the influence of IR radiation ( $\Phi_{r1}$ ); dependence of the change in the luminous flux  $\Delta\Phi_r$ , reflected c) - by a Fabry Perot microresonator, d) - Smith microresonator, under the influence of IR radiation on the change in the initial temperature of the resonator  $\Delta T$

According to calculations, in order to increase the temperature stability of Fabry-Perot and Smith microresonator for their use in devices for converting information from the IR region of the spectrum to another, a prerequisite is that their initial temperature matches the extremum of the function of the dependence of the change in the luminous flux on temperature. In this case, the dynamic temperature range of the Fabry-Perot microresonator is  $0.3^\circ\text{C}$ , which is 20 times less than that of the Smith microcavity ( $6^\circ\text{C}$ ). In this case, the change in the light flux under the influence of IR radiation at the output of the Fabry-Perot microcavity will be 20 times greater than after the Smith microresonator.

#### IV. CONCLUSION

Thus, in order to obtain a more temperature-stable operation of both a Fabry-Perot microinterferometer and a Smith microresonator, operating in the mode of converting information from the IR spectral region to another, for example, a shorter wavelength, it is necessary that their initial temperature corresponds to the extremum of the dependence of the change in the light flux on temperature. In this case, the dynamic temperature range of the Fabry-Perot microinterferometer (0.3°) will be 20 times less than that of the Smith microresonator (6°). In this case, the change in the luminous flux under the influence of IR radiation at the output of the Fabry-Perot microinterferometer will be 20 times greater than after the Smith microresonator.

#### REFERENCES

- [1] Tarasov, V.V. Modern problems of infrared technology / V.V. Tarasov, Yu.G. Yakushenkov // M.: MIIGA and K, - 2011. -- 84 p.
- [2] Smith, S.D. Design of Multilayer Filters by Considering Two Effective Interfaces / S.D. Smith // Journal of the optical society of America. - 1958. = Vol. 48. No. 1. - P. 43-50.
- [3] Novel low-cost uncooled infrared camera / Ming Wu [et al.] // Infrared Technology and Applications XXXI. - 2005. - Vol. 5783 - P.69401I-1. <https://doi.org/10.1117/12.603905>
- [4] Born, M. Fundamentals of optics / M. Born, E. Wolf; translation from English. S. N Breus, A. I. Golovashkin, A. A. Shubin, [ed. G. P. Motulevich] // M.: Nauka, - 1973. - P. 719
- [5] Mustel, E. P. Methods of modulation and scanning of light / E. P. Mustel, V. N. Parygin // Moscow: Nauka, - 1970. - P. 296
- [6] Yariv, A. Optical waves in crystals / A. Yariv, P. Yuh; translation from English. S.G. Krivoslykova, N.I. Petrova; [ed. I. N. Sissakian] // M: Mir, - 1987. - P. 616.

### CIRCULAR PHOTOVOLTAIC EFFECT IN AN ANISOTROPIC GRAPHENE SUPERLATTICE IN THE PRESENCE OF A CONSTANT ELECTRIC FIELD

P. Badikova, D. Zav'yalov, D. Zharikov  
Volgograd State Technical University, Volgograd, Russia

[polin.badicova@gmail.com](mailto:polin.badicova@gmail.com)

#### I. INTRODUCTION

The unique electrical and optical properties of graphene-based materials and the development of techniques for fabricating low-dimensional structures motivate intensive efforts to implement graphene-based nano- and optoelectronics. However, the pseudo-relativistic behavior of charge carriers was found in the energy bands of not only graphene.

There is a certain class of two-dimensional (2D) materials, which includes graphene, silicene, germanene, phosphoric, etc. It is called Dirac materials or graphene-like materials. Currently, the possibility of creating an electronic band structure of graphene by using an additional periodic potential has aroused increased research interest in superlattices (SLs) based on graphene-like materials (GSL) [1]. In this paper, the influence of a constant electric field on the circular photovoltaic effect in an anisotropic GSL at normal incidence are investigated. The expression for the current density in such a superlattice is obtained.

#### II. MAIN FORMULAS

The energy spectrum of the structure in the low-energy approximation has the following form [2]

$$\varepsilon(\mathbf{p}) = \pm 2F \sqrt{\sin^2\left(\frac{px}{2}\right) + \frac{1}{4}(p_y^2 + \Delta_{eff})^2} \quad (1)$$

where  $\Delta_{eff} = \frac{\Delta_1 + n\Delta_2}{1+n}$ ,  $F = \frac{Q}{shQ}$ ,  $Q = \frac{n(\Delta_1 - \Delta_2)}{(1+n)^2}$ ,  $n = b/a$ ,  $a$  is the height of the hole,  $b$  is the barrier width,  $p_x = p_x d$ ,  $p_y^2 = \alpha p_y^2 d / v_F$ ,  $d = a + b$ . Different signs are applicable the valence and conduction bands.

We will consider the response of the superlattice to the action of constant and alternating electric fields.  $\vec{E} = (E_{0x} \cos(\omega t) + E_0; E_{0y} \cos(\omega t + \varphi))$  where  $E_0$  is the modulus of the intensity of the constant electric field,  $E_{0x,y}$ ,  $\omega$  are the amplitude and frequency of the alternating electric field.

The current density  $j_y$ , along the Y-axis is determined by the formula:

$$j_y = \langle e \sum_p v_y f(\mathbf{p}, t) \rangle_t \quad (2)$$

where  $e$  is the electron charge,  $f(\mathbf{p}, t)$  is the nonequilibrium carrier distribution function.

The distribution function will be found using the classical Boltzmann equation

$$\frac{\partial f(\mathbf{p}, t)}{\partial t} + e\mathbf{E} \frac{\partial f(\mathbf{p}, t)}{\partial p} = -v[f(\mathbf{p}, t) - f_0(\mathbf{p})] \quad (3)$$

where  $f_0(\mathbf{p})$  is the equilibrium distribution function.

The electron velocity along the Y-axis is given by

$$v_y = \frac{\partial \varepsilon(\mathbf{p})}{\partial p_y} = \frac{F p_y (p_y^2 + \Delta_{eff})}{\sqrt{\sin^2(\frac{p_x}{2}) + \frac{1}{4}(p_y^2 + \Delta_{eff})^2}} \quad (4)$$

After expanding the velocity in terms of  $p_y$ , we get the following expression

$$v_y \approx \frac{2F \Delta_{eff} p_y}{\sqrt{\sin^2(\frac{p_x}{2}) + \Delta_{eff}^2}} \quad (5)$$

$$v'_y(x) = \frac{1}{\sqrt{\sin^2(\frac{p_x}{2}) + \Delta_{eff}^2}} \quad (6)$$

Expand (6) into a complex Fourier series

$$v'_y(x) = \sum_{m=-\infty}^{+\infty} \hat{a}_m e^{imx} \quad (7)$$

where  $\hat{a}_m = \frac{1}{2\pi} \int_{-\pi}^{\pi} \frac{e^{imx} dx}{\sqrt{\sin^2(\frac{p_x}{2}) + \Delta_{eff}^2}} = \frac{{}_3F_2(\frac{1}{2}, \frac{1}{2}, 1; 1-m, m+1; 4/(\Delta_{eff}^2+4))}{\sqrt{\Delta_{eff}^2+4}}$ .

Solving equation (3) by the method of characteristics, substituting it and (4) in (2), an expression for the constant component of the current is obtained.

$$j_y = \frac{2ev}{(2\pi\hbar)^2} \left( \int_{-\pi}^{\pi} \int_{-\infty}^{\infty} \int_{-\infty}^{\infty} e^{-v(t-t')} v_y(p_x; p_y) \times f_0(p_x - \frac{e}{c}(A_x(t) - A_x(t')); p_y - \frac{e}{c}(A_y(t) - A_y(t'))) d^2 p dt' \right) \quad (8)$$

We substitute (5) taking into account the expansion (7) into (8), integrate, and after some transformations, expression (8) takes the form:

$$j_y = j_0 \text{Re} \left[ \sum_{m=-\infty}^{+\infty} \hat{a}_m C_m \sum_{l=-\infty}^{\infty} \frac{\beta_{0y} J_l I_{l+1}(\alpha_{0x}) \cos(\varphi)}{(\tilde{\alpha}_0 - i\tilde{v} + l)(\tilde{\alpha}_0 - i\tilde{v} + (l+1))} dx dy \right] \quad (9)$$

where  $\tilde{v} = v/\omega$ ,  $\alpha_{0x} = \frac{medE_{0x}}{\hbar\omega}$ ,  $\alpha_0 = \frac{medE_0}{\hbar}$ ,  $\beta_{0y} = \sqrt{\frac{\alpha d}{v_F \hbar \omega}} E_{0y}$ ,  $\tilde{\alpha}_0 = \alpha_0/\omega$ ,  $C_m = \frac{1}{I_0} \int_{-\pi}^{\pi} \int_{-\infty}^{\infty} e^{-\frac{\varepsilon(x,y)}{kT}} e^{imx}$ ,  $I_0 = \int_{-\infty}^{\infty} \int_{-\pi}^{\pi} e^{-\frac{\varepsilon(x,y)}{kT}} dx dy$ ,  $j_0 = \frac{\hbar e \tilde{v} F \Delta_{eff} n_0}{d} \sqrt{\frac{v_F \hbar}{\alpha d}}$ ,  $v_F = 10^8$  cm / s,  $J_l(z)$  is the Bessel function.

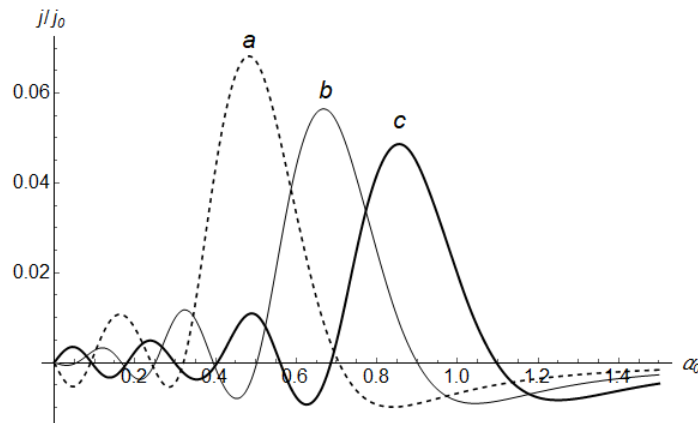


Figure 1. Dependence of the current density on the strength of a constant electric field applied along the X-axis at fixed values of  $\beta_{0y} = 1.0$  and  $\varphi = \pi/4$  a)  $\alpha_{0x} = 0.6$  b)  $\alpha_{0x} = 0.8$  c)  $\alpha_{0x} = 1.0$

### III. CONCLUSIONS

The influence of a constant electric field on the circular photovoltaic effect in an anisotropic graphene superlattice at normal incidence is investigated. An expression is obtained for the current density in such a superlattice. The features of the photovoltaic effect in such a structure are noted. The dependence of the

current density on the strengths of the applied fields has a non-monotonic, oscillating, alternating character (Figure 1). The largest amplitude of oscillations is achieved in the region of low fields.

## REFERENCES

- [1] D.V. Zav'yalov, V.I. Konchenkov, S.V. Kryuchkov, "Transverse current straightening in a graphene-based superlattice", *Semiconductors*, Vol. 46(1), pp. 113-120, 2012.
- [2] E.I. Kukhar, S.V. Kryuchkov, "Topological phase transitions in superlattice based on 2D Dirac crystals with anisotropic dispersion" *Superlattices and Microstructures*, Vol.133, p. 106183, 2019.

## DEVELOPMENT OF A PACKAGE FOR AUTOMATING THE PIPELINE PROCESSING OF QUANTUM-CHEMICAL CALCULATIONS USING GAMESS ON A CLUSTER WITH A SLURM QUEUING SYSTEM

N. Demidovich, D. Zav'yalov, A. Polikarpova  
Volgograd State Technical University, Volgograd, Russia

[n.a.demidovich@gmail.com](mailto:n.a.demidovich@gmail.com)

### I. INTRODUCTION

The GAMESS package [1] is designed for computational quantum chemistry using ab initio methods. The package allows you to perform calculations in parallel on both shared and distributed memory systems. The experience of using computational quantum-chemical packages shows that it is often necessary to perform pipeline calculations, that is, such calculations in which a number of sequential calculations are automated and the results of each stage serve as input data for the next. For example, in the simplest case, the geometry of the calculated molecule is first optimized, and then some other calculation in which the coordinates optimized at the first stage serve as the initial ones. Existing wrappers for quantum-chemical packages, such as MacMolPlt, Avogadro and a number of others, only allow visualizing the results of calculations or help to compose input files for calculations. Therefore, it was decided to write our own wrapper for GAMESS, which performs the task of automating and pipelining calculations. At the same time, it is necessary that such a program also be able to work with the cluster queuing system - in our case, Slurm [2].

### II. MAIN FORMULAS

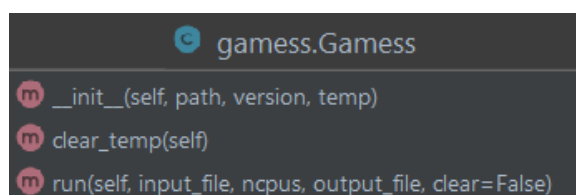
Python was used as the main development language. The following third-party tools were used along with the standard library: ASE (Atomic Simulation Environment) and the Python interface for Open Babel. The first library was used to form the structure of the input file of the GAMESS package; the second is for correct conversion of files into .mol and .gamout formats.

The program is used for calculations of optimized geometry, subsequent energy calculations and report generation. The report is generated in accordance with the requirements of a specific task, therefore, for each task, you can write your own logic for its formation.

The structure of the program is such that pipeline calculations can be done. Before use, you only need to compose a text file with one or several SMILES-structures of chemical compounds and determine the calculation parameters.

During the development, an object-oriented approach was used to provide for further expansion of the program.

To implement the GAMESS package, the Gamess class was written (Figure 1), which allows you to create an object with initial parameters responsible for the location of the runngms script, the version of GAMESS and the location of the folder with temporary files. The clear\_temp method clears the temporary files folder if necessary; the run method takes the name of the input file for calculations, the number of processors used, the name of the output file and runs the runngms script using the methods of the standard Python library.



```
class games.Gamess:
    def __init__(self, path, version, temp):
    def clear_temp(self):
    def run(self, input_file, ncpus, output_file, clear=False):
```

Figure 1. Gamess class structure

To create an input file for calculations, the GamessInput class was implemented (Figure 2). The object of this class is initialized with parameters that are responsible for the file name in the .mol format and with the calculation parameters.

```
class gamess.GamessInput
  __init__(self, mol_filename, params)
  create_inp_file(self)
```

Figure 2. GamessInput class structure

All the work of the program is performed using the Job class (Figure 3). The object of this class is initialized with the material for which the calculations are carried out, the name of this material (optionally a number), configuration (from a JSON file), parameters of optimization and energy calculations. When calling the job method, the initialization logic of the Gamess class object is executed, the creation of a .mol file, which is converted into an input file for calculations using the GamessInput class object, and the optimization calculations process starts. After that, according to the optimized coordinates, an input file for energy calculations is generated using an object of the GamessInput class, and the process of energy calculations is started.

```
class job.Job
  __init__(self, material, material_name, config, opt_params, nrg_params)
  job(self)
```

Figure 3. Job class structure

The code repository [3] contains a special sbatch.py script that iterates over chemical compounds and runs the job.sh script to perform calculations on a cluster [4] with a Slurm queuing system.

The written package was used for calculations, for example, in works [5,6] and showed that with its help it was possible to significantly save time for organizing calculations and processing intermediate results.

### III. CONCLUSIONS

A program has been written to automate chemical calculations using a package for computational quantum chemistry. The program allows you to consistently perform optimization and energy calculations for a group of chemical compounds. To generate reports on the results of calculations and perform calculations on a cluster, the code repository contains special scripts. The development plans of the package include support for other queuing systems and implementation of more pipeline use scenarios.

### REFERENCES

- [1] GAMESS — URL: <https://www.msg.chem.iastate.edu/gamess/> (date of visit 09/04/2021).
- [2] Slurm — URL: <https://slurm.schedmd.com> (date of visit 09/04/2021).
- [3] Github-repository — URL: <https://github.com/nidemidovich/gamess-calculations> (date of visit 09/04/2021).
- [4] Cluster used — URL: <https://cluster.vstu.ru> (date of visit 09/04/2021).
- [5] Synthesis and properties of new transparent (co) polyimides based on adamantane-containing diamines and aromatic tetracarboxylic dianhydrides / I.A. Novakov et al. // Russian Chemical Bulletin. - 2021. - Vol. 70, issue 6. - P. 1141-1148. - DOI: <https://doi.org/10.1007/s11172-021-3196-1>.
- [6] Adamantylation of N-aryl and N-arylalkylacetamides in trifluoroacetic acid / I.A. Novakov et al. // Russian Chemical Bulletin. - 2020. - Vol. 69, Issue 6. - P. 1096-1101.

## MODELING AlGaIn p-i-n PHOTODIODES

N. Vorsin, A. Gladyshchuk, T. Kushner, N. Tarasiuk, S. Chugunov, M. Borushko

Brest State Technical University, Brest, Belarus

[phys@bstu.by](mailto:phys@bstu.by)

### I. INTRODUCTION

Until recently the main technique for modeling physical processes was to compose equations that would describe the processes and solve them with some math package, like in [1, 2]. But today's expert systems

for modeling different processes are not worse than “manual” modeling. At the same time they provide a rich apparatus to program equations and present their results. This report considers using COMSOL MULTIPHYSICS software to create a model of a p-i-n photodiode based on AlGa<sub>x</sub>N alloy.

## II. METHOD AND RESULTS

The model created makes it possible to estimate I–V curve, spectral sensitivity, absorption coefficient, and other parameters as a function of the proportion of aluminum in the alloy and the thicknesses of the layers forming the photodiode.

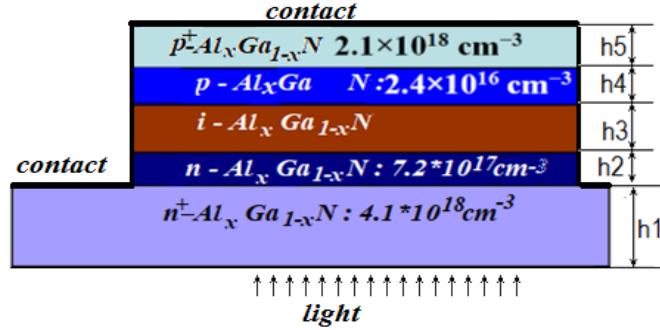


Figure 1. The model of the typical p-i-n photodiodes

The structure shown in Figure 1 is typical for nitride photodiodes. Between the n and p layers which have moderate electron and hole conductivity there is a pretty thick i-layer where most light is absorbed and converted into free charge carriers. This three-layer structure is complemented with highly doped n<sup>+</sup> and p<sup>+</sup> layers at the top and bottom which make it possible to obtain ohmic contacts with metallic leads. The lower n<sup>+</sup> layer solves some other problems except for contacting the leads. It reduces an intergrowth of dislocations from contact with the substrate into the overlying layers and compensates for errors in the etching depth of the upper layers when separating diodes. Therefore, the lower n<sup>+</sup> layer is much thicker than the others. It is applied on an AlN buffer layer which, in turn, rests on a sapphire substrate which does not participate in the modeling. Thicknesses of the h1 - h5 layers are parameters that can be easily changed before the model is calculated.

Taking into account the same processes along the horizontal axis, the structure shown in the figure is actually one-dimensional, which simplifies calculation. The COMSOL "optoelectronics" module solves the system of equations of the diffusion-drift model. It also offers several contemporary physical models for the interaction of a semiconductor with EMR.

The band gap  $E_g$  for Al<sub>x</sub>Ga<sub>1-x</sub>N at room temperature is calculated by using the well-known formula (1) which approximates actual dependence of  $E_g$  on x molar fraction of aluminum by the quadratic dependence [3]:

$$E_g^{AlGaN} = x E_g^{AlN} + (1 - x) E_g^{GaN} - 1.1x(1 - x) \quad (1)$$

It is known that electronic affinity potential of AlGa<sub>x</sub>N decreases as the proportion of aluminum increases and the band gap increases according to a law close to linear. The calculation is based on the following formula from [4]:

$$\chi = 4.1 + 0.7(E_g^{GaN} - E_g^{AlGaN}) \quad (2)$$

Effective densities of the states in the conduction and valence bands are approximated by linear dependences on the fraction of aluminum [4]:

$$N_c^{AlGaN} = \left(\frac{T}{1K}\right)^{\frac{3}{2}} ((1.8x + 4.6(1 - x))10^{14} cm^{-3}) \quad (3)$$

$$N_v^{AlGaN} = \left(\frac{T}{1K}\right)^{\frac{3}{2}} ((10.6x + 9.2(1 - x))10^{15} cm^{-3})$$

The dielectric constant  $\epsilon$  and the relative effective masses of electrons (holes),  $m_e$  ( $m_h$ ) are also assumed to be linearly dependent on the fraction of aluminum and determined as [4]:

$$\begin{aligned} \epsilon^{AlGaN} &= 10.1x + 10.4(1 - x) \\ m_e^{AlGaN} &= 0.314x + 0.2(1 - x) \\ m_h^{AlGaN} &= 0.417x + 1.0(1 - x) \end{aligned} \quad (4)$$

Other parameters and results of modeling are presented in the report.

### III. CONCLUSIONS

We proposed the new numerical model using COMSOL MULTIPHYSICS software to estimate I–V curve, spectral sensitivity, absorption coefficient, and other parameters as a function of the proportion of aluminum in the AlGaIn alloy and the thicknesses of the layers forming p-i-n photodiode based on AlGaIn. This model was able to calculate the voltage and current dependency similar to device simulation as a continuous solution and could be useful for device development as a quick calculation. It could be also useful to academical and educational understanding the behavior of the electrical characteristics.

### ACKNOWLEDGMENTS

This work was supported by the National Science Research Program «Photonic and Electronic for Innovations», by Ministry of Education of Republic of Belarus, by Brest State Technical University (GB No. 21/204).

### REFERENCES

- [1] N.N.Vorsin, A.A.Gladyschchuk, T.L.Kushner, N.P.Tarasiuk, S.V.Chugunov, “Modelirovanie i razrabotka AlGaIn p-i-n fotodiodov”, Vestnic BSU, № 4. pp. 5-14, 2018.
- [2] E.V.Lutsenko, A.V Danilchyk, N.P.Tarasuk, A.Andryeuski, V.N.Pavloskii, A.L.Gurskii, G.P.Petrovich, H.Kalish, R.H.Jansen, Y.Dikme, B.Schineller, M. Heuken.” Laser threshold and optical gain of blue optically pumped InGaIn/GaIn multiple quantum wells (MQW) grown on Si”, Phys. Stat. Sol. (c) , Vol. 5, Iss. 6, pp. 2263–2266.
- [3] A.P.Nikonov, K.O.Boltar, N.I.Yakovleva, “Jpticheskie svoistva geteroepekitalnih sloev AlGaIn”, Prikladnaya fizika, № 2. pp. 50-52, 2014.
- [4] ATLAS User’s Manual, Device Simulation Software, Version 5.20.2. R, SILVACO International, Santa Clara, CA, 2016.

## PHOTOACOUSTIC EFFECT IN MICRO- AND NANOSTRUCTURES: NUMERICAL SIMULATIONS OF LAGRANGE EQUATIONS

O. Romanov, Ya. Shtykov, I. Timoshchenko  
Belarusian State University, Minsk, Belarus

[romanov@bsu.by](mailto:romanov@bsu.by)

### I. INTRODUCTION

The photoacoustic effect is the formation of sound waves due to absorption of the modulated light pulse by irradiated medium. At the present time, the photoacoustic effect is widely used in biomedical studies, photoacoustic spectroscopy etc. Of particular interest are studies of the interaction of pulsed laser radiation with absorbing micro- and nanostructures. Absorption of laser pulse energy in micro- and nanostructures allows exciting acoustic oscillations in the frequency range from gigahertz to terahertz. Terahertz frequency acoustic vibrations are of special interest for fundamental research and have numerous potential applications (acoustic imaging of nano-objects, acoustic nanocavities, phononic crystals).

### II. METHOD AND RESULTS

This work provides the description of theoretical and numerical modeling techniques of thermomechanical effects that take place in absorbing one-, two- and three-dimensional micro- and nanostructures of different materials under action of pulsed laser radiation. A proposed technique of the numerical simulation is based on the solution of equations of motion of continuous media in the form of Lagrange for a spatially inhomogeneous media. This model allows calculating fields of temperature, pressure, density and velocity of the medium depending on the parameters of laser pulses and the characteristics micro- and nanostructures. The problems of excitation and propagation of acoustic oscillations in homogeneous and heterogeneous media and structures are considered, and the potential applications of the photoacoustic effect in medicine and nanotechnology are discussed. Examples of implementation of the model in connection with possible applications in the area of nanophotonics, nanoacoustics, and nanoplasmonics are presented.

Absorption of the energy of a pulsed laser beam in the medium leads to its local heating, thermal expansion and generation of acoustic (shock) waves. These processes can be described by the equations of motion of the medium in the form of Lagrange. For many practical cases, it is informative modeling of one-dimensional tasks (planar, cylindrical or spherical) for appropriate geometry of energy release [1]. Based on this approach, the processes of excitation of acoustic waves in one-dimensional metallic [2] and carbon [3] nanostructures (nanofilms, nanowires, spherical micro- and nanoparticles) have been investigated. The



heating of metals under the action of ultrashort laser pulses is described in terms of two-temperature model for the electron gas and the ionic lattice, and spatial-temporal dynamics of excitation and propagation of terahertz acoustic oscillations is investigated based on the numerical solution of equations of motion of layered media, and two-dimensional plasmonic nanostructures [4, 5].

### III. CONCLUSIONS

As a generalization, for theoretical description of thermomechanical phenomena in three-dimensional absorbent nanostructures under the action of pulsed laser radiation a technique has been developed for numerical simulation of three-dimensional equations of motion of continuous media in the form of Lagrange and three-dimensional heat conduction equation. The fields of temperature, pressure, density and velocity of the medium have been calculated for different geometries of micro- and nanostructures.

### REFERENCES

- [1] O. Romanov, G. Zheltov, G. Romanov, "Numerical modeling of thermomechanical processes in absorption of laser radiation in spatially inhomogeneous media", Journal of Engineering Physics and Thermophysics, Vol. 84, Issue 4, pp.772-780, 2011.
- [2] O. Romanov, G. Zheltov, G. Romanov, "Action of Femtosecond Laser Pulses on Metal Nanoparticles in a Liquid", Bull. of the Rus. Acad. of Sc.: Phys., Vol. 75, Issue 12, pp.1589-1591, 2011.
- [3] L. Golubewa, I. Timoshchenko, O. Romanov, R. Karpicz, T. Kulahava, D. Rutkauskas, M. Shuba, A. Dementjev, Yu. Svirko, P. Kuzhir, "Single-walled carbon nanotubes as a photo-thermo-acoustic cancer theranostic agent: theory and proof of the concept experiment", Scientific Reports, Vol. 10, pp.22174, 2020.
- [4] N. Khokhlov, G. Knyazev, B. Glavin, Y. Shtykov, O. Romanov, V. Belotelov, "Interaction of surface plasmon polaritons and acoustic waves inside an acoustic cavity", Opt. Lett., Vol. 42, pp. 3558-3561, 2017.
- [5] V. Belotelov, A. Kalish, G. Knyazev, E. Nguen, O. Romanov, A. Tolstik, "Optoacoustical transducer based on plasmonic nanoparticles", Nonl. Phen. in Compl. Syst., Vol. 22, Issue 1, P.55-63, 2019.

## INFLUENCE OF SUPPLY VOLTAGE ON THE VELOCITY OF FLIGHT OF DOMAINS IN A GUNN DIODE

G. Kostrov, D. Zav'yalov  
Volgograd state technical university, Volgograd, Russia  
[kostroff.jora@mail.ru](mailto:kostroff.jora@mail.ru)

### I. INTRODUCTION

At the present time, more and more attention is paid to modeling physical processes in semiconductor radioelements operating in the gigahertz and terahertz ranges [1, 2]. With the help of an accurate physical model, it becomes possible to predict changes in radiation characteristics due to factors such as semiconductor material, doping, supply voltage, and others.

### II. RESULTS

To study the processes of formation and motion of a domain in a crystal structure, the local-field model of the Gunn diode is used, based on the assumption that the average drift velocity of electrons depends on the instantaneous value of the electric field, and the diffusion coefficient does not depend on the applied electric field [3]. A sequential circuit for switching on a diode with a power supply and a resistive load is simulated.

To describe the behavior of the domain inside the diode, the intensity formula is used in an explicit form, obtained from the Poisson equation for the field distribution:

$$E_i^{k+1} = E_i^k + \Delta t \left[ D(E_i^k) \frac{E_{i+1}^k + E_{i-1}^k - 2E_i^k}{\Delta x^2} - V(E_i^k) \frac{E_{i+1}^k - E_{i-1}^k}{2\Delta x} + \frac{e}{\varepsilon_a} \left( D(E_i^k) \frac{n_{0i+1} - n_{0i-1}}{2\Delta x} - n_{0i} V(E_i^k) + \frac{U_0 - \frac{1}{2}\Delta x \sum_{j=2}^N (E_{j-1}^k + E_j^k)}{eRS} \right) \right], \quad (1)$$

where  $\Delta t$ – time interval of integration;  $D(E_i^k)$ – diffusion coefficient;  $\Delta x$ – spatial interval of integration;  $\varepsilon_a$ – absolute dielectric constant of GaAs;  $n_{0i}$ – value of the local concentration of dopants;  $U_0$ – supply voltage of the Gunn diode;  $N$ – the number of spatial intervals of the diode splitting;  $R$  – load resistance;  $S$  – cross-sectional area of the crystal structure of the diode.

The speed of electrons at adjusted point in space at a given time  $V(E_i^k)$  is responsible for the nonlinear part of the device which is defined as:

$$V(E_i^k) = \frac{\left[ \mu_a E_i^k + V_{\text{sat}} \left( \frac{E_i^k}{E_{\text{threshold}}} \right)^4 \right]}{\left[ 1 + \left( \frac{E_i^k}{E_{\text{threshold}}} \right)^4 \right]}, \quad (2)$$

where  $\mu_a$  – electron mobility;  $V_{\text{sat}}$  – the speed corresponding to the saturation of the characteristic with a large field;  $E_{\text{threshold}}$  – the threshold value of the intensity in the field.

For the equation (1), the Neumann conditions for the boundaries with the diode contacts must be satisfied:

$$E_1^k = E_2^k \quad E_N^k = E_{N-1}^k \quad (3)$$

At each time step, the field strength is found at all points in space in the diode. Thus, it becomes possible to track the movement of the intensity maxima corresponding to the strong field domain. Figure 1 shows the graphs of the intensities, which can be used to trace the dynamics of the movement of charges. The maxima located on the left side are formed by inhomogeneities, from which generation begins when the supply voltage overcomes the threshold field strength.

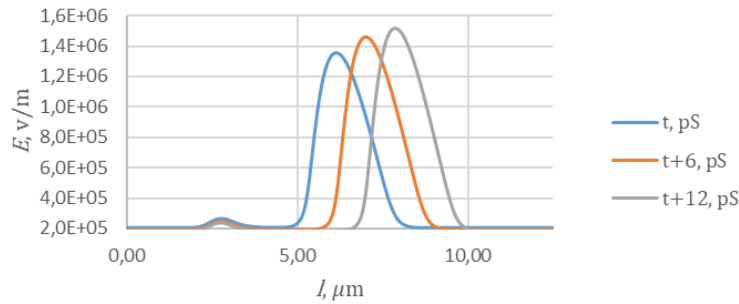


Figure 1. Change in the field strength inside the diode over time at a constant voltage  $U_0$

The velocity of domain movement is determined by the change in the position of the tension maxima after their separation from the inhomogeneities. For various values of the supply voltage, a graph of the dependence of the speed of movement of charges on the supply voltage is obtained, shown in Figure 2.

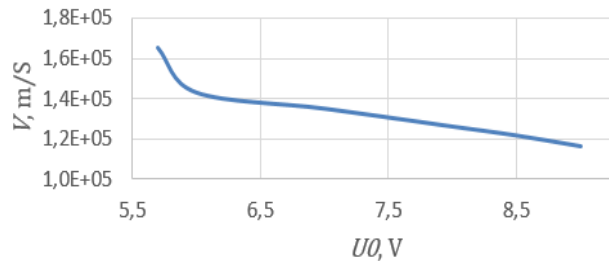


Figure 2. Change in the velocity of flight of the domain depending on the supply voltage of the Gunn diode

The resulting graph shows that with an increase in the supply voltage of the diode, the rate of movement of charges decreases. This is due to the fact that when a larger external field is applied, the Q-factor of the domain decreases, the number of main charge carriers increases, while the inhomogeneity in the diode remains constant. For the formation of a new domain, a stronger field is formed, and the effective mass increases.

### III. CONCLUSIONS

The experiments carried out show that with an increase in the supply voltage, the speed of movement of the domains decreases, which coincides with the experimental characteristics of Gunn diodes operating in the sections after the nominal supply voltage on the slope of the frequency characteristics.

The shape of inhomogeneities in the crystal lattice with the same width does not affect the formation of domains. The rectangular, parabolic and gradient functions of the change in the concentration of dopants are investigated. If the function changes more smoothly, then the maximum amplitude of the domain strengths will be greater, but the domain will take a little longer to form. The resulting model can be used to calculate fields with different loads in an electrical circuit. It is planned to add an LC circuit to the circuit, which will allow calculations for different waveguides. This should make it easier to design and debug experimental circuits.

The resulting model can be used to calculate fields with different loads in an electrical circuit. It is planned to add an LC circuit to the circuit, which will allow calculations for different waveguides. This should make it easier to design and debug experimental circuits.

## REFERENCES

- [1] Wafaa Abd El-Basit, "Computer Modeling, Characterization, and Applications of Gallium Arsenide Gunn Diodes in Radiation Environments" Nuclear Engineering and Technology, Vol. 48, Issue 5. pp 1219-1229, October 2016.
- [2] Chong Li, "Design, fabrication and characterization of  $\text{In}_{0.23}\text{Ga}_{0.77}\text{As}$ -channel planar Gunn diodes for millimeter wave applications" Solid-State Electronics, Vol 64, Issue 1. pp 67-72, October 2011.
- [3] G. I. Veselov, "Microelectronic microwave devices: a textbook for radio engineering universities" Moscow: High school, p 280, 1988.

## ANALYSIS AND PREDICTION OF THE DEVELOPMENT OF MICROPROCESSOR CHARACTERISTICS

I. N. Staroverov, R. I. Dzerzhinsky

RTU MIREA, Institute of Information Technologies, kaf. Applied Mathematics, Moscow, Russia

[st.igornik@gmail.com](mailto:st.igornik@gmail.com)

### I. INTRODUCTION

In the modern world of technology, the speed of development of computer technology is growing rapidly. At the same time, the question arises about the limited computer resources, in particular, to which the well-known Gordon Moore's law is reduced [1].

### II. METHODS AND RESULTS

In this work, the following characteristics of microprocessors were taken for analysis: frequency (GHz), process technology (nm), number of transistors (million), heat dissipation (W) from 1971 to 2020. According to the presented data, a dimensionless analysis was carried out. Based on the analysis, critical levels were assessed [2] based on the historical development of microprocessors. A predictive assessment of the crisis in the development of microprocessor technologies is made and possible alternatives for solving the alleged crisis are proposed (Figure 1).

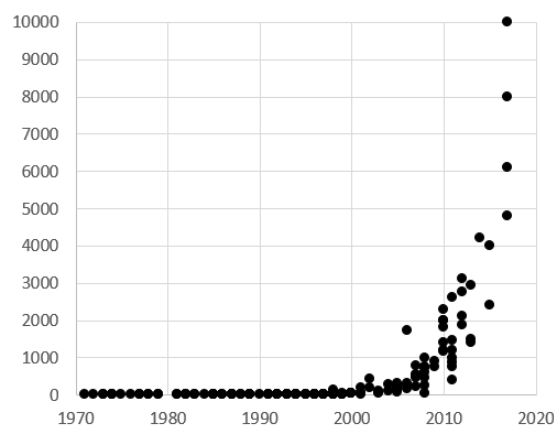


Figure 1. Number of transistors, million

### III. CONCLUSIONS

As one of the development options, we can assume an increase in the number of transistors per microprocessor, since the limit of the technological process has almost been reached. Also, along with the number of transistors, the area of the processor itself will increase.

## REFERENCES

- [1] Moore's Law / A. Skorobov.- Website of the Faculty of Mathematics and Mechanics of USU, 2015.
- [2] V.I. Kuzmin, A.F. Gadzaov. - Models and methods of scientific and technical forecasting: textbook / - Moscow: MIREA, 2016. - 90 p.

# AB INITIO CALCULATIONS OF ELECTRONIC BAND STRUCTURE OF CdMnS SEMIMAGNETIC SEMICONDUCTORS

M. Mehrabova<sup>1</sup>, N. Panahov<sup>2</sup>, N. Hasanov<sup>3</sup>

1 Institute of Radiation Problems, ANAS, Baku, Azerbaijan

2 Azerbaijan University of Architecture and Construction, Baku, Azerbaijan

3 Baku State University, Baku, Azerbaijan

[m.mehrabova@science.az](mailto:m.mehrabova@science.az)

## I. INTRODUCTION

CdS is an attractive semiconductor in the photoconductive, photovoltaic, optoelectronic materials. Doping of transition metals in nonmagnetic CdS is very important to make this material multifunctional. Room temperature CdS based semimagnetic semiconductors (SMSC), such as Mn doped CdS is a very good photo-luminescence compound due to d states at the top of the valence band and intra-d shell transitions. [1].

This work devoted to theoretical investigations of  $Cd_{1-x}Mn_xS$  SMSC. The Mn-CdS sheet with 16 atom supercell is analyzed by Kumar et al. [2]. The electronic band structure of wurtzite CdS calculated by Rantala et al. using two different self-consistent ab initio LDA methods [3]. Nabi [4] investigated electronic and magnetic properties of Mn doped CdS in wurtzite phase, using ab-initio calculations based on LDA, GGA and LDA + U exchange and correlation functionals. Ahmed et al. [1] investigated electronic band structure of  $Cd_{1-x}Mn_xS$  ( $x = 6.25\%$ ) using spin-polarized density functional theory (DFT) within the framework of Generalized Gradient Approximation (GGA), its extension via on-site Hubbard U interactions (GGA + U) and a model for exchange and correlation potential Tran modified Becke-Johnson (TB-mBJ).

The purpose of this work was to calculate the electronic band structure of ideal and defective  $Cd_{1-x}Mn_xS$  SMS in both antiferromagnetic (AFM) and ferromagnetic (FM) phases.

## II. METHODS AND RESULTS

Ab initio calculations are performed in the Atomistix Toolkit (ATK) program within the Density Functional Theory (DFT) and Local Spin Density Approximation (LSDA) on Double Zeta Double Polarized (DZDP) basis. We have used Hubbard U potential  $U_{Mn} = 3.59$  eV for 3d states for Mn atoms [5, 6]. Supercells of 8 and 64 atoms were constructed. After the construction of  $Cd_{1-x}Mn_xS$  ( $x = 0; 6.25\%; 25\%$ ) supercells, atom relaxation and optimization of the crystal structure were carried out. Electron band structure, density of states were calculated, total energy have been defined in AFM and FM phases (fig.1).

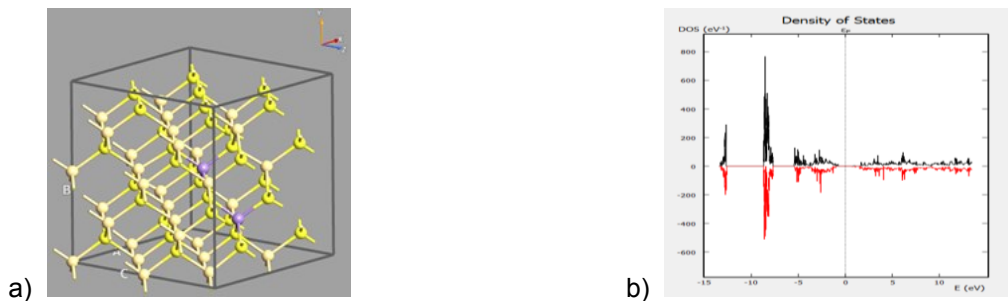


Figure 1.  $Cd_{30}Mn_2S_{32}$  supercell a) bulk configuration b) density of states

Our calculations show that the band gap increases with the increases in Mn ion concentration. Obtained theoretical results correspond to experimental investigations carried out by Selma M.H [7]. It has been established that Cd or S vacancy in the crystal structure leads to the change of band gap, deep levels appear in the band gap, Fermi level shifts towards the valence or conduction band (fig.2).

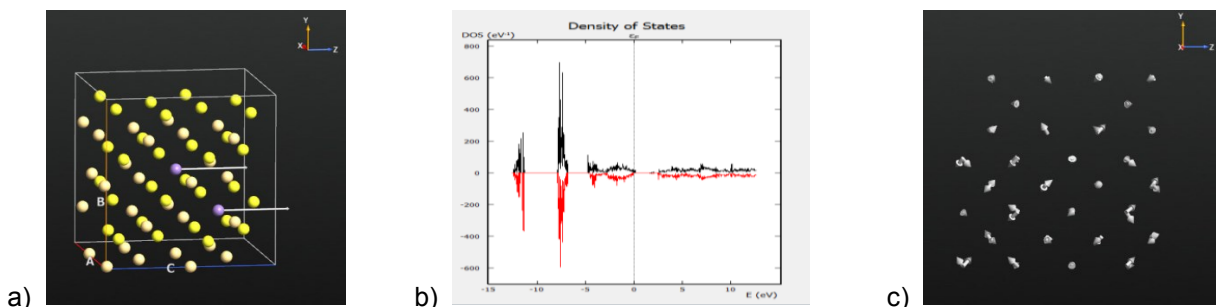


Figure 2. Cd vacancy in  $Cd_{30}Mn_2S_{32}$  supercell a) bulk configuration b) density of states c) forces

### III. CONCLUSIONS

It was defined that band gap of  $Cd_{1-x}Mn_xS$  SMSC increases with the increases in Mn ion concentration. It has been established that defects as Cd or S vacancy in the crystal structure leads to the change of band gap, formation of deep levels in the band gap, shifting of Fermi level towards the valence or conduction band.

### REFERENCES

- [1] N. Ahmed, A. Nabi, J. Nisar, M. Tariq, M.A. Javid, M.H. Nasim, "First principle calculations of electronic and magnetic properties of Mn-doped CdS (zinc blende): a theoretical study", *Materials Science-Poland*, Vol. 35, №3, pp. 479-485, 2017.
- [2] S. Kumar, A. Kumar, P.K. Ahluwalia, "First principle study of manganese doped cadmium sulphide sheet", *AIP Conference Proceedings*, AIP, New York, pp. 1732, 2014.
- [3] T.T. Rantala, T.S. Rantala, V. Lantto, J. Vaara, "Surface relaxation of the (1010) face of wurtzite CdS", *Surface Science*, Vol.352-354, pp.77-82, 1996.
- [4] A. Nabi, "The electronic and the magnetic properties of Mn doped wurtzite CdS: First-principles calculations", *Computer Material Science A*, pp.210-218, 2016.
- [5] M. A. Mehrabova, H. S. Orujov, N. H. Hasanov, A. I. Kazimova, A.A. Abdullayeva, "Ab Initio Calculations of Defects in CdMnSe Semimagnetic Semiconductors", *Mechanics of Solids*, Vol.55, №1, pp.108–113. 2020.
- [6] M.A. Mehrabova, N.H. Hasanov, N.I. Huseynov, A.I. Kazimova, "Ab initio calculations of defects in  $Cd_{1-x}Mn_xTe(Se)$  semimagnetic semiconductors", *Journal of Radiation Researches*, Vol. 7, № 2, pp.39-42, 2020.
- [7] M.H. Selma, "Optoelectronic characteristics and optical properties for  $Cd_{1-x}Mn_xS$  nanocrystalline thin films prepared by chemical bath deposition", *International journal of application or innovation in engineering and management*, Vol. 3, № 2, pp.329-333, 2014.

## EFFECTS OF TECHNOLOGICAL REGIMES AND SURFACE MORPHOLOGY ON WETTABILITY PROPERTIES OF POROUS $Al_2O_3$ COATINGS

D. Shimanovich<sup>1</sup>, D. Tishkevich<sup>2</sup>, A. Vorobjova<sup>1</sup>, A. Trukhanov<sup>2</sup>

<sup>1</sup> Belarusian State University of Informatics and Radioelectronics, Minsk, Belarus

<sup>2</sup> Scientific-Practical Materials Research Centre of National Academy of Sciences of Belarus, Minsk, Belarus

### I. INTRODUCTION

In recent years coatings with special wettability such as hydrophobic (superhydrophobic) or hydrophilic (superhydrophilic) have attracted considerable interest due to their practical application – from self-cleaning surfaces to microfluidic and drip technologies.

Electrochemical anodization is one of the most effective methods of surface treatment and the formation of a nanostructured  $Al_2O_3$  surface matrix. Structural and topological parameters of  $Al_2O_3$  matrix significantly affect the functional characteristics and quality of coatings. Materials with low or high surface energy are usually combined with surface structuring with hierarchical topography on the nano- or micrometer scale for the hydrophobic or hydrophilic coatings synthesis. Therefore, due to the possibility of controlling the pore size and regulating the chemical composition of the surface the porous anodic alumina structures represent a great potential for obtaining surfaces with special wettability [1]. Alumina itself has a certain tendency to be wetted with water and therefore is a moderately hydrophilic with a contact angle in the range of 45-60°. However, in combination with its specific surface structure and surface chemistry high hydrophilicity or hydrophobicity can be achieved.

### II. RESULTS AND DISCUSSION

Based on experimental data the effect of technological regimes of an aluminum electrochemical anodizing and pores chemical modification on morphological parameters of nanoporous  $Al_2O_3$  and on the contact angle of alumina structures in order to increase the hydrophilic properties of the final modified coatings was studied. Two- and three-step anodization methods were carried out in a 4%  $H_3PO_4$  at 18-20 °C under various galvanostatic modes at each stage (current densities of 15, 20 and 25 mA/cm<sup>2</sup>) during 60-240 min for the synthesis of various types of  $Al_2O_3$  structures. The methods based on increasing the electrolyte temperature to 30-35 °C at the final anodization stage or post-anodizing chemical etching of  $Al_2O_3$  in a 5%  $H_3PO_4$  solution at 40 °C for various times from 7 to 25 min were used for the chemical modification of the alumina porous

structure combined with pore expansion. It was shown that it is possible to obtain high hydrophilic parameters with a contact angle value up to 17-20° using high values of current density, anodizing time, and electrolyte temperature by adjusting the electrochemical conditions. It was found that the obtained Al<sub>2</sub>O<sub>3</sub> coatings with a thickness of 5-12 μm have a disordered branched porous structure with a pore diameter from 120 to 180 nm. The average pores diameter increased up to 210 nm with significant thinning and destruction of the pore walls after expansion of the pores using chemical etching (Figure 1).

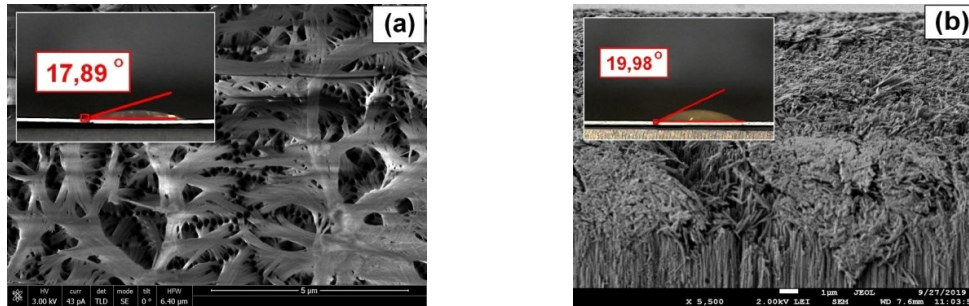


Figure 1. SEM images of modified porous alumina coatings and associated low contact angles: (a) - three-step anodization (15-20-25 mA/cm<sup>2</sup>), 7 μm Al<sub>2</sub>O<sub>3</sub>; (b) - two-step anodization (15-20 mA/cm<sup>2</sup>), 5 μm Al<sub>2</sub>O<sub>3</sub>

### III. CONCLUSIONS

The comparative analysis of Al<sub>2</sub>O<sub>3</sub> coatings and effect of surface morphology on the wettability properties were discussed. It was seen that this type of modified Al<sub>2</sub>O<sub>3</sub> structures provides direct experimental evidence for the theory of three-dimensional capillaries regarding superhydrophilicity.

### REFERENCES

[1] D.L. Shimanovich [et al], "Preparation and Morphology-Dependent Wettability of Porous Alumina Membranes", Beilstein J. of Nanotechnology, Vol. 9. pp. 1423-1436, 2018.

## DEVELOPING A Seq2Seq NEURAL NETWORK USING VISUAL ATTENTION TO TRANSFORM MATHEMATICAL EXPRESSIONS FROM IMAGES TO LaTeX

P. Vyaznikov, I. Kotilevets

Federal State Budget Educational Institution of Higher Education «MIREA - Russian Technological University», Moscow, Russia

[sha.cehca@yandex.ru](mailto:sha.cehca@yandex.ru)

### I. INTRODUCTION

In the modern world, Optical Character Recognition technology finds an incredible number of applications (text recognition quickly scanning document). Progress in this area is due to the emergence of advanced deep learning algorithms and neural network models, which, learning from a huge number of examples, can make very accurate predictions.

The task of im2latex, known thanks to the OpenAI company, is to create an OCR neural network capable of converting an image with mathematical expressions into a similar expression in the LaTeX markup language with high accuracy. This problem belongs to the Image Captioning type - the neural network scans the image and, based on the extracted features, generates a description in natural language.

The proposed solution uses the seq2seq architecture, which contains the Encoder and Decoder mechanisms, as well as Bahdanau Attention [1]. This approach makes it possible to achieve high efficiency and accuracy in generating captions of mathematical expressions. The principle of operation of the neural network is shown in Figure 1.

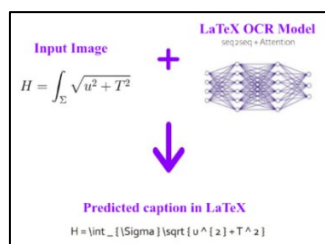


Figure 1. Principle of im2latex

## II. DATASET

The training data for im2latex contains 100000 images with mathematical expressions, paired with their true LaTeX label. Before training, all captions are being tokenized (represented as numbers) and then a dictionary is assembled from all individual tokens (i.e., individual LaTeX words), which is used during training process.

## III. NEURAL NETWORK ARCHITECTURE

Sequence to Sequence architecture consists of two main components: Encoder and Decoder. These are two connected neural networks training simultaneously, but performing different tasks.

Encoder is the mechanism, that contains a set of convolutional layers and is designed to extract features from photos, which can then be used by Decoder and Attention to generate an output sequence. The number of layers and their settings are very important and may vary depending on the task. After extracting the features, Encoder summarizes it in a form called the Internal State Vector.

After extracting the features, the Decoder begins to train, which in the future will be able to generate caption for any image. The mechanism is based on a recurrent neural network (RNN), which is able to identify and remember important information and ignore irrelevant information.

An important element of Decoder is the Attention mechanism. Its essence is to generate “importance weights”, called the Context Vector, for the output sequences of the Encoder (image features), which are then combined with the input data of the Decoder, which allows the network to learn much more efficiently.

The input data of the Decoder are the real captions corresponding to the dataset images passed through the Encoder. The whole training loop of the neural network is shown on Figure 2.

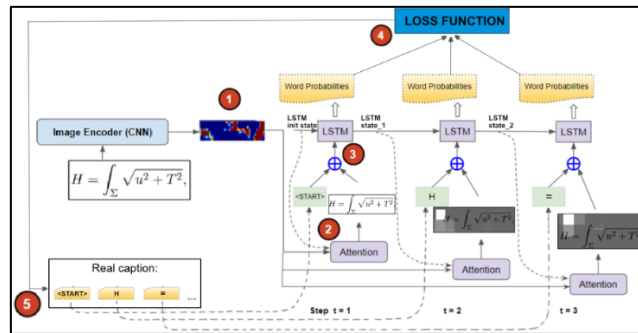


Figure 2. Seq2Seq training loop

## IV. HYPERPARAMETERS

The neural network uses SparseCategoricalCrossentropy as a loss function and Adam as an optimizer, “batch\_size” is equal to 24 and epochs is set to 15. With such parameters, the network trained for about 14 hours using Nvidia RTX 3080 and 32 gigabytes of RAM. The lowest average loss obtained is 0.025, which is an excellent result for Image Captioning neural networks. The loss graph is shown of Figure 3.

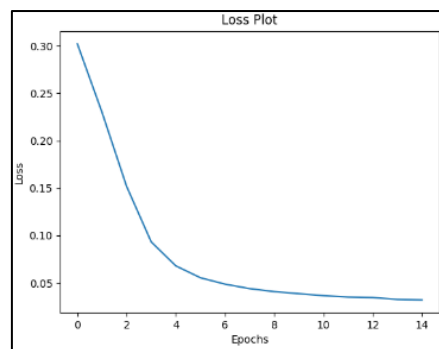


Figure 3. Training Loss graph

## V. EVALUATION

Measured BLEU [2] score is about 70% and Levenshtein distance metric is 31. In comparison with similar works [3], the obtained metric measurements are quite high. The competing solution has 40% for BLEU against 70% of the reviewed and 44 for Minimal Edit Distance against 31. Based on the above data, it can be argued that the developed neural network has high efficiency.

## VI. CONCLUSIONS

The presented neural network with the seq2seq architecture and Attention mechanism successfully solves the im2latex problem, which is confirmed by the results of measuring metrics. Generated captions for images with equations are quite accurate and, in most cases, coincide with the real ones.

Such a solution can be used in mathematical programs to automatically translate images into LaTeX and further solve and analyze the resulting equations or expressions.

The scope of use can be expanded by training the network on images with handwritten equations. A similar technology is used in the PhotoMath application, however, it has low accuracy and a small set of supported mathematical symbols. The described solution is devoid of both problems.

## REFERENCES

- [1] NEURAL MACHINE TRANSLATION BY JOINTLY LEARNING TO ALIGN AND TRANSLATE. // <https://arxiv.org/pdf/1409.0473.pdf>
- [2] BLEU: a Method for Automatic Evaluation of Machine Translation // <https://aclanthology.org/P02-1040.pdf>
- [3] Im2Latex // <https://github.com/luopeixiang/im2latex>.

## DESIGN OPTIMIZATION OF THE GALLIUM NITRIDE HETEROSTRUCTURE FIELD-EFFECT TRANSISTOR WITH A GRAPHENE HEAT-REMOVAL SYSTEM

V. Volcheck, I. Lovshenko, V. Stempitsky

Belarusian State University of Informatics and Radioelectronics, Minsk, Belarus

[vlad.volchek@bsuir.by](mailto:vlad.volchek@bsuir.by)

## I. INTRODUCTION

The self-heating effect has a considerable influence on the characteristics of the heterostructure field-effect transistor (HFET) based on gallium nitride (GaN) [1,2]. To reduce the maximum temperature in GaN HFETs, a variety of thermal solutions has been attempted. These include diamond substrate [3], flip-chip bonding [4], backside metal deposition [5] and heat-eliminating element [6]. We have recently investigated [1] the dc and small signal performance of the HFETs with a graphene heat-removal system closely resembling that used by Yan *et al.* [6]. The graphene heat-eliminating element is connected with a heat sink outside the device structure and is designed specifically for removing the heat immediately from the maximum temperature region, thus providing an additional heat-escape route. To enhance the graphene heat-removal system, we have proposed [2] the formation of a trench in the passivation layer in which a high thermal conductivity material, such as boron nitride, boron arsenide or synthetic diamond is deposited.

This paper is dedicated to the design optimization of the GaN HFET with a graphene heat-removal system enhanced by a trench in the passivation layer filled by diamond.

## II. DEVICE STRUCTURE

The main object of the research is a GaN HFET with a graphene heat-removal system shown in Figure 1. After the solidus signs, the region thicknesses are indicated. The source-to-gate and gate-to-drain distances equal to 2 and 3  $\mu\text{m}$ , respectively. The length and the width of the gate are 0.5  $\mu\text{m}$  and 1 mm. The lengths of the diamond layer and the graphene heat-eliminating element equal to 2.8 and 3.9  $\mu\text{m}$ .

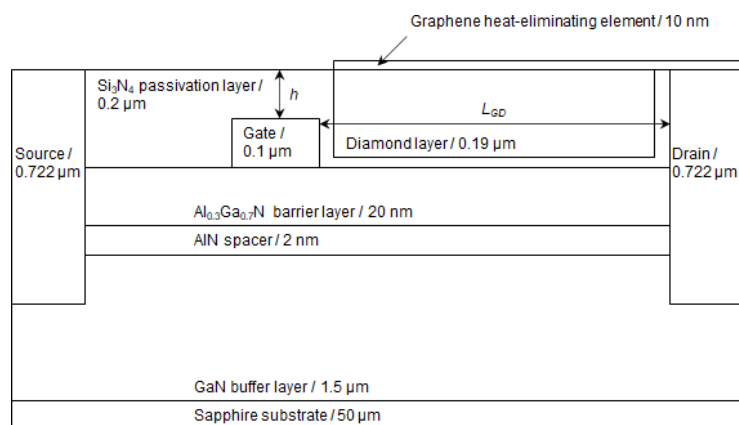


Figure 1. GaN HFET with a graphene heat-removal system



### III. RESULTS

In Figure 1, the parameter  $h$  denotes the distance between the gate and the top surface of the GaN HFET uncovered by the graphene heat-eliminating element. If the top surface of the device is lowered by 0.05 and 0.1  $\mu\text{m}$ , which corresponds to  $h$  values of 0.05 and 0  $\mu\text{m}$ , the cut-off frequency increases by 1.2 and 3.3%, from 33.0 to 33.4 and 34.1 GHz, respectively. The maximum frequency of oscillation grows by 3.0 and 9.0%, from 114.0 to 117.4 and 124.2 GHz, respectively.

Figure 2 shows the dependence of the cut-off frequency and the maximum frequency of oscillation on the gate-to-drain distance ( $L_{GD}$ ). If the parameter  $L_{GD}$  is raised from 3 to 6  $\mu\text{m}$ , leading to an increase in the lengths of the diamond layer and the graphene heat-eliminating element, the cut-off frequency and the maximum frequency of oscillation decrease by 11.0 and 10.0%, to 29.4 and 102.6 GHz, respectively.

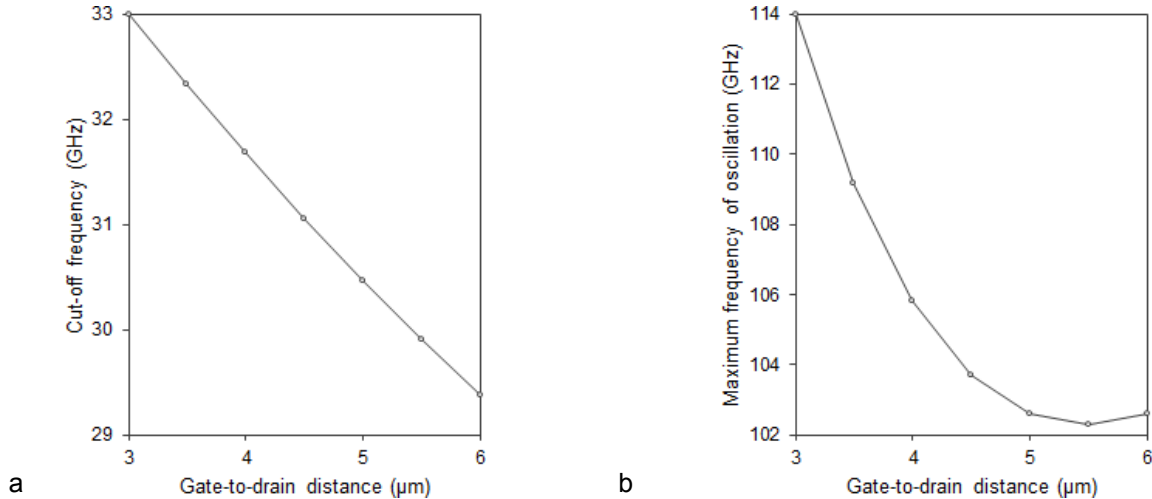


Figure 2. Cut-off frequency (a) and maximum frequency of oscillation (b) as functions of the gate-to-drain distance

### IV. CONCLUSIONS

We have conducted the design optimization of the GaN HFET with a graphene heat-removal system enhanced by a trench in the passivation layer filled by diamond. A reduction in the parameter  $h$  leads to a relatively small improvement in the small-signal performance quantities, since the heat-eliminating element approaches the maximum temperature region.

### ACKNOWLEDGMENTS

This work is supported by the grant 3.1 of Belarusian National Scientific Research Program “Photonics and Electronics for Innovations”.

### REFERENCES

- [1] V. S. Volcheck, I. Yu. Lovshenko, V. T. Shandarovich, Dao Dinh Ha, “Gallium Nitride High-Electron Mobility Transistor with an Effective Graphene-Based Heat Removal System”, Doklady BGUIR, Vol. 18, pp. 72-80, 2020.
- [2] V. S. Volcheck, V. R. Stempitsky, “Gallium Nitride Heterostructure Field-Effect Transistor with a Heat-Removal System Based on a Trench in the Passivation Layer Filled by a High Thermal Conductivity Material”, Doklady BGUIR, Vol. 19, pp. 74-82, 2021.
- [3] K. Hiram, Y. Taniyasu, M. Kasu, “AlGaIn/GaN High-Electron Mobility Transistors with Low Thermal Resistance Grown on Single-Crystal Diamond (111) Substrates by Metalorganic Vapor-Phase Epitaxy”, Appl. Phys. Lett., Vol. 98, Art. no. 162112, 2011.
- [4] J. Sun, H. Fatima, A. Koudymov, A. Chitnis, X. Hu, H.-M. Wang, J. Zhang, G. Simin, J. Yang, M. Asif Khan, “Thermal Management of AlGaIn-GaN HFETs on Sapphire Using Flip-Chip Bonding with Epoxy Underfill”, IEEE Electron. Device Lett., Vol. 24, pp. 375-377, 2003.
- [5] G. Pavlidis, S. H. Kim, I. Abid, M. Zegaoui, F. Medjdoub, S. Graham, “The Effects of AlN and Copper Back Side Deposition on the Performance of Etched Back GaN/Si HEMTs”, IEEE Electron. Device Lett., Vol. 40, pp. 1060-1063, 2019.
- [6] Z. Yan, G. Liu, J. M. Khan, A. A. Balandin, “Graphene Quilts for Thermal Management of High-Power GaN Transistors”, Nat. Commun., Vol. 3, Art. no. 827, 2012.

# MACHINE LEARNING METHODS FOR PREDICT ELECTROPHYSICAL PROPERTIES OF SEMICONDUCTOR MATERIALS FOR OPTOELECTRONIC AND ENERGY STORAGE DEVICES

A. Khinevich, A. Stsiapanau, A. Smirnov

Belarusian State University of Informatics and Radioelectronics, Minsk, Belarus

[hinevics@gmail.com](mailto:hinevics@gmail.com)

## I. INTRODUCTION

There were several notable attempts at utilizing Machine Learning to predict physical properties of various materials. Huang et al. reported prediction of band gap properties for ternary metal nitride compounds using ML approach based on the calculated data using Heyd–Scuseria–Ernzerhof (HSE) hybrid functionals and Perdew–Burke–Ernzerhof (PBE) DFT methods. In that study electronegativity, valence and covalent radius were used as feature for the training of the ML algorithm and prediction. In another study, high accuracy of the prediction was achieved for the ML algorithm trained on the dataset with 3 only features such as ionic radius, electronegativity and number of row associated with position of specific element in the periodic table [1].

## II. DEFINING THE MACHINE LEARNING PROBLEM

Firstly, earth abundant and non-toxic ternary metal nitrides were pre-selected. This is followed by screening of computational databases for the predicted ternary metal nitride compounds suitable for solar energy harvesting with formation energy of  $< 0$  eV/atom, energy above hull of  $< 0.3$  eV/atom, band gap of 0.5 – 3.2 eV. Generalized gradient approximation (GGA) and PBE DFT methods that are known to underestimate the actual value of band. However, they methods are also widely used in materials databases [2]. Therefore, the compounds with band gap of over 0.5 eV were selected for the further processing.

Prior to DFT analysis, the screened nitride compounds were also sorted according to their effective masses for electrons and holes and ratio of direct and indirect band gaps available in [3] to identify materials with the most promising electronic and optical properties for further study.

The algorithm was trained using a dataset of experimentally reported band gap values of about 360 ternary metal nitrides, oxides, sulfides and phosphides compounds. A lack of data is a common problem in machine learning. This usually imposes limitations on various parts of machine learning pipeline, which we will discuss below in details.

## III. FEATURE EXTRACTION AND PROCESSING

Having low amounts of data also imposes certain limits on the amount of features that can be used without causing the curse of dimensionality [4]. This suggests us to pick a number of features  $d \ll N$ , where  $N=360$  is the total number of data samples available in the training split. Some models, like deep neural networks are able to extract features from the raw data fed as input. In our case of small data however, we resorted to hand picking useful features by utilizing our domain knowledge.

The previous works that used machine learning for band gap prediction have prioritized electronegativity, covalent radius and valence of each element in the compound as the key features. For example, authors in [4] have successfully used this feature combination and highlighted that those properties of an element are the most important from the physical viewpoint. A similar set of features including electronegativity, ionic radius, and row in the periodic table was found in the band gap prediction study done by [5]. Some additional physical information in the form of ionic charge, period in the periodic table, atomic number, atomic mass, van der Waals radius, and the first ionization energy was used as features for band gap prediction in [6].

Thus, our choice of a list of characteristic element-specific features used for the machine learning prediction included detailed electronic configuration, maximum valence, atomic mass, electronegativity, atomic and covalent radius, ionization potential, electron affinity, period, group and block of the constituent elements. We later processed the electronic configuration and extracted a set of features out of it, such as the number of electrons on the last orbital, the number of electrons before the last orbital, number of electrons at last level, and number of vacancies at the outer orbital.

After removing some of the redundant features and highly correlated features, we ended up with  $d=51$  total features for our experiments.

## IV. MODEL

Limited dataset size also affects the choice of the model and limits our choices depending on the model's complexity, since a very sophisticated model, e.g. deep neural network with many parameters, will tend to overfit when the number of training samples is too low. We used support vector regression (SVR) with

the nonlinear radial basis function (RBF) kernel as a machine learning model in our experiments. The model of choice was implemented with the use of the Scikit-learn framework and Python 3.7.

## V. RESULTS

ML predictions of band gap values were used in combination with data available in open access databases to reduce the number of potential candidates for subsequent theoretical modeling with hybrid HSE functionals. In addition, the remaining compounds were sorted based on the value of effective electron and hole masses.

## REFERENCES

- [1] Venkatraman V., The utility of composition-based machine learning models for band gap prediction., Department of Chemistry, Norwegian University of Science and Technology, Norway, 2021, 0927-0256.
- [2] Liu, Yue, et al. "Materials discovery and design using machine learning." *Journal of Materiomics* 3.3 (2017): 159-177.
- [3] Li, Yuheng, and Kesong Yang. "High-throughput computational design of organic–inorganic hybrid halide semiconductors beyond perovskites for optoelectronics." *Energy & Environmental Science* 12.7 (2019): 2233-2243.
- [4] Trunk, G. V. (July 1979). "A Problem of Dimensionality: A Simple Example". *IEEE Transactions on Pattern Analysis and Machine Intelligence*. PAMI-1(3): 306–307.
- [5] L. Weston and C. Stampfl, Machine learning the band gap properties of kesterite<sub>2</sub>–II–IV–V<sub>4</sub> quaternary compounds for photovoltaics applications, *Phys. Rev. Mater.*, 2018, 2(8), 085407.
- [6] J. Lee, A. Seko and K. Shitara, et al., Prediction model of band gap for inorganic compounds by combination of density functional theory calculations and machine learning techniques, *Phys. Rev. B*, 2016, 93(11), 115104.

## THE PROTON FLUX INFLUENCE ON ELECTRICAL CHARACTERISTICS OF A DUAL-CHANNEL HEMT BASED ON GaAs

I. Lovshenko, A. Voronov, P. Roshchenko, R. Ternov, V. Stempitsky  
Belarusian State University of Informatics and Radioelectronics, Minsk, Republic of Belarus

[lovshenko@bsuir.by](mailto:lovshenko@bsuir.by)

### I. INTRODUCTION

The Element base of modern objects of space and nuclear technology is exposed to ionizing radiation, the main of which are gamma rays ( $\gamma$ ), neutron (n), electron (e) and proton (p) radiation. Alfa-particles ( $\alpha$ ), fission fragments Fp and other particles from a nuclear reactor or nuclear explosion zone can also influence the degradation of performance characteristics. However, their influence is not so significant (for example, neutrinos, mesons, etc.).

When a particle flux affects microelectronic device structure, two main mechanisms are possible: ionization and damages caused as a result of elastic scattering of primary particles and fragments formed in nuclear reactions (inelastic scattering) of incident protons or neutrons on target's nucleuses. Ionization is not considered in this work. The magnitude of the manifestation of displacement effects depends on the type of particles radiation, the total dose, radiation flux and energy, ambient temperature, operating voltage, the state of the device at the moment of irradiation. These problems complicate testing, increase the complexity of using theoretical calculations to predict radiation effects, increase the time of designing device structures and require a significant number of test samples.

### II. RESULTS

A typical device structure of a dual-channel GaAs-based high electron mobility field effect transistor (HEMT) is shown in figure 1. Cut-off voltage and maximum drain current for the resulting structure at ambient temperature  $T = 303$  K are equal to  $V_{TH} = -0.9$  V and  $I_{Dmax} = 1.7$  mA (at drain voltage  $V_D = 0.1$  V and gate  $V_G = 1$  V) respectively.

The formation of bulk defects in semiconductor device structure is proportional to non-ionizing energy loss (NIEL) - total kinetic energy transferred to the lattice atoms. Parameter NIEL can be used to the extrapolation of device parameters degradation measured for particle with given energy to other energies ("NIEL scaling"). The Radiation Fluence Model is used in microelectronics TCAD software packages to describe the impact of particle flux on material characteristics, which makes it possible to predict the rate of defect generation.

According to the model the total density of defect states depends on the radiation flux, NIEL, damage coefficient and the density of material. The non-ionizing energy losses for GaAs are determined using SR-NIEL project for displacement threshold energy values  $E_{d1} = 9,5$  eV [3],  $E_{d2} = 10$  eV [4],  $E_{d3} = 21$  eV [5] and  $E_{d4} = 25$  eV [6]. For the obtained values mean values were determined, which are described by approximating dependence (figure 2). The obtained results fully agree with the data presented in the paper [7]. The total NIEL for GaAs is calculated by summing the contributions of each element weighted by its atomic fraction [8].

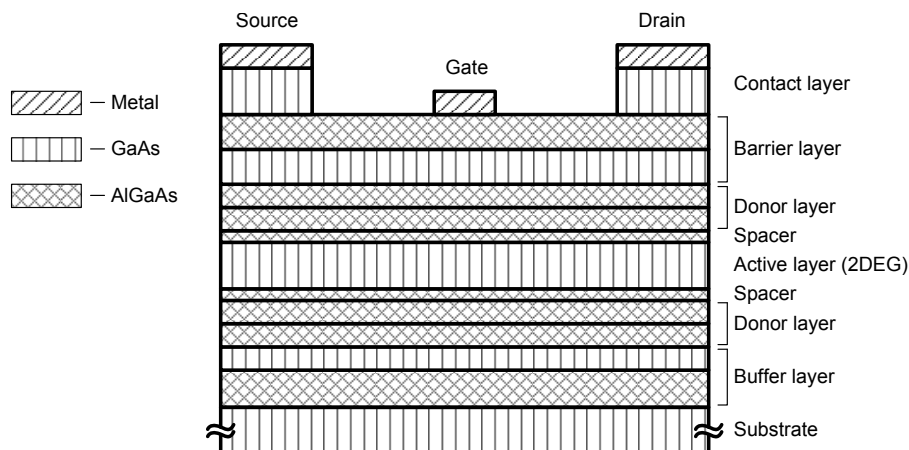


Figure 1. Device structure of a dual-channel GaAs-HEMT

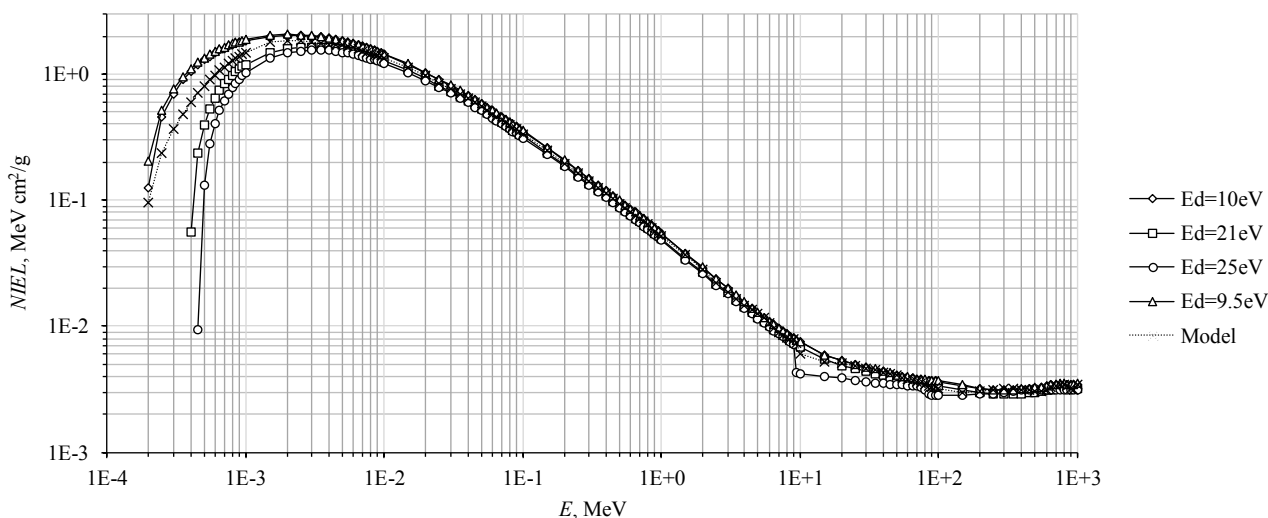


Figure 2. The dependence of non-ionizing energy loss on the proton energy

A simulation of the effect of proton flux on the performance characteristics of a dual-channel GaAs-based HEMT device structure was carried out. The results obtained are in agreement with theoretical data for the flux of protons with energies  $E_p$  from 0.1 to 10 keV at temperature  $T = 303$ .

### III. CONCLUSIONS

The model of the dependence of NIEL on the proton energy with different values of threshold energy of defect formation for GaAs and AlGaAs, that are described in the literature and comply with the latest theoretical and experimental data, has been developed.

### ACKNOWLEDGMENTS

The research is funded by and carried out within the state program of scientific research "Photonics and electronics for innovations" (task 3.04)

### REFERENCES

- [1] V.M. Kulakov, E.A. Ladygin, V.I. SHahovcov, "Dejstvie pronikayushchej radiacii na izdeliya elektronnoj tekhniki", Sov. Radio, C. 224, 1980. [in Russian]
- [2] <http://www.sr-niel.org/index.php>.

- [3] E. Mansouri, "Studies on Radiation-induced Defects in InP/InAsP Nanowire-based Quantum Disc-in-wire Photodetectors", Halmstad University, P. 48, 2018.
- [4] D. Pons, P.M. Mooney, J.C. Bourgoin, "Energy Dependence of Deep Level Introduction in Electron Irradiated GaAs", J. Appl. Phys, Vol. 51, pp. 2038-2042, 1980.
- [5] E.E. Allam [et al.] "Gamma and Electron NIEL Dependence of Irradiated GaAs", NSREC, P. 7, 2016.
- [6] C. Claeys, E. Simoen, "Radiation effects in Advanced Semiconductor Materials and Devices", Springer, P. 404, 2002.
- [7] N.J. Chen, "Computational simulation of threshold displacement energies of GaAs", J. Materials Research, Vol. 32, Issue 8, pp. 1555–1562, 2017.
- [8] J.F. Ziegler, J. P. Biersack, U. Littmark, "The Stopping and Range of Ions in Solids", Pergamon, P. 321, 1985.

## THE EFFECT OF A HIGH-FREQUENCY ELECTROMAGNETIC FIELD ON THE BREATHER-ELECTRIC EFFECT IN A NON-ADDITIVE SUPERLATTICE

D. Zavyalov, E. Sivashova, E. Denisov  
Volgograd State Technical University, Volgograd, Russia

[laei@mail.ru](mailto:laei@mail.ru)

### I. INTRODUCTION

Superlattices (SL) are still of interest to researchers for several reasons. One of them is the possibility of propagation of nonlinear electromagnetic waves at relatively small field strengths (about  $10^3$  V / cm) [1-4]. In this case, the propagation of electromagnetic waves in the superlattice is described by the sine-Gordon equation, which also describes a few physical phenomena in various systems [5].

The effect of charge entrainment by a breather in superlattices with a model spectrum in the strong coupling approximation in the presence of a warming electromagnetic field is investigated.

### II. MAIN PART

Let us consider an SL that is periodical along the Oz axis. The dispersion law for this SL has the form ( $\hbar = 1$ )

$$\varepsilon(\mathbf{p}) = \varepsilon(\mathbf{p}_\perp) + \Delta(1 - \cos(p_z d)) \quad (1)$$

where  $d$  is the superlattice period,  $\Delta$  is the half-width of the conduction miniband. In this case, the form of the transverse part of the energy spectrum  $\varepsilon(\mathbf{p}_\perp)$  depends on the material on the basis of which the superlattice is made. For GaAs / AlGaAs-based superlattices  $\varepsilon(\mathbf{p}_\perp) = \frac{p_\perp^2}{2m}$ . For graphene-based superlattices  $\varepsilon(\mathbf{p}_\perp) = \sqrt{\Delta_1^2 + v_F^2 p_z^2}$ .

The propagation of short electromagnetic pulses in an SL along its layers in the collisionless approximation is described by the sine-Gordon equation

$$\frac{\partial^2 \varphi}{\partial \tau^2} - \frac{\partial^2 \varphi}{\partial \chi^2} + \sin(\varphi) = 0 \quad (2)$$

where  $\chi = \frac{\omega_{pl} z}{c}$  – is the dimensionless coordinate,  $\tau = \omega_{pl} t$  – is the dimensionless time,  $\varphi = \frac{edA}{\hbar c}$  – is the dimensionless vector potential of the pulse electromagnetic field associated with the electric field strength  $E(t)$  by the relation  $\varphi = ed \int_{-\infty}^t E(t') dt'$ ,  $\omega_{pl} = \frac{2\pi ed}{\hbar \sqrt{\frac{2n\Delta I_1(\theta)}{I_0(\theta)}}}$  is the plasma frequency of electrons in the conduction miniband,  $n$  – is the concentration charge carriers in the SL,  $c$  – is the rate of electromagnetic radiation in vacuum,  $I_1(\theta), I_0(\theta)$  – are the modified Bessel functions,  $\theta$  – is the temperature in energy units.

Some of the simplest and most studied solutions of equation (2) are the so-called  $N$ -soliton solutions [6]. However, this equation also has more complex solutions. In addition to soliton solutions, a doublet solution stands out, otherwise called a bion or breather (the term "breathing" solution is also encountered). The possibility of propagation of electromagnetic breathers in a semiconductor superlattice was demonstrated in [7]. Mathematically, the doublet solution looks like this (in dimensional coordinates):

$$\varphi(y, t) = 4 \operatorname{arctg} \left( \alpha \frac{\sin \left( \omega^* \left( t - \frac{uy}{c^2} \right) \right)}{\operatorname{ch} \left( \omega_1^* \left( t - \frac{y}{u} \right) \right)} \right)$$

where  $\alpha = \frac{\omega_1}{\omega}$ ,  $\omega_1 = \sqrt{\omega_{pl}^2 - \omega^2}$ ,  $\beta = \frac{u}{c}$ ,  $\gamma = (1 - \beta^2)^{-\frac{1}{2}}$ ,  $\omega^* = \gamma\omega$ ,  $\omega_1 = \gamma\beta\omega$ .

Physically, the doublet solution can be interpreted as a coupled (oscillating with frequency  $\omega$ ) state of a soliton-antisoliton pair.

For the experimental detection of breathers in superlattices, the effect of dragging electrons by them (breather-electric effect) can be used. A similar effect is also observed in the case of propagation of solitons (solitonoelectric effect).

It was shown in [6] that in the case of application of a high-frequency field with an intensity along the SL axis, equation (2) is modified as follows [8]

$$\frac{\partial^2 \varphi}{\partial \tau^2} - \frac{\partial^2 \varphi}{\partial \chi^2} + J_0(a) \sin(\varphi) = 0 \quad (3)$$

where  $a = eEd / \omega$ .

We will assume that the width of a solitary wave is large in comparison with the mean free path of an electron, and the time of action of a solitary wave on an electron is small in comparison with the time of free path of an electron; at typical values of the parameters, these assumptions are fulfilled. Under these conditions, we obtain an expression for the drag current density, determined by the following formula:

$$j(\tau) = \frac{4n_0 \Delta e}{mV} \int_{-\infty}^{\tau} F(\tau_1) \sin(\varphi(\tau_1)) d\tau_1 \quad (4)$$

where

$$F(\tau) = \tilde{\omega}^* \tilde{\alpha} \frac{\tilde{\alpha} \sin(\tilde{\omega}^* \tau) \operatorname{sh}(\tilde{\omega}_1^* \tau) - \beta \cos(\tilde{\omega}^* \tau) \operatorname{ch}(\tilde{\omega}_1^* \tau)}{\operatorname{ch}^2(\tilde{\omega}_1^* \tau) + \tilde{\alpha}^2 \sin^2(\tilde{\omega}^* \tau)} \quad (5)$$

$$\tilde{\alpha} = \sqrt{J_0(a) \omega_{pl}^2 / \omega^2 - 1}, \tilde{\omega}^* = \frac{\gamma \omega}{\omega_{pl}}, \tilde{\omega}_1^* = \gamma \beta \sqrt{J_0(a) - \omega^2 / \omega_{pl}^2}$$

To find the transferred charge (namely, it is detected experimentally), it is necessary to integrate expression (5) from minus to plus infinity. In the case of  $\alpha \ll 1$  this can be done analytically, but in the general case of an arbitrary bond strength, the study can only be carried out numerically. Let us immediately note the main feature in expression (5) - for a certain value of the dimensionless strength of the high-frequency field  $a$ , the value of  $\tilde{\alpha}$  can become complex, since in the expression under the root  $J_0(a) \omega_{pl}^2 / \omega^2 - 1$  the first term decreases with increasing  $a$ . We can say that at this point the breather solution loses its stability and the breather-electric effect disappears. Earlier in [7], it was noted that when considering the soliton-electric effect under the conditions of an alternating field, a similar effect occurs - the soliton solution loses its stability at a field value for which  $J_0(a) = 0$ . However, this condition has a simple physical interpretation: the high-frequency field heats up the electron gas and at  $J_0(a) = 0$  the average energy becomes greater than the half-width of the conduction miniband, and the propagation of amplified pulses becomes possible - an autosoliton solution. In the case of a breather solution, it loses stability even before the distribution of electrons is inverted; therefore, the physical reason for the loss of stability is still unclear and the issue requires additional research.

### III. CONCLUSIONS

The paper investigates the propagation of the breather of the sine-Gordon equation under the influence of a high-frequency field. The features of the entrainment of the charge by such a pulse are noted.

### REFERENCES

- [1] E.M.Epshtein, "Drag of Electrons by Solitons in Semiconductor Superlattice," *Sov.Phys.Solid State*. 14(12), 2422 (1980) [in Russian].
- [2] F.G. Bass and A.A. Bulgakov, *Kinetic and Electro- dynamic Phenomena in Classical and Quantum Semiconductor Superlattices* (Nova Science Publ., N.Y., 1997).
- [3] S.Y.Mensah, F.K.A. Allotey, and N.G.Mensah, "Excitation of Breather (Bion) in Superlattice," *Phys. Scripta*. 62, 212 (2000).

- [4] S.V.Kryuchkov and E.I.Kukhar', "TheSolitaryElec- tromagnetic Waves in the Graphene Superlattice" Physica B. 408, 188 (2013).
- [5] K. Lonngren and A. Scott, Solitons in Action (Aca- demic Press, N.Y., 1978).
- [6] J. L. Lamb. Elements of soliton theory / J. L. Lamb (New York etc., 1980).
- [7] S.V. Kryuchkov and G.A. Syrodoev, 1990, Fiz. Tekh. Poluprovodn. (Leningrad), 24, no. 6, 1120.
- [8] S. V. Kryuchkov and E. I. Kukhar', «Possibility of Propagation of Dissipative Solitons in AC-Driven Superlattice», Physics of Wave Phenomena, 2015, Vol. 23, No. 1, pp. 21–27.

## THE COMPARATIVE ANALYSIS OF TECHNOLOGICAL REGIMES FOR IMPROVING THE ELECTRICAL INSULATION STRENGTH OF DOUBLE-SIDED ALUMINA BASES WITH VIAS

D. Shimanovich<sup>1</sup>, D. Tishkevich<sup>2</sup>

1 Belarusian State University of Informatics and Radioelectronics, Minsk, Belarus

2 Scientific-Practical Materials Research Centre of National Academy of Sciences of Belarus, Minsk, Belarus

### I. INTRODUCTION

The aim of the presented research is developing of the methods and techniques using optimized technological regimes to improve the electrical insulation strength of anodic  $Al_2O_3$  in vias of double-sided alumina bases for potential use in power multichip modules [1].

Preliminary experimental studies of fabricated alumina bases with vias matrices showed that in the process of electrochemical anodization at the junction of horizontal and vertical surfaces in vias, microcracks inevitably appeared due to anodizing fronts competing in different directions, restructuring of the porous structure and arising mechanical stresses, even if on the continuous surface of alumina bases, microcracks were completely absent.

### II. RESULTS AND DISCUSSION

It was shown that the dielectric strength of anodic  $Al_2O_3$  in vias increased by minimizing the number of microcracks due to vias have chamfers (at an angle of up to  $45^\circ$ ), a smooth profile at the inputs with satisfactory roughness parameters were formed on the initial samples of aluminum bases by machining and due to the smoothing of microcracks during reanodization. Various methods and techniques were developed and investigated consisting the compositions of single- and multicomponent electrolytes and the electrochemical conditions of multistage anodizing for the beneficial (in terms of increasing the breakdown voltages in vias) structural rearrangement of anodic  $Al_2O_3$  and the formation of multilayer elastic and flexible coatings with minimization of the number of microcracks and internal mechanical stresses. It was found that to ensure the high breakdown voltages, it is necessary to prime (fill the pores) of anodic  $Al_2O_3$  and heal defective microcracks in vias with organosilicon varnish in an ultrasonic bath at a frequency of  $\sim 20\text{--}40$  kHz at a maximum power of  $\sim 0,5$  kW and temperature  $\sim 30$  °C during 20 min. Moreover, this technological technique should be carried out in two cycles. Then after filling the excess varnish in the vias should be blown out with compressed air and after removed from the surface with a squeegee and treated with a toluene solution, after which a multistage heat treatment procedure is carried out with a maximum temperature of 280 °C.

It was shown that after using of the appropriate technological methods the breakdown voltages of the obtained test samples (Figure 1 (a)) were up to  $\sim 6$  kV on working surfaces without holes and up to  $\sim 2,5$  kV in vias (Figure 1 (b)).

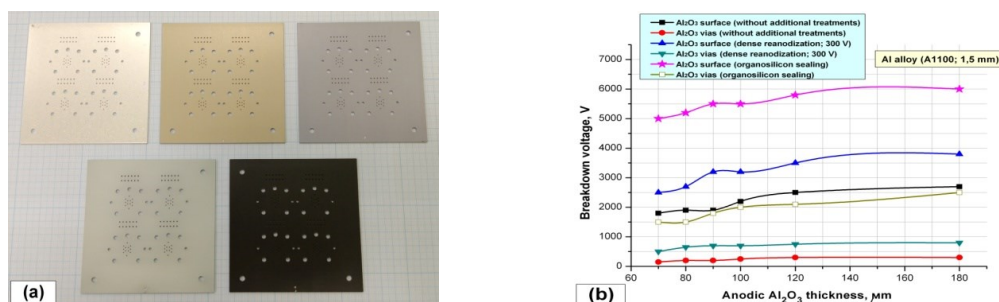


Figure 1. Photo of various double-sided alumina bases with vias (a) and comparative analysis of technological methods influence on the breakdown voltage (b)

### III. CONCLUSIONS

Thus, the comparative analysis of optimized methods and technological regimes for improving the electrical insulation strength of anodic Al<sub>2</sub>O<sub>3</sub> in vias of double-sided alumina bases for potential use in power multichip modules were discussed.

### REFERENCES

[1] D.L. Shimanovich, V.A. Yakovtseva, "Electrochemical alumina technology for power electronics devices", Doklady BGUIR, Vol. 3 (121). pp. 5-11, 2019.

## STUDY OF THE INFLUENCE OF TEMPERATURE AND LOAD ON THE MECHANICAL PROPERTIES OF UNIRRADIATED AND IRRADIATED PLEXIGLASS OF DIFFERENT TYPES IN THE FLAT STRAIGHT BENDING TEST

A. Kupchishin<sup>1,2</sup>, M. Niyazov<sup>1</sup>, B. Taipova<sup>1</sup>, D. Utepova<sup>1</sup>, B. Tronin<sup>1</sup>  
1 Abai Kazakh National Pedagogical University, Almaty, Kazakhstan  
2 Al-Farabi Kazakh National University, Almaty, Kazakhstan

marat--90@mail.ru

### I. INTRODUCTION

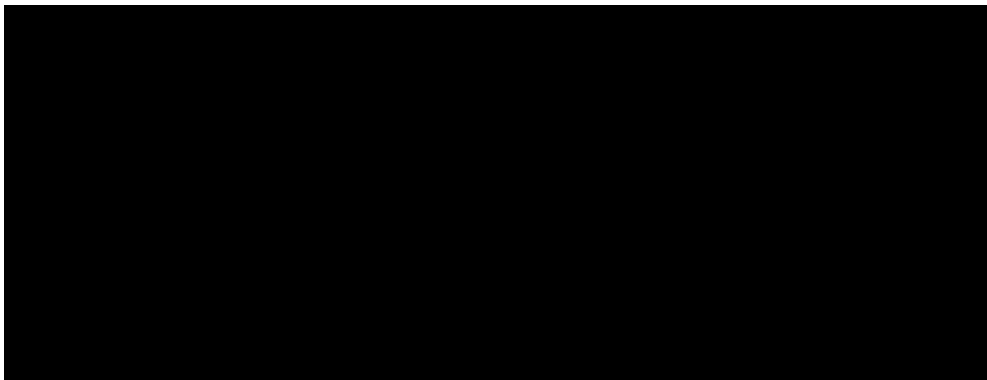
Polymer materials have several of advantages over traditional products [1]. The mechanical properties of composites can change at high strain rates and after irradiation with high – energy particles [2 - 4]. Such materials will also vary with increase of the load. This makes it possible to take into account changes in the design and operation of structures operating in harsh conditions [5, 6]. This work is devoted to a comprehensive study of various types of unirradiated and irradiated Plexiglas, which are tested for plane straight bending under the influence of temperature.

### II. RESEARCH METHODS

Two types of smooth and corrugated plexiglass (pyramids and stripes) were taken as the materials under study. Specimens of smooth plexiglass had thickness (h) of 1 mm and a width (b) of 5 and 10 mm and with different working lengths (L) – 20, 30, 40, 50, 60 and 70 mm. The experiment was carried out at temperature of 20, 25 and 50 °C. Electron irradiation of corrugated plexiglass samples was carried out on an ELA-6 linear accelerator with an energy of 2 MeV in air. The radiation dose was 100 kGy. For bending tests under various load conditions, a BI (bursting installation)-50 tensile testing machine was used. It is a setup consisting of a loading device, a control panel and rods connecting the loading device with a control panel. On the bottom of the device were a force sensor, a temperature chamber, and various supports.

### III. RESULTS AND DISCUSSION

As a result of the experiments carried out on testing samples of smooth plexiglass of various sizes for a flat straight bend, the dependences of deformation on stress were obtained. From the data obtained, the dependence of deformation on stress for unirradiated samples of smooth Plexiglas 5 mm wide and of various lengths at 20 °C (room) temperature is satisfactorily described by a linear model for all sizes. Moreover, the maximum deformation of the samples, depending on the length of the samples and the stress, varies in the range of 35 – 60%.



1 – 20; 2 – 40; 3 – 70 mm

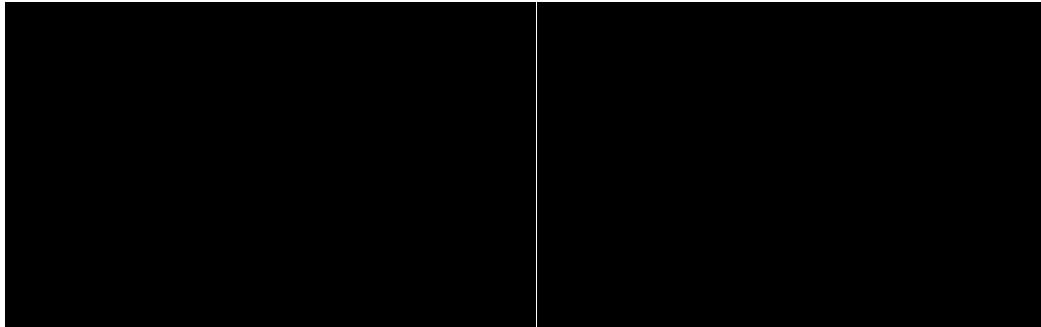
Figure 1. Dependence of deformation on stress when testing specimens of smooth PMMA 5 mm wide (left) and 10 mm (right) for bending at a temperature of 25 °C



From Figure 1 it follows that with an increase in the width of the samples, the deformation decreases. Strength characteristics are also undergoing significant changes. The article shows the dependence of deformation on stress for unirradiated and irradiated samples of corrugated plexiglass, in which plane bending occurs with and without taking into account the horizontal component. From the result of the experiment, it follows that smooth and corrugated plexiglas (both unirradiated and irradiated) are described with good accuracy by a linear model:

$$\varepsilon = \alpha \sigma,$$

where  $\alpha$  is the slope tangent. For unirradiated striped-corrugated glass,  $\alpha = 0.14$ , and for pyramid-corrugated glass,  $0.2\%/MPa$ . For irradiated materials,  $\alpha = 0.1$  and  $0.13\%/MPa$ , respectively.



1 – 20; 2 – 40; 3 – 70 mm

Figure 2. Dependence of deformation on stress when testing samples of smooth polymethylmethacrylate 5 mm wide (left) and 10 mm (right) for bending at a temperature of 50 °C

With a further increase in temperature, the samples begin to bend without load, which made it difficult to analyze the behavior of the material. It can be seen from the figures that a long sample has a greater deflection (regardless of temperature) than a short one and breaks at a lower value of mechanical stress. With an increase in the temperature of the test specimen in the range of 20 – 50 °C, an increase in deformation characteristics by 20 % is observed for all sizes of the material, and the strength characteristics deteriorate by 10-30%.

#### IV. CONCLUSIONS

Experiments on the dependence of deformation on stress during flat straight bending testing of unirradiated and irradiated Plexiglas samples of various types in a temperature chamber have been carried out. It was found that the maximum deformation of samples of various sizes varies in the range of 50 – 60%, depending on the stress, length and width of the material. It was found that electron irradiation leads to a noticeable change in the deformation-strength characteristics of the material, which manifests itself in an improvement in plasticity. With an increase in the temperature of the test specimen in the range of 20 – 50 degrees, an increase in deformation characteristics is observed by another 20 % of the maximum for all sizes of the material, and the strength characteristics deteriorate by 10 – 30 %.

#### ACKNOWLEDGMENTS

This research has been/was/is funded by the Science Committee of the Ministry of Education and Science of the Republic of Kazakhstan (Grant No. AP08855701).

#### REFERENCES

- [1] M. Kazemi, "Experimental analysis of sandwich composite beams under three-point bending with an emphasis on the layering effects of foam core", *Structures*, Vol. 29, pp. 383-391, 2021.
- [2] S.C. Angelides, J.P. Talbot, M. Overend, "High strain-rate effects from blast loads on laminated glass: An experimental investigation of the post-fracture bending moment capacity based on time-temperature mapping of interlayer yield stress", *Construction and Building Materials*, Vol. 273, 2021.
- [3] Y. Qureshi, M. Tarfaoui, K.K. Lafdi, K. Lafdi, "Development of microscale flexible nylon/Ag strain sensor wire for real-time monitoring and damage detection in composite structures subjected to three-point bend test", *Composites Science and Technology*, Vol. 181, 107693, 2019.
- [4] J. Zhou, W. Jiang, Y. Ao, W. Zeng, J. Liu, J. Mei, W. Huang, "The three-point bending responses of carbon fiber composite sandwich beams with Y-frame cores at high and low temperatures", *Thin-Walled Structures*, Vol. 162, 107595, 2021.

[6] H. Liu, J. Liu, Y. Ding, J. Zhou, X. Kong, L.T. Harper, ... J. Dear, "Modelling damage in fibre-reinforced thermoplastic composite laminates subjected to three-point-bend loading", Composite structures, Vol. 236, 111889, 2020.

[7] C. Cerbu, M. Botis, "Numerical modeling of the Flax/Glass/Epoxy hybrid composite materials in bending", Procedia Engineering, Vol. 181, pp. 308-315, 2015.

**COMPUTER MODELING OF CASCADE PROBABILISTIC FUNCTIONS, ENERGY SPECTRA OF PKA AND CONCENTRATION OF VACANCY CLUSTERS IN MATERIALS IRRADIATED WITH LIGHT IONS**

N. Voronova<sup>1</sup>, A. Kupchishin<sup>1</sup>, A. Kupchishin<sup>1,2</sup>, T. Shmygaleva<sup>2</sup>

1 Kazakh National Pedagogical University named after Abai, Almaty, Kazakhstan

2 Kazakh National University named after al-Farabi, Almaty, Kazakhstan

*ankupchishin@mail.ru*

**I. INTRODUCTION**

As is known, the main cause of changes in the structure and physicochemical properties of materials during radiation exposure is the formation of defects [1 - 4]. In contrast to light particles (electrons, photons, etc.), the interaction of ions with matter forms cascade regions, vacancies, clusters of interstitial atoms (and not Frenkel pairs, as is considered in many papers), etc.

Thus, when considering the passage of ions (including light ions: protons and alpha particles) through the matter, it is necessary to solve the cycle of physical and mathematical problems. Most of our work in this direction will be carried out in the framework of the cascade-probability method [5].

**II. RESULTS AND DISCUSSIONS**

As the calculations show, approximation describes the modified cross sections quite well with a correlation coefficient above 0.99, in particular for molybdenum (Table 1).

Table 1. Approximation values and theoretical correlations for protons in Mo

$E_0$ , [MeV]	$\sigma_0$	$a$	$E_0'$	$K$	$\eta$
1	17176	0.22	4.39	5600	0.999
5	2919	0.0249	31.35	3719	0.9999
10	2123	1.45	1.06	42.1	0.999
15	1694	2.68	0.84	16.92	0.999
20	1413	2.33	1.23	15.19	0.997
25	1227	1.89	1.85	15.64	0.99
30	1067	1.60	2.43	15.01	0.996
40	912.2	0.13	37.98	142.36	0.996
50	790.3	0.11	53.77	136.92	0.99

The software package for calculating CP-functions and selecting the type of theoretical curves is implemented in Visualbasic 6.0, C ++ Builder 6.0, Delphi 6.0. Calculations are made for protons and  $\alpha$ -particles in various targets. As an example, Figures 1 and 2 show the dependences of CPF on the number of interactions and the penetration depth for alpha particles in Mo at  $E_0 = 10$  MeV. The calculation results show that with values of  $n = 0.1$  CPF decrease, depending on  $h$ , with increasing  $n$ , they increase, reaching a maximum and begin to decrease. As  $E_0$  grows, the curves shift to the right.

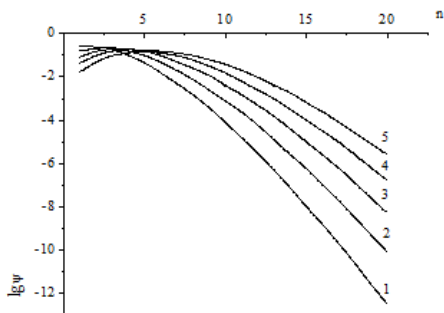


Figure 1. Dependence of CPF on the number of interactions for alpha particles in molybdenum at  $E_0 = 10$  MeV,  $h = 0.006; 0.008; 0.01; 0.012; 0.014$  cm (1-5)

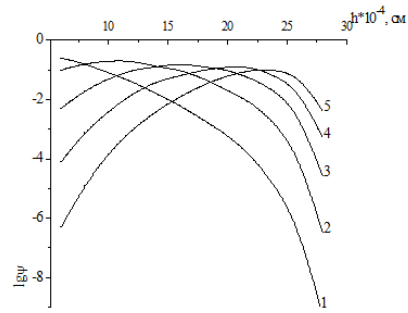


Figure 2. Dependence of CPF on the depth of penetration for alpha particles in molybdenum at  $E_0 = 10$  MeV;  $n = 1, 4, 7, 10, 13$  (1-5)

Further, the energy spectra of PKA were calculated, in particular, for  $\alpha$ -particles in Mo. It can be seen that these are decreasing functions. In a good approximation,  $W(E_2) \sim 1/E_2$ . The concentrations of vacancy clusters were calculated at  $E_0 = 10, 50$  MeV. With increasing depth  $h$ ,  $C_k$  increases, and at the end of the run it drops sharply to zero. With increasing  $E_c$ , the concentration of clusters decreases.

### III. CONCLUSIONS

1. The analysis of modified sections and the calculation of cascade-probability functions for alpha particles were carried out. It was shown that the correlation coefficients  $\eta > 0.99$  (calculated and modified values), which is a good approximation.
2. CPF were analyzed and its main properties were established. When  $k = 0$ , this function goes to the simplest CPF. There are inflection points and maxima. With increasing  $n$ , CPF increases, reaches a maximum, and further decreases. As  $h$  increases, the maxima of the curves shift to the right.
3. The energy spectra of PKA in Mo were calculated. In a good approximation,  $W(E_2) \sim 1/E_2$ . With increasing depth,  $C_k$  increases slowly, reaches a maximum near the end of the path, and drops sharply to zero. With increasing  $E_c$ ,  $C_k$  decreases.

### ACKNOWLEDGMENTS

This research has been/was/is funded by the Science Committee of the Ministry of Education and Science of the Republic of Kazakhstan (Grant No. AP08855701).

### REFERENCES

- [1] V.M. Agranovich, V.V. Kirsanov, "Simulation problems of radiation defects in crystals", Uspekhi Fizicheskikh Nauk, Vol. 118 (1), pp.3-51,1976.
- [2] O.V. Aleksandrov, S.A. Visotskaya, V.S. Zhurkin, "Model of charge of accumulation in MOS-transistors at ionizing irradiation", Izvestiya St. Petersburg State Electrotechnical University «LETI», No.7, pp. 20-27, 2012.
- [3] Yu.V. Bogatyrev, S.B. Lastovsky, S.A. Soroka, S.V. Shwedov, D.A. Ogorodnikov, "Influence of gamma radiation on MOS/SOI transistors", Reports of BGUIR, No. 3(97), pp. 75-80, 2016.
- [4] M.N. Levin, A.V. Tatarintsev, V.A. Makarenko, V.R. Gitlin, "X-ray or UV adjustment of MOS threshold voltage: Analytical and numerical modeling", Russ.Microelectronics, Vol.35, Issue 5, pp. 329-336, 2006.
- [5] E.G. Boos, A.I. Kupchishin, A.A. Kupchishin, Ye.V. Shmygalev, T.A. Shmygaleva, "Cascade-probabilistic method. Solution of radiation-physical problems, Boltzmann equations. Connection with Markov's chains", Monograph, Almaty, Abay KazNPU, SRINCTaM al-Farabi KazNU, Kama LLP, 388 p. 2015.

## SIMULATION OF RADIATION DAMAGE OF THE SEMICONDUCTOR DEVICES

S. Miskiewicz, A. Komarov, F. Komarov, V. Yuvchenko, G. Zayats  
Institute of Applied Physics Problems, Minsk, Belarus

[sergei.miskevich@inbox.ru](mailto:sergei.miskevich@inbox.ru)

### I. INTRODUCTION

Semiconductor devices are extensively used in many sectors of modern electronics. Operation under irradiation can be impossible through their high radiation sensitivity. To forecast their radiation hardness it is important to develop efficient models of radiation effects on semiconductors. In this paper, the model of integral  $n$ - $p$ - $n$  BJT operating in radiation environment is considered.

### II. MODEL OF BJT RADIATION DEGRADATION

Bipolar junction transistors (BJT) are mostly affected by the accumulated defects in semiconductor lattice which are generated by high-energy particles. BJT operating characteristics such as the current gain and the output current decrease mostly as a result of the decrease of minority-carrier lifetime in the base [1].

Model of space-time evolution of minority charge carriers in BJT base includes the equation of continuity of electrons (in case of  $n$ - $p$ - $n$  BJT) [2]:

$$\frac{\partial n(x)}{\partial t} = -\frac{\Delta n(x)}{\tau_n(x)} + D_n(x) \frac{\partial^2 n(x)}{\partial x^2} - \mu_n E(x) \frac{\partial n(x)}{\partial x} - n(x) \mu_n \frac{\partial E(x)}{\partial x}, \quad (1)$$

where  $n$  is concentration of non-equilibrium (minor) electrons,  $\tau_n$  is lifetime,  $\Delta n$  is difference between the concentrations of non-equilibrium and equilibrium electrons,  $D_n(x)$  is diffusion coefficient,  $\mu_n$  is mobility,  $E(x)$  is intensity of electric field induced by the impurity uneven distribution in the base.

The electron lifetime dependence on the radiation dose is defined as [3]:

$$\frac{1}{\tau_\Phi} = \frac{1}{\tau_0} + k_\tau \Phi, \quad (2)$$

where  $\tau_0$  is the initial lifetime,  $\tau_\Phi$  is the irradiated lifetime,  $\Phi$  is the absorbed radiation dose,  $k_\tau$  is the radiation factor depended on the type and energy of radiation. In [2],  $k_\tau$  is calculated for the 0.2 – 5 MeV electron and 1.4 MeV neutron radiation.

The model details, difference approximation of (1), border conditions and numerical solution [4] are presented in [5]. The software (Fig. 1) was developed. Results are shown in Fig. 2 - 3.

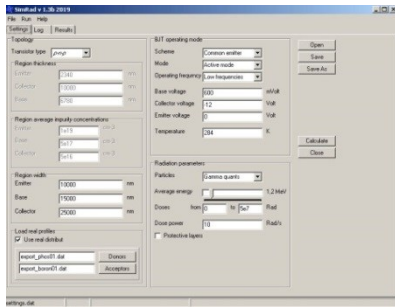


Figure 1. Control panel

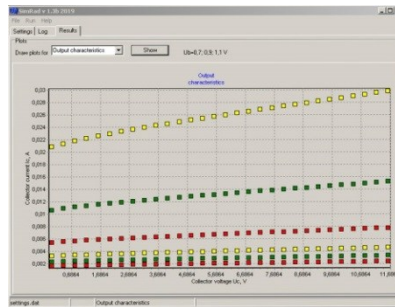


Figure 2. Output characteristics

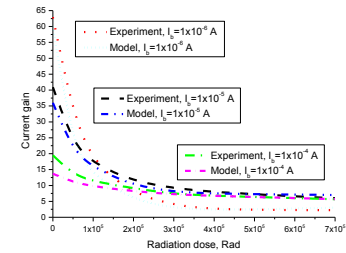


Figure 3. Current gain

### III. CONCLUSIONS

Calculated results demonstrate the significant fall of BJT characteristics that is confirmed experimentally.

### REFERENCES

- [1] A.N. Belous, V.A. Solodukha, S.V. Shvedov, "Space electronics", Moscow, Technosfera, 2015.
- [2] E. Vologdin, A. Lysenko, "Radiation resistance of the bipolar transistors", Moscow, 2000.
- [3] K. Zejeger, "Physics of semiconductors", Moscow, 1977.
- [4] A. Samarskij, "Theory of difference schemes", Moscow, 1989.
- [5] S.A. Miskiewicz, A.F. Komarov, F.F. Komarov, G.M. Zayats, S.A. Soroka, "Radiation degradation of bipolar transistor current gain", Acta Physica Polonica, Vol. 132, pp. 288–290, 2017.

## THE EFFECT OF THE ELECTROMAGNETIC RADIATION WAVELENGTH ON THE NEAR-FIELD CHARACTERISTICS OF FINITE-LENGTH DIELECTRIC CYLINDERS

V. Kovtun-Kuszhel, M. Bachko, Ya. Drobatau  
Yanka Kupala State University of Grodno, Belarus

[vkovtun@grsu.by](mailto:vkovtun@grsu.by)

### I. INTRODUCTION

Numerical studies of the near and internal fields distribution (NFD and IFD) for a single dielectric cylinder of finite length are necessary in order to identify the prerequisites for electrodynamic interaction in systems of such particles. The study of the dependence of the NFD and IFD of single cylinders on the wavelength of electromagnetic radiation at constant values of the dielectric permittivity of the cylinders, their environment and dimensions was carried out [1].

### II. METHOD AND RESULTS

Numerical studies were carried out for direct systems. Direct systems are understood as structures for which the refractive index of the cylinders exceeds the refractive index of the environment on the base of the volume integral equation formalism.

Figure 1 shows the distributions of the inner and near fields in the central sections of a single cylinder, which is located in the field of a plane electromagnetic wave propagating along the OZ axis, having an amplitude of

$E_0 = 1$  and polarized along the OY axis. Note that the mapping of the internal field distribution is obtained in the planes defined by the partition grid, which corresponds to the number of partitions used. Therefore, it is usually possible to get the NFD and IFD not in the exact geometric center of the cylinder, but only near this exact center. In this paper, a cylinder with a refractive index  $n = 1.73$  is presented. The geometric dimensions of the particle were:  $d=100\text{nm}$ ,  $l=1500\text{nm}$ . The wavelength of electromagnetic radiation is  $600\text{nm}$ . The sections ZOY, ZOY, YOZ are considered. The value of the maximum intensity gain is  $k_{\max}=0.86$ .

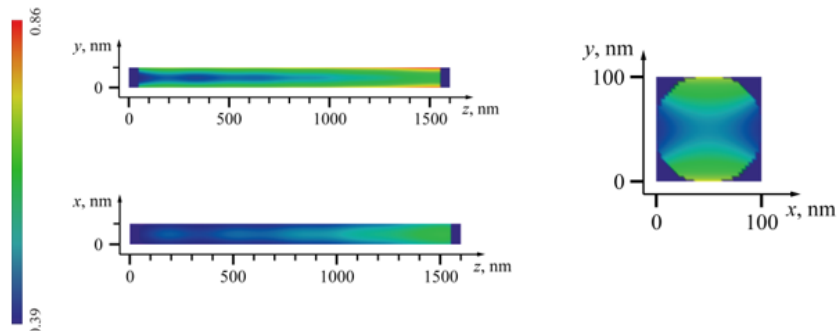


Figure 1. NFD and IFD for a single cylinder with  $n=1.73$  and  $\lambda=600\text{nm}$

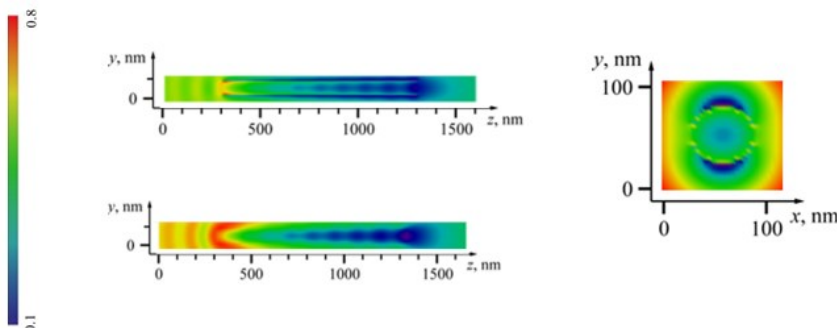


Figure 2. NFD and IFD for a single cylinder with  $n=1.73$  and  $\lambda=400\text{nm}$

Comparing Figures 1 and 2, it can be observed that, with a decrease in the wavelength of electromagnetic radiation from  $600\text{ nm}$  to  $400\text{ nm}$ , the NFD and IFD change. Namely, for  $\lambda = 600\text{nm}$ , the non-monotonic change in the intensity of the field along the entire length of the cylinder is much weaker than for  $\lambda= 400\text{nm}$ . There are also field intensity modulations along the length of the cylinder, attenuating along the direction of propagation of electromagnetic radiation. The modulation of the internal field in the cylinders is more pronounced, the shorter the wavelength of electromagnetic radiation.  $k_{\max}$  is also reduced to  $0.8$ .

### III. CONCLUSIONS

In this paper, we conducted a comparative study of the NFD and IFD was carried out for individual dielectric cylinders with  $n = 1.73$  with a change in the wavelength of electromagnetic radiation.

### REFERENCES

- [1] V.A. Kovtun-Kuszhel, R.A. Dynich, A.N. Ponyavina. Localization and scattering of electromagnetic waves in ordered arrays of finite cylinders / Problems of mathematics, physics and technics. №2(11). – pp.27 – 33, 2012.

## EFFECT OF THERMAL TREATMENT ON THE ELECTRICAL AND PHOTOVOLTAIC CHARACTERISTICS OF METHYLAMMONIUM LEAD TRIIODIDE PEROVSKITE FILMS

I. Vrublevsky<sup>1</sup>, A. Tuchkovsky<sup>1</sup>, N. Lushpa<sup>1</sup>, Pham Gia Vu<sup>2</sup>, Tran Dai Lam<sup>2</sup>

<sup>1</sup> Belarusian State University of Informatics and Radioelectronics, Minsk, Belarus

<sup>2</sup> Institute for Tropical Technology Vietnam Academy of Science and Technology, Hanoi, Vietnam

[lushpa@bsuir.by](mailto:lushpa@bsuir.by)

### I. INTRODUCTION

Recently, many new technologies for solar cells have appeared that make solar energy even cheaper. One promising direction is the use of photovoltaic converters based on organometallic perovskites, the use of

which promises to solve the whole range of complex problems, combining, ultimately, low manufacturing cost and high conversion efficiency [1,2].

The perovskite semiconductor triiodide methylammonium lead ( $\text{CH}_3\text{NH}_3\text{PbI}_3$ ) has a high carrier mobility and a long carrier lifetime. It allows light to generate electrons and holes that can move far enough to reach electrodes and generate current in an external circuit, rather than participate in recombination processes with energy loss in the form of heat. The energy zones of the perovskite photoconversion structure ensure the separation of charge carriers generated by absorption of photons (Figure 1).

In the process of creating solar cells based on organometallic perovskite, it is important to choose such modes of perovskite layer formation, which ensure obtaining the minimum electrical resistance and a high level of photocurrent. Analysis of the literature showed that the formation of the surface morphology of perovskite films with a uniform grain structure meets such requirements in the first place.

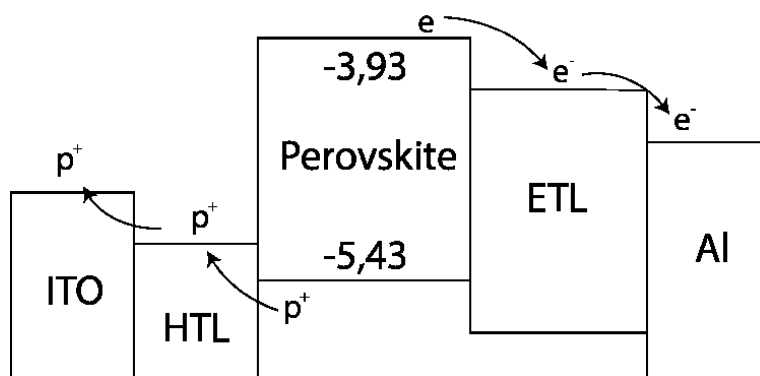


Figure 1. Zone diagram of a perovskite photoconverter structure

The effect of annealing temperature in the range from 80 to 150 °C on the surface morphology and photoelectrical characteristics of perovskite films, both after annealing and after solvent application to the perovskite film, was investigated. N-methylpyrrolidone was used as the solvent for application to the perovskite film.

## II. RESULTS AND DISCUSSION

According to the results of optical investigations the crystal sizes after the application of the film of organometallic perovskites at 80, 90, 100 and 110 °C were determined and their values were 8.2x9.6, 9.3x11.0, 15.1x17.8 and 11.7x13.4  $\mu\text{m}$  respectively. It was found that after treatment with solvent at temperature the film becomes more uniform and pronounced round-shaped germs can be seen on the surface. The dimensions of such germs were 10.3x12.3, 15.9x16.7 and 16.4x17.8  $\mu\text{m}$  after solvent treatment at 80, 90 and 100 °C, respectively. The results of the measurements show that the germs sizes are larger than the crystals of organometallic perovskites. This indicates that the resistivity of such films will be lower than before the solvent treatment. This effect can be explained by a decrease in the number of interfaces that act as defects, which leads to a decrease in resistivity. It was found that the temperature treatment at 110 °C formed an almost completely uniform surface morphology of the perovskite film without germs formation. Organometallic perovskite film with such morphology makes it possible to create the most efficient solar cells with a maximum photocurrent of 270  $\mu\text{A}$  and higher.

Samples with higher temperature treatment were also investigated: 120, 130, 140 and 150 °C. According to the results of the studies, the crystal sizes after applying the film of organometallic perovskites at 120, 130, 140 and 150 °C were determined, which were 32.9x50.7, 31.5x67.0, 29.3x34.3 and 6.9x8.2  $\mu\text{m}$ , respectively. It was found that the size of crystals increased with increasing temperature and only at  $T = 150$  °C crystals significantly decreased in size. This effect was explained by the fact that the thermal influence becomes so large that the atoms become very mobile and, as a result, they cannot form crystals of larger size. After this solvent treatment, even more germs are formed in the film compared to the lower treatment temperature. However, this can have an undesirable effect on the resistance of the films and the final quality of the solar cell. It is shown that solar cells based on such perovskite films are the least efficient and show a photocurrent of 5 to 20  $\mu\text{A}$ .

## III. CONCLUSIONS

As a result of studies it was found that the most optimal treatment temperature of perovskite films based on  $\text{CH}_3\text{NH}_3\text{PbI}_3$  is 110 °C. Films obtained at this temperature have a uniform morphology and relatively low resistivity.

## ACKNOWLEDGMENTS

This work was supported by the State Committee on Science and Technology of the Republic of Belarus (project № F21VTNG-001) and Ministry of Science and Technology of Vietnam.

## REFERENCES

- [1] J.Y. Kim, J-W. Lee, H.S. Jung, H. Shin, N-G. Park, High-Efficiency Perovskite Solar Cells / Chemical Reviews, Vol 120(15), pp. 7867–7918, 2020.
- [2] Y. Chen, L. Zhang, Y. Zhang, H. Gao, H. Yan, Large-area perovskite solar cells – a review of recent progress and issues / RSC Advances, Vol. 8(19), pp. 10489–10508, 2018.

## STUDY OF PHOTONIC NANOJETS IN THE DIFFRACTION WAVE FIELDS OF COMPLEX-SHAPE DIELECTRIC PARTICLES

A. S. Rudnitsky, N. N. Poleschuk  
Belarusian State University, Minsk, Belarus

[polestchuk@bsu.by](mailto:polestchuk@bsu.by)

### I. INTRODUCTION

In diffraction fields of dielectric particles, with the dimensions of the wavelength order, the areas formed in their vicinity are characterized by the increased intensity of the wave field, with a subwavelength size of the photon flux, called the photonic nanojets. This feature is of particular importance for practical applications in nanophotonics, biology, medicine, nanoelectronics, and data storage systems [1].

### II. METHODS AND RESULTS

Based on a rigorous solution of the two-dimensional wave field diffraction problem for the dielectric cylinder, the structure of photonic nanojets has been investigated. The dielectric permeability of the cylinder material is equal to 2 and that of the environment to 1. The section dimensions at wavelengths are equal to  $1 \leq x \leq 2, 1 \leq z \leq 2$ . It has been established that, on propagation of the exponential flat wave along the diagonal of the square, the increased intensity area of the wave field is formed near the angle vertex from the outer side of the surface, i.e., at the edge of the surface. Maximal excess of the intensity for the incident wave is approximately equal to 4. When deviation of the particle shape from the regular one is minor, as shown in the figure, a decrease in the cross-sectional size of a photonic jet is observed. Further improvement of the photonic jet parameters is achieved by exposing the dielectric particle to superposition of two flat waves and we have

$$u_0(x, z) = \cos[k\sin\gamma(x\sin\vartheta - z\cos\vartheta)] \times \exp[-ik\cos\gamma(x\cos\vartheta + z\sin\vartheta)]$$

A peak intensity of the diffraction wave field exceeds the intensity of the incident wave field by more than a factor of seven. The figure shows the geometrical shape of a particle and the two-dimensional distributions of a relative intensity of the diffraction wave field ( $B(x, z) = |u(x, z)|^2 / |u_0(0, 0)|^2$ ), inside and outside the particle at a wavelength distance from the surface ( $1 \leq x \leq 3, 1 \leq z \leq 3$ ) as well as at the diagonal normalized to the wavelength  $l$ , where  $\vartheta = \pi/4, \gamma = \pi/8$ .

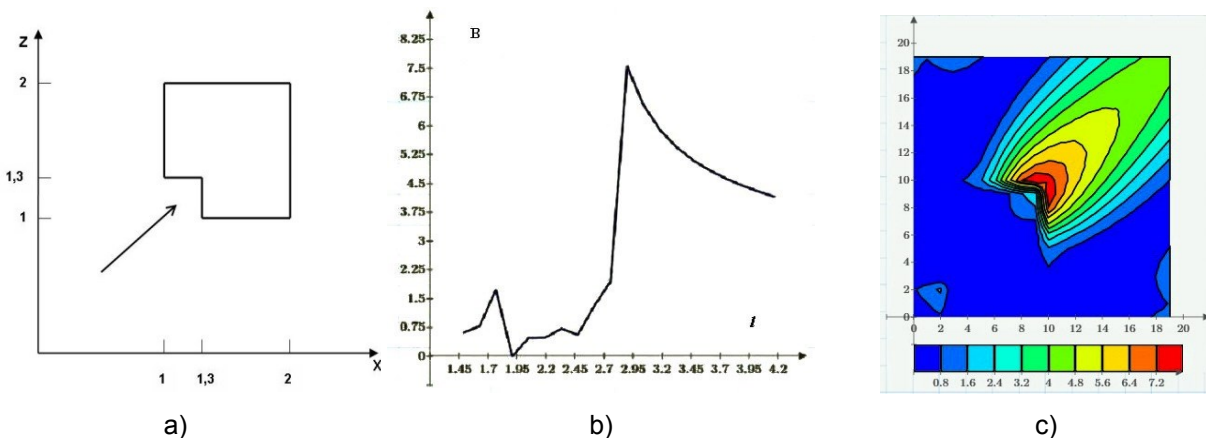


Figure 1. The geometrical shape of particle (a), the diagonal (b) and two-dimensional (c) distributions of a relative intensity of the diffraction wave field inside and outside the particle at a wavelength distance from the surface

### III. CONCLUSIONS

When deviation of the particle shape from the regular one is minor a decrease in the cross-sectional size of a photonic jet is observed. Further improvement of the photonic jet parameters is achieved by exposing the dielectric particle to superposition of two flat waves. A peak intensity of the diffraction wave field exceeds the intensity of the incident wave field by more than a factor of seven.

### REFERENCES

[1] Heifetz A., Kong S.-C., Sahakiana A. V., Taflove A., Backman V. "Photonic Nanojets" J.Comput. Theor. Nanosci., V.6, № 9. pp. 1979–1992, 2009.

## PHOTOSENSITIVE PROPERTIES OF AVALANCHE LEDs BASED ON NANOSTRUCTURED SILICON

S. Lazarouk, U. Dudzich, A. Klyutsky, A. Dolbik, V. Labunov

Belarusian State University of Informatics and Radioelectronics, P. Browka 6, 220013 Minsk, Belarus

[serq@nano.bsuir.edu.by](mailto:serq@nano.bsuir.edu.by)

### I. INTRODUCTION

Avalanche LEDs have attracted the attention of scientific community due to their fast time response (less than 1 ps). It allows to use avalanche LEDs for optical interconnects in silicon chips and between silicon chips. In this case avalanched LEDs can be used as light sources as well as light detectors [1]. We have studied the photosensitive properties of avalanched LEDs in this work.

### II. RESULTS AND DISCUSSIONS

The photosensitive properties have been measured in avalanche LEDs fabricated by the technology described in [2, 3]. The photocurrent and photovoltage responses have been registered at light exposition from the neighbor LED. Figure 1-a shows the photocurrent in investigated diodes versus light power of neighbor diodes. Photocurrent was measured at diode bias 1V and for different temperatures. Figure 1-b shows the photovoltage versus light power of the neighbor LED at different temperatures. The low temperatures are more attractive for diode operation. Thus the developed avalanche diodes can operate as a light source at bias more than avalanche breakdown voltage as well as photodetectors or photovoltage cells at bias less than avalanche breakdown voltage.

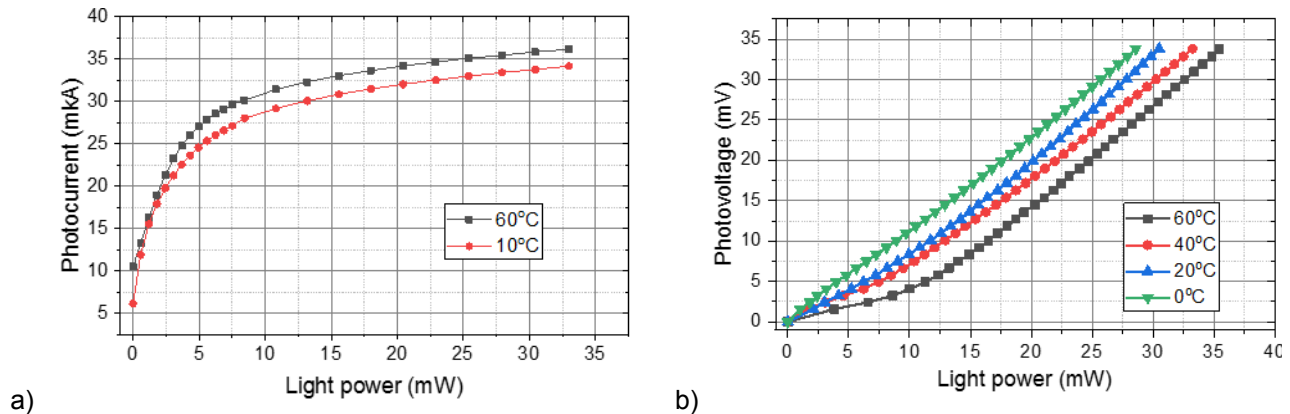


Figure 1. Photocurrent (a) and photovoltage (b) in investigated diodes versus external light power

### III. CONCLUSIONS

The performed studying showed the perspective of avalanche LED applications for light signal processing in silicon photonics [4, 5].

### ACKNOWLEDGMENTS

This work was supported by the Project No. T20KITG-011 of BRFFR.

### REFERENCES

[1] S. Lazarouk, A. Leshok, T. Kozlova, A. Dolbik, Le Dinh Vi, V. Ilkov, V. Labunov, "3D Silicon Photonic Structures Based on Avalanche LED with Interconnections through Optical Interposer" International Journal of Nanoscience, Vol. 18., № 3-4, pp. 1940091(1-4), 2019.



- [2] S. Lazarouk, A. Leshok, A. Dolbik, Le Dinh Vi, A. Klyutsky, "Influence of anodic alumina used as separating dielectric of silicon avalanche LEDs on diode characteristics", Doklady BGUIR, № 7-8(126), pp. 165-172, 2019.
- [3] S. Lazarouk, A. Leshok, A. Dolbik, Le Dinh Vi, S. Perko, "Avalanche LEDs based on nanostructured silicon for optical interconnections", Doklady BGUIR, № 18(3), pp. 63-71, 2020.
- [4] S. La Monica, G. Maiello, A. Ferrari, G. Masini, S. Lazarouk, P. Jaguiro, S. Katsouba, "Progress in the field of integrated optoelectronics based on porous silicon", Thin Solid Films, Vol. 297., pp. 261-264, 1997.
- [5] S. Lazarouk, A. Leshok, V. Borisenko, C. Mazzoleni, L. Pavesi, "On the Route Towards Si-based Optical Interconnects", Microelectronic Engineering, Vol. 50., № 1-4, pp. 81-86, 2000.

## NON-STATIONARY ELECTROLYSIS FOR NICKEL NANOCOMPOSITE PLATING

L. Kushner, I. Kuzmar

Belarusian State University of Informatics and Radioelectronics, Minsk, Belarus

[kushner@bsuir.by](mailto:kushner@bsuir.by)

### I. INTRODUCTION

The results of studies of the electrochemical processes of the formation of nanostructured thin-film nickel-based coatings modified with ultradispersed carbon aggregates under conditions of non-stationary electrolysis are generalized.

The inclusion of dispersed materials in the metal matrix during the formation of composite electrochemical coatings (CEC) makes it possible to increase the physicomechanical, functional and protective properties of coatings. An increase in the level of dispersion of the hardening phase and the use of nanoparticles for modifying metal coatings contributes to a decrease in the porosity and roughness of precipitates, an increase in the uniformity of the distribution of particles, the hardness and wear resistance of the coatings due to dispersion hardening and the stability of the electrolyte-suspension, in which the dispersed phase practically does not sediment.

The effect of the dispersed phase, parameters of non-stationary electrolysis and ultrasonic (US) on the electrodeposition process and the properties of nanocomposite nickel coatings has been investigated.

### II. RESULTS AND DISCUSSION

Electrodeposition of nickel-based CEC was carried out in Watts sulphate electrolyte modified with ultradispersed carbon aggregates: ultradispersed diamond (UDD), fullerenes (C60), nanotubes (CNT) at a constant and periodic current with a frequency of 0.1-1000 Hz when exposed to ultrasonic (US) frequency 35 kHz and intensity 0.2-1.5 W/cm<sup>2</sup>. Ultrasound has been used both to disperse and deagglomerate particles in a plating bath and to improve the incorporation of well-dispersed and evenly distributed particles into a metal matrix.

It was found that the introduction of 0.1-10 g/L UDD and fullerenes into the nickel-plating electrolyte leads to the co-precipitation of nanoparticles with nickel with the formation of composite coatings with a dispersed phase content of 0.01-1.2 wt. % (Figure 1), which depends on its concentration in the electrolyte, the nature of the electrolyte, cathode current density, ultrasound intensity, and periodic current parameters. The large specific surface area of nanoparticles ensures their high absorption capacity, which facilitates the introduction of particles into the sediment and has a significant effect on the kinetics of deposition of nickel coatings, their structure and properties.

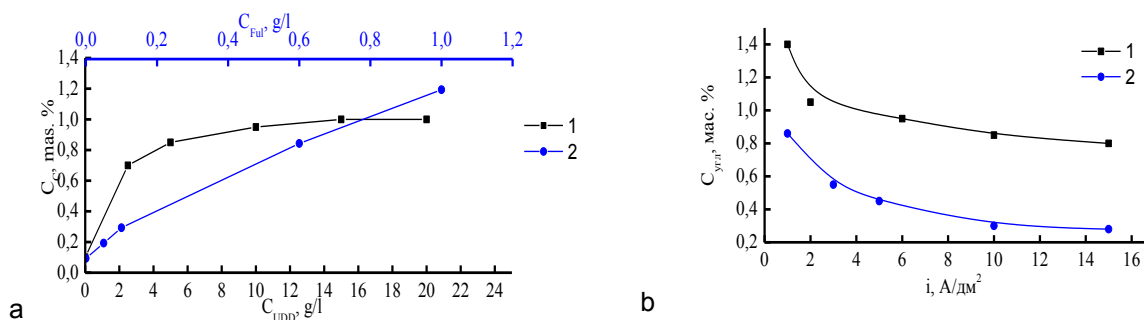


Figure 1. Dependence of the carbon content in the CEC of nickel-UDD (1) and nickel-fullerenes (2) on the concentration of the dispersed phase in the electrolyte (a) and current density (b)

The introduction of 0.01-0.1 g/l CNT into the electrolyte, previously ground and treated in a mixture of acids during high-power ultrasonic treatment, makes it possible to obtain composite coatings with a carbon content of 1-3 vol. % or 0.1-0.3 wt. %.

Dispersed phase nanoparticles, concentrating along the grain boundaries and preventing their growth, refine the CEC structure. Due to the adsorption of particles on nickel nuclei, the active nucleation centers are blocked, the growth rate of the latter decreases and, accordingly, nuclei appear on less active centers, i.e. the number of active centers increases and, as a consequence, the number of new nuclei increases.

A promising way, allowing a wide range of effects on the structure and physical properties of the resulting coatings, is the use of non-stationary electrolysis. The use of a periodic current of various shapes and parameters for electrolysis makes it possible to change the composition, structure and properties of the coatings in the desired direction within a relatively wide range, and it is easy to control the quality of deposited precipitates.

The use of a pulsed current makes it possible to obtain smoother fine-crystalline deposits with an isotropic developed microrelief, which can be explained by a high instantaneous current density and the nucleation of a large number of crystals, the growth of which is limited by the duration of the current pulse, with their subsequent passivation during a pause [1]. This creates conditions for the formation of nuclei at a new location on the cathode surface. Thus, a uniform grain size and fine-crystalline structure of coatings is formed, which depends on the parameters of the periodic current (Figure 2, DC – direct current, IC – impulse current, RC – reverse current).

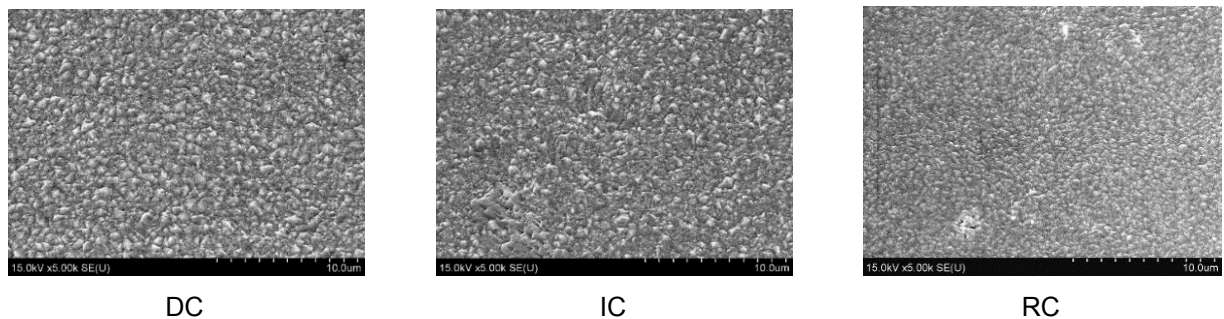


Figure 2. Influence of the current shape on the microstructure of nickel-CNT nanocomposites

The introduction of nanoparticles into the electrolyte makes it possible to significantly increase the microhardness (by 11-50%) due to a decrease in the grain size and precipitation hardening and wear resistance (by a factor of 1.05-3), to reduce the coefficient of friction of coatings without deteriorating their electrophysical and operational properties (Figure 3). Deposition under ultrasound increase the microhardness, wear and corrosion resistance CEC (Figure 4).

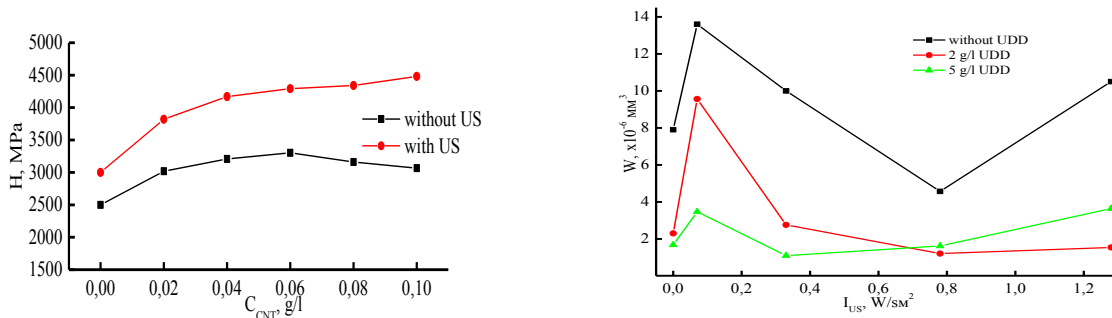


Figure 3. Influence of the dispersed phase concentration and ultrasound on the microhardness and wear resistance of the CEC

Depending on the parameters of the pulsed current, the microhardness of nanocomposite coatings increases to 3700-7000 MPa, wear resistance - by 1.5-3 times, the porosity of the coatings and the corrosion rate are significantly reduced (by 1.2-4 times).

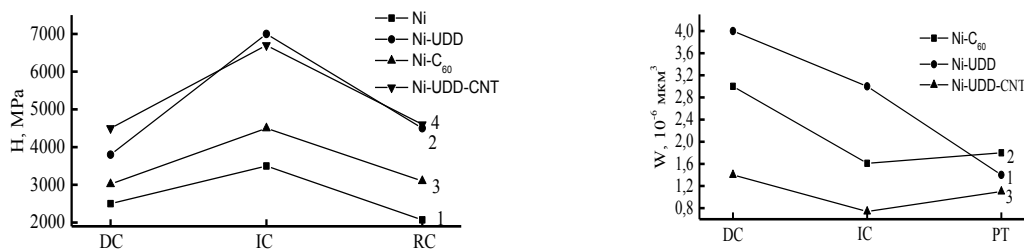


Figure 4. Influence shape current on the microhardness and wear resistance of the CEC,  $i_{av}=5 \text{ A/dm}^2$

### III. CONCLUSIONS

As a result of the studies carried out, it was found that the inclusion of a dispersed phase in the thin-film structures of nanoparticles, the variation of the parameters of the pulsed current and the intensity of ultrasound can significantly increase the operational properties of nickel coatings.

### REFERENCES

[1] Kushner, L.K. Nanocomposite nickel plating under non-stationary electrolysis / L.K. Kushner, I.I. Kuzmar, A.A. Khmyl, N.V. Dezkunov // *Nanoscience and Technology: An International Journal. Special Issue: Fullerenes and Nanostructures in Condensed Matter*, Vol. 10, Issue 4, 2019. – P. 355-363.

## MODIFICATION OF ANODIC ALUMINA BY LASER IRRADIATION DURING ANODIZING

A. Poznyak<sup>1</sup>, A. Kukhta<sup>2</sup>

1 Department of Electronic Technology and Engineering, Belarusian State University of Informatics and Radioelectronics, Minsk, Belarus

2 Laboratory of NanoElectroMagnetics, Institute for Nuclear Problems, Belarusian State University, Minsk, Belarus

[poznyak@bsuir.by](mailto:poznyak@bsuir.by)

### I. INTRODUCTION

Anodic oxide films of aluminum (AOFA) and other valve metals are promising materials for creation of functional materials [1, 2]. In the present work, irradiation of a pulsed N<sub>2</sub> laser was employed to possibly modify of morphological parameters and optical properties of porous alumina during the anodizing.

### II. MATERIALS AND METHODS

The initial experimental samples were 1.1 μm thick Al layers (99.99%) sputtered in vacuum on polished silicon plates. Anodizing was carried out in galvanostatic mode, in a stirred citric acid solution ( $j_a = 3.9 \text{ mA} \cdot \text{cm}^{-2}$ ) for 13 min. Temperature of the electrolyte was kept in the range of 20–22°C. Anodizing was carried out in a specialized PTFE electrochemical cell with a horizontal sample and a tantalum cathode and a protective ring, providing an anodization area of 1.54 cm<sup>2</sup>. The studied samples were irradiated during anodic polarization with a pulsed N<sub>2</sub> laser (LGI-21) with a Gaussian energy distribution through a quartz lens and directed normally to the sample and electrolyte surface. The laser beam had a wavelength of 337 nm, a pulse frequency of 100 Hz, a pulse duration of 10 ns, and an intensity of 5 kW.

Surface morphology and composition of the AOFAs was examined by scanning electron microscopy (SEM), Fourier transform infrared (FTIR) spectroscopy, and Auger electron spectroscopy (AES), respectively.

The samples surface was observed in a SEM Hitachi S-4800 operated at 10–15 kV, after over coating the specimens with a thermally evaporated 3 nm thick gold layer. AES surveys were registered using a PHI-660 spectrometer after 1 min sputtering of the specimen's surface layer with argon ions with an energy of 3 keV. FTIR spectra of AOFAs were registered with a Thermo Nicolet Nexus IR-spectrometer with a wave number range of 4000 cm<sup>-1</sup> to 400 cm<sup>-1</sup> and a resolution of 2 cm<sup>-1</sup>, after 128 scans using a Deuterated Tri Glycine Sulfate (DTGS) detector.

### III. RESULTS AND DISCUSSION

The optical image of the experimental AOFA sample and FTIR spectra are shown in Figure 1 a, b, respectively. As can be seen in Figure 1 a, the irradiated area looks lighter compared to the unirradiated area. It is noteworthy (Figure 1 b) that the IR transmittance of the AOFA in the irradiated area (curve 1) is also significantly higher than in the unirradiated area (curve 2).

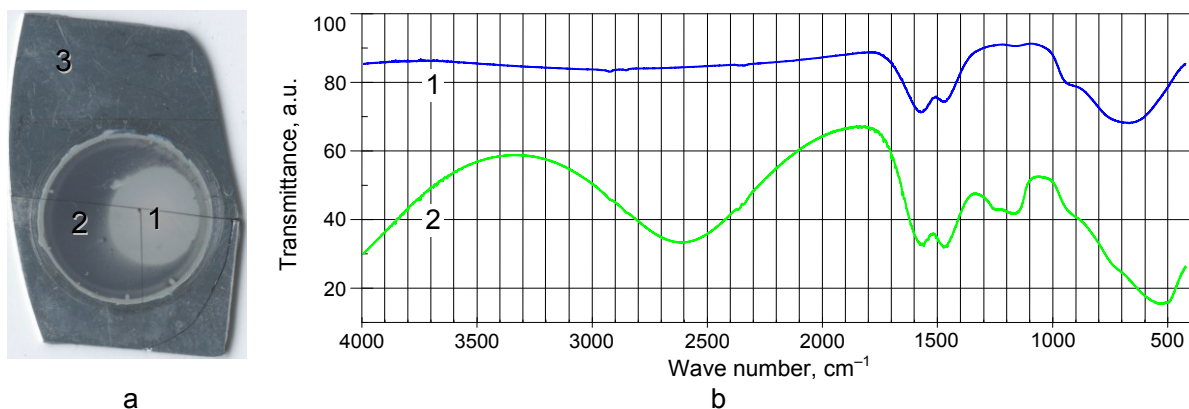


Figure 1. Optical image of the experimental sample: 1 — irradiated area, 2 — unirradiated area, 3 — unoxidized aluminum (a); FTIR-spectroscopy: curve 1 — irradiated area, curve 2 — unirradiated area (b)

As seen in Figure 1 b, the intensity of the absorption bands near  $1570$  and  $1470\text{ cm}^{-1}$ , which characterize the stretching vibrations of C-O, is markedly higher in the non-irradiated part (curve 2), which suggests a decrease in the incorporation of electrolyte derivatives in the presence of a high electric field into the structure of growing aluminum oxide. The wide absorption band in the  $1000\text{--}400\text{ cm}^{-1}$  range, due to the bending vibrations of Al-O, also becomes significantly more intense in the unirradiated area. Moreover, additional absorption bands at  $2750$ ,  $1250$ , and  $1150\text{ cm}^{-1}$  are detected in the IR spectrum of the non-irradiated oxide film. The identification of the new absorption bands is ambiguous.

Two assumptions arise: that these bands are due to nitrogen-containing groups, or the maximum in the region of  $2750\text{ cm}^{-1}$  may be due to the presence of C-H-groups. The final elucidation of the origin of the new bands is especially interesting if we consider that nitrogen could only be present in the anodizing electrolyte in the form of  $\text{N}_2$  dissolved from the atmosphere.

Figure 2 shows SEM images of experimental sample surfaces and AES surveys of sample surfaces. SEM images show no significant differences in the morphology of the both anodized surfaces. Auger-electron analysis revealed increased carbon content in the unirradiated area. At the same time, nitrogen was not detected. Consequently, we can attribute the detected absorption band in the region of  $2750\text{ cm}^{-1}$  to C-H-groups.

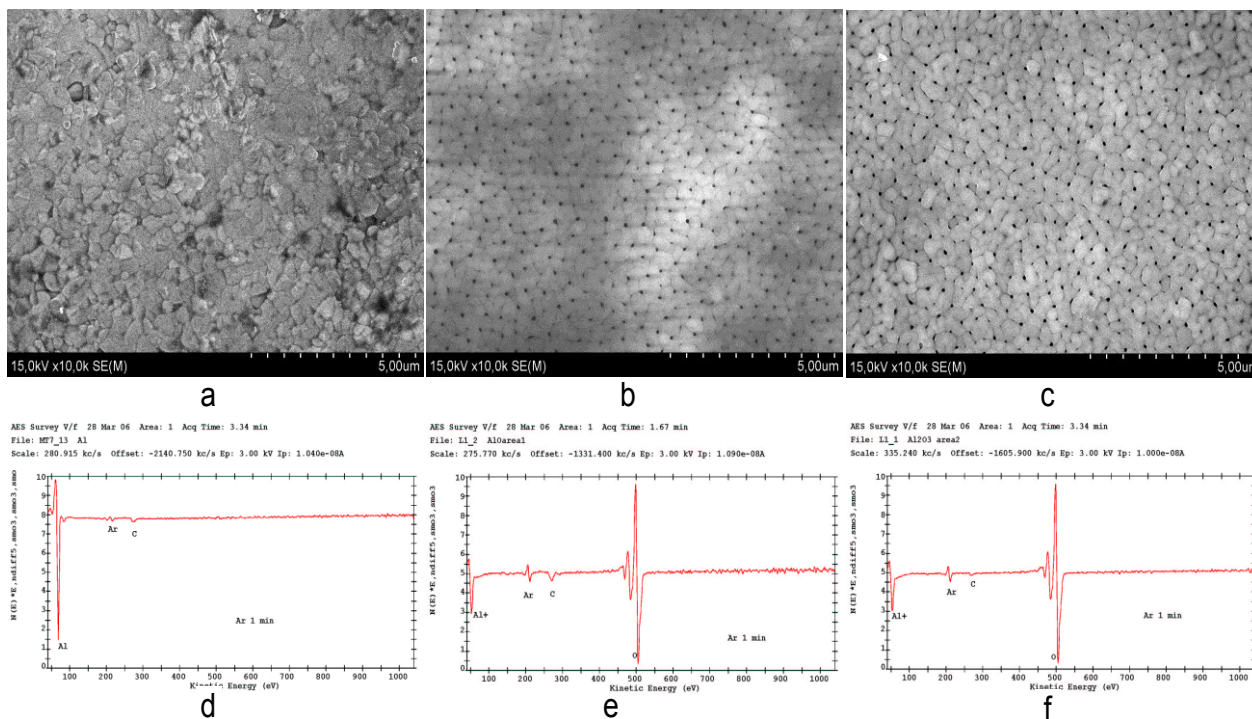


Figure 2. SEM images of experimental sample surfaces: unoxidized aluminum (a), unirradiated area (b), and irradiated area (c); AES surveys of sample surfaces after 1 min  $\text{Ar}^+$  sputtering: unoxidized aluminum (d), unirradiated area (e), and irradiated area (f)

#### IV. CONCLUSIONS

Irradiation with a pulsed N<sub>2</sub> laser beam employed during anodic oxidation of aluminum in a citric acid electrolyte was found to significantly affect optical properties of porous alumina oxide, providing no significant changes in its morphological parameters. The combination of anodizing and laser techniques enables it to modify functional properties of AOFA without introducing morphological defects.

#### ACKNOWLEDGMENTS

This work was partially supported by the state program for scientific research of the Republic of Belarus “Convergence 2025” (task 3.03.3), and by the Belarusian Republican Foundation for Fundamental Research, grant # T20PTĖ-006. The authors thank Researcher of Central European Institute of Technology BUT, Alexander Mozalev, for valuable discussions.

#### REFERENCES

- [1] A. Pligovka, A. Poznyak, M. Norek, “Optical Properties of Porous Alumina Assisted Niobia Nanostructured Films—Designing 2-D Photonic Crystals Based on Hexagonally Arranged Nanocolumns”. *Micromachines*, Vol. 12, p. 589, 2021. DOI:10.3390/mi12060589.
- [2] J. Santos, P. Araújo, Y. Pissolitto, P. Lopes, A. Simon, M. Sikora, F. Trivinho-Strixino, “The use of anodic oxides in practical and sustainable devices for energy conversion and storage”, *Materials*, Vol. 14, p. 383, 2021. DOI:10.3390/ma14020383.

### DENSITY FUNCTIONAL THEORY-BASED STUDY OF Cu<sub>2</sub>TiSnS<sub>4</sub> AND Cu<sub>2</sub>VSnS<sub>4</sub> FOR PHOTOVOLTAIC APPLICATIONS

A. Kistanov<sup>1</sup>, R. Botella<sup>1</sup>, E. Korznikova<sup>2</sup>, A. Smirnov<sup>3</sup>, S. Zhuk<sup>3</sup>

1 Nano and Molecular Systems Research Unit, University of Oulu, 90014 Oulu, Finland

2 Institute for Metals Superplasticity Problems, Russian Academy of Sciences, 450001 Ufa, Russia

3 Belarusian State University of Informatics and Radioelectronics, 6 P. Brovki str., Minsk, Belarus

[smirnov@bsuir.by](mailto:smirnov@bsuir.by)

#### I. INTRODUCTION

Cu<sub>2</sub>ZnSnS<sub>4</sub> (CZTS) is a promising earth abundant and non-toxic intrinsic p-type semiconducting material [1]. However, similar radii of Cu and Zn atoms facilitates formation of anti-site defects which degrade performance of CZTS solar cells [2]. Thus, there is need to find an alternative to Zn to reduce cation disordering. In the present work, we fully replace Zn atoms in CZTS by Ti and V atoms and study the effects of the substitution on the band structure and stability of the alternative kesterite material using density function theory (DFT) [3].

#### II. METHODS AND RESULTS

The calculations have been performed by Vienna Ab initio Simulation Package (VASP). It has been found that upon Zn substitution by Ti in CZTS its band gap ( $E_g$ ) decreases and shifts from direct to indirect compared to that of pristine CZTS (Fig. 1a-b). On the other hand, there is no  $E_g$  upon Zn substitution by V (Fig. 1c). The calculated binding energies of CZTS (10.16 eV), Cu<sub>2</sub>TiSnS<sub>4</sub> (11.23 eV) and Cu<sub>2</sub>VSnS<sub>4</sub> (11.52 eV) suggest high stability of the material after the Ti and V substitution.

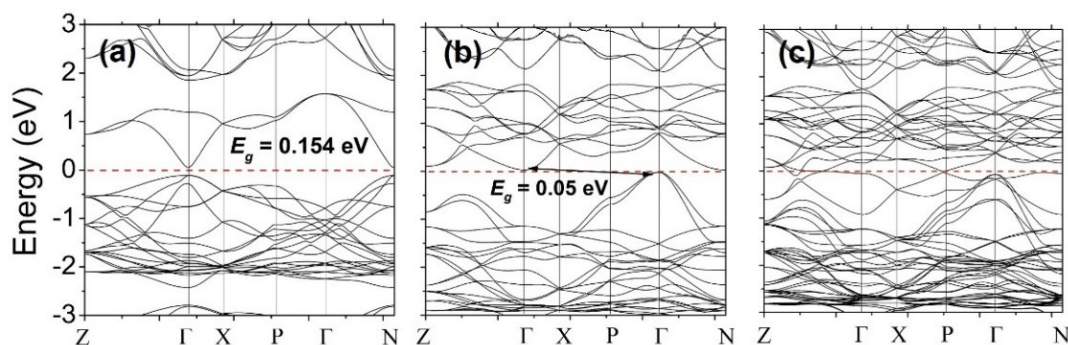


Figure 1. Band structure of (a) pristine CZTS, (b) Cu<sub>2</sub>TiSnS<sub>4</sub>, (c) Cu<sub>2</sub>VSnS<sub>4</sub>

#### III. CONCLUSIONS

In conclusion, Ti substitution enables to tune  $E_g$  and enhance thermodynamic stability of the material.

## ACKNOWLEDGMENTS

K.A.A. acknowledges Academy of Finland grant #311934 for the financial support. B.R. thanks funding from the European Research Council (grant agreement No. 101002219). K.E.A. acknowledges the financial support from the Russian Science Foundation grant No. 21-12-00275. The authors acknowledge CSC – IT Center for Science, Finland, for computational resources.

## REFERENCES

- [1] X. Liu, The current status and future prospects of kesterite solar cells: a brief review, Prog. Photovolt: Res. Appl. 2016, 24, 879-989.
- [2] S. Bourdais, Is the Cu/Zn disorder the main culprit for the voltage deficit in kesterite solar cells? Adv. Energy Mater. 2016, 6, 1502276.
- [3] A.A. Kistanov, Impact of various dopant elements on the electronic structure of Cu<sub>2</sub>ZnSnS<sub>4</sub> (CZTS) thin films: a DFT study, CrystEngComm. 2020, 22, 5786 – 5791.

## INFLUENCE OF RADIATION EXPOURE ON THE PROPERTIES OF DIELECTRIC LAYERS BASED ON ANODIC ALUMINUM OXIDE

S. Biran, D. Korotkevich, A. Korotkevich, K. Garifov, A. Dashkevich  
Belarusian State University of Informatics and Radioelectronics, 6 P. Brovki str., Minsk, Belarus

[biran@bsuir.by](mailto:biran@bsuir.by)

### I. INTRODUCTION

Anodic aluminum oxide films are widely used in various fields such as biomedical, nanophotonics, microelectromechanical systems and aerospace industry. In space, electronic equipment is exposed to various types of radiation including electrons, protons, neutrons and heavy ions. Devices with a high degree of integration can be sensitive to natural radiation even at the surface of the Earth. Radiation can affect electronic equipment, degrading performance and resulting in loss of data. Degradation of characteristics occurs due to the formation of electron-hole pairs in the gate and insulating dielectrics. Anodic aluminum oxide film shows good resistance to radiation because captures a significant number of electrons, which compensate for hole traps. In addition, Al<sub>2</sub>O<sub>3</sub> has several levels of traps in the band gap, which facilitates easy tunneling of electrons from the dielectric to the substrate [1]. Exposure by medium energy hydrogen and helium ions can lead to delamination of the anodic alumina film. Oxide delamination is caused by residual stresses resulting from oxide growth and irregularities in the substrate [2]. The effect of radiation exposure on thin-film structures depends not only on the chemical composition of the films, but also on mechanical stresses at the interfaces. In order to increase the radiation resistance of thin-film structures based on Al<sub>2</sub>O<sub>3</sub>, it is necessary to improve the technology of forming the interface between layers.

### II. EXPERIMENT

The study of the effect of radiation on the dielectric properties of anodic aluminum oxide films was carried out using capacitor structure in which aluminum base was used as the lower plate and sprayed contact pad as the upper plate. Aluminum 1 mm thick was used as a material for the test structures. Anodizing was carried out in a solution based on oxalic acid with constant stirring of the electrolyte in a galvanostatic mode. The electrolyte temperature was maintained at 15°C. The thickness of the obtained anodic oxide films of aluminum was 60 μm. 1 μm thick aluminum film was deposited on the surface of the anodic aluminum oxide. Electric capacitance of the samples was measured using an R, L, C meter at a frequency of 1 MHz. The temperature dependence of alumina substrates was studied in a helium cryostat in the range from 4 to 300 K. After measuring the temperature dependence of the electrical capacitance of unirradiated samples, they were irradiated with α-particles with energy 5 MeV from source <sup>239</sup>Pu with dose 3,1·10<sup>14</sup> sm<sup>-2</sup>. Measurement was repeated after irradiation. Temperature dependence electrical capacity of samples before and after irradiation presented on figure 1.

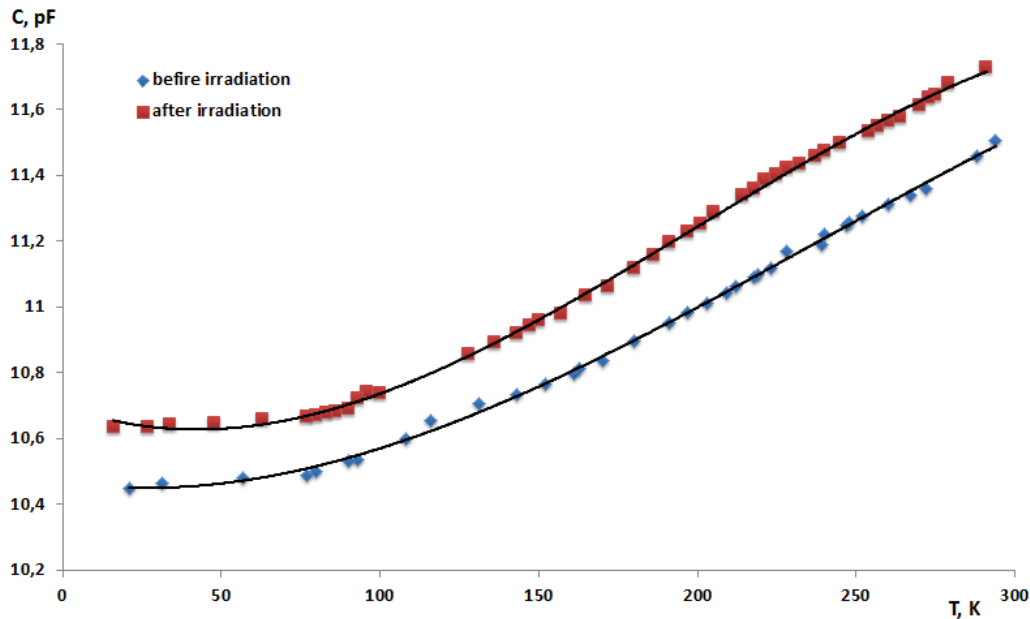


Figure 1. Temperature dependence electrical capacity of samples before and after irradiation with  $\alpha$ -particles

### III. CONCLUSIONS

Temperature dependence of the electrical capacitance for unirradiated and irradiated samples has the same form in the entire temperature range. This indicates the absence of any significant changes in the internal structure of the investigated dielectric layers. Quantitative differences in the capacity of unirradiated and irradiated samples are 2%, formation of radiation defects in a dielectric leads to a decrease in its dielectric constant. Taking into account the high ionizing ability of  $\alpha$ -particles, their high energy, it can be concluded that capacitor structures are resistant to this radiation effect.

### REFERENCES

- [1] E. Harari, B.S.H. Royce, " Trap structure of pyrolytic Al<sub>2</sub>O<sub>3</sub> in MOS capacitors " Appl. Phys. Lett., Vol. 22, pp. 106-107, 1973.
- [2] Meng Li, De-Gang Xie, Evan Ma, Ju Li, Xi-Xiang Zhang, Zhi-Wei Shan " Effect of hydrogen on the integrity of aluminium–oxide interface at elevated temperatures", Nature Communications volume 8, Article number: 14564, 2017.

## OPTICAL PROPERTIES OF THIN METALLIC NANO-PATTERNED FILMS FOR DISPLAY APPLICATIONS

A. Hubarevich, Ya. Mukha, A. Smirnov

Laboratory for Information Display and Processing Units, Belarusian State University of Informatics and Radioelectronics, 6 P. Brovki, Minsk, Belarus

[hubarevich@bsuir.by](mailto:hubarevich@bsuir.by)

### I. INTRODUCTION

Transparent conductive films are a crucial component of many optoelectronic devices such as displays, solar cells, touch screens, and light-emitting diodes. To date, indium tin oxide (ITO) based TCFs dominate the electronics industry. But a high fabrication cost and non-flexibility of the ITO prevent its application in future generation devices. Among potential candidates such as graphene, polymers and zinc oxide, metallic nanowire and nanoporous layers demonstrate a large potential to replace the ITO [1-4]. Besides low fabrication cost, flexibility and stretchability, they surpass the optoelectronic performance of ITO. Here we demonstrate silver nanowire (AgNW) and nanoporous (AgNP) layers, which possess the transmittance up to 10% higher than ITO at 20 $\Omega$ /□ sheet resistance.

### II. METHODOLOGY

A commercial-grade simulator based on the finite-difference time-domain (Lumerical Solutions, Inc., <https://www.lumerical.com/products/fdtd-solutions>) method was used to perform the optical calculations. The incident light in the visible wavelength range from 400 to 700 nm was illuminated along Z axis. The periodic boundary conditions and perfectly matched layers were applied perpendicular to Z and X(Y) axes,

respectively. The ITO thickness was set to 100nm. The AgNW diameter and AgNP thickness were set to 30nm and their surface coverage was set to 90%. For more information about simulation, see our previous work [2-4].

### III. RESULTS AND DISCUSSION

Figure 1 shows the simulation model configurations of ITO, AgNW, AgNP and their transmission spectra. We selected the thickness, diameter and surface coverage to obtain  $20\Omega/\square$  sheet resistance for all three layers since this is a common indicator for most display applications. At the same time, the accepted transmittance is about 80% and ITO satisfies such parameter. AgNW outperforms this value and demonstrates the transmittance up to 90%, which is 10% higher than ITO. AgNP has almost the same superiority but in the wavelength range from 500 to 700nm and has slightly higher transmittance (up to 5%) from 400 to 500nm.

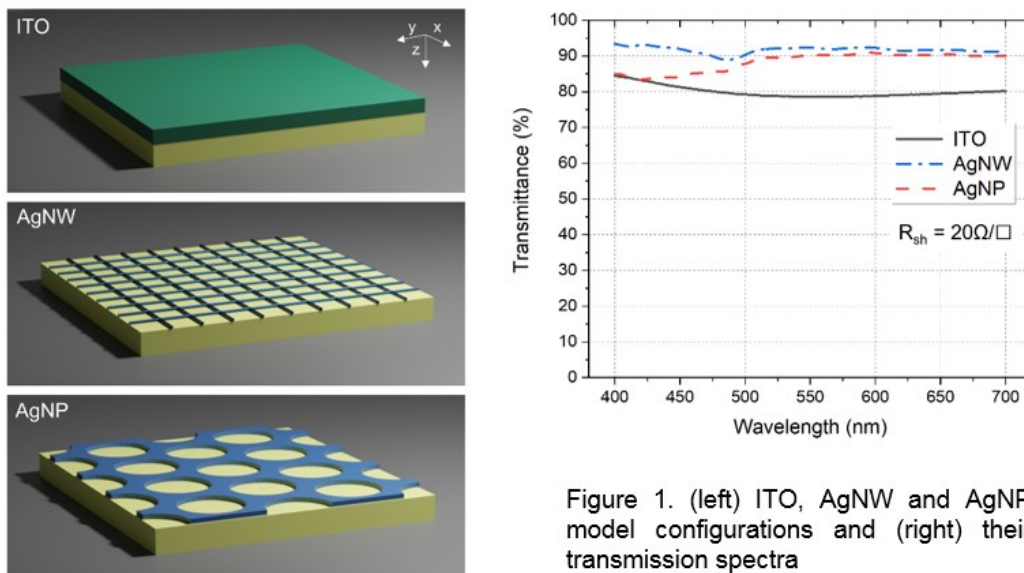


Figure 1. (left) ITO, AgNW and AgNP model configurations and (right) their transmission spectra

### IV. CONCLUSIONS

We investigated ITO, AgNW and AgNP as TCFs for display applications. AgNW and AgNP exceed the transmittance by 10% compared to ITO at  $20\Omega/\square$  sheet resistance. Considering this, AgNW and AuNP may become potential candidates to replace the ITO in the near future.

### ACKNOWLEDGMENTS

Authors would like to acknowledge the funding from State Programs of Scientific Research of the Republic of Belarus "Materials science, new materials and technologies" (2.17) and "Convergence-2025" (3.02.5)

### REFERENCES

- [1] P. Jaguiro, A. Stsiapanau, A. Hubarevich, Y. Mukha, A. Smirnov, "Self-organized nanostructured anodic oxides for displays applications", *Semicond. Phys. Quantum Electron. Optoelectron.*, Vol. 13, pp. 305-308, 2010.
- [2] M. Marus, A. Hubarevich, H. Wang, A. Stsiapanau, A. Smirnov, X.W. Sun, W.J. Fan, "Comparative analysis of opto-electronic performance of aluminium and silver nano-porous and nano-wired layers", *Opt. Express*, Vol. 23, pp. 26794-26799, 2015.
- [3] M. Marus, A. Hubarevich, W.J. Fan, H. Wang, A. Smirnov, K. Wang, H. Huang, X.W. Sun, "Optical haze of randomly arranged silver nanowire transparent conductive films with wide range of nanowire diameters", *AIP Advances*, Vol. 8, 035201, 2018.
- [4] A. Hubarevich, M. Marus, Y. Mukha, K. Wang, A. Smirnov, X.W. Sun, "Optoelectronic performance of AgNW transparent conductive films with different width-to-height ratios and a figure of merit embodying an optical haze", *AIP Advances*, Vol. 9, 045226, 2019.



# DEVELOPMENT OF THE LIBRARY FOR 3D MODELING AND COMPUTER-AIDED DESIGN OF PLATED KNITTED FABRICS

D. Bykouski, A. Charkovskij  
Vitebsk State University of Technology, Vitebsk, Belarus

[denisbykouskij@yandex.ru](mailto:denisbykouskij@yandex.ru)

## I. INTRODUCTION

3D technologies and computer-aided design (CAD) systems are used in various fields of human activity. 3D modeling allows to estimate the physical properties, appearance and other characteristics of products before they are made. The use of CAD systems reduces product cost, and automates the production process.

The task of developing a program for 3D modeling and computer-aided design of knitted fabrics is relevant. The program should be able to automatically create 3D models of knitted fabrics made of different raw materials. The fabrics yarns can be of different linear densities. The program should be able to calculate the structure parameters of knitted fabrics.

## II. PROGRAM DEVELOPMENT

The program was developed as a library (external module) for CAD system KOMPAS-3D. The program algorithm is as follows:

- 1) allowing the user to select the stitch pattern of knitted fabric, raw material of yarns, linear density of yarns, set the number of courses and wales;
- 2) calculation of knitted fabric parameters based on the input data entered by the user;
- 3) connection to the KOMPAS-3D system installed on the user's computer;
- 4) opening of a base 3D model file in KOMPAS-3D system;
- 5) replacing the model variables with the new values calculated in step 2 and thus creating a new knitted fabric 3D model with custom parameters;
- 6) saving the new 3D model file to the hard drive;
- 7) display the calculated parameters of the knitted fabric on the screen;
- 8) allowing the user to save the values of these parameters to a text file.

The structure of knitted fabric is represented by a geometric model to facilitate the study and prediction of its properties. The geometric model approximates the actual knitted fabric structure and the shape of its loops with varying degrees of accuracy. The yarn thickness of the geometric model of the knitted fabric is the same in all parts of the loop. The cross-sectional shape of its yarn is a circle. The yarn thickness is averaged and characterized by the average diameter [1].

The program is able to work with 3D-models of double-layer plated knitted fabrics. In the process of development it was also necessary to implement the possibility to work with 3D models of single-layer plain knitted fabrics. Geometric models of these fabrics are shown in Figure 1 (a – single-layer plain knitted fabric; b – double-layer plated knitted fabric).

Plain knitted fabric (Fig. 1a) consists of loops of the same shape and size, formed one after another along a course. The loops of the plain knitted fabric are formed from a single yarn. The loops of the plated knitted fabric (Fig. 1b) are formed from two yarns: ground *a* and plated *b*. Plated yarn forms the face side 2 of the fabric. Ground yarn forms the backing side 1 of the fabric.

The first step in the development process was the creation of a basic parametric three-dimensional model of single-layer plain knitted fabric in the KOMPAS-3D system. The variables of the model were defined in the KOMPAS-3D system: *d* – yarn diameter; *A* – wale space; *B* – course space; *Columns* – number of wales; *Rows* – number of courses. Then, based on the described 3D-model, a basic parametric three-dimensional model of double-layer plated knitted fabric was built in the KOMPAS-3D system. The variables of the model were defined in the KOMPAS-3D system: *d1* – face side yarn diameter; *d2* – backing side yarn diameter; *A* – wale space; *B* – course space; *Columns* – number of wales; *Rows* – number of courses.

Creating of the visual interface was the next step in the development of the library. After that, program code was written to calculate the parameters of knitted fabric structure and rebuild the 3D model. The Embarcadero RAD Studio system and the C++ programming language were used for this purpose.

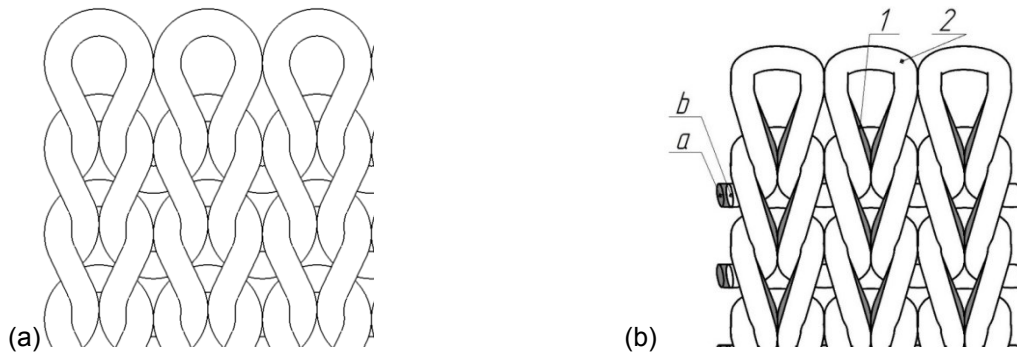


Figure 1. Geometric models of the knitted fabrics

The interface contains an element for selecting a knitted fabric structure (plain or plated), numeric fields for entering the linear density, elements for selecting the raw materials, a block with two numeric fields for entering the numbers of wales and courses, button "Build Model". Pressing the button launches the 3D model building process. Geometric parameters of knitted fabric structure are calculated in the program in accordance with [2]. Examples of 3D models built with the help of the library are shown in Figure 2 (a – single-layer plain knitted fabric; a – front view of the single-layer plain knitted fabric; b – side view of the single-layer plain knitted fabric; c – front view of the double-layer plated knitted fabric; d – side view of the double-layer plated knitted fabric).

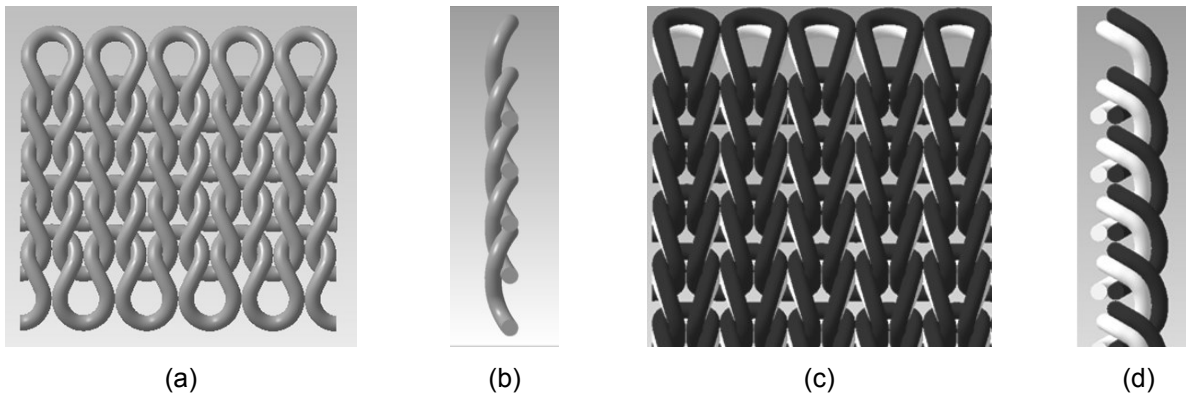


Figure 2. Geometric models of the knitted fabrics

### III. CONCLUSIONS

The library for 3D modeling and computer-aided design of single-layer plain knitted fabrics and double-layer plated knitted fabrics has been developed. It is advisable to use the library in the educational process to visually demonstrate to students the features of structure of knitted fabrics. The library was used by the authors in scientific research on the development of knitted fabrics with improved hygienic properties.

### REFERENCES

- [1] L. Kudryavin, I. Shalov, Fundamentals of knitting technology, Legprombytizdat, Moscow, Russia, p. 496, 1991.
- [2] A. Charkovskij, The basics of knitting processes, Vitebsk State Technological University, Vitebsk, Belarus, p. 165, 2005.

## DESIGN AND SIMULATION OF 3D MAGNETIC FIELD SENSORS WITH INTEGRATED MAGNETIC CONCENTRATOR

Dao Dinh Ha<sup>1</sup>, V. R. Stempitsky<sup>2</sup>

1 Le Quy Don Technical University, Ha Noi, Viet Nam

2 Belarusian State University of Informatics and Radioelectronics, Minsk, Belarus

[daodinhha@lqdtu.edu.vn](mailto:daodinhha@lqdtu.edu.vn)

### I. INTRODUCTION

Today, along with the strong development of the Internet of Things (IoT), new scientific directions are opening up, that is, the development and production of microelectronic sensor devices that combine

applications for controlling physical, chemical and biological parameters. Sensors used to measure magnetic field induction have a sensitivity and measurement range limited by the materials used, in addition, their main applications - measuring magnetic fields in a plane, applications in three-dimensional space have many limitations. Therefore, the study of the IC design of a magnetic field sensor in combination with the application of an integrated magnetic concentrator for three-dimensional magnetic field measurement is very relevant.

## II. DEVICE STRUCTURE

In this paper, the structure of magnetic field sensors based on high electron mobility transistors (HEMT, High Electron Mobility Transistor) and materials with large band gap GaN is studied. Conduct simulation of the characteristics and calculate the sensor sensitivity values at different polarization conditions. In addition, the sensor is built with a long guide channel for enhanced Hall geometry correction ( $G_H$ ) combined with a cone magnetic amplifier integrated with the sensor to improve the conversion factor.

Figure 1,a shows the structure of the sensor with the magnetic field components in space, where  $\varphi$  is the angle between the magnetic field component  $B_z$  placed perpendicular to the sensor surface and the effective magnetic field  $B$ . Under the influence of the magnetic field component  $B_z$  leads to a current difference between the drain electrodes  $D_1$  and  $D_2$  called the Hall current ( $I_H$ ) and is expressed by [1]:

$$I_H = \mu_H B_z (L/W) I_D G_H$$

where:  $\mu_H$  - Hall electronic mobility;  $B_z$  - magnetic field perpendicular to the sensor surface;  $L$ ,  $W$  - sensor length and width;  $I_D$  - drain current;  $G_H$  - Hall geometry correction factor, this is the ratio of the Hall voltage in an actual semiconductor wafer to an ideal Hall plate of infinite length.

The sensor current difference can be measured across the drains and the sensitivity of the sensor  $S$  is calculated according to the following expression:

$$S = \frac{|I_{D1} - I_{D2}| - I_{off}}{(I_{D1} + I_{D2})|B|} \times 100\%$$

where:  $I_{D1}$ ,  $I_{D2}$ : drain current;  $I_{off}$ : drain current difference in the absence of a magnetic field.

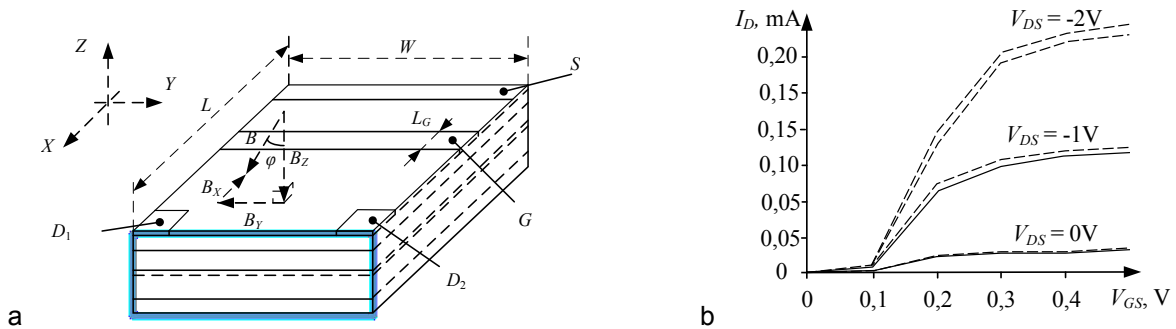


Figure 1. Simulation of the structure (a) and characteristics of the sensor (b)

Simulation of the structure of the Hall sensor with gate length  $L_G = 5 \mu\text{m}$ , sensor length  $L = 65 \mu\text{m}$  and width  $W = 20 \mu\text{m}$ . The distance between the drain electrodes is  $10 \mu\text{m}$ . Figures 1, b show the transfer characteristics of the sensor under the influence of a magnetic field perpendicular to the sensor surface with the value  $B = 25 \text{ mT}$  [3]. The output current from the two drain electrodes depends on the input voltage ( $V_{GS}$ ) representing the difference in the case of an external magnetic field acting perpendicular to the sensor surface. The relative sensitivity of the sensor obtained at the highest level is  $S = 15.21\%/T$  and the lowest is  $S = 5.69\%/T$  at  $V_{DS} = -2V$  and  $V_{DS} = 0V$ , respectively.

The structure of the magnetic amplifier consists of two cylindrical rods in the form of truncated cones with opposite pointed ends separated by a distance  $d$  (Figure 2). The angle between the truncated cone and its axis is denoted  $\omega$ , the length of each bar  $L$ , the clearance between the two rods  $d$  and the diameters of the large and small bases of the truncated cone are  $2R$  and  $2r$  respectively. The distance  $d$  is limited by the thickness of the Hall sensing element (approximately  $0.15 \text{ mm}$ ).

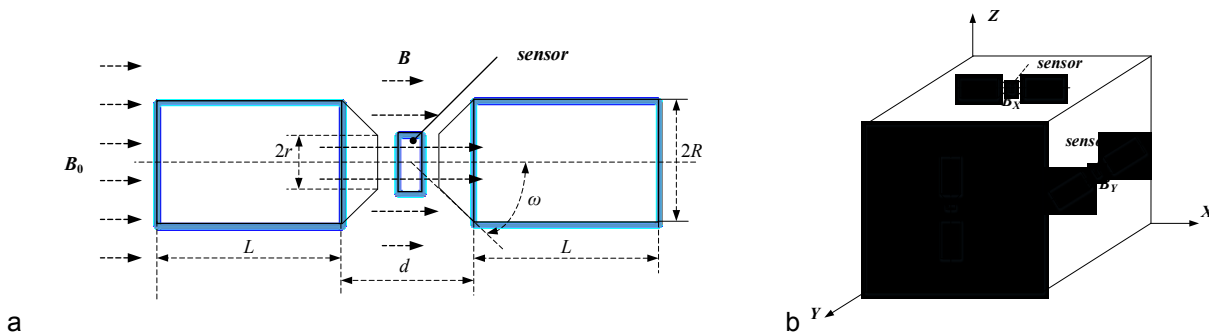


Figure 2. Structure of the integrated magnetic concentrator and 3D magnetic field sensor

Magnetic field gain  $K = B/B_0$ , this is the ratio between the magnetic field induction in the gap of the magnetic amplifier where the Hall sensor  $B$  is installed and the external magnetic field  $B_0$ , this is the main parameter of the magnetic amplification. The difficult problem is choosing the material and size for the magnetic amplifier for the magnetic field sensor, but it is important to establish the relationship and influence of the geometrical dimensions on the uniformity magnetic field perpendicular to the sensor surface, thereby providing design principles and sensor optimization [2]. The results by calculation show that with the length of each rod being 100 mm and the spacing 0.15 mm, a flux gain of about 400 times can be achieved.

Figure 2, b depicts the structure of a 3D magnetic field sensor combined with a magnetic field amplifier. Hall sensor probes  $0.3 \times 0.3 \times 0.15$  mm in size placed in planes in space, created on the basis of AlGaIn/GaN heterostructure with magnetic amplifier. These sensors are capable of calculating the components of the magnetic field along the coordinate axes in space.

### III. CONCLUSIONS

Study the structure and simulate the properties of Hall sensors based on the operation of high electronic mobility transistors using AlGaIn/GaN heterostructured materials. The simulation results show that the relative sensitivity of the sensor obtained at the highest level is  $S = 15.21\%/T$  at  $V_{GS} = -2V$ .

The simulation results contribute to the selection of the amplifier structure in combination with the Hall sensor to ensure the parameters of sensitivity and suitable measuring range. When using magnetic materials increases the gain and can reach a value of about 400 times.

Research on the structure of the 3D magnetic field sensor combined with a magnetic amplifier to increase the sensitivity and measuring range of the magnetic field, from which it is possible to apply the sensor in space for the weak magnetic field measurement range from  $0.01 \mu T$  to 2 mT.

### REFERENCES

- [1] Dao Dinh Ha, Stempitsky V. R. Investigation of the Hall Sensor Characteristics with Various Geometry of the Active Area // Nano- i Mikrosistemnaya Tekhnika.– 2018.– Vol.20, N 3.– P. 174–186. <https://doi.org/10.17587/nmst.20.174-186>.
- [2] Stempitsky V. R., Dao Dinh Ha. Device-technological simulation of the magnetosensitive sensor with integrated magnetic concentrator. Tekhnologiya i Konstruirovaniye v Elektronnoy Apparature, 2018, no. 3, pp. 15-21. <http://dx.doi.org/10.15222/TKEA2018.3.15>.
- [3] <http://www.silvaco.com>.
- [4] Meeker D. Magnetics Finite Element Method (femm). version 4.2 [Electronic resource]. Mode of access: <http://www.femm.info/wiki/HomePage> (date of access: 12.01.2016).

### SCHOTTKY BARRIER HEIGHT AND IDEALITY FACTOR OF CVD GRAPHENE/n-Si HETEROJUNCTION

A. Golovach<sup>1</sup>, N. Kovalchuk<sup>1</sup>, M. Mikhalik<sup>1</sup>, Y. Kukuts<sup>1</sup>, L. Dronina<sup>1</sup>, I. Komissarov<sup>1,2</sup>, S. Prischepa<sup>1,2</sup>  
<sup>1</sup> Belarusian State University of Informatics and Radioelectronics, P. Browka 6, 220013 Minsk, Belarus  
<sup>2</sup> National Research Nuclear University «MEPhI» Kashirskoe highway 31, 115409 Moscow, Russia

[komissarov@bsuir.by](mailto:komissarov@bsuir.by)

### I. INTRODUCTION

Due to high optical transparency and high charge mobility graphene emerges as a perspective material for transparent electrode in photodetectors. It made a new turn in using novel 2D materials in combination with

the standard silicon technology. From the electronic point of view, when an intimate contact between graphene and silicon is established the Schottky barrier is formed. According to the standard Schottky model the current through the heterojunction semiconductor/metal can be written as

$$\ln I = \ln I_0 - \frac{e}{\eta k T} V \quad (1)$$

where  $I_0 = AA^*T^2 e^{-\frac{\Phi_B}{kT}}$ ,  $k$  – Boltzmann constant,  $\Phi_B$  – barrier height,  $T$  – temperature,  $A$  – square of active area,  $A^*$  – Richardson constant ( $\approx 112 \text{ A cm}^{-2} \text{ K}^{-2}$ ),  $\eta$  – ideality factor. The barrier height together with the ideality factor are not universal parameters and depends on many aspects, including graphene doping level, transfer technology, the state of Si surface and so on. Moreover, these parameters are crucial for the performance of photodetectors based on graphene/Si heterojunctions.

## II. RESULTS

In this work we demonstrate the experimental IV characteristic of graphene/n-Si heterojunction and evaluate its barrier height and ideality factor.

For the device fabrication, graphene growth was performed through the atmospheric pressure chemical vapour deposition using methane as a precursor. After the growth graphene was transferred onto structured n-Si substrates with metallic contacts by a wet-chemical process without using polymeric frame. The sketch of the structure and the measurement scheme are shown in Fig.1. The IV characteristic of fabricated device measured in dark conditions is presented in Fig. 2. The experimental data follows the typical Schottky junction dependency. For the barrier height and quality factor evaluation the experimental dependency was replotted in  $\ln$  scale, see Fig 3. Following the standard Schottky model  $I_0$  and consequently, barrier height is extracted from the intersection of the linear fit (red line in figure 3) with  $I$  axis, whereas the ideality factor can be obtained from the slope of the linear fit. The fitting procedure leads to the following parameters: ideality factor  $\eta \approx 5$ , barrier height  $\Phi_B = 0,422 \text{ eV}$ .

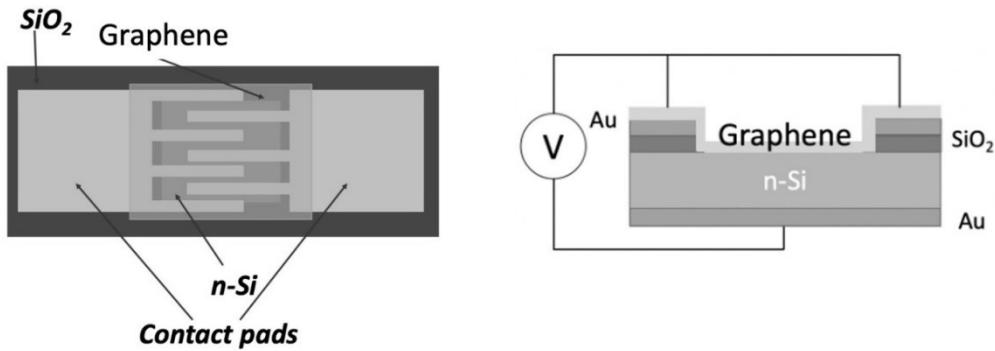


Figure 1. Top view of the structure (left) and measurement scheme (right) of the studied sample

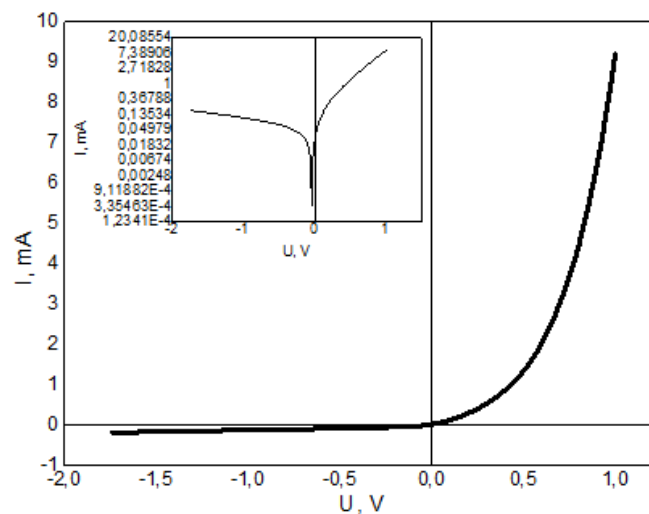


Figure 2. The experimental IV characteristic of the CVD graphene/n-Si heterostructure measured in dark conditions. The inset show the experimental data plotted in semi-log scale

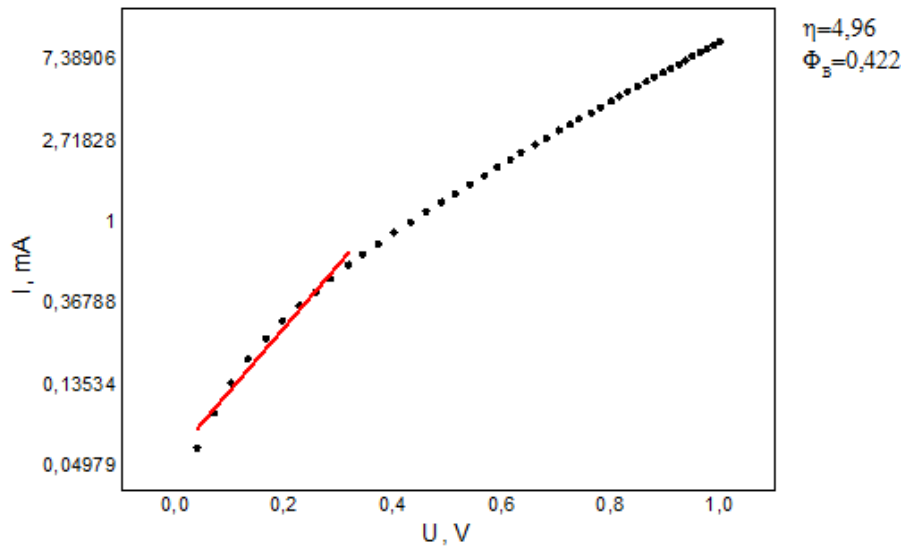


Figure 3. The positive part of experimental IV dependency plotted in ln scale, the red line represents the fitting to Schottky model (see the main text for more details)

The value of Si affinity (4.05 eV) together with the Schottky barrier height gives graphene work function  $\phi_{gr} \sim 4.5$  eV, what is in very good agreement with the values reported for graphene [1]. The ideality factor also agrees with the values which can be found in the literature [2].

### III. CONCLUSIONS

We fabricated and measured IV characteristic of CVD graphene/n-Si heterojunction. Based on the standard Schottky model ideality factor  $\eta \approx 5$  and barrier height  $\Phi_B = 0,422$  eV were extracted from the experimental data. Our results show the perspective of studied heterojunction for photodetection application.

### REFERENCES

- [1] S. Tongay, M. Lemaitre, X. Miao, B. Gila, B.R. Appleton, A.F. Hebard, "Rectification at graphene-semiconductor interfaces: zero-gap semiconductor-based diodes", *Phys. Rev. X*, Vol. 2(1). p. 011002, 2012.
- [2] H. Wong, M. A. Anwar, S. Dong, "Effects of silicon surface defects on the graphene/silicon Schottky characteristics", *Res. in Phys.*, Vol. 29, p. 104744, 2021.

## STUDYING THE INFLUENCE OF MICROBOLOMETER STRUCTURE AND GEOMETRY ON THE PARAMETERS OF INFRARED DETECTORS

Tran Van Trieu, I. Lovshenko, V. Sadchenko, V. Stempitsky  
 Belarusian State University of Informatics and Radioelectronics, Minsk, Republic of Belarus

[lovshenko@bsuir.by](mailto:lovshenko@bsuir.by)

### I. INTRODUCTION

The fields of application of thermal detectors are constantly expanding, for example in areas such as security, surveillance, fire fighting, biomedicine. A microbolometer based on a microbridge structure has an advantage over the other capabilities of IR detectors: it has low power, low cost, and can operate at room temperature [1-3]. The main requirements for thermosensitive materials used in microbolometers are high TCR ( $\alpha$ ), moderate resistivity, low noise, and compatibility with silicon (Si) integrated circuit (IC) technology. The most common materials are VOx, amorphous and polycrystalline silicon, and some metals [4-6]. The use of amorphous Si makes it possible to reduce the pixel size [7]. It is necessary that the sensing element of the IR sensor is thermally insulated. Various manufacturing processes have been proposed to reduce heat loss. The best thermal insulation and lowest thermal performance are obtained in microelectromechanical systems (MEMS) designs, which are used in Infrared Focal Plane Arrays (IRFPA) systems. Micromachining techniques are used to suspend the thermosensitive member of the substrate in a jumper shape to minimize heat loss due to conduction through the substrate. The structure and geometrical size affects the thermal performance of bolometer structures. In addition, the small pixel size requires a more complex mechanical and electrical design. In this article, special attention is paid to the study of the design parameters of the microbolometer, as well as the procedure for its manufacture.

## II. RESULTS

The standard design of a microbolometer consists of a single suspended multilayer membrane and long support legs [8]. The membrane includes films made of dielectric and thermosensitive material, conductive and absorbing layers. The main mechanism for heat transfer is thermal conductivity from the temperature-sensitive material to the substrate through the support structure, which performs three functions: mechanical, conductive, and heat-conductive.

The paper considers several design solutions of a microbolometer, which differ in the suspension width ( $2w$  for structure 1 and  $w$  for structure 2), the number of thin TiN films (one for type 1 and two for type 2). Each structure is considered in three versions, differing in size:  $37.5 \mu\text{m}$  (a),  $25 \mu\text{m}$  (b) and  $12.5 \mu\text{m}$  (c). Amorphous silicon was chosen as a heat-sensitive material. Instrument structure 2 of type 2b is shown in Figure 1.

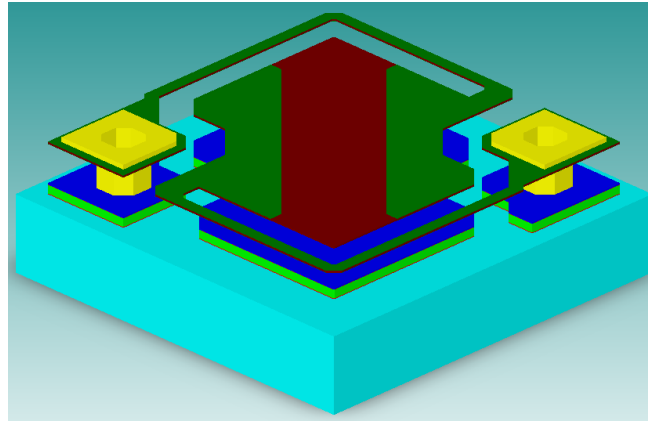


Figure 1. Device structure 2 (type 2b) of the microbolometer

Table 1 shows the main parameters of the structures under consideration. Thermal conductivity  $G$  is determined by means of stationary thermal analysis. The time constant  $\tau$  is obtained from a temperature response curve fit (transient thermal analysis). Specific heat  $C$  was calculated from the known values of  $G$  and  $\tau$ . The resistance value is determined from the results of stationary electrothermal analysis at a reference temperature of  $300 \text{ K}$  (with a voltage between the contacts of  $0.1 \text{ V}$ ).

Table 1. Results of modeling the operational characteristics of microbolometer device structures

Design Parameter	Value					
	Structure 1					
	a		b		c	
	Type 1	Type 2	Type 1	Type 2	Type 1	Type 2
Thermal conductance $G$ , (W/K) $\times 10^{-8}$	5.320	9.300	5.310	9.266	5.312	9.265
Thermal time constant $\tau$ , ms	3.240	2.130	1.382	0.890	0.798	0.529
Specific Heat $C$ , (J/K) $\times 10^{-11}$	17.24	19.80	7.33	8.25	4.24	4.90
Resistance 300K R, MOhms	9.140	9.108	9.162	9.074	9.186	9.108
Thermal coefficient of resistance TCR, 1/K	-0.0269	-0.0268	-0.0273	-0.0267	-0.0269	-0.0267
Maximum deflection 300K MD, $\mu\text{m}$	2.400	0.019	1.120	0.090	0.650	0.006
Fill factor of the sensor $\beta$	0.61	0.61	0.66	0.66	0.61	0.61
Responsivity $R_v$ , (V/W) $\times 10^6$	2.165	1.337	2.710	1.530	2.520	1.430
Design Parameter	Structure 2					
	a		b		c	
	Type 1	Type 2	Type 1	Type 2	Type 1	Type 2
Thermal conductance $G$ , (W/K) $\times 10^{-8}$	2.560	4.494	2.560	4.494	2.560	4.491
Thermal time constant $\tau$ , ms	5.660	3.650	2.458	1.565	1.590	0.900
Specific Heat $C$ , (J/K) $\times 10^{-11}$	14.490	16.388	6.290	7.033	4.070	4.042
Resistance 300K R, MOhms	9.140	9.100	9.163	9.103	9.207	9.107
Thermal coefficient of resistance TCR, 1/K	-0.028	-0.027	-0.028	-0.027	-0.028	-0.028
Maximum deflection 300K MD, $\mu\text{m}$	2.300	0.019	1.068	0.009	0.615	0.057
Fill factor of the sensor $\beta$	0.517	0.517	0.560	0.560	0.517	0.517
Responsivity $R_v$ , (V/W) $\times 10^6$	3.148	2.096	4.530	2.640	4.488	2.595

## III. CONCLUSIONS

The influence of the shape and width of the support structure of the device on the operational characteristics of thermal detectors of the bolometric type has been studied. The thermal conductivity of the considered design solutions is relatively low, especially for structure 2 (due to the doubled shoulder width). Type 1 have

a higher thermal conductivity than type 2 for the same structure. Moreover, for them the maximum deflection is greater from above, since they are only one film TiN. Structure 2 has the best sensitivity  $R_v$ . Summarizing all the parameters, it is shown that the microbolometer 2b of structure 2 has the best characteristics.

#### ACKNOWLEDGMENTS

The research is funded by and carried out within the state program of scientific research "Photonics and electronics for innovations" (task 3.04).

#### REFERENCES

- [1] R.A. Wood, C.J. Han, P.W. Kruse, "Integrated uncooled infrared detector imaging arrays", Solid-State Sensor and Actuator Workshop, 5th Technical Digest, IEEE, pp. 132-135, 1992.
- [2] D. Takamuro, M. Tomohiro, S. Takaki, "Development of new SOI diode structure for beyond 17um pixel pitch SOI diode uncooled IRFPAs", Proceedings of SPIE - The International Society for Optical Engineering, 8012, 80121E, 2011.
- [3] C. Li, C.J. Han, G.D. Skidmore, C. Hess, "DRS uncooled VOx infrared detector development and production status", Proc SPIE, Vol.7660, 76600V, 2010.
- [4] B.E. Cole, R.E. Higashi, R.A. Wood, "Micromachined pixel arrays integrated with CMOS for infrared applications", Int. Conf. on Optical MEMS, IEEE, P. 63, 2000.
- [5] A.J. Syllaios, et al., "Amorphous Silicon Microbolometer Technology", Proc. Mater. Res. Soc., San Francisco, CA, USA, 2000, Vol. 609, pp. A14.4.
- [6] E. Mottin, et al., "Uncooled amorphous silicon technology enhancement for 25-um-pixel pitch achievement" Proc. SPIE Infrared Technology and Applications XXVIII, Seattle USA, 2003, Vol. 4820, pp. 200.
- [7] C.-L. Tisse, J.-L. Tissot, A. Crastes, "An information-theoretic perspective on the challenges and advances in the race toward 12 $\mu$ m pixel pitch megapixel uncooled infrared imaging", Proc. SPIE 2012, 8353, 83531M1.
- [8] J. Wang, et al., "Fabrication and parameters calculation of room temperature terahertz detector with micro-bridge structure", J. Infrared Milli Terahz Waves, 35(12), 987-1082, 2014.

### **MODIFICATION OF THE RLA MODEL FOR PRESENTING A CLUSTER SYSTEM OF A COMPOSITE MATERIAL WITH A FRACTAL FILLER STRUCTURE**

A. Belko, N. Babarika, I. Zeylikovich, A. Nikitin  
YankaKupala State University of Grodno, Grodno, Belarus

*[belko\\_av@grsu.by](mailto:belko_av@grsu.by)*

#### I. INTRODUCTION

In [1 - 4], the quantitative characteristics of the spatial distribution of filler-copper particles in the matrix of a composite material based on polytetrafluoroethylene were investigated and determined using images of the surface obtained by optical microscopy methods. To determine the quantitative parameters of the structure of clusters, the method of cluster recognition based on threshold segmentation (Otsu method) was applied. Analysis of the distribution structure of copper particles in a polymer matrix at filler concentrations in the range of 1-20 wt. % shows that the structure of the filler forms clusters can be described within the reaction-limited aggregation (RLA) model. It was found that the fractal dimensions of the profile of the selected segments of copper clusters in the polytetrafluoroethylene matrix are in the range from 1.65 to 1.72 with a change in the mass concentration of copper from 1% to 20%. The fractal dimensions of the profile of the clusters, the structure of which was calculated within the framework of the RLA model (for three-dimensional lattices), vary from 1.62 to 1.72 when the probability of adhesion of a diffusing particle and cluster particles in the adhesion zone changes from 0.2 to 1. The fractal dimensions of the profile of the clusters, the structure of which was calculated within the framework of the RLA model (for three-dimensional lattices), vary from 1.62 to 1.72 when the probability of adhesion of a diffusing particle and cluster particles in the adhesion zone changes from 0.2 to 1. Such a parameter of the RLA model, as adhesion probability, can serve as a link between the fractal dimension of the cluster profile and its mass fractal dimension.

In accordance with the RLA model, one seed particle of the cluster is placed in the space under consideration, and then one new particle is added to the space. Each new particle moves according to the law of random walks. If a particle reaches the boundary of space, it is reflected from it. The particle continues



to move until it is in the vicinity of one of the cluster particles. Further, the diffusing particle is attached to the cluster in accordance with the given probability of adhesion of the diffusing particle and the configuration of the cluster particles in the adhesion zone. If a diffusing particle joins a cluster, then the next particle is launched into space. If the attachment of the particle to the cluster did not occur, then the particle continues to move according to the law of random walks. Thus, a cluster is formed [5–7].

## II. DESCRIPTION OF THE MODEL AND OBTAINED RESULTS

One of the options for modifying the RLA model is the condition for the termination of cluster growth. Usually, in the RLA model, the condition for the termination of cluster growth is that the cluster reaching the boundaries of the region. However, this condition can be changed by setting a finite amount (volume concentration) of primary particles from which a cluster is formed. Calculations, provided that the cluster reaches the boundaries of the region, show that the volume concentration of particles corresponds to 2%. The volume concentration of primary particles is related to the mass concentration of copper in the matrix of the composite material based on polytetrafluoroethylene and can be another parameter for comparing real clusters and model objects.

Real physical systems usually consist of several clusters (cluster system). In order to obtain a model of such a system, the RLA method can also be modified. In our case, unlike the RLA model, during the clustering process, seed particles are randomly added that do not move over the region and from which clusters can be formed. Also, during the clustering process, in accordance with the RLA model, particles are sequentially launched that diffuse over the area. If a diffusing particle enters a cell next to a cluster, then, depending on the adhesion probability, it either joins the cluster or continues to diffuse over the region. Thus, it is possible to build a cluster system. In this work, the RLA model was modified to study the properties of the cluster system in the range of the volume concentration of particles from 2 to 5% and the probability of adhesion of diffusing particles and cluster particles in the adhesion zone from 0.2 to 1.

In this case, an informative characteristic of fractal clusters of the system can be their average fractal dimension. Calculations have shown that the average fractal dimension of clusters in the system corresponds to the fractal dimension of clusters, the structure of which was calculated within the RLA model with the corresponding probability of adhesion of diffusing particles and cluster particles in the adhesion zone.

A computational experiment to determine the mutual influence of the adhesion probability and the volume concentration of particles on the formation of fractal clusters in a cluster system was carried out in accordance with the second-order orthogonal central compositional plan (OCCP) [8]. As a result of a computational experiment in accordance with the OCCP, the dependence of the mass fractal dimension of clusters from the volume concentration of particles and the probability of diffusing particles adhesion and cluster particles in the adhesion zone was obtained:

$$D = 2,524 + 2,167 n - 0,385 P + 0,5 nP + 0,175 P^2 \quad (1)$$

where  $D$  is the average mass fractal dimension of clusters,  $n$  is the volume concentration of primary particles,  $P$  is the probability of adhesion of diffusing particles and cluster particles in the adhesion zone.

## III. CONCLUSIONS

The paper proposes a modification of the RLA model to study the properties of a cluster system. A computational experiment to determine the mutual influence of the adhesion probability and the volume concentration of particles on the formation of fractal clusters in a cluster system was carried out in accordance with the second-order orthogonal central compositional plan. As a result of the computational experiment in accordance with the OCCP, an equation was obtained for the dependence of the mass fractal dimension of clusters on the volume concentration from 2 to 5% and the adhesion probability of diffusing particles and cluster particles in the adhesion zone from 0.2 to 1. The developed methods for modeling a cluster system can be used to present the structure of the filler in composite materials and predict the physical properties (thermal conductivity) of composite systems.

## REFERENCES

- [1] A.V. Belko, A.V. Nikitin, "Fractal structure copper clusters in a matrix of polytetrafluoroethylene" NDTCS-2017. 17th International Workshop on New Approaches to High-Tech: Nano-Design, Technology, Computer Simulations October 26-27, 2017, Minsk, Belarus, pp.140-141, 2017.
- [2] A.V. Belko, N. N. Babarika, I. S. Zeyikovich, A. V. Nikitin, "Diagnostics of the structure of fractal copper clusters in a polytetrafluoroethylene matrix" Pattern Recognition and Image Analysis, Vol. 9. № 1. pp. 1-6, 2020.

- [3] A. Belko, N. Babarika, I. Zeylikovich, and A. Nikitin, "Diagnostics of the structure of fractal copper clusters in a matrix of polytetrafluoroethylene," in Proc. 14th International Conference on Pattern Recognition and Information Processing (PRIP'2019) (Minsk, Belarus, May 21–23, 2019), pp. 316-319, 2019.
- [4] A. V. Belko, A. V. Nikitin, "Fractal structure copper clusters in a matrix of polytetrafluoroethylene" Vesn. Grod. Dzyarzh. Univ., Ser. 2, Vol. 7. № 3. pp.90–97, 2017.
- [5] B. M. Smirnov, "Fractal clusters," Sov. Phys. Usp., Vol.9. № 6. pp.481-505, 1986.
- [6] A. V. Belko and A. V. Nikitin, "Methods for constructing objects with fractal structure" Vesn. Grod. Dzyarzh.Univ., Ser. 2, Vol.11. № 2. pp.133-137, 2002.
- [7] A. V. Belko, A. V. Nikitin, A. A. Skaskevich, A. Yu. Bachurina, and S. I. Sarosek, "Models of fractal structures in composite systems on the basis of polymers," Vesn. Grod. Dzyarzh. Univ., Ser. 2, Vol.129. № 2. pp.95-104, 2012.
- [8] A. V. Belko, N. N. Babarika, A. V. Nikitin, "Effect of double electric layers of disperse particles on structure and mechanisms of formation of fractal clusters in disperse systems" Vesn. Grod. Dzyarzh. Univ., Ser. 2, Vol. 9. № 1. pp.68-77, 2019.

## **FORECASTING THE LEVEL OF ASSIMILATION OF MATHEMATICAL KNOWLEDGE AS A STAGE IN MODELING THE EDUCATIONAL PROCESS OF A UNIVERSITY IN A BLENDED LEARNING ENVIRONMENT**

E. Zhuravleva, L. Studenikina  
RTU MIREA, Moscow, Russia

[lena-jur@yandex.ru](mailto:lena-jur@yandex.ru)

### I. INTRODUCTION

In the context of building an individual educational scheme for students, it becomes especially important to analyze the assimilation of theoretical and practical material in order to make corrections in the methodological aspects of teaching the mathematical cycle disciplines. As well as forecasting the level of mastering disciplines. This approach is especially important in a blended learning environment, when knowledge control takes place in a distance format.

### II. MAIN TEXT

In the first semester, the working curriculum for students of economic training areas provides for the study of two disciplines of the mathematical cycle: linear algebra and mathematical analysis. As shown by the analysis of the final testing in the discipline "mathematical analysis", less than 10% of students scored more than 20 points out of 50 possible. The main part barely crossed the required minimum of 16 points to get credit. In this regard, an analysis was made of possible difficulties that students faced when completing assignments. The main problems include:

- Weak basic mathematical preparation, caused by the usual memorization of only the necessary mathematical apparatus for the successful passing of the exam.
- Lack of skills for attentive work with the text of the assignment.
- The use of Internet resources, which knocked off the correct decision inherent in the software testing algorithms.

The performed correlation analysis of the test results in the disciplines of linear algebra and mathematical analysis showed the presence of a close linear relationship between the test results and the exam, and the analysis of the exam results in linear algebra, that the same problems were present during testing in this discipline.

To reduce the dependence of the results of mastering the material on the identified problems, at the beginning of the semester, a repetition of what was learned was carried out at the beginning of the semester, analysis of typical mistakes made when completing the test assignment, as well as the order of studying the sections assigned to the second semester was changed. These measures led to an improvement in the assessment of the forecast of the success of the exam, which was confirmed by the results of examination testing. The projected 30% of those passing increased to 57%.

The exam result, from our point of view, is still unsatisfactory. The reasons for this result are the following:

-Lack of students' skills in working with theoretical material, which was presented at webinars and video lectures ("I watched the lecture and remembered everything, only now I forgot", i.e. «I went to a concert and learned to play a musical instrument»);

-lack of motivation to do homework ("I understood everything in practice")

- the teacher's lack of the ability to insist on retaking topics that are poorly developed by the student, i.e. rewrite control and independent work to a satisfactory result

- a student have the opportunity not to attend classes to take the exam, which reduces the value of both the full-time study itself and devalues the teacher's work on the examination test.

### III. CONCLUSIONS

The study shows that predicting the results of success in mastering the discipline based on the results of previous tests and exams leads to an increase in the level of mastering the material in mathematical disciplines. As a guideline, you can do the following:

1. To organize for first-year students with a low USE score (less than 60 points) a compulsory elective course during the first month of study (at least 2 times a week) in order to explain forgotten or missed topics in the school mathematics course, which will increase their level of perception of theoretical mathematics

2. Students who missed most of the classes (more than 40%) should be offered to take this course again, since in 90% of cases these students have an unsatisfactory exam result.

### REFERENCES

[1]. Zhuravleva E.V., Studenikina L.I. Methodological features of the compilation of examination tests in mathematical disciplines during the period of distance learning Higher education today, No. 5, May 2021, № P. 24-29.

[2]. Zhuravleva E.V., Studenikina L.I. Formation of general professional competencies in the study of mathematical disciplines. Materials of the Russian scientific and technical conference with international participation "Innovative technologies in electronics and instrument making", Physics and Technology Institute RTU MIREA, Volume 1, Moscow – 2020. - S.263-268.

[3]. Studenikina L.I., Shevtsova T.V. Information technology as a necessary component of the competence-based approach in the organization of university mathematical training. Bulletin of the Laboratory of Mathematical, Natural Science Education and Informatization: Collection of Scientific Papers of NIISO GBOU VPO MGPU, 2012. - pp. 359-365.

[4]. Zhuravleva E.V., Burilich I.N. Test technologies in the context of the competence-based approach // Actual research in the field of mathematics, computer science, physics and methods of their study in the modern educational space, the results of research in the field of mathematics, computer science, physics and methods of their study in the implementation of educational programs of higher education. - Kursk, 2017.S. 55-59.

[5]. Zhuravleva E.V., Burilich I.N. Mathematical game as a means of teaching and monitoring students' knowledge // Mathematical education at school and university: theory and practice (MATHEDU-2016) - Kazan, 2016. P. 134-137.

[6]. Vagramenko Ya.A., Yalamov G.Yu. Intellectualization of information systems included in the educational environment // Informatization of education and science, no. 4, p. 3-11.

[7]. Studenikina L.I. Pedagogical conditions for the effectiveness of the use of e-learning elements in university professional training of students (based on mathematical training (scientific monograph) Kursk: South-West State University; 2019. - 136s.

[8]. Zhuravleva E.V., Burilich I.N. Information technologies in organization of lectures on the disciplines of mathematical cycle : Bulletin of the Moscow City Pedagogical University. Series: Informatics and informatization of education. 2014. No. 2 (28). S. 45-50.

## INTEGRATION OF GENERAL PHYSICS EXPERIMENTS WITH MATHEMATICAL SIMULATION

I. Zeylikovich, A. Nikitin, A. Belko

YankaKupala State University of Grodno, Grodno, Republic of Belarus

[belko\\_av@grsu.by](mailto:belko_av@grsu.by)

## I. INTRODUCTION

Mathematical modeling in the subject area, and in particular in physics, with the advent of high-speed computers, allows solving problems that, in principle, could not be solved by analytical methods. The "computational experiment" term comes into use along with a full-scale physical experiment. The transfer of computerization to the educational sphere is primarily due to the wide computing and presentation capabilities of computers. The main problem of using computers in subject education is not to complicate the learning process. We have extensive experience in the use of modeling of physical processes in teaching [1-3]. Let's demonstrate this with a simple model.

Consider the ideal gas model. Its construction requires knowledge of only the laws of conservation of energy and momentum. This is enough to illustrate the "maxwellization" of molecular velocities and to introduce the concept of energy temperature [3]. The initial configuration of molecules can be chosen to be regular, and the velocities can be set to be the same and visually demonstrate how the movement of molecules is randomized as a result of collisions. You can also display the instantaneous and average energies of molecules and notice that the instantaneous energy fluctuates strongly, and the average takes the same definite value regardless of the selected molecule (Fig. 1). This particular value is the energy temperature. Of course, in a similar way, you can present more complex models that require the use of finite-difference methods, Monte Carlo methods.

There are problems in physics (percolation theory, cellular automata, fractals, kinetic growth models) that are difficult to study and understand without visual modeling. The use of computer modeling makes it possible to implement the deep thought of Confucius in teaching: I hear and forget, I see and remember, I do and comprehend. Consider another example from our educational practice: the application of simulation in a physics laboratory practice.

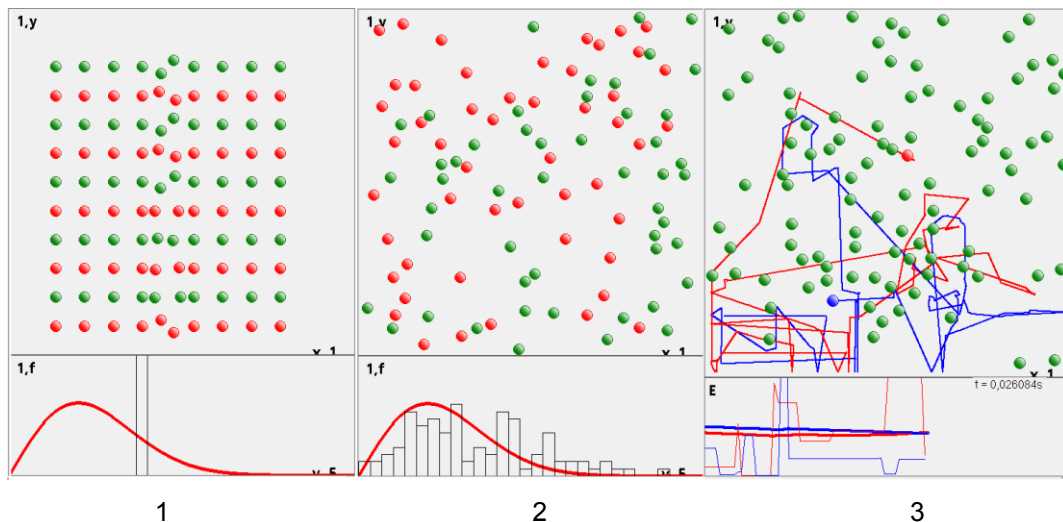


Figure 1. An ideal gas model to demonstrate the concept of "temperature" and "Maxwell distribution" (1- initial configuration; 2- velocity distribution; 3- interpretation of the concept of "temperature")

## II. LABORATORY PRACTICE AND MODELING

Physics is an experimental science. That is why laboratory practice takes an important place in teaching. At the same time, the laboratory implementation of physical processes during teaching is limited by technical capabilities. In this regard, considering the rapid development of computer technology (CT), computer modeling can be a good addition to the workshop. The traditional application of CT tools is process visualization, processing of experimental data. By extending this application to a computational experiment, learning efficiency can be improved. In this workshop, we limited ourselves to a few works, the implementation of which is possible on a unified installation. On the one hand, this allows one to reduce the cost of equipment, on the other hand, to show the connection between physical phenomena of various nature. We used the phenomenon of electromagnetic induction, both for diagnosing of process parameters and for studying the phenomenon itself [4, 5]. A unified setup for laboratory workshops and demonstrations in general physics (oscillations and electromagnetism) was developed. A distinctive feature of the proposed setup is related to simultaneous excitation and detection of linear and nonlinear oscillations and generation of dissipative forces with the aid of electromagnetic induction and Ampere force. The system allows integration of laboratory works with the simulation of the investigated processes and automation of the process of work execution and data processing. Low cost allows the purchase of several installations and the implementation of frontal laboratory work and lecture demonstrations.

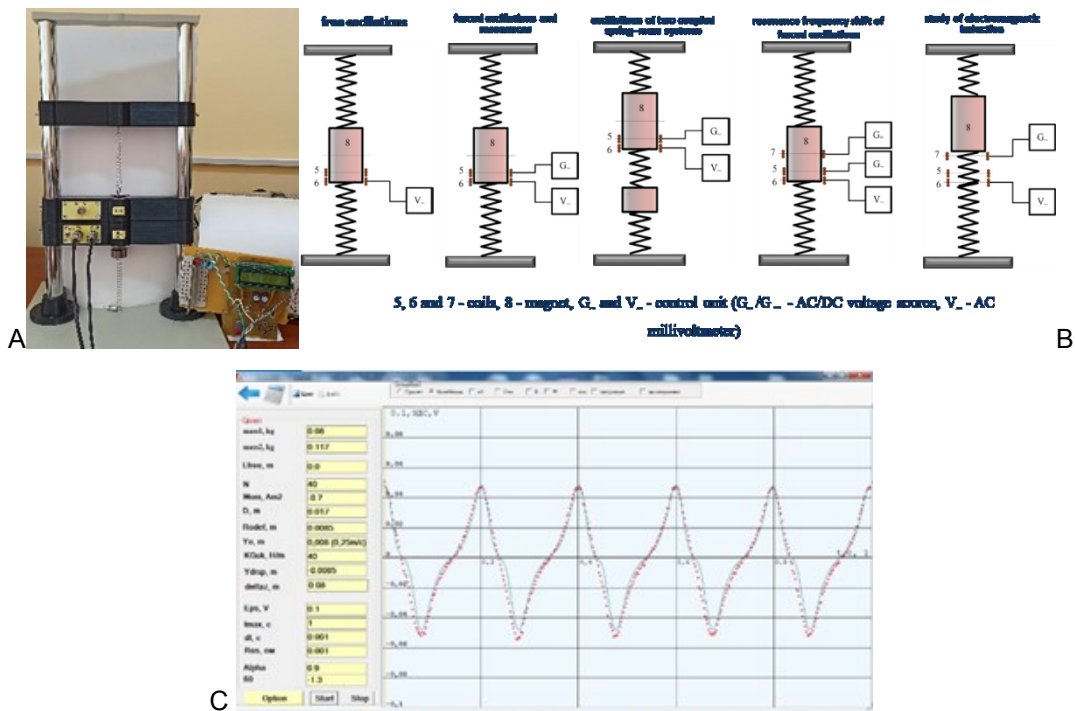


Figure 2. A – the experimental setup, B – arrangements of laboratory works, C – example of integration of laboratory work with the simulation of the investigated processes

### III. CONCLUSIONS

The modeling possibilities are as varied as the developer's fantasy is. It is important that the computer application does not complicate the understanding of the process under study. The possibility of combining a natural experiment and a process model can give an effective educational result.

### REFERENCES

- [1] Nikitin A.V, Zeylikovich I.S., Zukevich A.I., Babarika N.N., Belko A.V., "Forms and software for support of for lectural, practical and laboratory exercises in physics", Informatization of education and e-learning methodology: digital technologies in education: materials of the V International scientific. Conf., Krasnoyarsk, September 21-24, 2021: at 2 pm Part 1 / under total. ed. M.V. Noskova. - Krasnoyarsk: Sib. Feder. un-t, 2021.-356-360 pp.
- [2] Computer modeling of physical processes / A. V. Nikitin, A. I. Slobodyanyuk, M. L. Shishakov. - M.: Binom. Knowledge Laboratory, 2013. - 679 p.
- [3] <https://sites.google.com/view/physicscomputerforcolleges>.
- [4] I.S. Zeylikovich, A. V. Nikitin, N. V. Matetskiy, A. E. Vasilevich, D. Yu. Diagel, V. A. Zaman, K. Sh. Shunkeev, A. Z. Bekeshev "The phenomenon of electromagnetic induction and its application in a laboratory workshop" Physical education in universities. Vol. 24, No. 4, 2018.
- [5] I. S. Zeylikovich, A. V. Nikitin, and A. E. Vasilevich "Excitation and Detection of a Nonlinear Resonance of Oscillations of a Spring–Mass System Using Electromagnetic Induction" ZhTF, v. 90, p. 5-14, (2020).

## TIME SERIES ANALYSIS OF WATER POLLUTION DATA

I. Drozdov

Russian Technological University (MIREA), Prospekt Vernadskogo, 78, 119454 Moscow, Russia

[drozdov\\_i@mirea.ru](mailto:drozdov_i@mirea.ru)

### I. INTRODUCTION

Ecology and environmental sciences problems are very important in modern world. Time series analysis methods, particularly an ARIMA family of models and related Box-Jenkins methodology are powerful methods developed in econometrics field to describe complex time-dependent behavior of different processes. Also, it has been shown that such models could be used for analysis and prediction of ecological

data [1]. In particular, ARIMA models have been successfully applied to air pollution data around the world [2,3,4]. Aim of this paper is to apply time series analysis methods to investigate water pollution in Ukraine. We are using datasets provided by the Ukrainian government (State Water Resources Agency of Ukraine) which contain information about biochemical oxygen demand (BOD) [5], ammonium ions concentration [6] and phosphate ions concentration [7] in river water. Values of concentration are measured at eight consequent water stations. The original data contest was aimed to predict concentration level at one of the stations using values at the other ones. Time series values have got periods of missing data. First of all, these missing parts need to be calculated. Spline functions have been used to solve this task. In the paper mathematical models describing behavior of concentration and BOD level time series at the target station are built. Also, models aimed to describe dependence of concentration at the target station on levels at the other stations are constructed and investigated. Influence of pollution values at intermediate stations on levels at the target stations are investigated with statistical tests. The proposed technique can be used to investigate pollution at plants in other domains of industry and to handle missing values in various time series.

## II. DATA STRUCTURE

Three major indicators of water pollution are investigated: BOD (Biochemical Oxygen Demand), ammonium ions concentrations and phosphate ion concentrations (High phosphate and ammonium levels are usually detected in large cities and agricultural areas and could be sign of sewage contamination). We will refer to these datasets as BOD, ammonium and phosphate. There are values of seven water station measuring pollution level. Missing values in all analyzed time series have been handled by means of spline functions.

## III. EXPERIMENTS

Autoregressive moving-average (ARIMA) models have been used to describe temporal dependencies in selected time series. Orders of ARIMA models have been chosen through exploratory analysis of ACF/PACF plots and numerical optimization of information criteria. Some of models showed quarter seasonality, which have been used to describe data using seasonal ARIMA (SARIMA) models.

Linear regression models of ammonium and phosphates ions concentration level in river water have been constructed. The models describe dependence of values at the target station on values at the intermediate ones. Determination coefficients of these models are between 45% and 53%. Low determination coefficients in regression model between target station and stations 1 and 2 could indicate that pollution is introduced somewhere on this interval.

The ArDL models describing connection between the BOD value and phosphates concentration level have been constructed. Also, mutual dependence between ammonium concentration time series behaviour and phosphates concentration time series values has been proved with statistical tests.

The ArDL models of dependencies between values at the intermediate stations and at the target one for ammonium, phosphates and BOD values are also shown.

## IV. CONCLUSIONS

Exploratory data analysis detects irregular pollution spikes in the river water. ARIMA models have been used to describe how those spikes affect river water quality in the following periods and how river ecosystem responds to introduced external pollutants. Constructed ArDL models describe dependency between phosphates/ammonium and BOD, providing useful relations how pollutant ions affect BOD directly and over time. Coefficients of those model can be used to describe rates of those processes. Also, regression models fitted to spatially distributed data between water stations were able to predict where exactly pollutants have been introduced to the river and how long it affects quality of water further downstream.

This work is meant to show how simple and computationally inexpensive yet powerful and interpretable statistical methods could be used for analyzing environmental data to construct ecological mathematical models, which require only basic data that is currently collected due to governmental regulations. Alternative, more fundamental way of constructing such models would require extensive theoretical analysis of the problem, involving experts and field work; such models would generally be more correct and descriptive, but their construction is not always feasible.

## REFERENCES

- [1] Ives, Anthony & Abbott, Karen & Ziebarth, Nicolas. (2010). Analysis of ecological time series with ARMA (p, q) models. *Ecology*. 91. 858-71. 10.1890/09-0442.1.
- [2] Abhilash, M. & Thakur, Amrita & Gupta, Deepa & Sreevidya, B.. (2018). Time Series Analysis of Air Pollution in Bengaluru Using ARIMA Model. 10.1007/978-981-10-7386-1\_36.

- [3] Rahman, Md Arafat & Hossain, M.A.. (2012). Time series analysis model for particulate matter of air pollution data in Dhaka city. *Asian Journal of Water, Environment and Pollution*. 9. 63-69.
- [4] Guarnaccia, Claudio & Griselda, Cerón-Bretón & Breton, Rosa & Tepedino, Carmine & Quartieri, Joseph & Mastorakis, Nikos. (2018). ARIMA models application to air pollution data in Monterrey, Mexico. *AIP Conference Proceedings*. 1982. 020041. 10.1063/1.5045447.
- [5] Prediction BOD in river water. Retrieved from (the 1<sup>st</sup> of October, 2020): <https://www.kaggle.com/vbmokin/prediction-bod-in-river-water>.
- [6] Ammonium prediction in river water. Retrieved from (the 1<sup>st</sup> of October, 2020): <https://www.kaggle.com/vbmokin/ammonium-prediction-in-river-water>.
- [7] Phosphate prediction in river water. Retrieved from (the 1<sup>st</sup> of October, 2020): <https://www.kaggle.com/vbmokin/phosphate-prediction-in-river-water>.
- [8] Petrushevich D 2019 Time series forecasting using high order Arima functions *Proc XIX Int Multidisciplinary Scientific GeoConference SGEM 2019* **19(2.1)** pp 673-80 doi:10.5593/sgem2019/2.1/S07.088.
- [9] Kalugin T R and Kim A K and Petrushevich D A 2020 Analysis of the high order ADL(p, q) models used to describe connections between time series *Russ Tech J* **8(2)** pp 7-22 (In Russ) doi:10.32362/2500-316X-2020-8-2-7-22.
- [10] I. Yu. Drozdov et al «Analysis of ammonium and phosphates concentration time series in river water», 2021 IOP Conf. Ser.: Earth Environ. Sci. 684 012021.
- [11] I. Yu. Drozdov et al «Mathematical models of water pollution evaluation», 2021 IOP Conf. Ser.: Earth Environ. Sci. 684 012026.

## DELAUNAY VARIABLES IN MODEL PROBLEMS OF CELESTIAL MECHANICS AND COSMODYNAMICS

A. Shatina, A. Cheshkova

MIREA – Russian Technological University, 119454 Moscow, Russia

[shatina\\_av@mail.ru](mailto:shatina_av@mail.ru)

### I. INTRODUCTION

One of the most important model problems of celestial mechanics and cosmodynamics is the two-body problem, which describes the interaction of two-point mass, moving under the action of mutual gravitational attraction according to Newton's law of universal gravitation.

Integration of differential equations of motion in the two-body problem is reduced to quadratures. The trajectory of a point with mass  $m$  relative to a point with mass  $M$  is a conical section. From the point of view of applications, the most important case is the case of the Keplerian elliptic orbit. Whereas in unperturbed problem a point with mass  $m$  moves along an ellipse, to derive the equations of perturbed motion, the canonical Delaunay variables are used [1, 2], which in unperturbed problem are the "action-angle" variables.

The equations of motion in Delaunay variables are convenient to apply numerical and asymptotic research methods. This paper gives an example of using Delaunay variables in the model problem of motion of a satellite in the Earth's gravitational field, modeled by an axisymmetric rigid body compressed along the axis of rotation.

### II. DISTURBED SATELLITE MOTION

Consider the problem of the motion of a satellite (point particle P) with mass  $m$  in the Earth's gravitational field. Introduce a geocentric inertial coordinate system (ISC)  $OXYZ$ , which origin is coinciding with the center of the Earth  $O$ , and the  $OZ$  axis is directed along the axis of rotation of the planet. As an unperturbed problem, consider the motion of satellite in the gravitational field of a planet, modeled by homogeneous solid full-sphere, rotating evenly around its axis. In this case gravitational potential of the planet coincide with gravitational potential of particle point with mass equal to the mass of the planet, and the satellite's orbit is Keplerian. Lets consider the Keplerian elliptical orbit as the orbit of unperturbed motion.

Let  $\mathbf{R}$  denote the satellite radius vector and let  $R = |\mathbf{R}|$ . Introduce the following notation for the parameters of the satellite orbit:  $a$  – semi-major axis,  $e$  – eccentricity  $i$  – inclination (angle between plane  $OXY$  and plane of the satellite's orbit),  $h$  – longitude of ascending node (angle between the axis  $OX$  and the line  $OX_1$  intersection of the plane of the satellite's orbit and the plane  $OXY$ ),  $g$  – longitude of the periapsis  $\pi$  from the ascending node  $OX_1$ , ( $\pi$  – the closest to the center of the Earth  $O$  point of the satellite's orbit),  $\vartheta$  – true

anomaly. In unperturbed motion, the parameters  $a, e, i, h, g$  are constant values, true anomaly  $\vartheta$  is time function [1,2]:

$$\dot{\vartheta} = n(1 + e \cos \vartheta)^2 / (1 - e^2)^{3/2}.$$

In this formula,  $n$  – is the mean motion of satellite on the orbit, which is related with semi-major axis  $a$  by the equality  $n = \sqrt{f_0/a^3}$ , where  $f_0 = fM$ ,  $f$  – universal gravitational constant,  $M$  – Earth's mass.

To describe the orbital motion of the satellite, using canonical Delaunay variables  $L, G, H, l, g, h$  [1,2]. Here  $g, h$  – previously entered parameters of the satellite orbit. Variable  $l$  is mean anomaly. In unperturbed problem, mean anomaly is linear function of time:  $l = n(t - t_\pi)$ , where  $t$  – current time moment,  $t_\pi$  – moment of time, when satellite passage through the periapsis. The Delaunay variables  $L, G, H$  are related to the orbit parameters  $a, e, i$  by the equalities:

$$L = \sqrt{f_0 m^2 a}, \quad G = \sqrt{f_0 m^2 a (1 - e^2)}, \quad H = \sqrt{f_0 m^2 a (1 - e^2)} \cos i.$$

The module of satellite's radius vector  $R$  and true anomaly  $\vartheta$  are the functions of the Delaunay variables  $L, G, l$ . The dependence of  $R, \vartheta$  on these variables is implicit and expressed through the relations:

$$R = \frac{G^2}{f_0 m^2 (1 + e \cos \vartheta)}, \quad \cos w = \frac{e + \cos \vartheta}{1 + e \cos \vartheta}, \quad l = w - e \sin w.$$

In these formulas,  $w$  – eccentric anomaly.

The Hamiltonian of the unperturbed problem depends on only one Delaunay variable  $L$ :

$$\mathcal{H}_0 = -\frac{f_0^2 m^3}{2L^2}.$$

As a perturbing force function, consider the function [3,4]:

$$U_1 = -\frac{f_0 m J_2 r_0^2}{2R^3} (3 \sin^2 \varphi - 1),$$

where  $r_0$  – average radius of the Earth,  $\varphi$  – geographic latitude of the satellite,  $\sin \varphi = \sin i \sin(g + \vartheta)$ ,  $J_2$  – second zonal harmonic (dimensionless coefficient, that is characterizing the contribution of nonspherical components,  $J_2 = 1,0825 \cdot 10^{-3}$ ). The Hamiltonian of the problem, considering the indicated perturbation will take the form:

$$\mathcal{H} = \mathcal{H}_0(L) + \varepsilon \mathcal{H}_1(L, G, H, l, g, h),$$

$$\varepsilon \mathcal{H}_1(L, G, H, l, g, h) = \frac{f_0 m J_2 r_0^2}{2R^3} (3 \sin^2 i \sin^2(g + \vartheta) - 1)$$

And the equations of the disturbed motion will be written in the form:

$$\dot{L} = -\varepsilon \frac{\partial \mathcal{H}_1}{\partial l}, \quad \dot{G} = -\varepsilon \frac{\partial \mathcal{H}_1}{\partial g}, \quad \dot{H} = -\varepsilon \frac{\partial \mathcal{H}_1}{\partial h}, \quad \dot{l} = n + \varepsilon \frac{\partial \mathcal{H}_1}{\partial L}, \quad \dot{g} = \varepsilon \frac{\partial \mathcal{H}_1}{\partial G}, \quad \dot{h} = \varepsilon \frac{\partial \mathcal{H}_1}{\partial H}, \quad n = \frac{f_0^2 m^3}{L^3} \quad (1)$$

Based on system (1), can get the system of ordinary differential equations of the 6<sup>th</sup> order in dimensionless variables  $n_0, e, i, \beta, \vartheta, h$ , where  $\beta = g + \vartheta$ ,  $n_0 = n/\omega$ ,  $\omega$  – module of the angular velocity of the Earth's rotation. This system of equations has the form:

$$\begin{aligned} \dot{n}_0 &= -\frac{3\varepsilon_2 n_0^{10/3} p^4}{q^9} \{\Phi e \sin \vartheta - p \sin^2 i \sin 2\beta\}, \\ \dot{e} &= \frac{\varepsilon_2 n_0^{7/3} p^3}{q^7} \{p\Phi \sin \vartheta - \sin^2 i \sin 2\beta (2 \cos \vartheta + e + e \cos^2 \vartheta)\}, \\ \frac{di}{dt} &= -\frac{\varepsilon_2 n_0^{7/3} p^3}{2q^7} \sin 2i \sin 2\beta, \\ \dot{\beta} &= \frac{p^2 n_0 \omega}{q^3} + \frac{2\varepsilon_2 n_0^{7/3} p^3}{q^7} \cos^2 i \sin^2 \beta, \\ \dot{\vartheta} &= \frac{p^2 n_0 \omega}{q^3} + \frac{\varepsilon_2 n_0^{7/3} p^3}{q^7 e} \{p\Phi \cos \vartheta + \sin^2 i \sin 2\beta (2 + e \cos \vartheta) \sin \vartheta\}, \end{aligned}$$



$$\dot{h} = -\frac{2\varepsilon_2 n_0^{7/3} p^3}{q^7} \cos i \sin^2 \beta.$$

Here  $\varepsilon_2 = 1.5J_2 r_0^2 \omega^{7/3} f_0^{-2/3}$ ,  $\Phi = 3 \sin^2 i \sin^2 \beta - 1$ ,  $\beta = g + \vartheta$ ,  $p = 1 + e \cos \vartheta$ ,  $q = \sqrt{1 - e^2}$ .

### III. CONCLUSIONS

Based on the system of equations of the perturbed satellite motion in the canonical Delaunay variables, a system of ordinary differential equations of the 6<sup>th</sup> order is obtained, which described the satellite's orbital motion in the Earth's gravitational field, considering its compression along the axis of rotation. The specified system of equations can be used in mathematical modeling in problems related to remote sensing of the Earth.

### REFERENCES

- [1] C.D.Murray and S.F.Dermott. Solar System Dynamics. Moscow: Fizmatlit, 2010. – 588 p.
- [2] Vilke V.G. Mechanics of systems of material points and solids. Moscow: Fizmatlit, 2013. 268 p.
- [3] Demin V.G. The motion of an artificial satellite in an off-center gravitational field. – M. – Izhevsk: Research Center "Regular and Chaotic Dynamics", 2010. – 420 p.
- [4] Beletsky V.V. Essays on the motion of cosmic bodies. Moscow: LKI Publishing House, 2009. 432 p.

## COMPARISON OF HYBRID APPROACHES IN CLASSIFICATION USING DECISION TREES AND NEURAL NETWORKS

A. Fomchenko

MIREA – Russian Technological University, 119454 Moscow, Russia

[alexvin364@mail.ru](mailto:alexvin364@mail.ru)

### I. INTRODUCTION

Approaches combining methods based on decision trees and neural networks are an important examples of hybrid strategies. The problem of classification of the table-based data is considered.

There is a number of studies sharing the idea of unifying neural network and decision tree models. Besides the most common idea of straightforward using the ensemble of these two algorithms, there are Deep Neural Decision Trees (DNDF) – a notion for a neural decision trees with the split functions realised as a randomized multilayer perceptrons.

In the applications where the trees approach is feasible, forest of such trees also can be applied as a generalization. There are many approaches in constructing a forest of trees and different methods using the forest of these decision trees, like Neural Decision Forests (NDF), Neural Random Forests (NRF), Neural Deep Forests. The research deals with the elaboration and implementation of these methods.

Further on, all presented methods are to be compared with each other, as well as with the original algorithms themselves– the decision tree, ensemble of trees and the multilayer neural network.

It is important to note that the comparison is not reduced to answering the question, which of them have better result in different examples, because such properties are already studied and presented using different datasets. Instead of that we are looking for the "stability" of the result.

It is a known fact that for different examples specially selected different approaches are better – in one case it might be a decision tree, in another case it might be multilayer perceptron. So the idea for comparison is artificial creation of datasets with gradation from first case to second one. The more robustly the algorithm works on the aggregation of all sets the better we consider it.

### II. CONCLUSIONS

This research presents different methods that unify classification trees with the neural networks. Various options for forest construction are considered, but there is also a considerable potential for further research concerning modification of the neural network learning strategy. These changes are expected to lead to better performance.

Another direction in the research is combining the convolutional neural networks (CNN) and decision forests for solving problems of machine vision.

## REFERENCES

- [1] Y. Yang, I. Morillo, T. Hospedales, "Deep Neural Decision Trees", pp. 1-7, 2019.
- [2] R. Balestriero, "Neural Decision Trees", pp. 1-10, 2017.
- [3] S. Buló, P. Kotschieder, "Neural Decision Forests for Semantic Image Labelling", pp. 1-8, 2014.
- [4] P. Kotschieder, M. Fiterau, A. Criminisi, S. Buló, "Deep neural decision forests" pp. 1-4, 2015.
- [5] R. Polikar, "Ensemble learning" Ensemble Machine Learning: Methods and Applications, pp. 1–34, 2012.
- [6] L. Breiman, "Random Forests". Machine Learning Vol. 45, pp. 5–32, 2001.

## MATHEMATICAL MODELING OF THE DYNAMICS OF A FOUR-POINT PLATFORM OF A HEAVY-DUTY VEHICLE

A. S. Verkner, A. Z. Asanov

MIREA - Russian Technological University, Institute of Cybernetics, Department of Automatic Systems,  
Moscow, Russia

[aleksverk@mail.ru](mailto:aleksverk@mail.ru)

### I. INTRODUCTION

The suspension is designed to reduce the intensity of vibration and dynamic loads acting on a person, the cargo being transported and the structural elements of the car when it is moving on an uneven road [1].

The purpose of this work is to develop and study a model of a four-point suspension of a vehicle using the example of a heavy-duty vehicle (HDV). The choice of such an object of research is due to the fact that such vehicles \ platforms can be specialized for solving a variety of tasks with different requirements for speed and stability of movement, smoothness, permissible longitudinal transverse \ vertical overloads, etc.

### II. FORMATTING MATHEMATICAL MODEL OF THE PLATFORM WITH A FOUR-POINT SUSPENSION

When constructing the mathematical model, the following assumptions were made [2]:

1. Transport platform is a solid body with a longitudinal plane of symmetry, ie. frame deformations are not taken into account;
2. The contact of wheels / tires with the road is constant and point;
3. Vibrations of the platform and wheels are small;
4. The movement of the vehicle is straight and uniform;
5. Forces of rolling resistance and air resistance not taken into account;
6. The masses of the front wheels are equal  $m_1 = m_2 = m_f$ , the masses of the rear wheels are equal  $m_3 = m_4 = m_r$ ;
7. Tire damping is not taken into account, since tire damping is insignificant in comparison with suspension damping;
8. The suspensions of the right and left wheels are mirrored, matching in stiffness and damping.

The general vibration model of a vehicle is called a complete car model. Such a model, shown in Figure 1, includes vertical movement of the body  $x$ , body roll  $\phi$ , body pitch  $\theta$ , wheel deflections  $x_1, x_2, x_3, x_4$  and independent road excitations  $y_1, y_2, y_3, y_4$ .

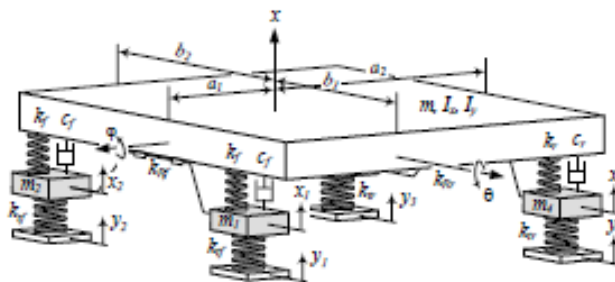


Figure 1. Four-point model of the platform

The equations of moments of inertia have the form

$$I_x = m b_1 b_2, \quad I_y = m a_1 a_2$$

$I_x$  – longitudinal moment of inertia of the mass,  $I_y$  – transverse moment of inertia of the mass,  $m$  – body weight,  $a_1$  – distance from the center of gravity of the car to the front axle,  $a_2$  – distance from the center of gravity of the car to the rear axle,  $b_1$  – the distance from the center of gravity of the car to the left side,  $b_2$  – the distance from the center of gravity of the car to the starboard side.

The stiffness of the front and rear tires is indicated by  $k_{if}$  and  $k_{ir}$  respectively. The suspension of the car has rigidity  $k_f$  and damping  $c_f$  in the front and rigidity  $k_r$  and damping  $c_r$  in the back [3].

The complete vibration model of the sprung part of the platform with a four-point suspension has seven degrees of freedom and can be described by the following equations obtained on the basis of Newton's laws:

$$m \ddot{z} + c_f (\dot{z}_1 + \dot{z}_2) + k_f (z_1 + z_2 - a_1 \theta) + k_r (z_3 + z_4 - b_2 \varphi - a_1 \theta) + k_r (z_3 - z_4 + b_1 \varphi + a_2 \theta) + k_r (z_4 + b_2 \varphi + a_2 \theta) = 0 \quad (1)$$

$$I_x \ddot{\theta} + b_2 c_f (\dot{z}_1 + \dot{z}_2) + b_2 k_f (z_1 + z_2 - a_1 \theta) - b_2 k_r (z_3 - z_4 - b_2 \varphi - a_1 \theta) - b_1 k_r (z_3 - z_4 + b_1 \varphi + a_2 \theta) + b_2 k_r (z_4 + b_2 \varphi + a_2 \theta) = 0 \quad (2)$$

$$I_y \ddot{\varphi} + a_1 c_f (\dot{z}_1 + \dot{z}_2) + a_1 k_f (z_1 + z_2 - a_1 \theta) - a_1 k_r (z_3 - z_4 - b_2 \varphi - a_1 \theta) + a_2 k_r (z_3 - z_4 + b_1 \varphi + a_2 \theta) + a_2 k_r (z_4 + b_2 \varphi + a_2 \theta) = 0 \quad (3)$$

$$m_f \ddot{z}_1 + k_{if} (z_1 - y_1) = 0 \quad (4)$$

$$m_f \ddot{z}_2 + k_{if} (z_2 - y_2) = 0 \quad (5)$$

$$m_r \ddot{z}_3 + k_{ir} (z_3 - y_3) = 0 \quad (6)$$

$$m_r \ddot{z}_4 + k_{ir} (z_4 - y_4) = 0 \quad (7)$$

### III. CONCLUSIONS

A mathematical vibration model of a vehicle platform with a four-point passive suspension is constructed. A computer numerical model of the vehicle platform with a four-point passive suspension is constructed. The conducted computer simulation using real numerical parameters of a specific vehicle - the KAMAZ-5490 heavy-duty vehicle showed the full operability and adequacy of the developed models.

### REFERENCES

- [1] Wong J.Y. Theory of ground vehicles. Third Edition. Ottawa: John Wiley & Sons, Inc, 2001.
- [2] Rajesh Rajamani Vehicle Dynamics and Control. State Minnesota: Springer, 2006.
- [3] Asanov A.Z. Introduction to mathematical modeling of control systems: Textbook / A.Z. Asanov. - M.: MIREA-Russian Technological University, 2019. -198 p.

## MATHEMATICAL SIMULATION OF THE SPATIAL SPREAD OF COVID-19 WAVES IN RUSSIA

V. V. Aristov<sup>1,2</sup>, A. V. Stroganov<sup>2</sup>, A. D. Yastrebov

1 Dorodnicyn Computing Center of Federal Research Center "Computer Science and Control" of Russian Academy of Sciences, Moscow, Russia

2 Federal State Budget Educational Institution of Higher Education «MIREA—Russian Technological University», Moscow, Russia

[aristovvl@yandex.ru](mailto:aristovvl@yandex.ru)

### I. INTRODUCTION

Problems related to the COVID-19 epidemic are of great interest around the world. The present work examines the processes of COVID-19 epidemic waves in Russia. There are assumptions that the main source of new infection carriers is Moscow and that the process of the virus' spread can be modeled by a kinetic equation. We develop our first results in [1]. The model under consideration makes it possible to judge the nature of the spread of a modern pandemic for some countries. For the first wave of the pandemic, the processes in Italy, Chile and Russia have been studied. Now the attention is paid on the epidemic events

in Russia for the second and third waves. The model has certain predictive capabilities, so the fourth wave is also studied.

## II. THE SPATIAL SPREAD OF THE WAVES OF THE COVID-19 PANDEMIC IN RUSSIA BASED ON THE KINETIC MODELS FOR A ONE- and TWO-DIMENSIONAL CASES

This work consists of two main parts. In the first part, the previously obtained one-dimensional kinetic model is used to predict and clarify the nature of the spread of the waves of the pandemic over the territory of Russia. In the second part, the model is generalized to a more complex and realistic two-dimensional case.

Since it is assumed that in the mentioned countries there were the main centers from where the spread of infection throughout the country took place, it is possible to determine the delay in the development of the disease in individual regions and in the country as a whole. This makes it possible to make certain predictions for the nature of the subsequent waves of the pandemic.

This work is a continuation of our previous one, in which the developed model is tested for the different waves of the pandemic in Russia. The present paper in particular examines the development of the third wave in Russia. The center of the spread of infection is, as in previous cases, Moscow. This seems to correspond to the real picture. This wave is associated with a new strain of the virus, penetrating mainly from India through Moscow airports. For the third wave, a prediction was made in early July that the number of infections per day for Russia as a whole would decline by mid-July of this year. This forecast was confirmed. Based on the values of the parameters found in the study of previous waves, predictions are made about the rate of spread of the pandemic, as well as about the speed of the "recovery wave". An important conclusion is that the maximums of infection in Moscow and Russia are separated by approximately 3 weeks. Comparisons are made with the actual data.

For a more detailed and accurate description of the spatial distribution of the epidemic, a problem with a two-dimensional geometry corresponding to the maps of the countries under study, and primarily the map of Russia. To do this, we write down the kinetic equation in two-dimensional form and use a numerical method to solve it, and thus acquire the first results for this model. The beginning of the fourth wave is also considered.

## REFERENCES

[1] Aristov, V.V.; Stroganov, A.V.; Yastrebov, A.D. Simulation of Spatial Spread of the COVID-19 Pandemic on the Basis of the Kinetic-Advection Model. *Physics* 2021, 3, 85-102. <https://doi.org/10.3390/physics3010008>.

## MODEL OF LOSSY LAYERED SYSTEMS

Y. I. Hudak, D. V. Parfenov, A. L. Beskin, I. P. Dragileva  
MIREA - Russian Technological University, Moscow, Russia

[hudak@mirea.ru](mailto:hudak@mirea.ru)

## I. INTRODUCTION

The analysis of energy relations in layered dielectric systems (LDS) with losses is important for many applications, mainly because it enables comparison of the obtained formulas with their counterparts for lossless systems.

## II. RESULTS

It turned out that for effective study of energy relations and their implications, it is necessary to refine significantly the conceptual and mathematical apparatus for solving the direct problem of the propagation of plane waves in lossy LDS. Under minimal assumptions, universal analytical expressions are derived for the elements of the transfer matrix  $T$ . This matrix describes all possible in such systems relations between plane electromagnetic fields to the left and to the right of the LDS in the form of functionals on the physical characteristics of the LDS and the field frequency, which allow understanding the spectral laws. A description of the spectral characteristics of an arbitrary LDS with losses is proposed and substantiated based on significantly expanded interpretation of the formulas found by P.G. Kard [1], refined in [2] and widely used for lossless LDS in [3] and [4].

This rises the theory of the direct problem to the level that provides the necessary data for the further development of the mathematical apparatus for the formulation and solution of optimization and inverse problems.

### III. CONCLUSIONS

Proof of the possibility of an extended interpretation of expressions derived by P.G. Kard will enable carrying out detailed analytical studies of the spectral properties of arbitrary LDS with losses, as well as estimation of their energy coefficients of reflection, transmission and losses. These are also necessary for the formulation and solution of problems of analysis and synthesis of dielectric filters for various purposes.

### REFERENCES

- [1] P.G. Kard. Analysis and synthesis of multilayer interference films, Valgus Publishing, 1971 [in Russian].
- [2] Yu.I. Hudak. On the translucence problem in the classical setting // Dokl. RAN, 2013, v. 448, № 5, pp. 1-4.
- [3] Yu.I. Hudak, D.V. Parfenov. Justification of profiling functions use for the efficient formulation of synthesis problems for layered dielectric filters. Radioengineering and Electronics, 2021, vol. 66, № 9, pp. 1–7.
- [4] Yu.I. Hudak, D.V.Parfenov, N.V. Muzylev, T.S. Khachlaev, The profiling function employment for task statement of layered dielectric filters synthesis. Russian Technological Journal. 2020, № 8 (5), pp. 103-114.

## 3D CAVE MODEL WITH SPARSE DATA

N. Lomov, A. Shelepin

Federal State Budget Educational Institution of Higher Education «MIREA—Russian Technological University», Moscow, Russia

[nikitalom@gmail.com](mailto:nikitalom@gmail.com)

### I. INTRODUCTION

Speleology is the science that studies caves. Currently, with the development and reduction of the cost of technology, an integral component of speleology is rapidly developing - topographic survey of caves, which involves determining the shape and size of the cave. The data collected in caves using various instruments (for example: compass, eclimeter, laser rangefinders) must be processed and visualized. This requires the appropriate programs. One of such programs is Topo [1].

Topo software allows you to process, edit and visualize the topographic data of the cave. An integral part of the visualization of the topographic survey of the cave is the display of its volumetric model. The volumetric model of a cave is needed to visualize it, to document the caves and to calculate such characteristics of the cave as length, surface area and volume. In addition, with the help of a volumetric model, it is possible to outline the most promising places for further research and search for the continuation of the cave.

The aim of this work is to construct a three-dimensional surface of a cave in conditions of sparse data within the Topo program.

### II. FORMULATION OF THE PROBLEM

The sparseness of the data means that intelligent algorithms are needed to process them and build on their basis the surface of the cave, which fill the "void". Without the use of such algorithms, an insufficiently visual representation of the cave is obtained, "twists" and sharp corners appear. The algorithm in the Topo program has these drawbacks. The algorithm is based on stitching polygons of adjacent pickets, which are obtained by traversing the shot points clockwise.

It is necessary to create and implement an algorithm for constructing a smooth three-dimensional cave model in conditions of sparse data.

### III. ALGORITHM FOR CONSTRUCTING A 3D CAVE MODEL WITH SPARSE DATA

The idea of the algorithm is as follows. First, the thread of the curve of the cave is smoothed out [2,3]. Then the shots are projected onto the normal plane of the resulting curve. After that, a normal vector is introduced on a smooth curve, which allows the connection of the coordinate systems from one section to another. Further, the interpolation of sections between pickets is carried out [4]. By sewing adjacent sections, the surface of the cave is obtained.

### IV. IMPLEMENTATION OF THE ALGORITHM WITHIN THE TOPO PROGRAM

Within the Topo program, the algorithm was implemented as a separate software module written in the C++ programming language. The input to the module is picket points with coordinates of shot points to neighboring pickets and coordinates of shots from pickets directly to the surface of the cave. The output is an array of polygons, which is directly used to display the cave model.

## V. CONCLUSIONS

The paper presents the results of the algorithm and carries out an analysis in comparison with the algorithm already available in the Topo program.

## REFERENCES

- [1] Speleology and Karstology Committee 2018. About Topo. URL: <http://rgo-speleo.ru/topo/topo.htm>.
- [2] A Primer on Bézier Curves 2020. A free, online book for when you really need to know how to do Bezier things. URL: <https://pomax.github.io/bezierinfo/> (accessed 27.09.2021).
- [3] V. V. Borisenko Construction of Optimal Bézier Splines. Journal of Mathematical Sciences. 2019. 237. pp. 375–386.
- [4] Seán Dineen, Multivariate Calculus and Geometry / Springer-Verlag London, 2014. – 257 p.

## DETERMINATION OF QUALITY INDICATORS OF CONTROLLED ELECTRIC DRIVES AT THE DESIGN STAGE BY THE METHOD OF CIRCUIT SIMULATION

V. Sleptsov, A. Ablaeva  
MIREA – Russian Technological University, Moscow, Russia  
[ablaeva@mirea.ru](mailto:ablaeva@mirea.ru)

## I. INTRODUCTION

At present, in industry the most widespread are flexible production systems, in which automated electric drives are the energy basis. In this case, the most common type of automated electric drive is a controlled electric drive (a drive closed in terms of the frequency of rotation of the shaft of the executive motor) – CED.

A lot of companies in developed countries are engaged in the development of CEDs - INDRAMAT, Siemens (Germany); Fanuc (Japan); Artech (Bulgaria), Triol (Russia), etc.

Due to the fact that the characteristics of technological machines largely depend on the quality indicators of electronic components, serious attention is paid to the issues of their improvement and regulation. This is how GOST 27803-91 "Adjustable electric drives for metalworking equipment and industrial robots. Technical requirements". It indicates the main technical characteristics of the CED and the ways of their determination, which should include the following: the speed control range, the coefficient of unevenness of the rotation frequency and the frequency bandwidth of the CED.

To determine the real quality indicators of the developed and produced electronic devices, rather complicated and expensive stands are used [1]. Therefore, an urgent and important task is the development of a mathematical and software apparatus that allows analyzing the quality indicators of a CED at the stages of development, manufacture and operation.

This work analyzes the quality indicators of a controlled electric drive based on an S-220-60-VD-2 servo amplifier and a KM-090-32-02 valve motor, built according to a typical scheme similar to EPS-B1-0D75AA (Germany).

## II. MATERIALS AND METHODS

To carry out circuit simulation, a mathematical model of the CED was developed. The authors found that for circuitry modeling of such a CED, the most convenient is the mathematical model of a valve motor (VM), described by the equations presented in [2].

The developed mathematical model of a controlled electric drive in the form of a structural diagram can be represented as in Fig. 1.

## III. RESULTS

The following designations are adopted:

$W_{rs}(S)$ ,  $W_{rc}(S)$  – transfer functions of the speed controller and currents;  $K_{psa}$ ,  $K_{psb}$ ,  $K_{psc}$  – transfer ratios of phase current sensors;  $F_1$  - nonlinearities of the "limiting" type of the signal;  $F_2$  – non-linearities of the PWM "relay" type;  $F_3$  – PWM nonlinearity;  $F_4$  – nonlinearity of positive signal extraction;  $K_{rps}$  – transmission coefficient of the rotor position sensor;  $K_{ss}$  – transmission coefficient of the speed sensor;  $A_{P_{PWM}}$ ,  $T_{P_{PWM}}$  – PWM amplitude and frequency;  $U_{rs}$ ,  $U_{ss}$  - signals of speed setting and from the speed sensor;  $U_{rca}$ ,  $U_{rcb}$ ,  $U_{rc}$ ,  $U_{csa}$ ,  $U_{csb}$ ,  $U_{csc}$  – assignment signals and from phase current sensors;  $U_{sr}$  – signal from the speed regulator;  $U_{rm}$  - torque setting signal;  $U_{cr}$  – signals from current regulators;  $U_y$  – control signals;  $U_{tv}$  –

signal from the triangular voltage generator;  $U_{sa}, U_{sb}, U_{sc}, I_{sa}, I_{sb}, I_{sc}$  – phase voltages and currents;  $V, P$  – speed and position of the motor shaft.

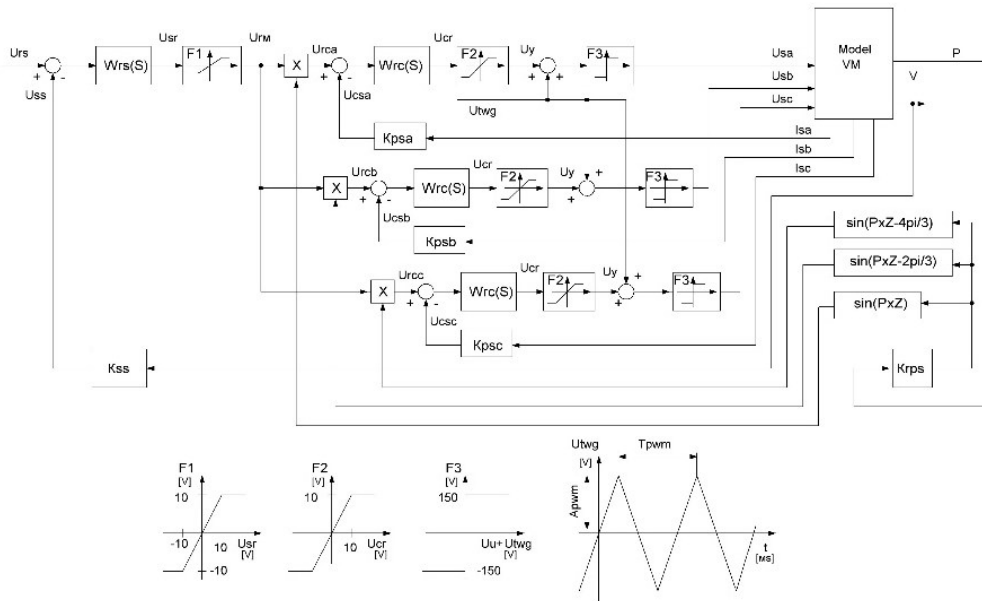


Figure 1. Mathematical model of a controlled electric drive with three current loops

The transfer functions of the phase current regulators are selected from the conditions for adjusting the circuits to the technical optimum, the transfer function of the speed controller is selected from the conditions for adjusting the circuit to the symmetric optimum [3].

Mathematical modeling of the CED will be carried out in accordance with the requirements and methodology set forth in GOST 27803-91:

- determination of the tachogram of the CED after the signal  $U_{rs}(t) = \pm 0.001 \text{ V}$  is fed to its input and the determination the coefficients of uneven rotation from the obtained tachogram;
- determination of the tachogram in the CED after the signal is applied to its input  $U_{rs}(t) = 0.1 \times \sin(3000 \times t)$  and the determination of the frequency bandwidth from the obtained tachogram.

The simulation results are shown in Fig. 2.

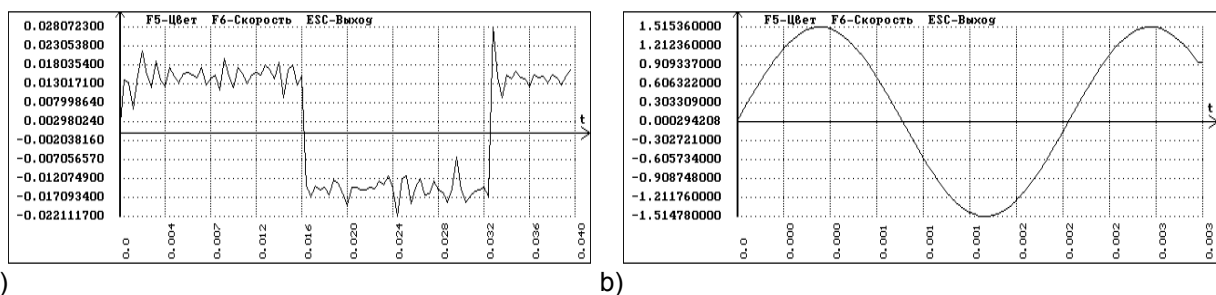


Figure 2. Tachograms at  $U_{rs}(t) = \pm 0.001 \text{ V}$  – a), at  $U_{rs}(t) = 0.1 \times \sin(3000 \times t)$  – b)

#### IV. CONCLUSIONS

Analysis of the obtained tachograms allows us to draw the following conclusions:

- the range of speed control of the considered electric drive is 10,000;
- the coefficient of unevenness of the rotational speed does not exceed 25%;
- the bandwidth of the frequencies is 480 Hz.

It should be noted that experimental studies of the prototype of the CED under consideration confirmed the correctness of the calculations – the range of the electric drive rotation frequency control was 10,000, but the frequency bandwidth was 450 Hz.

#### REFERENCES

[1] V.V. Sleptsov, A.G. Shmeleva, A.A. Galemina “Development of a stand for determining the technical characteristics of speed-controlled electric drives”, Instrumentation, Vol. 4 pp. 26-32, 2017.

[2] O.A. Rokachevskii, V.V. Sleptsov, A.E. Ablaeva, S.A. Kanaev and O.V. Moskalenko "Metrological assurance of the characteristics of electric drives at the design stage", Journal of Physics: Conference Series, Vol. 1889, ICMSIT-II 2021, pp.3-6. 2021, doi: 10.1088/1742-6596/1889/4/042057.

[3] V.V. Sleptsov, O.A. Rokachevskii, A.E. Ablaeva "Development of a highly efficient electric drive with a brushless motor", Instrumentation, Vol. 10, pp. 26-29, 2017.

## **MACHINE LEARNING METHODS FOR EVALUATING INNOVATIVE PROJECTS**

A. Shmeleva, I. Goldobin, E. Klimova, A. Moskvin, Y. Lygarev  
MIREA – Russian Technological University, Moscow, Russia

[ilya.goldobin1@gmail.com](mailto:ilya.goldobin1@gmail.com)

### **I. INTRODUCTION**

Modern trends in digitalization and the introduction of decision support information systems in various areas determine the need for the development of mathematical modeling methods applicable to data analysis. Machine learning methods are of particular relevance for solving applied problems, which allow, using the available data, to establish the mutual influence of the characteristics of the objects under study. Mathematical methods and their implementation in the form of machine learning algorithms allow the decision maker to rely on the results of solving problems using various algorithms to determine the optimal control strategy, comparing them by assessing the accuracy.

Strategic development and competitiveness in the market of a company, corporation - any organization of small, medium and large business requires the availability of market analysis tools, the creation and assessment of unique, innovative solutions (technologies) and their further implementation, which guarantees companies of any level of prosperity in the digital economy. Mathematical modeling and machine learning algorithms are gaining popularity in the field of analysis of heterogeneous data for decision-making due to the possibility of exploring alternatives using simulation of situations, varying parameters and evaluating them. The article presents an example of the applicability of the scoring model to the assessment of innovative projects.

### **II. MATERIALS AND METHODS**

The company's competitiveness in the market is ensured by the availability of innovative projects, start-ups, the selection and assessment of the characteristics of which is often a difficult task to formalize. Generators of startups and innovation projects are not always employees of the companies themselves. Often, campaigns looking through scientific project competitions, hackathons, and large companies organize their own competitions for the selection of promising projects. Any invention, innovative project, startup needs financial investment for development, and the creators of ideas are interested in finding companies that can evaluate the project and provide financial support. For example, various business angels and funds can act as an investor. A business angel is usually a private investor who is able to support a project, but finding an investor is a difficult task for a startup. In Russia, there are Funds aimed at financing innovative projects, Science Cities are being created, for example, Skolkovo, Innopolis, which are focused on finding and helping in the implementation of startups. Many young enterprises resort to the help of the Foundations, which organizes a competitive environment and allows the foundations to choose the most attractive projects in their opinion. For investors, the issue of evaluating innovative projects is relevant - this issue has acquired particular importance in connection with the current situation of necessary self-isolation in the context of a global pandemic and the need to support the transition to the digital economy to ensure competitiveness in the market. The paper presents the results of simulation modeling for evaluating innovative projects, we developed a mathematical model for evaluating innovative projects based on scoring modeling for evaluating the characteristics of projects. Scoring is well established in the banking industry and is widely used to assess customer creditworthiness.

Assessment of the borrower is carried out everywhere by banks and credit institutions when issuing funds for various needs. Banks have an information system based on a scoring model that takes into account various assessed characteristics of a person, which allows them to evaluate a client to form a final score in order to make a decision on the allocation of funds. In many banks forms of online interaction with a client for obtaining a loan have been developed, through a questionnaire presented on the bank's website. In Russia, there is a United Credit Bureau, which, based on a scoring model, provides clients with highly effective services for risk assessment, loan portfolio management and anti-fraud [1]. For innovative projects assessed by Foundations and companies, it is possible to use scoring to assess the prospects and competitiveness of the project in the first approximation. The digitalization of the economy and the transition to an online format for analyzing applications for financing innovative projects and use of mathematical methods have a number



of significant advantages in contrast to manual processing of applications, which contains the subjectivity of the decision maker and takes a lot of time to make decisions. Machine learning methods make it possible to automate these processes to a large extent. The training takes place on statistically collected data and solutions. The sample must be divided into training and test components to check the parameters of the trained algorithm in order to eliminate the problem of overfitting. The authors have developed a scoring model for evaluating innovative projects. To solve this problem, the following artificial intelligence methods can be applied: logistic regression, support vector machine, random forest and decision trees.

To assess innovative projects, a scoring model was developed to support decision-making to determine whether the characteristics of the project meet the interests of the investor. For this model, machine learning algorithms are implemented and a comparison is made. The best answer was shown by the decision tree algorithm, the results of the constructed decision tree are presented in Figure 1. For model training we used such signs as the age of a person looking for an investment, whether he has a good presentation of a product and a prototype, an indicator of his environment, expressed in his professional maturity in its areas, the investments required for the project, the investor's interest in the subject of the project, the number of projects successfully implemented by the entrepreneur, the estimated payback period, as well as the completeness and breadth of the business plan.

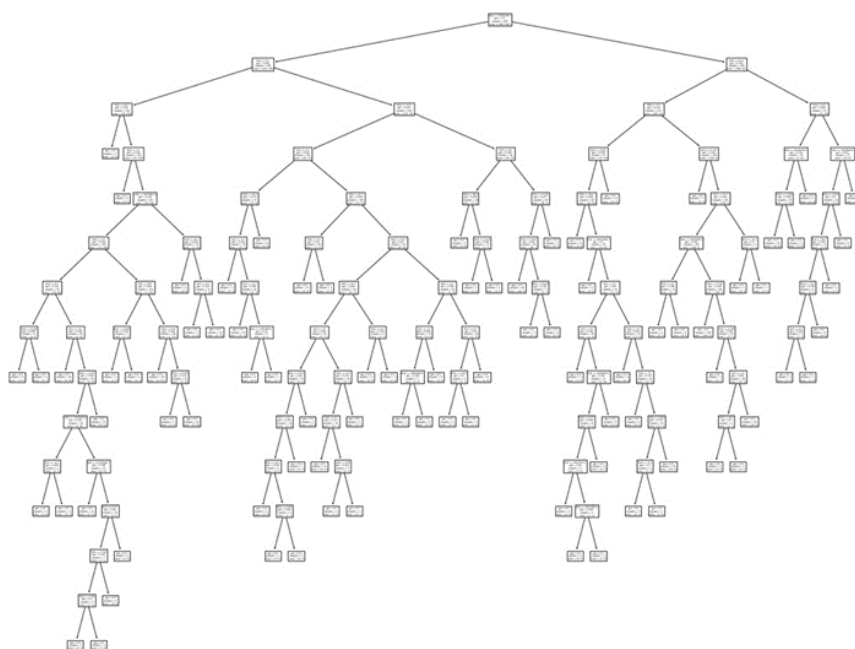


Figure 1. Visual representation of the decision making model

When constructing the model, a decision tree classifier was used, with the help of which the most important parameters in the data were identified, and a decision-making model was built and trained. To assess the quality of the decision tree model, cross-validation methods were used to evaluate the analytical model on independent data, however, the AUC-ROC metric is considered a better indicator for this task. The trained model has performance of 0.85 according to the AUC-ROC metric, which is considered an excellent result and indicates the possibility of using the constructed model in the consideration of existing investment funds for evaluating innovative projects.

### III. CONCLUSIONS

The use of mathematical methods and machine learning algorithms based on them for solving applied decision-making problems is an urgent development of information technologies. Note that the proposed methods will automate and optimize the processing of projects submitted for consideration. In essence, the developed mathematical model and its implementation are a prototype of an expert decision-making system. The results obtained when solving the problem of evaluating innovative projects show the applicability of machine learning and artificial intelligence methods, which allow evaluating the characteristics of a project and selecting the most promising ones in order to minimize the risks of investors.

### REFERENCES

[1] United credit bureau [Electronic resource]: [https://bki-okb.ru/sites/default/files/service\\_documents/scoring\\_2019.pdf](https://bki-okb.ru/sites/default/files/service_documents/scoring_2019.pdf) (date of access 05.10.2021).

## DISTANCE LEARNING AS AN IMPERATIVE FOR DIGITALIZATION OF EDUCATION

M. Beskhmel'nov, N. Shmeleva, S. Shilkov, M. Lygarev  
MIREA – Russian Technological University, Moscow, Russia

[beskhmel'nov@internet.ru](mailto:beskhmel'nov@internet.ru)

### I. INTRODUCTION

The rapid development and penetration of information technologies into various spheres of human life lead to significant issues of improving the learning processes and their partial digitalization in higher educational institutions. Initially, the processes of education digitalization were focused on the creation of sites made for practicing and video content accompanying the discipline, teaching of which was carried out in the classical form of traditional classroom learning, in order to provide free access to materials with the goal of a deeper education and understanding of the studied sections. The introduction of online lectures and master classes with the involvement of experts from companies and organizations interested in graduates of higher educational institutions made it possible to expand the degree of interaction with the target audience, to motivate the study of additional aspects of professional disciplines.

However, the events of 2020 have radically changed the role and significance of education digitalization. The coronavirus COVID-19 arrived in Russia at the end of January 2020. In March, a period of forced self-isolation started, which required the prompt formation of online education systems in higher education institutions.

The main issue of education digitalization today is development and creation of high-quality technologies. For professor of higher institutions, it is relevant to introduce technologies for effective interaction with students both in traditional classroom learning and online, creating high-quality video content, the ability to quickly respond to external factors and combine different forms of educational technologies to achieve the appropriate level of knowledge dictated by the modern market labor.

### II. MATERIALS AND METHODS

The main task of the Universities is to ensure the continuity of education processes both in traditional and online classes, regardless of the external negative factors that civilization has faced in recent years. In 2019, Russia identified national projects for the country's strategic development [1], which form a list of targets and key results up to 2025. One of the projects that is worth noting is " Human resources for the digital economy " of the national program "Digital Economy of the Russian Federation" [2], which defines the list of key competencies of the graduate: communication in the digital environment, self-development in conditions of uncertainty, creative thinking, information and data management. All of the above determines the need to modernize learning processes, including using online education technologies.

The implementation of distance learning is a complex task containing many requirements for higher education institutions and teachers. From the higher educational institution's side, online learning bears significant additional financial costs for providing the necessary tools for interaction between teachers and students: creating or conclusion of contract with services for providing online lectures (webinars), developing personal accounts, designing additional hardware (servers) for processing and data storage, creation of support centers, training of lecturers and many others. It should be noted that the introduction of online learning entailed an additional burden on teachers: studying online platforms, preparing presentations, reviewing assignments, interacting with students, clarification of discipline material, commenting on works. For students, the difficulty is in adaptation to the requirements and the ability to perceive information in the absence of control provided by the teacher during the lesson. When studying disciplines online, self-motivation for learning and the ability to concentrate on important concepts of the lecture has a huge role for students. The positive aspects of online education for students is the availability at any time of educational and methodological complexes of disciplines, and for the teacher the ability to control the completion of assignments, exam answers, which entails an increase in the objectivity of the assessment of knowledge.

Online learning is gaining popularity nowadays and it is the most widespread for teaching programming. There are a number of online platforms offering both fee-based and free training courses, you'll be rewarded with a certificate when you successfully complete your course. Large IT companies also organize such courses with the goal of training and attracting the best students for work. Let's analyze the structure of online training courses more closely. Usually, the course contains video lectures, practical exercises, assignments for self-educating and tests to check the acquired knowledge. We would like to draw your attention to the fact that the lectures are short in duration (15-20 minutes) videos this is done in order to present the material in a form that is easy to understand and eliminate the loss of the student's attention. After watching the video lectures, practical lessons are given in an online format, which are also not too long and try to fit into a time interval of no more than 30 minutes. For independent work, the student himself

determines the time in accordance with the amount of basic knowledge and the deadlines. An important aspect in online learning is the self-motivation of the listener. Most of the students studying on online platforms do not reach the final certification, stopping training for various reasons, for example, associated with the emerging difficulties of independent study of the material and lack of time.

The main issue of successful implementation of online learning for Universities is maintaining self-motivation and students' pursuit of knowledge. In our opinion, the necessary conditions for the formation of the competencies required by the market and the support of students' desire to set a goal and achieve excellent results largely depends on the teacher and his skills and in using information technologies in the educational process. In the classical offline form of studying, it is much easier for the teacher to contact the audience and monitor the level of mastering the given material, to maintain interest in the discipline being studied. In an online format, interaction with the audience is difficult, and the teacher is uncomfortable faced with a lack of understanding the amount of perception the material by students, therefore, the question of what requirements should be met by online learning is relevant at the present time.

A special role in the digitalization of education with online technologies is assigned to the study of disciplines related to mathematical modeling, including areas of applied mathematics and programming technology. In the market of professions, graduates with the knowledge and skills of mathematical modeling for processing and analyzing information are most in demand. The technologies of artificial intelligence and machine learning used to solve applied problems from different fields of knowledge are a combination of mathematical methods, algorithms and programming languages and are most in demand on the labor market, which determines the need to train personnel corresponding to the trends in time using, among other things, online learning technologies. ... Free software, containing many libraries, the presence of open information source, gives the teacher an opportunity to use modern technologies in the educational process, while we note that it imposes an additional burden on preparing for classes. The creation of online courses in the field of mathematical modeling and machine learning will be most in demand. The fact that the University has an online education system and online courses in partially open access is one of the indicators of a modern digital university.

### III. CONCLUSIONS

Online education technologies will develop rapidly in the upcoming years. For Universities, the creation of high-quality online courses and their partial placement in the open access will play a huge role in attracting applicants. We would like to note that in MIREA - the Russian Technological University, an online education platform successfully exists and is being modernized for emerging tasks, providing many opportunities for interaction between teachers and students. Of course, many issues of online learning remain open, but it should be noted that online learning also opens up many opportunities that are a huge part in the development of information technologies, digitalization of education processes, and training of in-demand personnel for the digital economy.

### REFERENCES

[1] National projects: targets and main results [Electronic resource]: <http://static.government.ru/media/files/p7nn2CS0pVhvQ98OwAt2dzCIAietQih.pdf> (date of access 05.10.2021).

[2] Personnel for the digital economy of the national program "Digital Economy of the Russian Federation" [https://www.economy.gov.ru/material/file/bd31fe31b5135c35e402b702c346f304/41\\_24012020.pdf](https://www.economy.gov.ru/material/file/bd31fe31b5135c35e402b702c346f304/41_24012020.pdf) (accessed 05.10.2021).

## **DESTRUCTION PROCESSES IN POWER PLANTS AS A PRACTICAL EXAMPLE FOR THE COURSE OF MATHEMATICAL MODELING**

V. P. Kulagin, A. E. Alexandrov  
MIREA – Russian Technological University, Moscow, Russia

[corresponding.author@email.com](mailto:corresponding.author@email.com)

### I. INTRODUCTION

The study of various disciplines related to mathematical modeling often raises the question of selecting a successful subject area for building a model. In the framework of this work, a model of progressive destruction of pipelines used in power plant power units is considered. The destruction of such pipelines can lead to catastrophic consequences. Mathematical modeling is used to reduce the amount of work on "physical" diagnostics.

The model described in the paper allows students to become more familiar with the basic approaches used in statistical modeling, the use of various types of probability distributions, and the use of the Monte Carlo method for calculations.

The mathematical model of the destruction of elements of power systems, analyzed in the classroom, is considered in the form of a computer program with the with a fairly wide functionality.

In order to simplify understanding, it is divided into separate modules, each of which is considered in a separate lesson.

Module №1 "Calculation of defect size distributions parameters";

Module №2 "Import of stress condition";

Module № 3 "Formation of real flaws parameters distributions tables";

Module №4 "Calculation of cyclic flaw growth";

Module №5 "Probabilistic analysis of ductile fracture".

#### a. Calculation of defect size distributions parameters

The specified module calculates the distribution parameters for the provided sample of the detected defects sizes. The calculation is performed for the following distributions: normal, lognormal, exponential, two-parameter Weibull. In addition, the module calculates the parameters of the histogram of relative frequencies. There are no restrictions on the use of this module.

The input data of the module are: a sample of N elements  $x_1, x_2, \dots, x_N$ , each element describes the size of an individual detected defect in mm;

k is the number of columns (intervals) of the histogram of relative frequencies.

The output data of the module are: parameters of the distributions of the dimensions of the detected defects in mm; parameters of the histogram of relative frequencies (columns and their heights).

#### b. Module №2 "Import of stress condition";

The calculation of the stress state is performed in a third-party program and is not considered in this paper.

#### c. Module №3 Formation of Real Fractures Parameters Distributions Tables

The specified module is designed to perform the following operations:

– formation of a table of the function  $g(a)$ , approximating the density of distribution of the depths of real fractures in the interval  $[a_{min}, s]$ , depending on the options selected;

- formation of a table of the function  $g(ac\_ratio)$  approximating the distribution density of the ratio of the semiaxes of the flaws in the interval  $[0, 1]$ ;

– calculating the value of the density of defects in a pipeline element for real flaws.

The described operations are performed based on the data for the detected flaws and depending on the options selected. Available options:

– only detected defects;

– discovered defects with the addition of undetected defects;

– detected defects with the addition of undetected defects and modeling of the repair.

The module has the following limitations of applicability:

#### d. Probabilistic Analysis of Ductile Fracture

The module calculates the probability of ductile fracture from through flaws, the probability of ductile fracture from surface flaws, the probability of the formation of a through flaw, the probability of a stable through flaw, using Monte Carlo method for a pipeline element at a given operating mode. The results for the element are obtained based on the calculation in the section of the pipe in the presence of one flaw.

Based on the lengths of stable through flaws, the probability of a stable through flaw in the element and the specified intervals of the nominal leak diameters, the module calculates the probability of stable leak formation for the intervals of the nominal diameters.

The module's limitations are as follows:

The random parameters are: flaw depth, ratio of flaw semiaxes.

The operating mode is set by voltage and temperature [4]. It is assumed that the regime consists of one moment in time.

The load and temperature are assumed to be uniform over the pipe wall thickness.

In direct modeling of random flaws in the entire probability space, a problem arises - the events under study have a nonzero probability only for large defects. However, the probability of the appearance of a defect with large dimensions is very small, which leads to the need for a large number of experiments with a corresponding increase in the calculation time. To get around this problem, the ability to divide the probabilistic space into non-intersecting regions called cells was implemented (implementation of a stratified sample).

## II. CONCLUSIONS

For each cell, separate Monte Carlo simulation is performed, and then the results of all cells are combined. To do this, each result obtained inside a cell must be multiplied by the probability of a flaw hitting the corresponding cell.

The use of cells can significantly reduce the variance of the results, reduce the number of experiments and the calculation time.

## REFERENCES

- [1] Berens, A. P.: Probability of Detection (PoD) Analysis for the Advanced Retirement for Cause (RFC). Engine Structural Integrity Program (ENSIP) Nondestructive Evaluation (NDE) System Development, vol. 1, PoD Analysis. Finalreport p. 88 (2000). AFRL-ML-WP-TR-2001-4010.
- [2] Berens, A. P.: NDE Reliability Data Analysis in Non-Destructive Evaluation and Quality Control: Qualitative Non-Destructive Evaluation, ASM Metals Data Book, ASM International 17, 689 (1989).
- [3] Filinov, V. V., Mikaeva, S. A., Rodyukov, M. S., Filinova, A. V.: Modern Architecture Board Information and Control Systems of Heavy Vehicles. Russian Technological Journal 5(3), 114-123 (2017). [https://rtj.mirea.ru/upload/medialibrary/2c4/rtzh\\_3\\_2017\\_114\\_123.pdf](https://rtj.mirea.ru/upload/medialibrary/2c4/rtzh_3_2017_114_123.pdf).
- [4] Getman, A. F., Kozin, Yu. N.: Non-Destructive Control and Safety of Operation of Pressure Vessels and Pipelines. Energoatomizdat, Moscow, Russia p. 288 (1997).
- [5] Gandossi, L., Annis, C.: Probability of Detection Curves: Statistical Best-Practices. ENIQ report No. 41, European Commission Joint Research Centre Institute for Energy, EUR 24429 EN, (2010).
- [6] Casella, G., Berger, R: Statistical Inference, Duxbury Press (1990).
- [7] Berens, A. P., Hovey, P. W.: Flaw Detection Reliability Criteria. vol. 1. Methods and Results, AD-A142 001, Dayton Univ OH Research Inst, Final technical report (1984).
- [8] Kryzhanovsky, A. D., Pastushkova, A. A.: Nonparametric Method of Reconstructing Probability Density According to the Observations of a Random Variable. Russian Technological Journal 6(3), 31-38 (2018). [https://rtj.mirea.ru/upload/medialibrary/a84/RTZH\\_3\\_2018\\_31\\_38.pdf](https://rtj.mirea.ru/upload/medialibrary/a84/RTZH_3_2018_31_38.pdf).

## **SIMULATION OF SOME SECURITY TASKS FOR SECURE TELECOMMUNICATIONS USING A QUANTUM-COMPUTING SIMULATOR IN ONE OF THE QUANTUM PROGRAMMING LANGUAGES**

A. A. Kryuchkov, A. V. Korolkov  
RTU MIREA, Moscow, Russian Federation

[andrai12@mail.ru](mailto:andrai12@mail.ru)

## I. INTRODUCTION

In Russia, as part of the implementation of the national program "Digital Economy of the Russian Federation", a roadmap for the development of the high-tech area "Quantum Communications" is being implemented since 2020. One of the most important elements that ensure the effective use of quantum communications are quantum key distribution protocols. These protocols must be resistant to known attacks on quantum communication channels, as well as to the possible appearance of quantum computers that implement threats to decrypt information.

The main issue of symmetric cryptography is how to securely distribute the secret key among legitimate users. Quantum cryptography provides the ability to securely generate a secret sequence between

participants in information exchange, ensuring that the key cannot be intercepted by an intruder. Quantum protocols are based on the fundamental laws of quantum physics combined with a provable mathematical apparatus.

The BB84 protocol is widely used to implement quantum key distribution. Modeling this protocol using remote quantum programming on a quantum computer is the main subject of this article.

In the submitted article:

1. Quantum programming methods are applied to simulate quantum key distribution according to the BB84 protocol. The process of quantum key distribution was simulated using a quantum computer model and also by means of a real 5-qubit quantum computer provided by IBM.
2. An attempt to intercept a private key by an intruder with an attack "man-in-the-middle" was simulated.
3. The results of modeling the BB84 protocol are presented. The security of the mathematical model for generating a secret key between users has been confirmed.
4. The analysis of practical implementations of quantum key distribution to date is given.

## II. MAIN DIAGRAMS AND FORMULAS



Figure 1. The scheme of the quantum protocol BB84

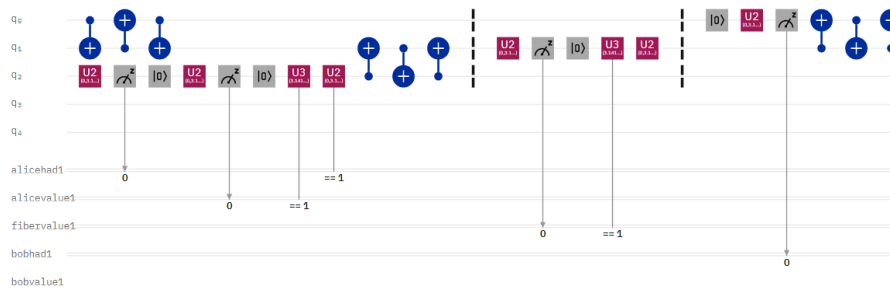


Figure 2. The scheme of the quantum protocol BB84 on an IBM quantum simulator

A two-level quantum mechanical system is defined by a linear superposition of its own states  $|0\rangle$  and  $|1\rangle$  (1)

$$|\Psi\rangle = \alpha|0\rangle + \beta|1\rangle, \quad (1)$$

where  $\alpha$  and  $\beta$  are complex coefficients satisfying equality:

$$|\alpha|^2 + |\beta|^2 = 1 \quad (2)$$

The description of the quantum states of the system is given by the following expressions:

$$|0_x\rangle = \frac{1}{\sqrt{2}}(|0_+\rangle + |1_+\rangle) \quad (3.1)$$

$$|1_x\rangle = \frac{1}{\sqrt{2}}(|0_+\rangle - |1_+\rangle) \quad (3.2)$$

## REFERENCES

- [1] C. H. Bennett and G. Brassard. "Quantum cryptography: Public key distribution and coin tossing". In Proceedings of IEEE International Conference on Computers, Systems and Signal Processing, volume 175, page 8. New York, 1984.
- [2] I. Chang M. Nilsen, "Quantum computation and quantum information", Mir, pp. 711-714, 2006.

# SOFTWARE TOOL FOR EVALUATION OF RELIABILITY AND SURVIVABILITY OF COMPLEX TECHNICAL SYSTEM BASES ON LOGICAL-PROBABILISTIC METHODOLOGY

V. Skobtsov<sup>1</sup>, N. Lapitskaja<sup>2</sup>

1 United Institute of Informatics Problems, National Academy of Sciences of Belarus Minsk, Belarus

2 Belarusian State University of Informatics and Radioelectronics, Minsk, Belarus

[vasko\\_vasko@mail.ru](mailto:vasko_vasko@mail.ru)

## I. INTRODUCTION

The paper presents software tool for evaluation of reliability and survivability for complex systems based on the logical-probabilistic approach. The correctness of suggested method and software tool was shown by computational experiments on some onboard equipment systems of small satellites (SS) similar to Belarusian SS, later compared with "Arbitr" software complex (certified by Rostekhnadzor, RF [1]) results.

The software tool was integrated into the system of methodologies and software tools for evaluation, analysis and prediction of the values of reliability and survivability indicators for complex system. The system was integrated with the distributed software system for multi-objective assessment, analysis and prediction of values of reliability and survivability for OE SS developed in SPIIRAS (Saint-Petersburg, RF).

## II. THE LOGICAL-PROBABILISTIC METHODOLOGY

In logic-probabilistic methodology a Boolean function as a logical model of system reliability and survivability is applied. It is called a logical function of the system operability (FSO).

A logical function of the system operability represents a set of states in which the system implements an appropriate criterion of its functioning (system health state). A logical criterion can be determined by different properties of the system.

The initial data for determining a logical FSO are:

- diagram of functional integrity (DFI),
- logical criteria of functioning (LCF) of system.

The features and restrictions of complex system design allow to apply one of the simplest methods of direct analytic substitution for FSO construction.

It provides a consistent replacement in the logical FSO of all integrative functions by their equations selected from the system. Such substitution is performed until there are no undeclared functions in the resulting expression. In other words, all integrative functions will be replaced by simple logical variables.

The functional elements commute with each other only through logical elements. Introduction of these vertices does not change the probability of failure-free operation and the reliability and survivability of the systems at all. As a rule, the scheme is created on the basis of four logical constructions (see Fig.1).

In order to create more complex structures, logical elements can be commuted with each other in any quantity. The width and depth search algorithms are used for graph navigation.

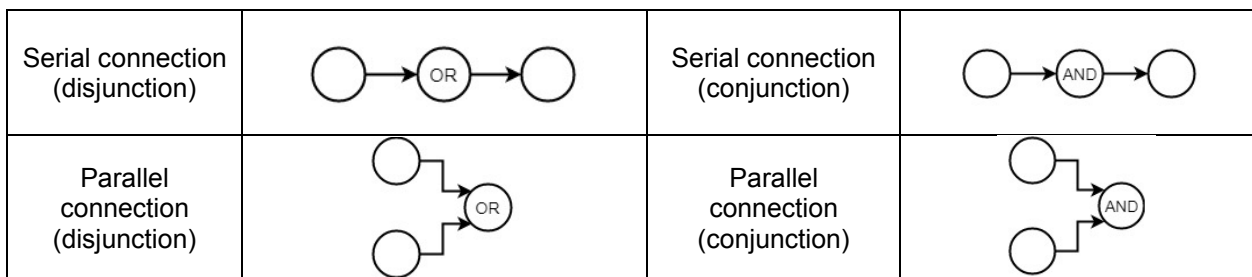


Figure 1. Basic types of logical constructions

At each stage for each structural node, the probabilities of failure-free operation and survivability are recalculated and transferred to the next vertex. Thus, each vertex contains information about calculations on all previous vertices. And whenever we get to any vertex, we can always get the probabilities obtained for the previous vertices.

Correspondent software tool, based on the logical-probabilistic approach and the proposed algorithm, was developed in two versions: a desktop version and web one. The software tool was designed to automate the process of evaluating the reliability and survivability of complex systems. The tool implements the following functions:

- graphical input and editing DFI representing a device under analysis (Fig.2);
- input and editing the system elements;
- calculating the single value of the system reliability for the given single arguments of failure-free operation probability for structural nodes;
- reliability analysis – calculating the values of the complex systems reliability for the series of elements probability arguments and drawing graphics (Fig.2), in this case elements probability parameters are equally changed by step;
- survivability analysis – calculating the survivability of complex systems with full and partial failure and drawing graphic, the damaging factor is applied to randomly selected  $k$  elements which reduces the probability of failure-free operation  $p_i$  of these elements to 0 in case of full failure and in case of partial failure to  $\tilde{p}_i < p_i$  that can OE set throw interface. The experiment is repeated  $N$  times.

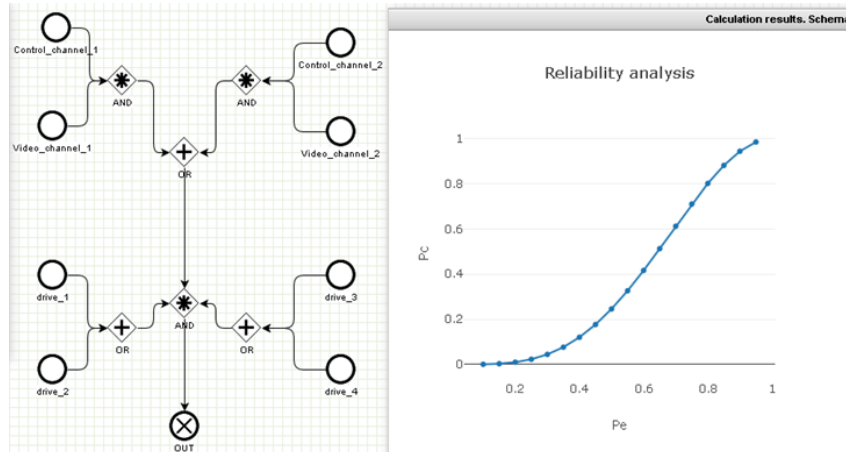


Figure 2. Window for calculating, reliability analysis (web-interface)

### III. CONCLUSIONS

The evaluation of reliability and survivability of the complex technical systems, like BE SS is an important task of their safe and reliable design and operation. The logical-probabilistic theory of reliability and survivability allows objective identification of the "thinnest" and most dangerous places, causes and preferred combinations of initiating conditions, the protection against which prevents the system from getting into a dangerous state. Therefore, suggested approach and tool could be applied at the step of the development and modeling complex systems for project reliability and survivability assessment.

### ACKNOWLEDGMENTS

The research described in this paper is supported by Program of Union State "Monitoring-SG" (project 6MCG/13-224-2).

### REFERENCES

- [1] V. Skobtsov, N. Lapitskaja, R. Saksonov, and S. Potryasaev, "Automated Logical-Probabilistic Methodology and Software Tool as Component of the Complex of Methodologies and Software Tools for Evaluation of Reliability and Survivability of Onboard Equipment of Small Satellites", Proc. of 7th Computer Science On-line Conference 2018 (CSOC 2018) "Software Engineering and Algorithms in Intelligent Systems". In Advances in Intelligent Systems and Computing, Vol. 763, Springer, pp.452-463.

## REPRESENTATION OF A TRANSMISSION MODEL WITH CONTINUOUS POWER FLOW IN STATE SPACE

A. Z. Asanov, E. O. Guryanova

MIREA – Russian Technological University, Moscow, Russia

[guryanova-e.o@yandex.ru](mailto:guryanova-e.o@yandex.ru)

### I. INTRODUCTION

Continuous flow power transmissions are widely used in the construction of land vehicles operating in difficult operating conditions. The dual-clutch transmission can also be used on robotic vehicle modifications. Comparative analysis of various types of double-flow clutches shows the preference of using wet double-flow clutches in high-power transport complexes [1].



In this paper, a model of a two-stream transmission was considered, designed to build an integrated control system for the power units of a heavy vehicle for the most efficient movement, including in a semi-autonomous mode.

## II. MODELLING

The presence of a detailed model of the dual-clutch transmission makes it possible to switch to a simplified model with linearization of characteristics for the synthesis of an adaptive control system. In addition, the detailed model can be used to verify adequacy.

A scheme was used in which the components of the transmission can be described in the form of elements characterized by either inertia or compliance:  $J_e$  is the moment of inertia of the engine,  $J_{cl1}$ ,  $J_{cl2}$  is the moment of inertia of the 1st and 2nd clutch, respectively,  $J_{g1}$ ,  $J_{g2}$  is the moment inertia for transmission channels of odd and even series, respectively,  $J_3$  is the moment of inertia of the wheel drive,  $J_v$  is the moment of inertia of the center of mass of the vehicle,  $\omega_e$  is the angle of rotation of the crankshaft of the internal combustion engine,  $\omega_{cl1}$ ,  $\omega_{cl2}$  is the angle of the input shaft of the 1st and 2nd clutches,  $\omega_{g1}$ ,  $\omega_{g2}$  is the angle of rotation of the intermediate shaft of the transmission,  $\omega_3$  – the angle of rotation of the wheel drive,  $\omega_v$  – the angle of the longitudinal axis of the vehicle.

Vibrations in such a description are reflected through the coefficients of stiffness and damping, which occur at certain sections of the joint [2].

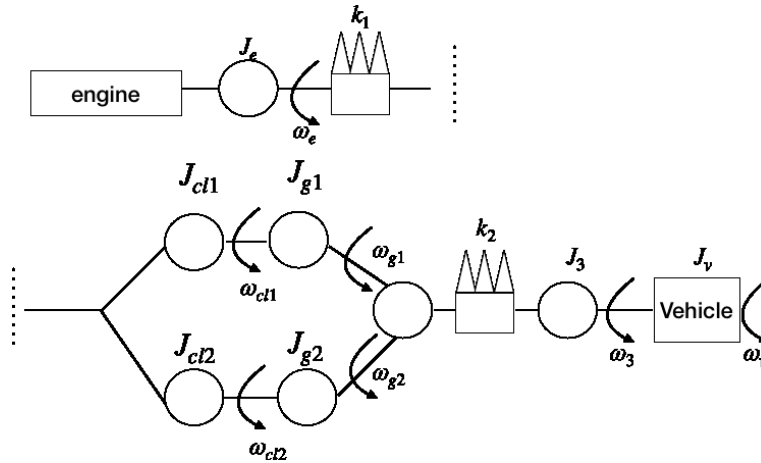


Figure 1. Dual clutch transmission diagram

Equations of moment equilibrium for the links shown in Figure 1:

$$J_e \ddot{\omega}_e = T_e - T_{cl1,2} \quad (1)$$

$$J_c \ddot{\omega}_c = T_{cl1} - k_1(\omega_{cl1} - \omega_{g1}); J_{g1} \ddot{\omega}_2 = k_1(\omega_{cl1} - \omega_{g1}) - i_{2n-1} k_2 (i_{2n-1} \omega_{g1} - \omega_3), \quad (2)$$

$$J_c \ddot{\omega}_c = T_{cl2} - k_1(\omega_{cl2} - \omega_{g2}); J_{g2} \ddot{\omega}_2 = k_1(\omega_{cl2} - \omega_{g2}) - i_{2n} k_2 (i_{2n} \omega_{g2} - \omega_3) \quad (3)$$

$$J_3 \ddot{\omega}_3 = k_2(i \omega_{g2} - \omega_3) - b(\dot{\omega}_3 - \dot{\omega}_v) - F_{r \text{ driving}} R \omega; \quad (4)$$

$$J_v \ddot{\omega}_v = b(\dot{\omega}_3 - \dot{\omega}_v) - T_l \quad (5)$$

where  $T_e$  – is the torque transmitted by the crankshaft of the internal combustion engine,  $T_{cl1,2}$  is the torque transmitted by the first and second clutches, respectively,  $T_l$  is the load moment from the side of the vehicle,  $i_{2n-1}$ ,  $i_{2n}$  are the gear ratios of the even and odd series;  $k_1$  – input shaft torsional stiffness,  $k_2$  – wheel drive shaft torsional stiffness,  $b$  – damping coefficient between wheel drive and vehicle inertia,  $F_{r \text{ driving}} R \omega$  – road drag force.

The approach, described in the study by F. Garofalo [3], was taken as a basis for the formation of state matrices that describe the phases of coupling and uncoupling. This model has been modified for continuous power transmission. The control vector in this system is the signals of the internal combustion engine torque  $T_e$  and the torque coming from the first or second clutch,  $T_{cl1,2}$ . Other vector and matrix parameters of the equations in the state space for the transmission as part of the system "engine – clutch – gearbox – wheel drive – car", where the dynamics of the car itself is considered simplified, take the form

$$x = \begin{pmatrix} \dot{\omega}_e \\ \omega_e - \omega_{cl} \\ \dot{\omega}_{cl} \\ \omega_{cl} - \omega_{g1,2} \\ \dot{\omega}_{g1,2} \\ k_2(i_{g1,g2}\omega_{g1,2} - \omega_3) \\ \dot{\omega}_3 \\ \dot{\omega}_v \end{pmatrix}, u = (T_e \quad T_{cl1,2})$$

$$A_{sl} = \begin{pmatrix} 0 & 0 & 0 & 0 & 0 & 0 & 0 & 0 \\ 1 & 0 & -1 & 0 & 0 & 0 & 0 & 0 \\ 0 & 0 & 0 & -k_1/J_{cl1} & 0 & 0 & 0 & 0 \\ 0 & 0 & 1 & 0 & -1 & 0 & 0 & 0 \\ 0 & 0 & 0 & k/J_2 & 0 & -i_{g1,2}/J_2 & 0 & 0 \\ 0 & 0 & 0 & 0 & k_2 i_{g1,2} & 0 & -k_2 & 0 \\ 0 & 0 & 0 & 0 & 0 & 1/J_3 & -b/J_3 & b/J_3 \\ 0 & 0 & 0 & 0 & 0 & 0 & b/J_v & -b/J_v \end{pmatrix}, B_{sl} = \begin{pmatrix} 1/J_e & -1/J_e \\ 0 & 0 \\ 0 & 1/J_c \\ 0 & 0 \\ 0 & 0 \\ 0 & 0 \\ 0 & 0 \\ 0 & 0 \end{pmatrix},$$

$$A_{st} = \begin{pmatrix} 0 & 0 & 0 & -k_1/(J_e+J_c) & 0 & 0 & 0 & 0 \\ 0 & 0 & 0 & 0 & 0 & 0 & 0 & 0 \\ 0 & 0 & 0 & k_1/(J_e+J_c) & 0 & 0 & 0 & 0 \\ 0 & 0 & 1 & 0 & -1 & 0 & 0 & 0 \\ 0 & 0 & 0 & k/J_2 & 0 & -i_{g1,2}/J_2 & 0 & 0 \\ 0 & 0 & 0 & 0 & k_2 i_{g1,2} & 0 & -k_2 & 0 \\ 0 & 0 & 0 & 0 & 0 & 1/J_3 & 0 & 0 \\ 0 & 0 & 0 & 0 & 0 & 0 & b/J_v & -b/J_v \end{pmatrix}, B_{st} = \begin{pmatrix} 1/(J_e + J_c) & 0 \\ 0 & 0 \\ 0 & 0 \\ 0 & 0 \\ 0 & 0 \\ 0 & 0 \\ 0 & 0 \\ 0 & 0 \end{pmatrix}$$

The ratio  $k_2(i_{g1,2}\varphi_1 - \varphi_2)$  characterizes the passage of the torque through an even or odd row with a shaft stiffness  $k_2$ . Introduced shift parameter  $d$  - to describe the clutch in the engaged and disengaged states. The general description of the transmission of torque through the transmission units during the operation of the two clutch modes is carried out using the state variables  $\dot{x}_{even}, \dot{x}_{odd}$ :

$$\begin{aligned} \dot{x}_{even} &= dA_{sl_{even}}x + (1-d)A_{st_{even}}x + dB_{sl_{even}}u + (1-d)B_{st_{even}}u + f(t); \\ \dot{x}_{odd} &= (1-d)A_{sl_{odd}}x + dA_{st_{odd}}x + (1-d)B_{sl_{odd}}u + (1-d)B_{st_{odd}}u + f(t); \end{aligned}$$

where  $f(t) = (0 \quad 0 \quad 0 \quad 0 \quad 0 \quad 0 \quad 0 \quad -\frac{T_l}{J_v})$  – vector describing the vehicle load.

### III. CONCLUSIONS

A dynamic transmission model was built with a continuous flow of power into the state spaces, taking into account the stages of clutching and decoupling of the discs for each row of gear ratios. This model makes it possible to estimate the angular velocities of the transmission elements; in the future, it can be used to develop a control system.

### REFERENCES

- [1] Asanov A.Z., Guryanova E.O. "Simulation of models of two-clutch transmission of robotic vehicles". Control and modeling problems in complex systems, 616 pp 54-59, 2017.
- [2] Dassen, M. H. M. Modelling and control of automotive clutch systems. (DCT rapporten; Vol. 2003.073). Technische Universiteit Eindhoven, 2003.
- [3] F. Garofalo, L. Glielmo, L. Iannelli and F. Vasca, "Smooth engagement for automotive dry clutch", Precision and Control 2001. Proceedings of the 40th IEEE Conference on, vol. 1, pp. 529-534, 2001.

# PARAMETERS OF LOAD TESTING MODELS: APPROACHES TO ESTIMATION

A. Markov, A. Paramonov

Belarusian State University of Informatics and Radioelectronics, Minsk, Republic of Belarus

[a.n.markov@bsuir.by](mailto:a.n.markov@bsuir.by)

## I. INTRODUCTION

The BigBlueButton video conferencing service was introduced to organize distance learning at BSUIR. Since April 2020, as Covid cases increased, the whole system load has increased drastically. During the testing phase, it turned out that increasing the capacity of the BigBlueButton server (BBB) relative to the initial parameters did not significantly increase the performance of the system. There were some problems with the translation of images and connections to the system. The problems started at video conferences with more than 50 participants. Also, there were time synchronization errors, new user login errors, errors adding a video stream. It became necessary to combine several computing facilities (servers and server clones) into a single cluster. A load balancing service was implemented on the video conferencing system to distribute load flows. By combining multiple servers into a single information space, the service allows you to access more resources and distribute the load between the connected servers, depending on the number of users (Round Robin algorithm). After load testing of servers with different configuration in the cluster, the output parameters were obtained to analyze the performance of the cluster and the balancer.

## II. RESULTS

Estimating the time graphs of the load testing model at the three stages, we can note a smooth increase in the number of users per time unit. Increase in the number of users per time unit proportionally loads computing power. So, for the cluster BBB1 (4 core CPU, 12 Gb RAM) with more than 200 users connected the load on the CPU increased and exceeded 100%. See on the Figure 1-a. Load growth above 100% is caused by execution of balancing algorithm on VCS entry point. Load above 100% can also be seen on BBB2 (8 core CPU, 14 Gb RAM) with increased parameters on CPU power. See on the Figure 1-b. Number of users with 200% load on BBB2. However, at the same time expanding the capacity of BBB3 cluster to 12 cores, the load at the connection moment exceeding 100% (Figure 1-c) did not affect the system performance. In this case, the number of users exceeded 300.

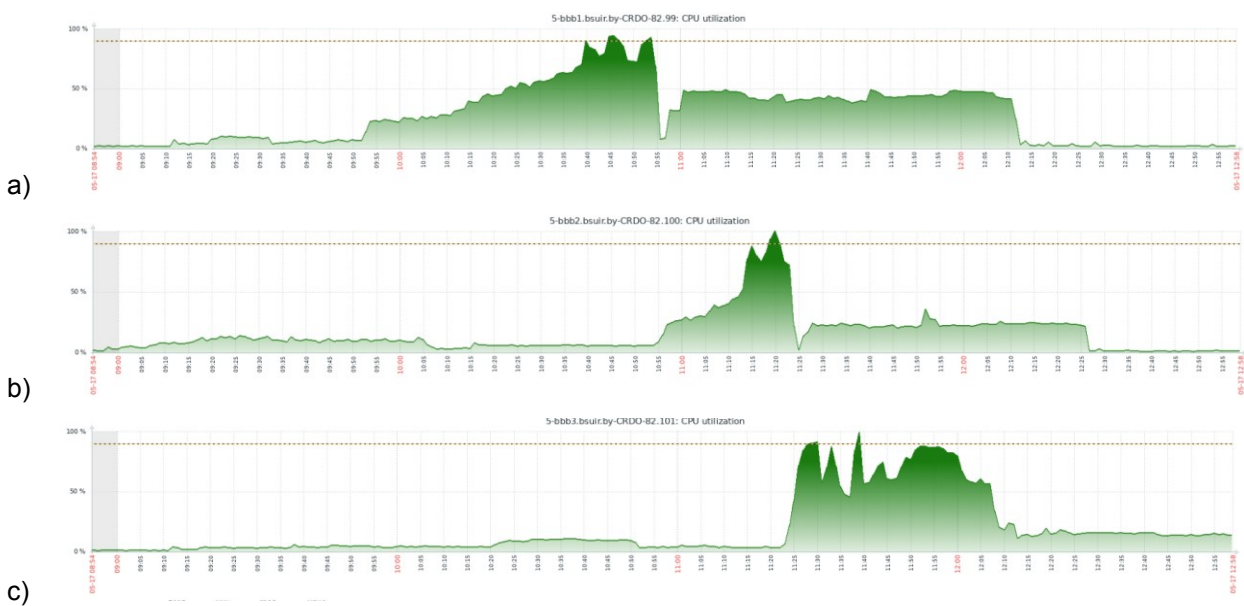


Figure 1. Load testing of the servers: a) BBB1, b) BBB2, c) BBB3

Regarding RAM load on the cluster, it can be noted that exceeding the 50% load mark is related only to the process of caching intermediate user data. However, given such an insignificant load on all tested clusters BBB1 and BBB2, the load can be considered minimal. At BBB1 and BBB2 testing stages multimedia flow from users' webcams was not tested. During the testing phases, a stream from user's webcams was added to the multimedia stream. Load percentage increase on RAM BBB3 – peaked at 65% of 12 Gb (about 8 Gb). See on the Figure 2.

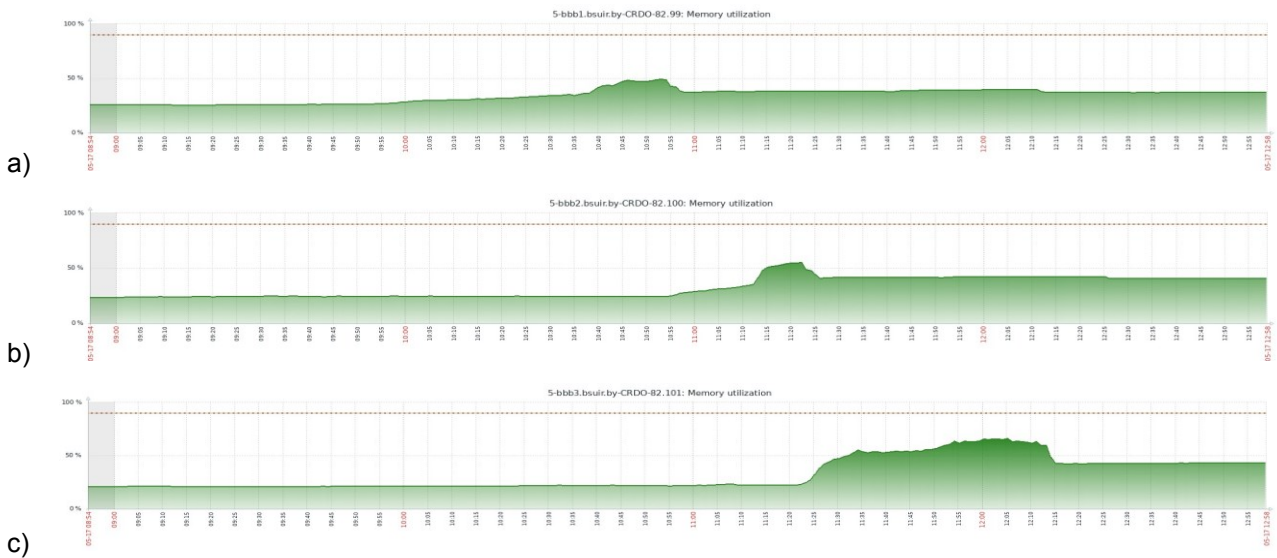


Figure 2. Load of RAM servers: a) BBB1, b) BBB2, c) BBB3

The network load when streaming video from users' webcams goes through the 192 interfaces to the internal bus. 160 interfaces are an external ISP bus. The video stream in case of the internal network reaches a network load about 150 Mbps, which is critical when building a network on unmanaged switches because of the bandwidth of the matrix and the aggregation channel. In case of access to the external network of the provider (as well as input from the external network) the load in the average values does not exceed 7 Mbit/s, which is enough even with a limited channel connection with speed up to 20 Mbit/s. The significant network load graph peaks (Figure 3 and 4) are related to the connection of an external video storage service (YouTube) to video broadcasting in VCS. It is also worth noting that video from a third-party service is cached in the stream, but doesn't have a critical effect on RAM, and works as a webcast, thereby not overloading the stream.

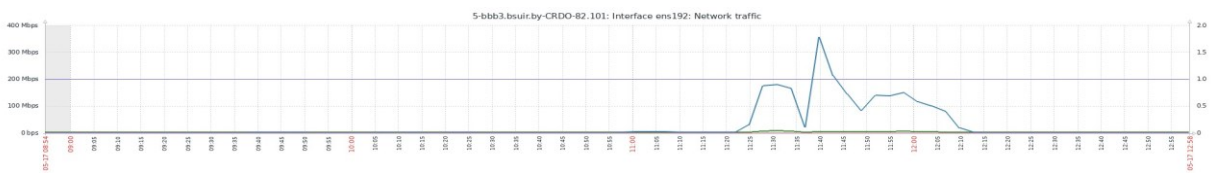


Figure 3. Internal network bus loading



Figure 4. Loading the external network bus to the provider

### III. CONCLUSIONS

Test methodology consisted of estimation of performance parameters both by control points – delays and response time of user connection to the room, control of CPU load, memory, network load (as well as in general and by interfaces of local network and provider), cache usage with unloading to disk array, and in visual quality control of system performance – control of audio and video stream desynchronization at the moment of video conference, delays during decoding of the final multimedia flow on endpoint users' devices, control over the package throughput on multimedia flow transfer step in real time. Quality characteristics, in this case, cannot be neglected as at the testing stage of cluster 3 with the use of web cameras on endpoints stable operation mode of VCS was achieved for up to 250 users. Cluster handled further load increase, but the quality of the conference deteriorated.

### REFERENCES

- [1] BigBlueButton documentation Available at: <https://docs.bigbluebutton.org/> (accessed 6 October 2021).
- [2] Round Robin Load Balancing Definition. Available at: <https://avinetworks.com/glossary/round-robin-load-balancing/> (accessed 6 October 2021).

## EFFECTIVENESS INDICATORS OF MODELING THE AIR SITUATION

R. R. Shatovkin, Y. A. Parshenkova, V. V. Filatov  
Federal State Budgetary Educational Institution of Higher Education "MIREA – Russian Technological  
University", Moscow, Russian Federation

[Shatovkin@yandex.ru](mailto:Shatovkin@yandex.ru)

### I. INTRODUCTION

Simulation of the air situation is aimed at ensuring the most accurate reproduction of the real situation at various levels of radar information processing. Reproduction of the air situation with high accuracy in aviation training complexes is necessary for the high-quality conduct of training for the flight management group and combat control officers.

Therefore, when modeling the air situation, it is important to achieve the required values of effectiveness indicators of its modeling, which is determined by the ability to simulate the situation of the required complexity with a high degree of accuracy and reliability. To assess the effectiveness of modeling, first of all, it is required to substantiate the indicators for which this assessment will be made.

The purpose of the work is to substantiate the effectiveness indicators of modeling the air situation, characterizing its accuracy and reliability.

### II. THE SOLUTION OF THE PROBLEM

Effectiveness indicators of modeling the air situation at the level of primary processing of radar information. At the output of the subsystem for the primary processing of radar information, data on the primary radar measurements (radar marks) are generated, containing the measured values of the observed parameters of the detected air targets.

The main observable parameters of the detected air targets include: the coordinates of the air target (slant range to the target, azimuth and elevation of the target relative to the radar station) and the radial speed of the air target relative to the radar station.

Measurements of the observed parameters are random variables with corresponding probability distribution laws. Consequently, the simulated situation at the level of primary processing of radar information should ensure that the distribution laws of the probabilities of measurements of the observed parameters coincide with those distribution laws that correspond to the tactical and technical characteristics of the radar station.

When simulating an air target of a given type, it is also necessary to form the law of the distribution of the amplitude of the echo-signal received by the radar station, which provides with a high probability the detection, measurement of parameters and identification of the air target.

The main characteristics of a radar station that affect primary measurements are: viewing area; review period; range and angular resolution; the accuracy of determining the coordinates of air targets [1].

To make a decision on the accuracy and reliability of modeling the air situation at the level of primary processing of radar information, a statistical decision criterion can be used with a given confidence level and a given confidence interval on the correspondence of the signal parameters of simulated air targets to the parameters of echo-signals of real air targets, taking into account the characteristics of the radar station.

Effectiveness indicators of modeling the air situation at the levels of secondary and tertiary processing of radar information. At the levels of secondary and tertiary processing of radar information, the same data composition is formed – time-related trajectory information about single and group air targets. The difference lies in the scale and completeness of the data on the air situation. Evaluation of the effectiveness of the simulation of the air situation can be carried out on the basis of particular indicators of the information capabilities of the radar station, the spatial and accuracy characteristics of the trajectory information, the characteristics of the continuity of the trajectory information, as well as the characteristics of the reliability and completeness of the trajectory information [2].

As well as for the level of primary processing, to make a decision on the accuracy and reliability of modeling the air situation at the levels of secondary and tertiary processing of radar information, a statistical decision criterion can be used with a given confidence level and a given confidence interval on the correspondence of the simulated air situation indicators to the considered indicators real air situation.

The effectiveness generalized indicator of modeling the air situation is a numerical measure of the correspondence of the real result obtained during the simulation to the required result. In this case, the real result is a random variable. This indicator has the physical meaning of the probability of meeting the requirements for modeling the air situation, in general, taking into account the requirements for the

performance indicators of modeling the air situation at the levels of primary, secondary and tertiary processing of radar information.

Figure 1 illustrates the proposed system of effectiveness indicators of modeling the air situation.

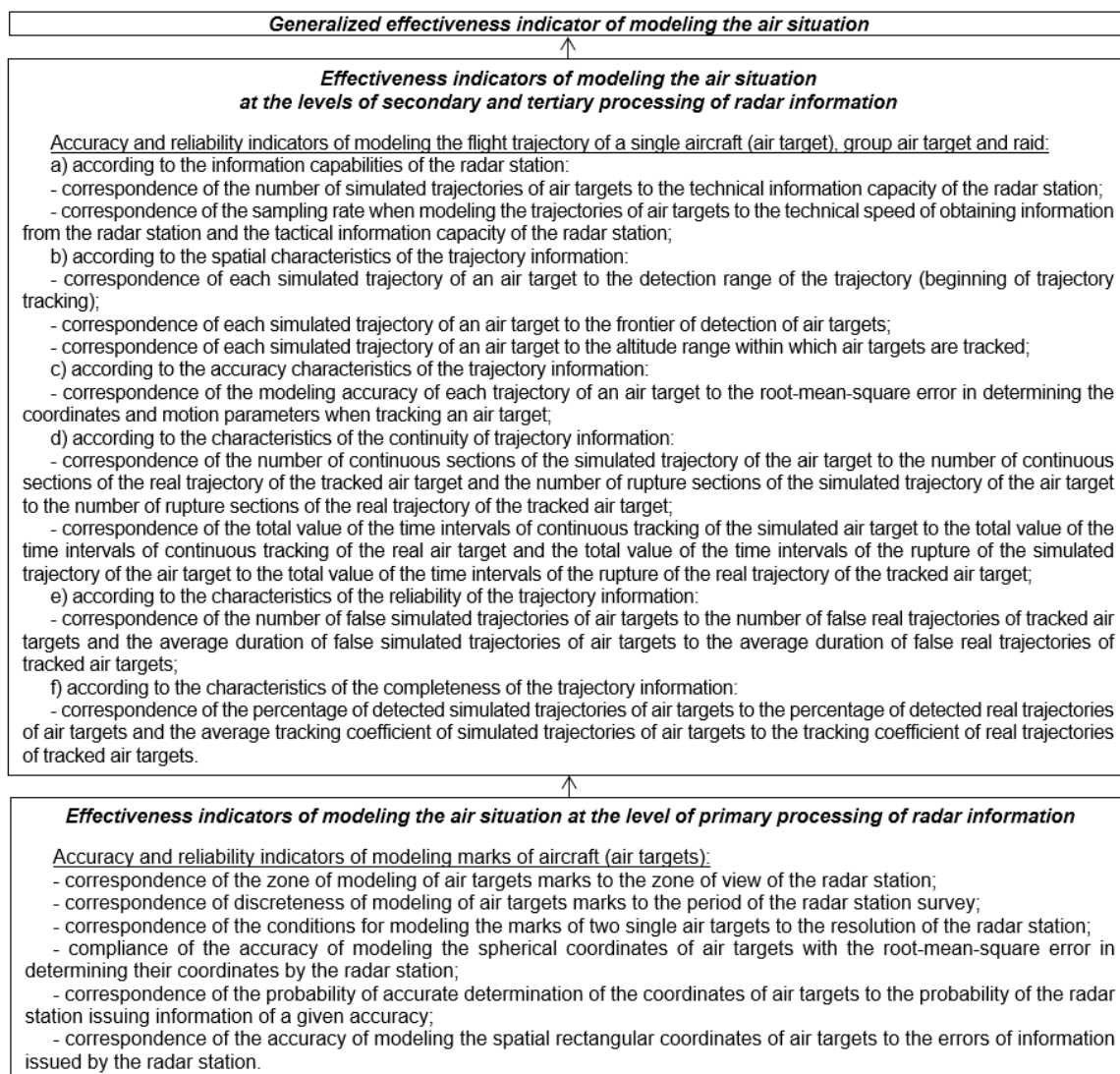


Figure 1. The system of effectiveness indicators of modeling the air situation

### III. CONCLUSIONS

As a result of the studies carried out, the indicators of the effectiveness of modeling the air situation were substantiated. These indicators characterize the accuracy and reliability of modeling for the levels of primary, secondary and tertiary processing of radar information, in particular, and the effectiveness of modeling the air situation, in general. The correspondence of the quantitative values of the accuracy and reliability indicators of modeling to the values of the quality indicators of the processing of radar information determines the effectiveness of the modeling. At the same time, the main feature characterizing the effectiveness of modeling the air situation according to the indicated indicators at the level of primary processing of radar information is the correspondence of the signal parameters of the simulated air targets to the parameters of the echo-signals of real air targets, and the main feature characterizing the efficiency of modeling the air situation according to the indicated indicators at the levels secondary and tertiary processing of radar information is the correspondence of the motion parameters and trajectories of simulated air targets to the motion parameters and trajectories of real air targets.

### REFERENCES

- [1] Finkelstein M.I. Fundamentals of radar: a textbook for universities. 2nd ed., Rev. and add. M.: Radio and communication, 1983.536 p.
- [2] Radio engineering systems / Yu.P. Grishin, V.P. Ipatov, Yu.M. Kazarinov and others; ed. Yu.M. Kazarinov. M.: Higher school, 1990.496 p.

## METHODOLOGY FOR ASSESSING THE EFFECTIVENESS OF MODELING THE AIR SITUATION

R. R. Shatovkin, A. M. Rusakov, B. G. Anufriev  
Federal State Budgetary Educational Institution of Higher Education "MIREA – Russian Technological University", Moscow, Russian Federation

[Shatovkin@yandex.ru](mailto:Shatovkin@yandex.ru)

### I. INTRODUCTION

When developing the technology of analytical-simulation modeling of the air situation, an important stage is the assessment of the values of the indicators of the effectiveness of its modeling, which will make it possible to make a well-founded conclusion about the degree of correspondence of the simulated air situation to the real situation.

It is quite obvious that to assess the effectiveness of modeling requires an appropriate methodology that takes into account the specifics and features of the subject area under consideration. The purpose of the work is to develop a methodology for assessing the effectiveness of modeling the air situation.

### II. THE SOLUTION OF THE PROBLEM

The results of the studies carried out aimed at developing a method for modeling the air situation, its conceptual model and substantiating the indicators for assessing the effectiveness of modeling the air situation showed that it is advisable to implement the methodology for assessing the effectiveness of modeling the air situation in three stages:

- the stage of assessing the effectiveness of modeling the air situation at the level of primary processing of radar information;
- the stage of assessing the effectiveness of modeling the air situation at the levels of secondary and tertiary processing of radar information;
- the stage of assessing the effectiveness of modeling the air situation, in general, according to the generalized indicator.

The stage of evaluating the effectiveness of modeling the air situation at the level of primary processing of radar information. At this stage, the parameters of the accuracy and reliability of modeling are calculated, characterizing the correspondence of the parameters (range, azimuth, elevation, radial speed) of the radar marks of the simulated air targets to the parameters of the radar marks of real air targets, and this compliance is checked.

The stage is based on the application of methods for testing hypotheses about the parameters of the probability distribution law and statistical estimation of the parameters of the probability distribution laws of random variables [1].

To implement the calculations, it is necessary to carry out a number of tests when simulating several variants of the air situation either in the form of field experiments or using a simulation model of the operation of the radar station.

At this stage of assessing the effectiveness of modeling the air situation, quantitative values of the indicators of accuracy and reliability of modeling are determined, characterizing the correspondence of the parameters of the radar marks of the simulated air targets to the parameters of the radar marks of real air targets, namely:

- estimates of the parameters of the empirical law of probability distribution of the parameter of the radar mark of the simulated air target;
- evaluating the accuracy of estimates of the parameters of the empirical law of probability distribution of the parameter of the radar mark of the simulated air target;
- assessing the reliability of estimates of the parameters of the empirical law of probability distribution of the parameter of the radar mark of the simulated air target.

These assessments make it possible to make a well-founded conclusion about the degree of correspondence of the simulated air situation to the real air situation at the level of primary processing of radar information.

The stage of evaluating the effectiveness of modeling the air situation at the levels of secondary and tertiary processing of radar information. At this stage, it is planned to carry out a number of statistical tests of the operation of the radar station when it is exposed to environment simulation tools for several variants of the virtual environment.

Evaluation of the effectiveness of modeling the air situation at the levels of secondary and tertiary processing of radar information is based on a comparison of reference information about the air situation and trajectory information issued by the radar station.

The input data for this stage of the proposed methodology are data on the reference air situation and data on the results of the operation of the radar station.

At this stage, assessing the effectiveness of modeling the air situation:

- by the method of simulation or semi-natural modeling, tests are performed several times for the same reference air situation;
- after each test, the identification of the trajectory information issued by the radar station and the reference trajectory information is performed;
- based on the results of identifying information about the trajectories of air targets, numerical values of indicators of trajectory information characteristics and information capabilities of a radar station are determined, which, in fact, are indicators of the effectiveness of modeling the air situation at the levels of secondary and tertiary processing of radar information;
- after the entire test cycle, the obtained values of the indicators are averaged;
- on the basis of the averaged values of the efficiency indicators for modeling the air situation, a substantiated conclusion is made about the degree of correspondence of the simulated air situation to the real air situation at the levels of secondary and tertiary processing of radar information.

The stage of assessing the effectiveness of modeling the air situation, in general, according to the generalized indicator. In the presence of random factors, the area of required values of efficiency indicators for modeling the air situation at the levels of primary, secondary and tertiary processing of radar information can be specified in the form of a fuzzy set. Then the probability of achieving the required level of efficiency of modeling the air situation is determined as the mathematical expectation of the membership function.

When calculating the generalized indicator by the method of statistical tests, a given membership function of a fuzzy set of values of modeling efficiency indicators at the levels of primary, secondary and tertiary processing of radar information is assumed.

The calculated value of the generalized indicator of the effectiveness of the simulation of the air situation allows us to make a well-founded conclusion about the degree of correspondence of the simulated air situation to the real air situation, in general.

### III. CONCLUSIONS

As a result of the research carried out, a three-stage technique for assessing the effectiveness of modeling the air situation has been developed, which allows:

- at the first stage – to determine the quantitative values of the parameters of the accuracy and reliability of modeling, characterizing the correspondence of the parameters of the radar marks of the simulated air targets to the parameters of the radar marks of real air targets, and, on their basis, make a well-founded conclusion about the degree of correspondence of the simulated air situation to the real air situation at the level of primary processing of the radar information;
- at the second stage – to determine the quantitative values of the parameters of the accuracy and reliability of modeling, characterizing the correspondence of the motion parameters and trajectories of the simulated air targets to the motion parameters and trajectories of real air targets, and, on their basis, make a substantiated conclusion about the degree of correspondence of the simulated air situation to the real air situation at the levels of secondary and tertiary processing of radar information;
- at the third stage – to determine the quantitative value of the generalized indicator of the effectiveness of modeling the air situation, and, on its basis, make a well-founded conclusion about the degree of correspondence of the simulated air situation to the real air situation, in general.

### REFERENCES

[1] Tikhonov V.I., Kharisov V.N. Statistical analysis and synthesis of radio engineering systems and devices. M.: Radio and communication, 1991. 608 p.



## ANALYTICAL-SIMULATION MODELING OF THE AIR SITUATION

R. R. Shatovkin, O. V. Trubienko, A. A. Khudyakov  
Federal State Budgetary Educational Institution of Higher Education "MIREA – Russian Technological University", Moscow, Russian Federation

[Shatovkin@yandex.ru](mailto:Shatovkin@yandex.ru)

### I. INTRODUCTION

Modeling the air situation, with a high degree of correspondence to the real air situation, in aviation training complexes in the interests of training and maintaining the necessary practical skills of the flight management group and combat control officers is a rather difficult task. The results of the analysis showed that it is impossible to effectively solve this problem only by analytical methods or only by methods of simulation modeling [1]. In this case, an appropriate approach is the combined use of analytical and simulation methods, which determines analytical-simulation modeling, which allows you to combine the advantages and eliminate the disadvantages of these methods.

In analytical-simulation modeling of the air situation, a preliminary decomposition of the modeling process into its constituent sub-processes is carried out. For those sub-processes, where possible, analytical models are used, and for the rest, simulation models are built. This approach makes it possible to cover qualitatively new properties that cannot be investigated using analytical or simulation modeling separately [2].

The diagram of analytical-simulation modeling of the air situation is shown in Figure 1.

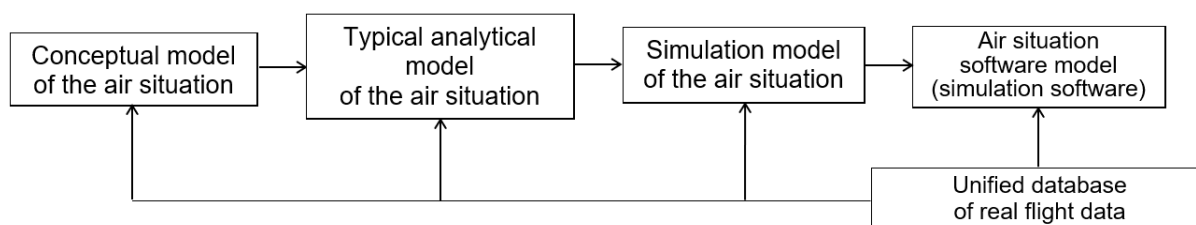


Figure 1. Scheme of analytical-simulation modeling of the air situation

With the indicated approach to modeling and the modeling scheme, it is required to develop an appropriate method of analytical-simulation modeling and a conceptual model of the air situation.

The purpose of the work is to develop a method of analytical-simulation modeling and a conceptual model of the air situation.

### II. THE SOLUTION OF THE PROBLEM

At present, the processing of radar information includes the following stages, corresponding to a change in the qualitative properties of the formed information: primary processing of information; secondary information processing; tertiary information processing [2].

The proposed method for modeling the air situation is determined by the established order of processing radar information and, by analogy with the processing stages, includes three levels of modeling:

- modeling the air situation at the level of primary processing of radar information;
- modeling the air situation at the level of secondary processing of radar information;
- modeling the air situation at the level of tertiary processing of radar information.

By modeling the air situation at the level of primary processing of radar information at time  $t$  is meant the formation of  $S$  marks of air targets.

The parameters of the echo-signal of each air target (delay time relative to the emitted signal, Doppler frequency, phase shift) are determined by its type and belonging to a particular type of aviation, location in space.

Modeling the air situation at the level of secondary processing of radar information at time  $t$  means the formation of trajectories  $S$  of air targets.

By modeling the air situation at the level of tertiary processing of radar information at time  $t$  is meant to simulate the tactical reception of aircraft of a specific type and type of aviation based on the trajectories of the corresponding  $S$  of air targets, which makes it possible to form a common air environment.

The proposed method for simulating the air situation is illustrated in Figure 2.

In accordance with the proposed method for modeling the air situation, due to the established order of processing radar information and implying three levels of modeling, a conceptual model of the air situation has been developed.

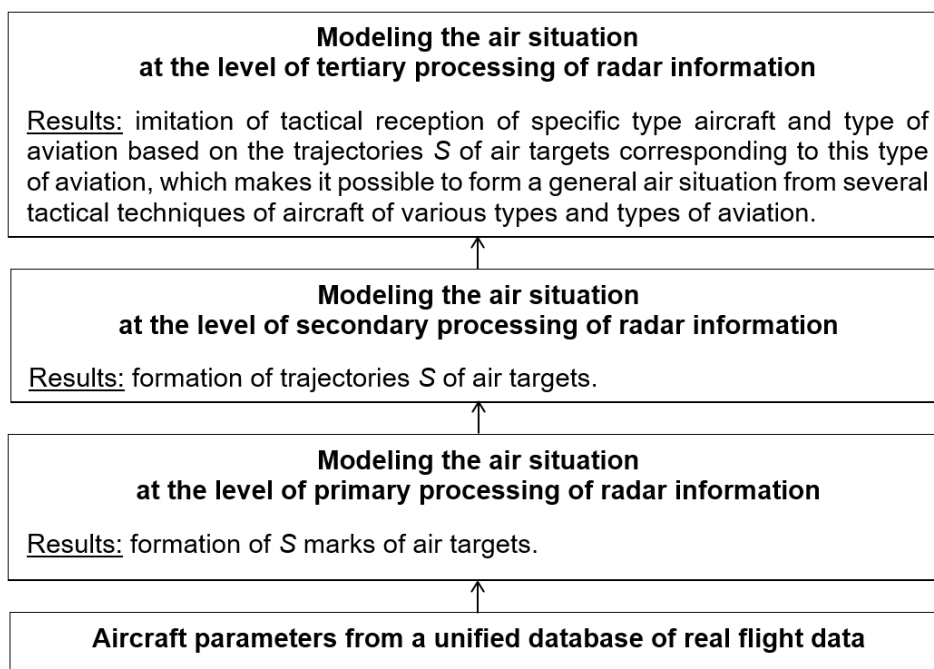


Figure 2. Method of analytical-simulation modeling of the air situation

The conceptual model of the air situation, in turn, reflects, with the completeness necessary for solving the task, the prototype system in one or another content aspect and is written in natural language using the provisions of naive logic. It is introduced in order to clarify the feasibility of using one or another theoretical apparatus when constructing a typical analytical and simulation models, concretizing this apparatus, taking into account the specifics of the modeled system.

The developed conceptual model of the air situation makes it possible to formally describe the air situation in accordance with the three accepted levels of its modeling and to determine for each level the corresponding type of modeling (for the first and second levels – the use of a typical analytical model and, accordingly, analytical modeling, for the third level – the use of a simulation model and, accordingly, simulation modeling).

### III. CONCLUSIONS

As a result of the research, a method for analytical-simulation modeling of the air situation has been developed, which makes it possible to form an air situation identical to the real air situation for three levels of radar information processing, due to: the formation of marks of air targets based on an analytical model – when modeling at the level of primary processing of radar information; formation of trajectories of air targets on the basis of an analytical model, taking into account the type of each air target, its belonging to one or another type of aviation, determining the parameters of the echo-signal of an air target – when simulating at the level of secondary processing of radar information; simulation of tactical reception of aircraft of a specific type and type of aviation based on the trajectories of the corresponding air targets and the formation of several tactical receptions of aircraft of various types and types of aviation of the general air situation – when simulating at the level of tertiary processing of radar information.

On the basis of the proposed method, a conceptual model of the air situation has been developed, which makes it possible to formally describe the air situation in accordance with the three adopted levels of its modeling and to determine the corresponding type of modeling for each level.

### REFERENCES

- [1] Babina O.I. Comparative analysis of simulation and analytical models // Simulation modeling. 2009. No. 1. P. 73–77.
- [2] Ermak S.N. Tactics of radio-technical troops: lecture notes. Minsk: Belarusian State University of Informatics and Radioelectronics, 2010. 281 p.

## ON THE RESTORATION OF THE BLURRED IMAGE OF A MOVING OBJECT

V. B. Feodorov, S. G. Harlamov

Russian University of Technology - MIREA, Cybernetics Institute, Department of Higher Mathematics,  
Moscow, Russian Federation

[fdorov@mail.ru](mailto:fdorov@mail.ru)

### I. INTRODUCTION

The task of restoring a blurred image of a moving object is well studied. In the case when the velocity of the object is known a priori, its solution is reduced, as is known, to the reversal of a discrete convolution.

However, in the case of restoring a blurred image obtained at the camera resolution limit, the traditionally used approach, based on replacing the integral in the convolution equation with the corresponding quadrature formula, leads to the need for interpolation of the original image, which is associated with an increase in the size of computer memory used in calculations. The report will show that this additional memory consumption can be avoided if, when sampling, the convolution equations are based not on quadrature formulas, but on the Kotelnikov interpolation row.

### II. RESULTS

Content: 1. Formulation of the problem. 2. Reduction restoring blurred image problem to the solution of first kind convolution type Fredholm integral equation. 3. Discretization of first kind convolution type Fredholm integral equation based on the trapezoids quadrature formula. 4. Discretization of first kind convolution type Fredholm integral equation based on the Kotelnikov interpolation row. 5. The influence of edge effects and the need to reconstruct the blurred edges of the image. Elimination of errors edges reconstruction by inverting convolution by Tikhonov regularization method. 6. The results of numerical experiments showing that if the value of the image "smudge" is expressed as an integer number of pixels, then the new approach works just as well as the traditional one based on the use of quadrature formulas. 7. The results of numerical experiments showing that the proposed method works even if the value of the image "smudge" is expressed in fractions of a pixel. At the same time, interpolation of the original image is not required.

### REFERENCES

- [1] G.I. Vasilenko, A.M. Taratorin. Vosstanovlenie izobrazhenij – M: Radio i svyaz', 1986. – 302 p. [in Russian].
- [2] V.S. Sizikov, Pryamye i obratnye zadachi vosstanovleniya izobrazhenij, spektroskopii i tomografii s MATLAB – SPb.: Lan', 2011. – 410 p. [in Russian].
- [3] R. Gonsales, R. Vuds. Cifrovaya obrabotka izobrazhenij — M.: Tekhnosfera, 2005. — 1072 p. [in Russian].

*Научное издание*

# **НАНОПРОЕКТИРОВАНИЕ, ТЕХНОЛОГИЯ, КОМПЬЮТЕРНОЕ МОДЕЛИРОВАНИЕ – NDTCS-2021**

Тезисы докладов XIX Международного симпозиума  
(Республика Беларусь, Минск, 28-29 октября 2021 года)

Book of abstracts of XIX International Workshop  
(Republic of Belarus, Minsk, October 28-29, 2021)

В авторской редакции  
Ответственная за выпуск *Л. А. Шичко*  
Компьютерная верстка *Д. Ч. Гвоздовский*

Подписано в печать 26.10.2021. Формат 60x84 1/8. Бумага офсетная. Гарнитура «Arial».  
Отпечатано на ризографе. Усл. печ. л. 15,58. Уч.-изд. л. 16,8. Тираж 30. Заказ 187.

Издатель и полиграфическое исполнение: учреждение образования  
«Белорусский государственный университет информатики и радиоэлектроники»  
Свидетельство о государственной регистрации издателя, изготовителя,  
распространителя печатных изданий № 1/238 от 24.03.2014,  
№ 2/113 от 07.04.2014, № 3/615 от 07.04.2014.  
Ул. П. Бровки, 6, 220013, г. Минск